

Models of bauxitic pisolith genesis: data from Weipa, Queensland

David Brenton Tilley

The Centre for Australian Regolith Studies



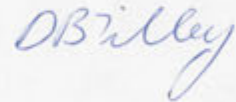
The Australian National University

A thesis submitted for the degree of Doctor of Philosophy
of The Australian National University

December 1994

DECLARATION OF ORIGINALITY

I David Brenton Tilley hereby declare that to the best of my knowledge the following thesis is original research carried out by me unless otherwise stated.



David Brenton Tilley

ACKNOWLEDGEMENTS

This Ph.D. project was made possible by the generous financial support of COMALCO Aluminium Ltd, for which we are most appreciative.

Several people have contributed significantly during the course of study, culminating in the writing of this thesis. My supervisors, Tony Eggleton of the Australian National University and Graham Taylor of the University of Canberra are thanked for their guidance and review of the thesis manuscript. A special thanks goes to Tony Eggleton for his transmission electron micrograph of tohdite and detailed revision of the chapter entitled "Tohdite ($5\text{Al}_2\text{O}_3 \cdot \text{H}_2\text{O}$) in bauxites from northern Australia". Lengthy discussions with Mike Morgan, Maité Le Gleuher, Ma Chi and Iain D. Campbell gave me valuable insights into the intricacies of bauxite mineralogy and evolution. Peter Fredericks and Ray Frost are gratefully acknowledged for the use of the Fourier transform infrared spectrometer at the Queensland University of Technology. The technical staff at the Geology Department of the A.N.U. are warmly thanked for their assistance they so freely gave over the three years. Electron microscopy was carried out at the Electron Microscopy Unit of the Research School of Biological Sciences. The staff at the unit are thanked for their tuition in the use of the equipment. John Taylor of the CSIRO helped with entering tohdite into the SIROQUANT system. Denes Bogsányi of the Research School of Chemistry, A.N.U. acquired the infrared spectra of tohdite and eta-alumina. Nick Ware and John Fitzgerald of the Research School of Earth Sciences are acknowledged for their instruction and use of the electron microprobe and analytical TEM.

DEDICATION

*I dedicate this thesis to my mother, Brenda Fay Tilley,
who passed away on the 1st July 1994
and to my father, Ronald Neville Tilley.*

ABSTRACT

The mineralogy of bauxitic pisoliths from Weipa and Andoom, North Queensland was investigated to establish the processes responsible for pisolith evolution.

Siroquant, a computer program developed by the CSIRO, was used in conjunction with XRD to quantify bauxite mineralogy. Analysis of 42 pisoliths selected randomly from 16 drill holes, showed that almost half contained more than 20 weight % of a material not accounted for by identifiable well-crystallised minerals and yielding very broad diffraction maxima. This component is termed poorly-diffracting material (PDM). Pisoliths containing a high proportion of PDM were examined using differential XRD techniques. The examination led to the discovery of tohdite ($5\text{Al}_2\text{O}_3\cdot\text{H}_2\text{O}$) and eta-alumina ($\eta\text{Al}_2\text{O}_3$): significant mineral phases that have not been reported in bauxites before now due to their poorly-diffracting nature. Other phases present in pisoliths from Weipa and Andoom include gibbsite (~ 51 wt. %), boehmite (~ 11 wt. %), kaolinite (~ 7 wt. %), hematite (~ 6 wt. %), anatase (~ 2 wt. %), quartz (~ 1 wt. %) and zircon (< 1 wt. %).

Micro-sampling and quantitative XRD analysis of concentric zones within individual pisoliths, demonstrated a radial variation in mineralogy. Analyses showed a strong tendency for kaolinite and gibbsite to be concentrated in the rim of pisoliths while PDM and quartz tended to be richer in the core. Pisoliths may either have a higher percentage of boehmite in the core or in the rim depending on the particular pisolith analysed. A hematite-rich band surrounding the core was observed in many pisoliths.

Pima II, a compact hand-held infrared spectrometer, was tested on bauxite samples which had previously been analysed with *Siroquant*, to assess its capability in determining bauxite mineralogy at the mine face and during drilling. The technique shows excellent promise for on-site grade control, particularly for determining the kaolinite content of bauxite.

Using the facilities of the Queensland University of Technology, infrared micro-spectroscopy was performed on individual pisoliths. Maps with a spatial resolution of 200 μm were constructed using the acquired data array. The study revealed the presence of mm-scale banding of gibbsite and boehmite in the cortex of pisoliths.

Pisolith thin-sections were mapped using techniques akin to geological field mapping. Textural and mineralogical maps were drawn on a photo-micrographic base. Mapping of the micro-sedimentological layering within pisoliths revealed the presence of unconformities, which are ascribed to periods of erosion or non-deposition.

Three different processes were found to be responsible for the development of pisoliths; namely spherulisation, agglomeration and cortication. Spherulisation is the development of aluminous spherules in a kaolinitic plasma, in response to the desilicification of kaolinite during bauxitisation. Agglomeration is associated with the epigenetic replacement of kaolinite with hematite, resulting in the formation of ferruginous-kaolinite nodules. The process of cortication, which is intrinsically linked to bauxitisation, leads to the formation of concentrically-banded cortices around spherules and nodules.

Constituting a minor part of the Weipa and Andoom bauxite deposits are egg-like and tubular structures of bauxitic composition, ranging in length from 2 to 5 cm which are designated *bauxitic compound pisoliths*. The internal chamber of such structures usually contain ordinary bauxitic pisoliths or oöliths, however occasionally they are found to be completely barren. Four different types of compound pisolith have been identified in the Weipa area. The *nodular* form externally resemble the underlying ferruginous-kaolinite nodules. *Common* compound pisoliths on the other hand, are more smoother and symmetrical in shape. Less common families include the root-like *tubular* compound pisoliths and the large *ovate* type.

It was shown that both common and nodular compound pisoliths are derived from the bauxitisation of large ferruginous-kaolinite nodules. The present-day distribution of compound pisoliths, provides a valuable tool for reconstructing the appearance of the weathering profile at specific times in the past. The study revealed evidence for three major periods of bauxitisation, each separated by a ferruginisation-kaolinisation phase associated with nodule development. The climatic and hydrological conditions of today favour the formation of a mottled zone and nodular ferruginous-kaolinite layer which overprints part of the previously occurring bauxite.

Ovate compound pisoliths, similar in morphology to calcareous structures found in South Australia, are believed to be the pupation cells of the large, wingless weevil, *Leptopius*. Tubular compound pisoliths are thought to be the bauxitised remains of root concretions.

CONTENTS

<i>chapter</i>		<i>page</i>
	Declaration of originality	ii
	Acknowledgements	iii
	Abstract	iv
	Contents	vi
	Preface	vii
	Aims of the study	viii
PART ONE REVIEW OF THE LITERATURE		
1.	Contemporary knowledge of laterite, bauxite and pisoliths	
1.1	Definitions	1
1.2	Evolution of deep weathering profiles	4
1.3	Chemistry of bauxite formation	9
1.4	Evolution of lateritic and bauxitic pisoliths	17
1.5	Other spherical structures in geology	21
1.6	Worldwide distribution of lateritic bauxite	21
1.7	Australian bauxite deposits	22
PART TWO METHODOLOGY AND RESULTS		
2.	Optical microscopy	28
3.	Scanning electron microscopy	48
4.	Fourier transform infrared spectrometry	66
5.	Near-infrared reflectance spectrometry	83
6.	Quantitative X-ray diffraction	104
PART THREE INTERPRETATION		
7.	Tohdite ($5\text{Al}_2\text{O}_3 \cdot \text{H}_2\text{O}$) in bauxites from northern Australia	138
8.	Eta-alumina ($\eta\text{Al}_2\text{O}_3$); a new bauxite mineral	148
9.	Compound pisoliths	157
10.	Evolution of bauxitic pisoliths	185
	Appendices	201
	Bibliography	207

PREFACE

Bauxite is a residually derived earthy rock or sediment composed mainly of aluminium hydroxide and oxy-hydroxide minerals such as gibbsite ($\text{Al}(\text{OH})_3$) and boehmite ($\text{AlO}(\text{OH})$). Other minerals which may be present in bauxite include hematite (Fe_2O_3), kaolinite ($\text{Al}_2\text{Si}_2\text{O}_5(\text{OH})_4$), quartz (SiO_2) and anatase (TiO_2). During bauxite's formation, relatively immobile elements such as aluminium and titanium are enriched while iron, silicon and more mobile elements are depleted. Constituting the bauxite deposits of the Weipa area are small spheroidal and rounded bodies 2 to 50 mm in diameter which possess internal concentric banding. These particles are termed bauxitic pisoliths.

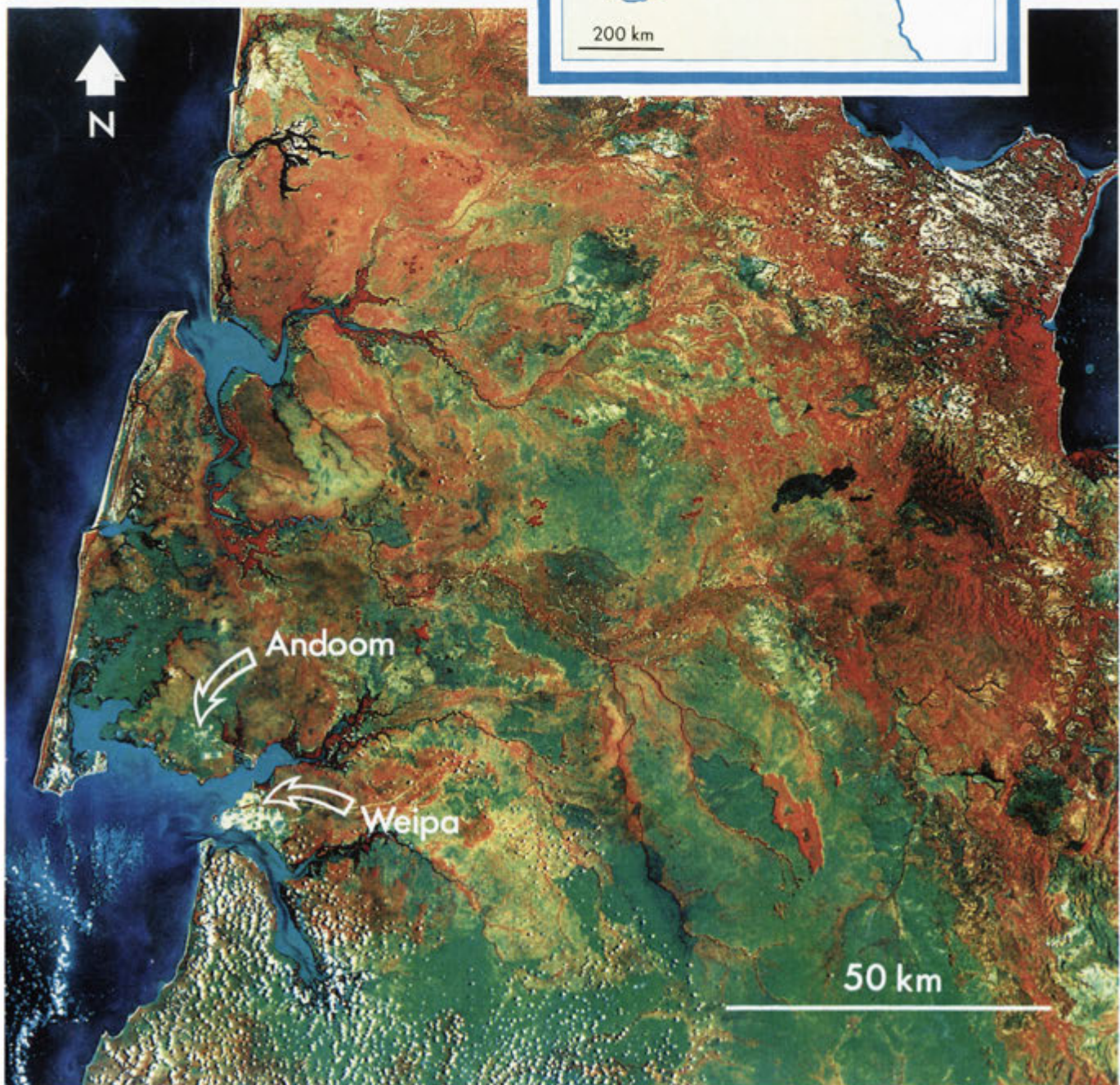
It is in the interest of Australia's economy to fully understand the mineralogy and evolution of our bauxite deposits. For over a decade Australia has been the major producer of bauxite to the world market. With the recent discoveries of large, high grade deposits elsewhere in the world, Comalco and other Australian producers have come under fierce competition. Comalco is looking towards improving mining and beneficiation techniques, so that the extensive bauxite deposits at Weipa in North Queensland can be utilised to their full potential. It is envisaged that these improved methods will help to increase the grade and thus add substantial value to the product ore. At present a number of research projects are being undertaken at various centres throughout Australia to address these problems. The collective title for this nationwide effort is the *Snow White Project*. The four centres involved are; the CSIRO, Division of Mineral Products, Perth; Comalco Mineral Products, Weipa; Comalco Research Centre, Melbourne; and the Centre for Australian Regolith Studies, Canberra. The following Ph.D thesis entitled 'Models of bauxitic pisolith genesis: data from Weipa, Queensland' is part of the Snow White Project and was funded by Comalco Aluminium Limited.

*Industrious mites build their castles,
Having done so for countless years,
Shifting and sorting the tiny red balls,
Upon an earth made of millions of spheres.*

Cape York Peninsula as seen from a satellite 620 kilometres above Earth. Comalco's Weipa bauxite mining operation appears as the small white area by the side of the large bay located in the middle of the west coast.

The red areas seen at the head of the broad estuaries and following seasonal creeks and rivers, depict dense mangrove vegetation. (Scale 1 centimetre equals 10 kilometres approx.)

Imagery reproduced with the permission of the Australian Landsat Station, Department of Science and Technology.



AIMS OF THE STUDY

The major objectives of the project are;

1. To determine the physico-chemical processes involved in bauxitic pisolith formation and to develop a theory for their evolution.

At present, there appears to be a general uncertainty in the literature regarding the physico-chemical processes responsible for the formation of bauxitic pisoliths, however those which form in ferruginous laterite are adequately explained by Nahon (1991). The study of the microstructure and mineralogy of bauxitic pisoliths is essential in understanding the physico-chemical processes involved in their formation. As very little is known of how long a pisolith takes to evolve, it is hoped that some insight into this matter will be gained thereby providing valuable clues to the timing of events leading to the formation of the bauxite deposit as a whole.

2. To develop an inexpensive routine method of mapping the mineralogy of individual pisoliths.

The development of an inexpensive routine method of mapping the mineralogy of pisoliths is the main economic objective of the Ph.D. project. Of particular interest is the gibbsite/boehmite and kaolinite distributions.

A boehmite-rich ore is of a lower value than a gibbsitic ore, as boehmite requires a higher temperature to dissolve in caustic soda, making the Bayer Process a more expensive stage in the refinement of alumina. The energy required to raise the temperature of the caustic soda so that boehmite dissolves, is an additional expense that can be best avoided by selective mining.

An ore containing even minor quantities of kaolinite is reduced markedly in value, due to kaolinite being readily dissolved in caustic soda. When kaolinite is present in the ore, a greater quantity of caustic soda is required to dissolve the bauxite. As caustic soda is used in such vast quantities at alumina refineries, any small percentage decrease in kaolinite content not only substantially increases the value of the ore itself but there are consequential savings to the alumina refineries as well.

With the knowledge gained from mineral distribution maps, mine geologists will be able to control with greater accuracy, the mineralogical content of the product ore. Improvements in the beneficiation of the ore may also be brought about by knowing where particular minerals are distributed within pisoliths.

PART ONE

Review of the Literature

Chapter 1

Contemporary knowledge of laterite, bauxite and pisoliths

1.1 Definitions

1.1.1 Laterite

The term *laterite* which is derived from the Latin *later* meaning brick, was first used by Buchanan (1807) on his travels through India, to designate a ferruginous residual deposit having a porous structure. He observed that the fresh material could be cut with a knife and would subsequently harden irreversibly upon exposure to air. This made laterite an inexpensive building material which was comparable to bricks in its strength and durability.

In subsequent papers, the ability to harden no longer became essential in the definition, as difficulty arose in ascertaining the original hardness of many laterites. This coupled with inadequate measures of the hardness of the product led to broadening of the definition to include a variety of hard and potentially hard materials.

The combination of many chemical and mineralogical studies over the past century has led to a definition proposed by Schellmann (1983). "*Laterites are products of intense subaerial rock weathering. They consist predominantly of mineral assemblages of goethite, hematite, aluminium hydroxides, kaolinite minerals and quartz. The $\text{SiO}_2 : (\text{Al}_2\text{O}_3 + \text{Fe}_2\text{O}_3)$ ratio of a laterite must be lower than that of the kaolinized parent rock in which all the alumina of the parent rock is present in the form of kaolinite, all the iron in the form of iron oxides and which contains no more silica than fixed in the kaolinite plus the primary quartz. This definition includes all highly weathered materials, strongly depleted in silica and enriched in iron and alumina, regardless of their morphological and physical properties (fabric, colour, consistency, etc).*" Despite this, a universally accepted definition for *laterite* is still lacking.

Tardy *et al.* (1993) have classified laterites according to their degree of accumulated iron and aluminium. In their classification scheme, *ferrites* are dominantly iron-rich, composed almost entirely of hematite and goethite and are generally not nodular or pisolitic. *Ferallites* contain both iron and aluminium in the form of hematite and goethite in association with kaolinite and gibbsite. They generally occur as ferricretes in which hematite and kaolinite occur together to form mottles and nodules.

Allites or lateritic bauxites are mainly aluminium-rich and contain minerals such as gibbsite and boehmite in association with kaolinite. Iron-rich minerals such as hematite, goethite and maghemite may also be present within lateritic bauxites.

1.1.2 Bauxite

The term *bauxite* was first used by Berthier (1821) to denote an alumina-rich eluvial sediment found near Les Baux in France. Bauxite is a special type of laterite which is enriched in free aluminium hydroxide minerals such as gibbsite ($\text{Al}(\text{OH})_3$), boehmite ($\gamma\text{AlO}(\text{OH})$) and diaspore ($\alpha\text{AlO}(\text{OH})$). The formation of bauxite is the result of an intense form of lateritization whereby silica becomes severely depleted and alumina strongly enriched within the bauxite horizon. Bauxite, ferricrete and kaolin together with transitional rock types can be represented on a triangular diagram originally devised by Bárdossy (1963), (Figure 1.1).

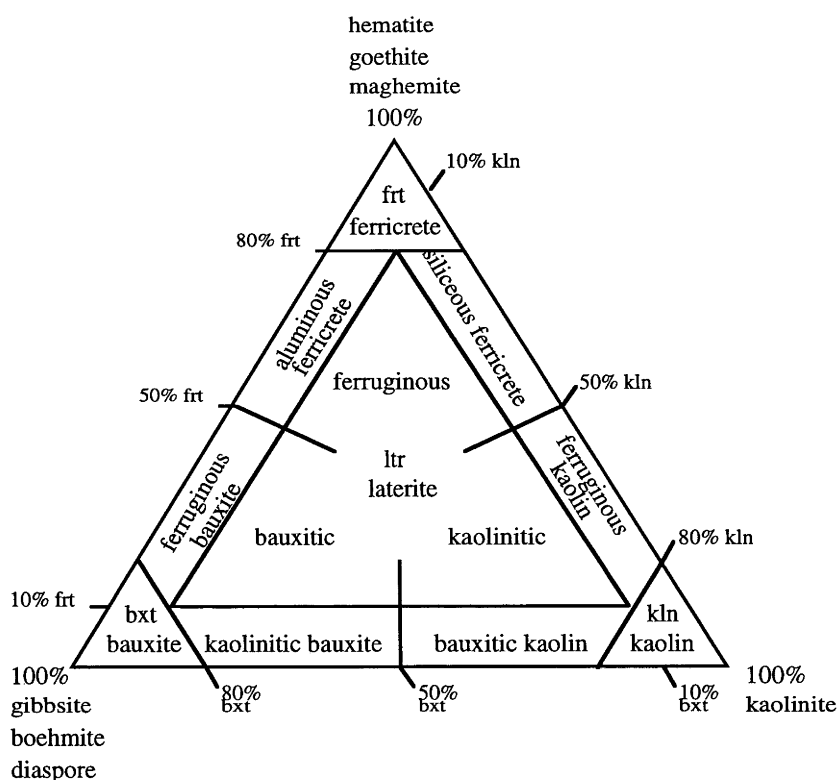


Figure 1.1

Tardy *et al.* (1993) have classified lateritic bauxites according to the nature of the constituent minerals and their relative distribution within the profiles. *Protobauxites* are lateritic soils formed in very humid climates in which gibbsite and goethite occur in association with each other. *Orthobauxites* are non-concretionary and dominantly gibbsitic. Iron in the form of hematite and/or goethite may be concentrated in the top part of orthobauxites. It is not a general requirement for kaolinite to be present at the base of the orthobauxite profile. The idealised laterite-saprolite profile discussed in the following pages is a typical orthobauxite. *Metabauxites* are concretionary and/or pisolitic and tend to be boehmitic. Iron is commonly dissociated from aluminium in metabauxites and often becomes concentrated as hematite and goethite in a ferruginous kaolinite layer at the base of the bauxite layer. Kaolinite is always present beneath the metabauxite profile. The bauxite deposit at Weipa is considered to be a typical example of a metabauxite. *Cryptobauxites* are gibbsitic and are interbedded between upper and a lower kaolinitic horizons.

1.1.3 Pisolith

The term *pisolith* is used in the literature to designate a small (2mm-50mm), generally spherical body, usually displaying internal concentric banding and commonly existing within a bauxite or laterite. Often the term *pisolite* is used as a synonym for pisolith, however in the strict sense, the term pisolite should only be used for a rock-like, consolidated mass of pisoliths. The term *pisoid* is sometimes used in the literature as a legitimate synonym for pisolith. A similar body of less than 2mm in diameter is termed an *oöolith*. An *oöolite* is a rock-like mass consisting of oöoliths. It is customary to use the term *pisolitic* or *oölitic* when describing the texture of any type of rock which is made up of such bodies. For example, a pisolitic bauxite, is a bauxite which is predominantly composed of pisoliths. Likewise, an oölitic limestone is a limestone which consists mainly of oöoliths.

The *cortex* of a pisolith is the soft, porous outer layer which is concentrically banded and is composed of relatively coarse, crystalline material. The *core* is made up of hard, dense and extremely fine crystalline material which may or may not contain relatively coarse grains of quartz. The cores of pisoliths are often dissected by a network of radial and cross-cutting veins and fissures. The *cortices* (plural form of cortex) of bauxitic pisoliths range in thickness from thin coatings to sets of concentric bands comprising the whole pisolith (Figure 1.2).

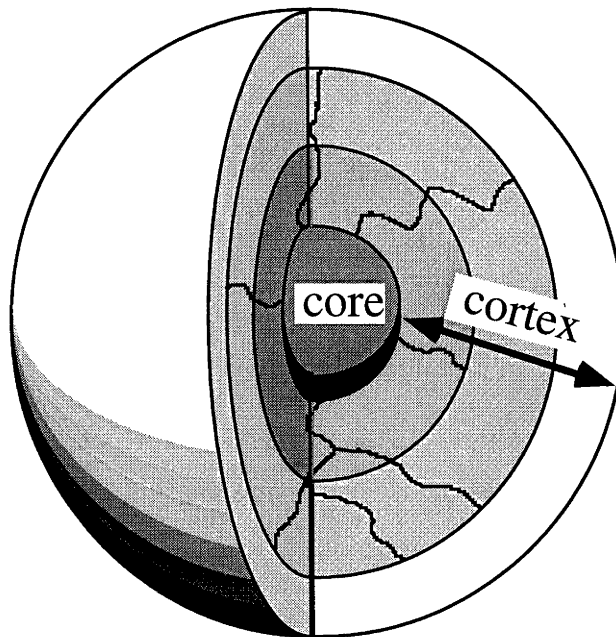


Figure 1.2

Bauxitic pisoliths are made up of complex mixtures of hydrated aluminium and iron-rich minerals. The dominant aluminium-rich mineral within the bauxitic pisoliths of Weipa is gibbsite ($\alpha\text{Al}(\text{OH})_3$), while boehmite ($\gamma\text{AlO}(\text{OH})$) and kaolinite ($\text{Al}_2\text{Si}_2\text{O}_5(\text{OH})_4$) are present in varying amounts. Iron occurs in the pisoliths as hematite ($\alpha\text{Fe}_2\text{O}_3$) and goethite ($\alpha\text{FeO}(\text{OH})$). Common accessory minerals identified, include quartz (SiO_2), anatase (TiO_2), rutile (TiO_2), and zircon (ZrSiO_4).

1.2 Evolution of deep weathering profiles

1.2.1 The idealised laterite-saprolite profile

There is so much variation in the scale and structure of lateritic weathering profiles that it is a misnomer to call any particular profile, 'typical'. The laterite itself may range in thickness from a few centimetres to tens of metres and the underlying saprolite from a few millimetres to over 100 metres. There appears to be no direct relationship between the thickness of the saprolite and the overlying laterite or bauxite (McFarlane, 1983). It must be emphasised that in reality there are no typical laterite-saprolite weathering profiles. The idealised profile described in the following paragraphs is greatly outnumbered by atypical profiles. For this reason it should be used only as a guide to what might be expected.

The idealised laterite-saprolite weathering profile consists of four distinct horizons (Figure 1.3). The uppermost one is the *residual soil horizon*. Mechanical and chemical weathering products of the underlying horizon are mixed with decaying organic matter to form the soil. The colour of the horizon depends on the underlying horizon, the degree of leaching and the amount of organic matter present. (Bárdossy and Aleva, 1990)

Below the residual soil horizon is the *duricrust horizon*. The formation and recrystallization of iron minerals within the horizon generally causes it to be the hardest part of the profile. The duricrust is usually strongly coloured, ranging from brick red through reddish brown to bluish black. (Bárdossy and Aleva, 1990)

Beneath the duricrust is the *bauxite horizon*. It is generally characterised by a decrease in iron accumulation with a corresponding decrease in hardness. The bauxite horizon may either be homogeneous throughout or consist of several layers which vary in colour, composition, texture and structure from one layer to another. At the other extreme the horizon may be laterally inhomogeneous. The bauxite horizon commonly varies in colour from off-white, through pinkish, yellowish and orange hues, to tan, orange and reddish brown. (Bárdossy and Aleva, 1990)

The underlying *saprolite horizon* contains mainly aluminium-sheet silicate weathering products of the parent rock such as kaolinite, as well as other minerals such as quartz, rutile and zircon which are resistant to weathering in the saprolite environment. Within the lower part of the horizon, minerals such as illite, nontronite and montmorillonite may exist. The saprolite horizon may sometimes consist of two zones; a lower thick zone which contains relict textures and structures and an upper thin zone devoid of such features. The saprolite is usually light in colour, with whitish, pinkish, orange and reddish hues. The colours may also be variegated or mottled (Bárdossy and Aleva, 1990).

1.2.2 Profile evolution

McFarlane (1983) explained the evolution of lateritic weathering profiles as a process involving three successive stages of development, termed *residual accumulation*. The first stage results in the loss of most mobile components and the accumulation of less mobile ones. During the second stage, less mobile components are lost while resistant ones are accumulated. Finally, the third stage involves the loss of resistant components and the accumulation of very resistant ones. Weathering products formed during each successive stage provide parent material for the following stage. This process results in the accumulation of the most resistant components during the third stage (McFarlane, 1983). It is more likely however, that residual accumulation is unpunctuated and that there is a progressive loss of less resistant components relative to more resistant ones.

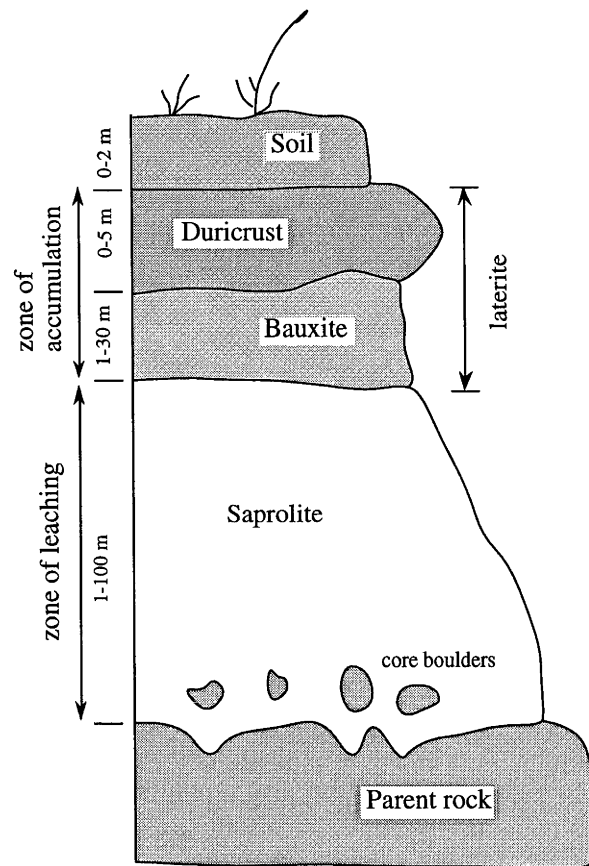


Figure 1.3

Sketch of an idealised laterite-saprolite weathering profile
(adapted from Bárdossy and Aleva, 1990).

An alternative hypothesis which may explain profile evolution is termed *upward enrichment*. The hypothesis attempts to explain profile evolution by way of seasonal oscillations of the water table and/or capillary action causing the simultaneous depletion of lower horizons and enrichment of upper ones. McFarlane (1983) pointed out that concentration of anatase (TiO_2) in the same horizon as aluminium enrichment goes strongly against the upward enrichment hypothesis because anatase is either a primary or an authigenic mineral which cannot move up the profile.

Whatever the case, it is apparent that both silica-alumina and iron-alumina separation have to occur during the formation of bauxite. Iron-alumina separation is important during the weathering of iron-rich parent rocks such as basalts, otherwise the end product would be iron-rich laterite rather than bauxite (Samama, 1986).

1.2.3 Climatic conditions

It is generally believed that millions to tens of millions of years are required for the bauxitisation of thick lateritic profiles. This allows for the possibility that the bauxite has evolved under many different climatic and geomorphological regimes during that time (Tardy, 1993).

Traditionally, tropical monsoon-type climates were viewed upon as being essential for laterite formation. Mounting evidence suggests that a tropical climate is not required and that a seasonally wet and dry climate with a high annual rainfall appear to be the only necessary climatic conditions.

Owen (1954) suggested that lateritization to maturity will eventually occur even in temperate climates as long as the rainfall is sufficiently high, there is tectonic stability and the relief is low. Owen's reasoning appears to be that lower temperatures merely slow down the rate of chemical weathering during lateritization.

The determination of the age, intensity and duration of weathering of the early Cainozoic inter-basaltic bauxites on the Monaro of New South Wales by Taylor *et al.* (1991), has contributed to our knowledge of the tectonic setting and climate in which lateritization occurred. Based on studies of fossil pollen and wood, Taylor *et al.* (1992) concluded that the bauxites on the Monaro developed during the late Palaeocene in a cool, wet and thermally seasonal climate. Oxygen isotope ratios in kaolinite formed in the weathering profiles indicate cool to cold climatic conditions existed at the time of lateritization (Bird and Chivas, 1988).

Notwithstanding these observations, the majority of lateritic bauxites have formed under the influence of tropical climates, which only differ slightly in their rainfall, temperature and the length of the dry season. Significant changes in the climate may result in the generation of a different type of laterite. For instance, under the influence of a drier climate, a ferricrete may be generated at the base of a bauxite profile, while under a wetter climate a pre-existing ferricrete may evolve into a bauxite within a soft kaolinitic horizon (Tardy, 1993).

Temperature appears to be an important factor in controlling the ratio $Hm/(Hm+Gt)$ formed from the aging of ferrihydrite. At a pH value of 7.0 and $a_w = 1$, the proportion of goethite (Gt) formed at low temperatures (eg. 4 - 15°C) is greater than hematite (Hm), whereas at higher temperatures (eg. >25°C) hematite becomes more dominant (Schwertmann, 1988).

1.2.4 Vegetation cover

Bauxite and laterite development is facilitated by the effects of vegetation cover. A dense forest cover regulates the moisture content of the soil, encourages better rainwater infiltration and substantially reduces erosion. The decay of organic matter causes the reduction and mobilisation of iron compounds. Plants help in the desilication of the weathering profile by extracting silica through their roots (Lovering, 1959; Mikhailov, 1964). Much of this silica may be returned to the soil in leaf litter and other plant debris.

1.2.5 Geomorphology

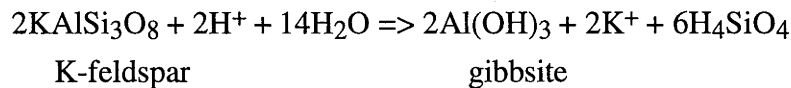
The surface morphology is an important factor in laterite formation. Good drainage aids in the lateritization process. A positive landform assists in drainage and helps protect the weathering profile from any transported sediment accumulation. In addition, a positive landform should be of low relief to keep erosion to a minimum (i.e. a plateau).

The ratio between infiltration and runoff is affected by the slope of the land. An optimum angle exists for each landform where infiltration and downward water migration is at its best. For rock with high permeability the optimum slope angle may attain 10-30° (Bárdossy and Aleva, 1990).

1.2.6 Hydrological conditions

Water is a vital agent in the lateritization process. The leaching of the parent rock/sediment and removal of the solute is greatly enhanced by good drainage. To assist in the downward and lateral percolation of water through the weathering profile the parent rock/sediment should have a high permeability and a high percentage of interconnected pore spaces. As lateritization progresses, the porosity and permeability increases to a point where any further increase would result in less efficient chemical weathering due to the infiltrating water being in contact with the rock/sediment for less time. Steeply dipping foliation and strata permit better access of rainwater into a parent rock thereby assisting the lateritization process.

These transformations are relatively straightforward for quartz-free rock such as basalt or a nephelinic syenite in the presence of silica-poor percolating surficial waters (Samama, 1986). In such cases, potassium feldspar is unstable and is increasingly altered to kaolinite and then into gibbsite. Under excellent drainage conditions the silica content of such waters may be very low (i.e. less than 1 ppm silica) causing the direct transformation of potassium feldspar into gibbsite (see below).



The system is somewhat more complex in quartz-potassium feldspar-bearing rocks and sediments. Potassium feldspar also undergoes transformation to kaolinite but according to the thermodynamics of the system, gibbsite should not form by the dissolution of kaolinite unless quartz is absent (Gardner, 1970). However, the relative kinetics of transformation must also be taken into account to understand the system fully. The relative rates of transformation are ordered as $V_1 > V_2 \gg V_3$, where:

V_1 = potassium feldspar \rightarrow kaolinite

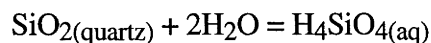
V_2 = kaolinite \rightarrow gibbsite

V_3 = quartz \rightarrow H_4SiO_4

As the rate of quartz solubilization is much slower than the potassium feldspar to kaolinite and kaolinite to gibbsite transformations, it is still possible to have waters with a very low silica content if the residence time of the water is sufficiently short (i.e. very good drainage conditions). Therefore, relative kinetics show that gibbsitisation is possible even when quartz is present (Samama, 1986).

1.3.3 Dissolution of quartz

The dissolution of quartz below a pH value of 9.0 may be represented by the equation:

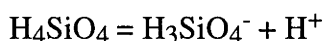


where $K_{\text{eq}} = a_{\text{H}_4\text{SiO}_4}$ (assuming that $a_{\text{H}_2\text{O}} = 1$) = 1×10^{-4} at 25°C

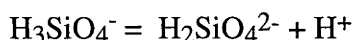
(Drever, 1988)

In a water saturated environment, the equilibrium constant (K_{eq}) = the activity of H_4SiO_4 ($a_{H_4SiO_4}$). Therefore at 25°C, any solution in which $a_{H_4SiO_4} = 1 \times 10^{-4}$ would be in equilibrium with quartz. A solution which has a lower activity of H_4SiO_4 would be undersaturated whereas one which has higher $a_{H_4SiO_4}$ values would be supersaturated (Drever, 1988). Amorphous silica has a higher solubility constant of 2×10^{-3} at 25°C (Drever, 1988) which implies that more SiO_2 can be dissolved before the solution is saturated with H_4SiO_4 .

At higher pH values, H_4SiO_4 behaves as an acid and dissociates into $H_3SiO_4^-$ and $H_2SiO_4^{2-}$. These dissociations may be represented by the following equations:



$$K_1 = a_{H_3SiO_4^-} a_{H^+} / a_{H_4SiO_4} = 10^{-9.9} \text{ (at } 25^\circ\text{C)}$$



$$K_2 = a_{H_2SiO_4^{2-}} a_{H^+} / a_{H_3SiO_4^-} = 10^{-11.7} \text{ (at } 25^\circ\text{C)}$$

(Drever, 1988)

At high pH values, the total dissolved silica concentration in equilibrium with quartz or amorphous silica dramatically increases (Drever, 1988) therefore at high pH values more silica can be dissolved before the water becomes saturated.

SEM studies by Berner *et al.*, (1980) and Berner & Schott (1982) have shown that the dissolution of quartz and formation of etch pits is crystallographically controlled. The development of an etch pit is a similar but opposite process to that of crystal growth. Dislocations in a crystal lattice are possible sites for etch pit nucleation. Other sites for the nucleation of etch pits may include, clusters of vacancies and impurities, growth bands, growth sector boundaries and fission tracks (Sangwal, 1986).

1.3.4 Formation of bauxite minerals from kaolinite

Garrels & Christ (1965) and Gardner (1970) both used thermodynamic data to construct theoretical solubility diagrams for quartz, kaolinite and gibbsite. Gardner (1970) using his diagrams showed that gibbsite should only precipitate when quartz is absent from the system, the pH is greater than 4.2 and the initial total dissolved silica concentration of the water is less than $10^{-4.6}$ moles per litre. He also indicated that for gibbsite to crystallise from an intermediate amorphous $Al(OH)_3$ phase, the pH must be greater than 5.6 and the initial dissolved silica concentration in the infiltrating water must be less than $10^{-6.3}$ moles per litre.

Gardner (1970) used the bauxite deposit at Weipa as an example of the retarding effect of quartz on the development of gibbsite. A cumulative plot of the mineralogy in an 11 m deep profile (Loughnan & Bayliss, 1961), showed that gibbsite does not appear until the quartz content is less than 10 %. Gardner (1970) ascribed the persistence of small quantities of quartz, present in the bauxite horizon, to the coarse quartz grains which compose the parent kaolinitic sandstone and to the protective coatings of Al and Fe minerals. Loughnan & Bayliss (1961) showed that the pH of the water at Weipa graded from approximately neutral at the water table to 5.5 near the surface. Thereby, according to Gardner (1970), providing suitable pH conditions for the formation of gibbsite.

Peryea and Kittrick (1988) studied the thermodynamic stabilities of four Al oxide minerals at standard state conditions and found that their relative stabilities were; corundum < gibbsite < boehmite < diaspore. Hemingway (1982) concluded that the rapid polymerisation of dissolved hydroxy-aluminium ions in lateritic soils and bauxites, favoured the metastable precipitation of $\text{Al}(\text{OH})_3$ at the expense of $\text{AlO}(\text{OH})$ phases.

1.3.5 The activity of water

Troland & Tardy (1987) showed that at 25 °C the chemical activity of water was a major factor in determining the degree of hydration in bauxite minerals.

Under normal atmospheric pressures and room temperatures, the activity of water, a_w , is equivalent to its partial pressure, p , divided by the partial pressure of the corresponding volume of water saturated air, p_0 :

$$a_w = p / p_0 = \text{R.H.} / 100.$$

In the unsaturated zone of the weathering profile, the activity of the capillary water when equilibrium is attained, is equal to the relative humidity, (R.H.), of the overlying blanket of air, divided by 100 (Hillel, 1971). As the weathering profile dries out, water is retained in progressively smaller pores, resulting in the activity of the water becoming correspondingly lower (Bourrie & Pedro, 1979). The relationship between pore diameter, $d(\text{m})$, and the activity of water, a_w , is outlined below:

$$d(\text{m}) = -0.0921 \times 10^{-8} / \log a_w \quad (\text{Tardy and Nahon, 1985}).$$

$$\log a_w = -9.21 \times 10^{-10} / d(\text{\AA}) \times 10^{-10}$$

$$\log a_w = -9.21 / d(\text{\AA})$$

$$\text{If } d = 30 \text{ \AA}$$

$$\text{Then } \log a_w = -9.21 / 30 = -0.307$$

$$a_w = 0.49$$

For example, in the voids between kaolinite grains (30 Å pore diameters) the activity of water can be as low as 0.49 even though the activity of water within neighbouring large voids may be almost 1.0 (i.e. 100% humidity). A micro-environment is therefore created, where dehydrated mineral phases can precipitate. This explains why during nodule formation, the dehydrated phase, Al-hematite, usually crystallizes in a kaolinitic plasma, rather than Al-goethite.

The activity of water in the unsaturated zone of the weathering profile varies seasonally and as a function of depth. At the soil surface, the activity of water is lower than unity, except when it rains. A hydric hollow exists at a depth from 1 - 5 m where the water activity throughout most of the year, is lower than in the soil during the wet season and less than the layer above the water table (Figure 1.4). In the hydric hollow, dehydration occurs throughout the year, while at the surface, dehydration takes place only during the dry season. At the surface, during the wet season, rehydration of previously dehydrated minerals occurs in the large voids where the activity of water is high. In small pores the activity of water remains low, so minerals remain dehydrated (Tardy & Roquin, 1993).

1.3.6 Effects of humic acid on the crystallisation of aluminium hydroxides

Within the soil horizon, the decay of plant and animal matter produces humic acids. These acids affect the crystallisation of $\text{Al}(\text{OH})_3$ in two ways. Firstly, the occupation of the coordination sites of Al by organic ligands appears to disrupt the hydroxyl bridging mechanism which is essential for the polymerisation of Al ions (Singer & Huang, 1990). Secondly, humic acids tend to make the infiltrating solutions acidic. If the solution has a pH value less than 4.2, it becomes thermodynamically unfavourable to precipitate gibbsite (Gardner, 1970).

Singer & Huang (1990) demonstrated that the presence of humic acid in mildly acidic to alkaline conditions substantially affected the crystallisation of aluminium hydroxide polymorphs, pseudoboehmite and short-range ordered mineral colloids. Pseudoboehmite is a term used for finely crystalline boehmite which contains more intercalated water than coarsely crystalline boehmite. The diffraction pattern of pseudoboehmite consists of diffuse, "long spacing" XRD reflections (Tettenhorst & Hofmann, 1980).

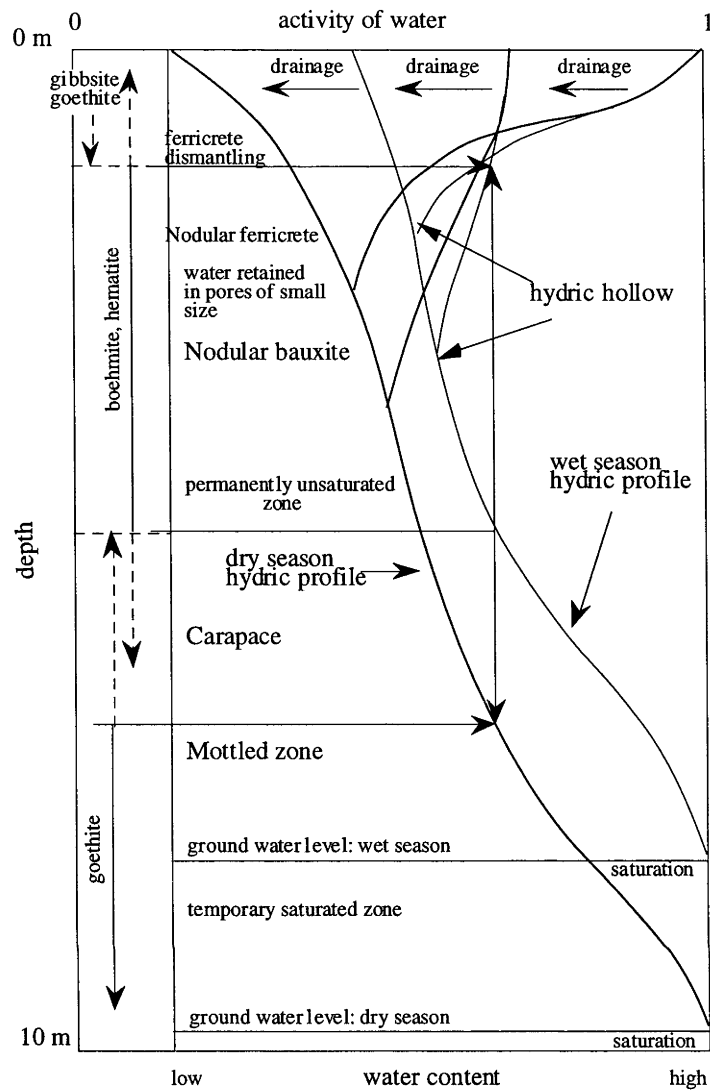


Figure 1.4

Seasonal distribution of water activity across a weathering profile, in a non-equilibrium situation, above a deep ground water level (10 m)

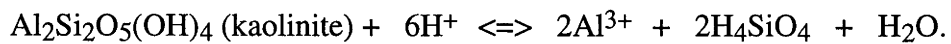
(after Tardy *et al.*, 1988a).

Singer & Huang (1990) showed that as humic acid concentration increased, the extent of Al precipitation substantially decreased. At a pH value of 6.0 and humic acid concentration of 37.5 mg/l, only noncrystalline precipitation products of Al were formed. At a pH of 8.0 and humic acid concentration of 12.5 mg/l, both gibbsite and bayerite were completely inhibited in their formation while only pseudoboehmite appeared in the XRD patterns. An increase in the humic acid concentration from 25 - 75 mg/l at a pH of 8.0 resulted in no precipitation of Al. In alkaline conditions at a pH of 10.0, even humic acid with a concentration as low as 2.5 mg/l resulted in only non-crystalline Al precipitation products to form (Singer & Huang, 1990).

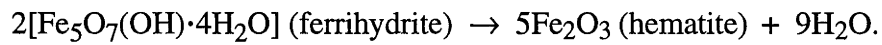
and the subsequent precipitation of hematite or goethite:



During the precipitation of hematite or goethite, kaolinite is dissolved by means of protons liberated during hydrolysis of the Fe^{3+} ion (Nahon 1991). The following equation represents the dissolution of kaolinite:



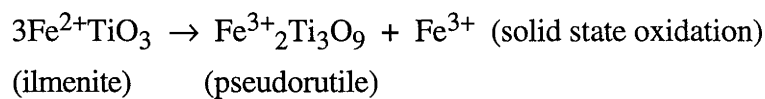
Schwertmann (1985) believes ferrihydrite ($\text{Fe}_5\text{O}_7(\text{OH})\cdot 4\text{H}_2\text{O}$), a metastable Fe-oxide of low structural order and high surface area, is the precursor of hematite. The formation of hematite involves a dehydration-rearrangement process within the defective hematite-like structure of ferrihydrite (see below) whereas goethite forms via a solution-nucleation-crystallisation process from various Fe sources (Schwertmann, 1985).



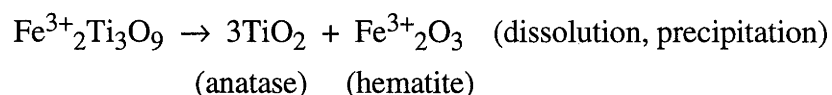
The process of iron mobilisation and accumulation will be dealt with in greater detail in section 1.4.

1.3.10 The formation of anatase from the weathering of ilmenite

Anand & Gilkes (1984) showed that in a lateritic pallid zone, ilmenite crystals alter via pseudorutile to porous leucoxene grains composed of randomly oriented aggregates of $\sim 0.06 \mu\text{m}$ anatase crystals. The first stage in the alteration of ilmenite occurs when iron oxidises and diffuses from the ilmenite, leaving pseudorutile behind.



During the second stage of alteration, pseudorutile dissolves, iron is removed by solution, and TiO_2 precipitates as anatase (Anand & Gilkes, 1984).



1.4 The evolution of lateritic and bauxitic pisoliths

In recent years, much of the knowledge gained about pisolith evolution has come from the French scientists, Daniel Nahon, Yves Tardy, Bruno Boulange and co-workers. Nahon (1991) explained the formation of pisoliths by a process he termed *centripetal three-dimensional glaebulization* (Figure 1.5). He believed that an inward migration of accumulating material such as hematite, to sites located within a host kaolinitic plasma, was responsible for the formation of spherical to subspherical concentrations of minerals, termed glaebules.

Brewer (1964) defined the term glaebule as being; "*a three dimensional unit within the s-matrix of the soil material, and usually approximately prolate to equant in shape; its morphology (especially size, shape and/or internal fabric) is incompatible with its present occurrence being within a single void in the present soil material. It is recognised as a unit either because of a greater concentration of some constituent and/or a difference in fabric compared with the enclosing soil material or because it has a distinct boundary with the enclosing soil material*".

The first stage in pisolith development as explained by Nahon (1991), occurs when weakly differentiated glaebular accumulations appear as small (< 1 cm), round and weakly indurated zones within the host plasma. The characterisation of these *initial glaebular concentrations* is based on structural, geochemical and mineralogical relationships which exist between them and the enclosing material. Initial glaebular concentrations are generally confined to localities which are more kaolinitic than the surrounding plasma. The concentration of kaolinite occurs when detrital and neofomed kaolinite collects in the network of tubular voids which often invade the mottled zone (Tardy and Nahon, 1985). Structurally, the boundaries between the accumulations and the surrounding material are gradual and very irregular. There is very little disturbance of host microstructures and components. Electron microprobe traverses across the accumulations exhibit an increasing centripetal chemical gradient for only one of the constituents (commonly iron) of the plasma. Initial glaebular concentrations develop without significant change in the mineralogy of the host plasma (Nahon 1991).

As centripetal three-dimensional glaebulization progresses, a significant change in the mineralogy takes place. Within the developing glaebule, the partial or total replacement of the host material with the accumulating material occurs. These moderately differentiated glaebular accumulations are termed *nodules*. The central part of nodules is structurally and mineralogically distinct from the enclosing plasma. Within the periphery however, a transitional zone exists between the plasma and the glaebular accumulation. Nahon *et al.* (1977), and Didier *et al.* (1983) studied the development of such nodules in the ferricrete profiles of the Ndias Massif, western Senegal, Africa.

In their studies, they showed how ferruginous nodules developed from a plasma consisting dominantly of kaolinite, associated with scattered quartz grains and disseminated goethite. Electron microprobe traverses of nodules revealed that Al and Si vary in parallelism in the outer zones of nodules, whilst in the cores, Si is eliminated and Fe and Al are concentrated. The epigenetic replacement of kaolinite by aluminous hematite is responsible for these trends (Nahon, 1991).

As centripetal three-dimensional glaebulization proceeds, the differentiation of the nodular structure from the enclosing plasma results in the formation of well defined nodules. Differences in the nature of the components of the nodule and the enclosing material, cause differences in their respective responses to wetting and drying. These different reactivities result in the development of a *constraint cutan* and a *peripheral cavity* around the nodule. A constraint cutan is a narrow zone of reoriented clay particles within the enclosing plasma and parallel to the surface of the nodule. It is formed in response to a localised pressure increase at the nodule-plasma boundary brought about by expansion of the plasma during the wetting phase. A peripheral cavity is a narrow circum-nodular cavity that forms when the plasma contracts during the drying phase. The formation of this structural discontinuity isolates the nodule from the enclosing plasma, thus changing the geochemical conditions at the surface of the nodule. Centripetal diffusion is hampered by the presence of the cavity. Internal restructuring of the nodule occurs from the margins, resulting in a change in mineralogy and orientation of the nodule components. The production of a banded cortex during the latter phase of centripetal three-dimensional glaebulization results in the formation of a *pisolith* (Nahon, 1991).

The ferruginous pisoliths that Nahon (1976) and Nahon *et al.* (1977) studied, ranged from ones having continuous and concentrically banded cortices to asymmetrically developed pisoliths displaying complex sets of discontinuous cortical layers separated by micro-unconformities. The appearance of the latter type is responsible for giving the impression that pisoliths form by accretionary processes. However, Nahon (1969) showed that complex sets of cortical layers can also be produced by a series of discontinuous centripetal reorganisations of the ferruginous matrix. Detailed microprobe studies by Muller (1979) and Muller *et al.* (1979) on ferruginous nodules from the weathering of a gneiss in Congo showed the existence of a mineralogical continuum from the ferruginous mottles at the base of the weathering profile, to nodules at the top. In the upper zones progressive cortical development resulted in the transition from ferruginous nodules to pisoliths. Although it is possible for centripetal evolution of the cortical layers to occur uniformly, it is also possible for cortical development to occur preferentially, resulting in the development of discontinuous and seemingly complex cortical layers. (Nahon *et al.*, 1980).

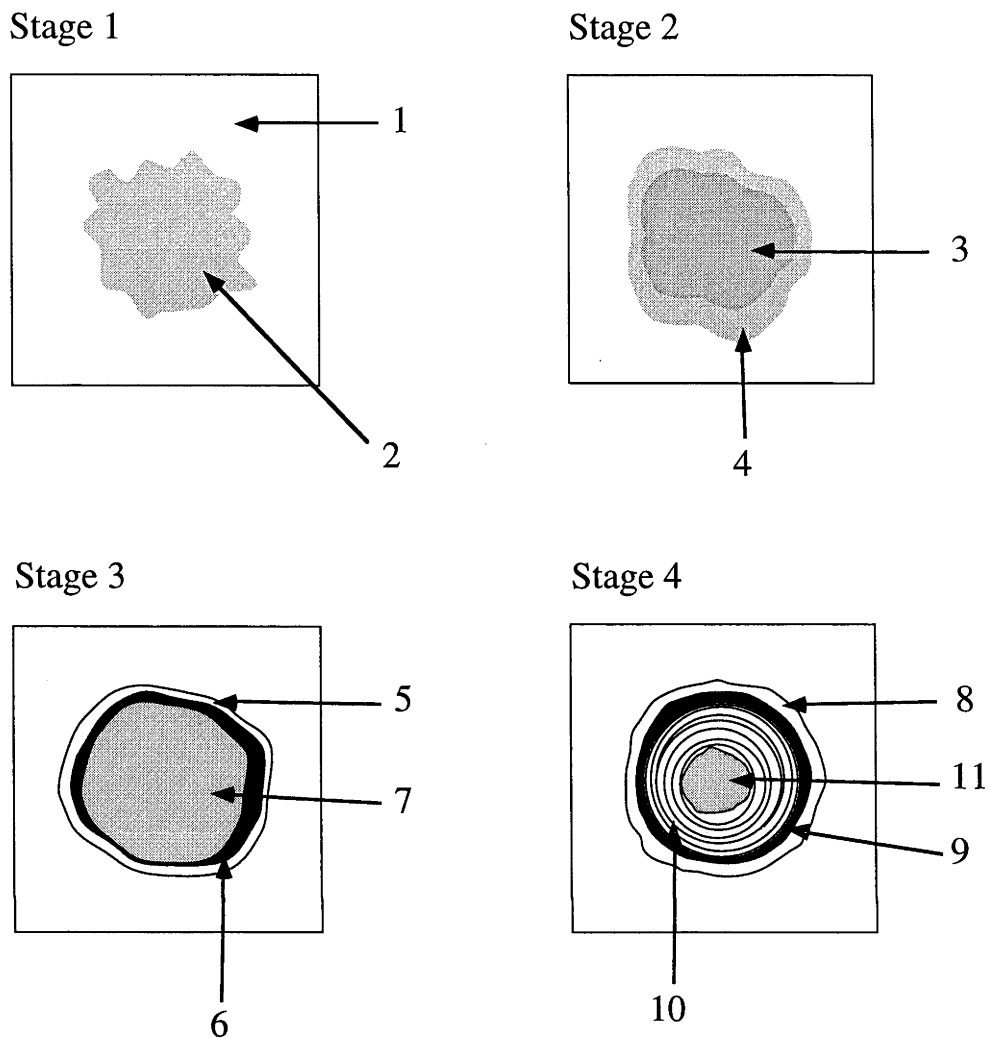


Figure 1.5

Stages of centripetal three-dimensional glaebulization. (1) kaolinitic plasma; (2) initial glaebular concentration; (3) glaebular concentration epigenetically replacing the plasma's constituents; (4) diffuse external boundary of the nodule; (5) reorientation of the plasma (constraint cutan); (6) peripheral contraction cavity; (7) indurated nodule; (8) constraint cutan; (9) peripheral contraction cavity; (10) concentrically banded cortex; (11) pisolith core (adapted from Nahon, 1991).

Pouliquen (written communication to Bárdossy and Aleva, 1986) observed an apparent genetic sequence in the Sangaredi bauxite deposit of Guinea (Figure 1.6). Pouliquen observed that bauxite pebbles appear to undergo nodulation followed by the development of pisoliths as the nodules' structure and mineralogy are reorganised.

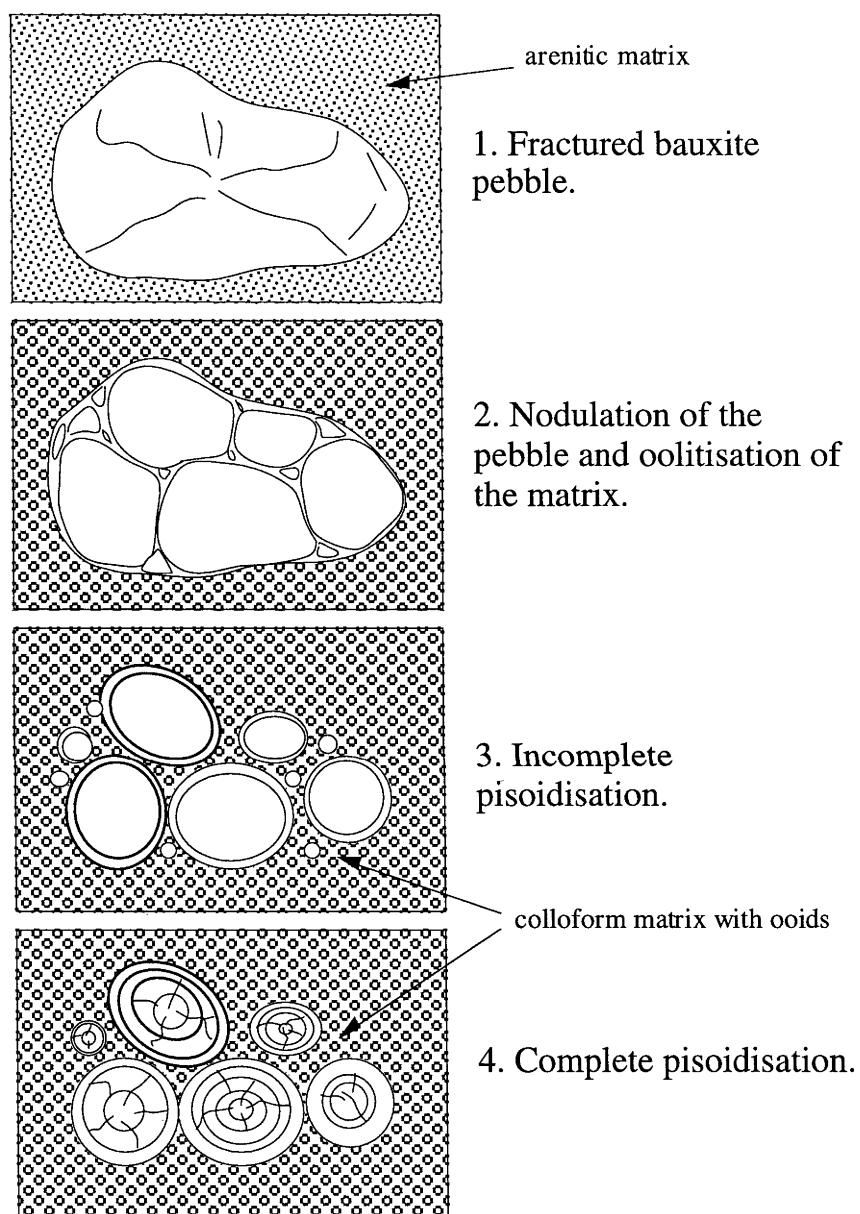


Figure 1.6

Pisolith (pisoid) formation in the Sangaredi bauxite deposit, Guinea, as observed by Pouliquen (adapted from Bárdossy & Aleva (1990)).

1.5 Other spherical structures in geology

Spherical structures similar to lateritic and bauxitic pisoliths can form in many different geological environments. Below is a brief description of the various types of spherical structures and their mode of formation.

Accretionary lapilli are accretionary accumulations of volcanic ash, generally of pisolith size. They are believed to form in volcanic ash clouds where successive accretionary layers of fine ash are plastered on a descending nucleus with the aid of condensing water vapour and electrostatic forces. (Reimer, 1983)

Calcareous oöliths and pisoliths are well rounded, spherical to slightly ovoid, carbonate particles having a detrital nucleus and a concentrically laminated cortex. They are generally of aragonitic or calcitic composition and often contain numerous thin layers of mucilaginous algae. Their environment of formation is normally shallow marine to littoral. (Leeder, 1982)

Vadose pisoliths are concretions associated with the diagenesis of carbonate sediments above the water table. They form when micritic calcite accretes around the brecciated fragments of carbonate host rock giving rise to spherical structures up to 10 cm in diameter. (Leeder, 1982)

Cave pearls are calcitic accretionary spheroids which form within splash cups created by dripping stalactites. They form when calcite precipitates around a detrital nucleus within a supersaturated solution of CaCO_3 . Constant agitation prevents the cave pearls from becoming stalagmites. (Brand & Veizer, 1983)

1.6 Worldwide distribution of lateritic bauxite

Bárdossy and Aleva (1990) undertook a joint worldwide survey of lateritic bauxite deposits. They found that the majority of them are distributed in five main regions: the South America Platform, West Africa, India, South-east Asia, and the West and North Australia provinces (Figure 1.7). Bauxite deposits in these regions display certain morphological, compositional and genetic similarities (Bárdossy, 1989). Smaller bauxite provinces occur in south-eastern Brazil, south-eastern Africa and south-eastern Australia, as well as numerous isolated deposits situated north and south of the main regions (Bárdossy, 1989).

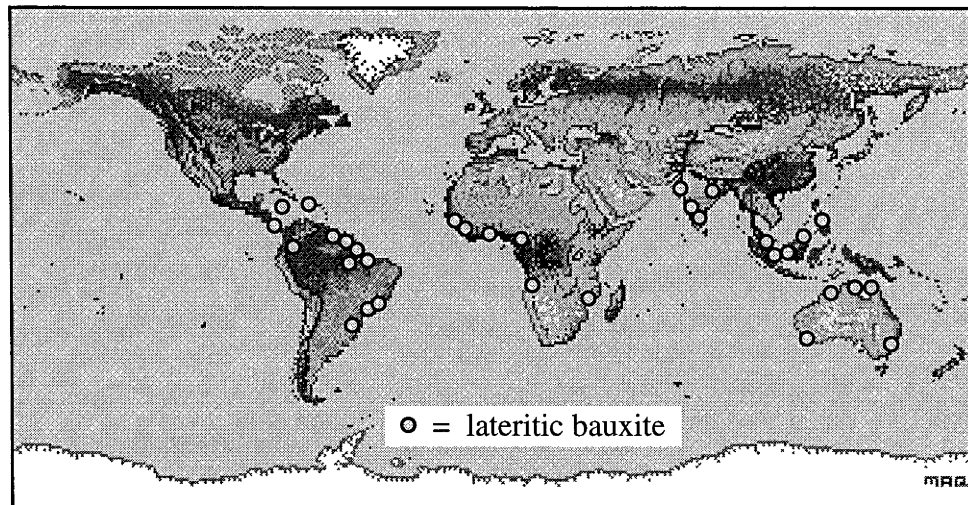


Figure 1.7

Worldwide distribution of lateritic bauxite.

1.7 Australian bauxite deposits

There are three major centres for the mining of bauxite in Australia: Weipa located on the northwestern edge of Cape York Peninsula, Queensland; Gove on the northeastern tip of Arnhem Land, Northern Territory; and the Darling Range in the southwestern part of Western Australia (Figure 1.8). Several significant deposits which are at present not being mined, occur on the Mitchell Plateau and at Cape Bougainville in the Kimberley region of Western Australia. Many minor deposits are formed upon the Tertiary sediments and basalts of eastern Australia, such as in the Wingello-Moss Vale district and on the Monaro of New South Wales.

1.7.1 The Weipa bauxite deposit

It is generally considered that the bauxite deposits of the Weipa area are some of the largest and finest in the world. The aluminous laterites cover more than 2500 square kilometres, and have thicknesses ranging from 1 to 9 metres. Beneficiated ore contains between 50 and 55 percent alumina with only 5 percent silica. It is estimated that total bauxite reserves amount to more than 3700 million tonnes. However, what is considered economic, varies according to market demand.

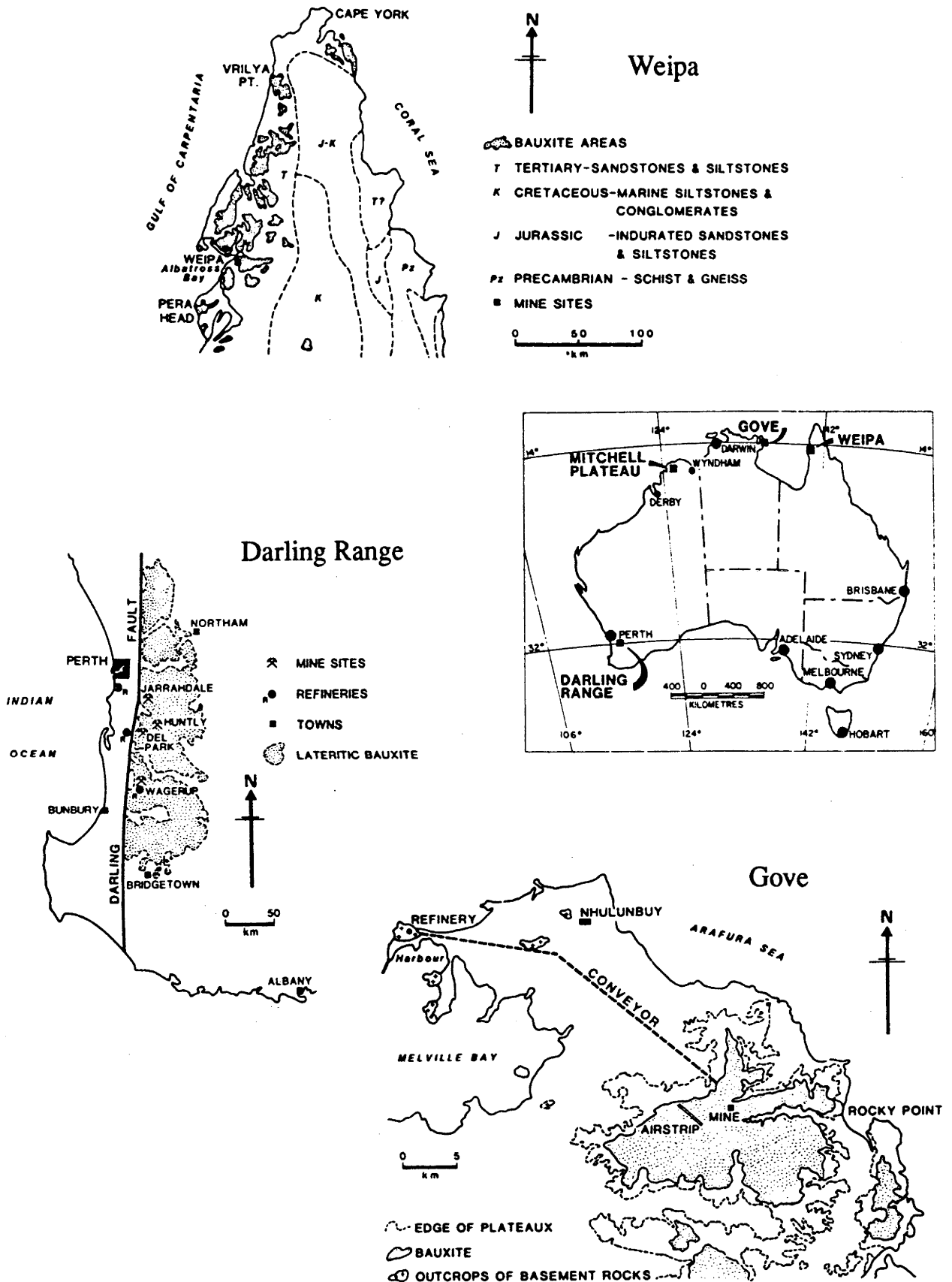


Figure 1.8

Major bauxite-producing areas in Australia, (after Jacob, 1984).

PREVIOUS INVESTIGATIONS

There have been several general studies done on the bauxites in the Weipa area. In 1955, Evans (1959, 1965) led the way with his pioneering work on the deposit, providing an outline of the regional geology as well as discussing the chemistry and probable origin of the deposit. McAndrew and Edwards (1956) compiled a report on the bauxite's mineralogy. Studies of the heavy minerals and quartz grains contained within the bauxite and underlying Bulimba Formation were undertaken by Edwards (1957, 1958) and Baker (1958). A description of the mineralogy and possible origin of the deposit was presented by Loughnan & Bayliss (1961). Grubb (1971) discussed its genesis with respect to the mineralogy and heavy mineral content. MacGeehan (1972) studied the bauxite deposit in the Aurukun area and reported on the petrology and put forward a theory on its probable genesis. Plumb & Gostin (1973) described the petrology of the bauxite and compared it to the Gove and Mitchell Plateau deposits (Smart, 1977). The last major study of the Weipa bauxite deposit was by Jepsen & Schellmann (1974). They undertook a very detailed description of the chemistry and mineralogy of two profiles; one deep and one shallow. With the aim of controlling the grade of ore by judicious mine planning, an extensive drilling program undertaken since the bauxite's discovery, has led to a very good knowledge of the bauxite's bulk mineralogy and chemistry.

GEOLOGY

The Weipa bauxite deposit is situated on the northwestern edge of Cape York Peninsula in northern Queensland. On the Weipa Peninsula, development of the economic deposit is generally confined to the highly permeable kaolinitic sands and clays of the early Tertiary Bulimba Formation. However, 15 km northwest of Weipa at Andoom, the bauxite is formed upon the "glaucinitic" siltstones of the early Cretaceous Rolling Downs Group. The bauxite horizon is dominantly pisolitic at both localities and is mainly composed of gibbsite and boehmite. Other minerals present in varying amounts are quartz, hematite, kaolinite and anatase; with goethite, rutile and zircon composing the remainder. The bauxite horizon has an average thickness of 2.4 m and dips gently towards the sea with an average gradient of 0.1°. An abrupt boundary exists between the bauxite horizon and the underlying mottled zone. A nodular ferruginous kaolinite layer constitutes the top part of the mottled zone. No conclusive evidence exists for extensive lateral transportation of the bauxite. The deposit is most likely residually derived from the intensive *in situ* leaching of the parent rock. Heavy mineral studies by Baker (1958) and Edwards (1957, 1958) have shown that Weipa bauxites are genetically related to the underlying parent material.

Evidence for the bauxite's *in situ* origin exists at Pera Head where Evans (1965) described a quartz pebble zone, which could be traced up-dip from the underlying clay, through the mottled zone and into the bauxite. He believed that the pisolitic bauxite formed by concretionary processes within the very limited zone of annual water table fluctuation whereas the underlying nodular and tubular iron-rich material formed within the relatively static zone of the water table.

MacGeehan's (1972) study of the Aurukun bauxite deposit showed that the bauxite had formed in two stages. During the first stage gibbsitic pisoliths formed in the zone of wet season saturation of a fluctuating water table. The permanent dry season water table was responsible for the enrichment of iron within the mottled zone. Subsequent uplift of the Weipa Peninsula and lowering of the water table brought about changes in the chemical environment resulting in the formation of boehmite sheaths around pisoliths in the upper oxidised zone and gibbsitic sheaths around pisoliths in the new zone of wet season saturation. He also noted the presence of compound pisoliths at the base of the bauxite horizon and suggested they formed by growth of gibbsitic membranes. MacGeehan considered that the second stage of development is still happening.

HISTORY

Captain Matthew Flinders and his crew may have been the first Europeans to have sighted the bauxite deposit at Weipa, when on his expedition in 1802, he described in his journal the presence of some "some reddish cliffs" south of Albatross Bay at Pera Head. During the early 1880's the first European settlements were established in the Weipa area at Batavia and York Downs. Four years after their establishment, the assistant Queensland Government Geologist, C.F.V. Jackson referred to the existence of "brown pisolitic ironstone" located between the Mission and Embley Rivers. In his report he wrote:

"But I think it is probable that if these deposits were systematically examined and sampled, they would be found to include masses of higher grade ores and if such were the case they might ultimately prove of some value, especially on account of their ready accessibility from the sea."

Unfortunately, follow up investigations were not carried out until 1947 when Dr. F.W. Whitehouse collected samples of bauxite at the mouth of the Archer River, south of Weipa. Because of the good grade he collected, a geological survey was considered. However the survey was soon abandoned, when samples requested from the three mission stations were found to be of low grade. In 1955 while leading a reconnaissance expedition of possible oil bearing structures, geologist H.J. Evans discovered a large bauxite outcrop near Weipa.

After the discovery he continued collecting samples over a wide area before returning to Melbourne. Analysis of the bauxite showed it to be of high grade. Soon after the discovery, Enterprise Exploration Pty. Ltd. a subsidiary of Consolidated Zinc did further exploration and calculated the proven and probable reserves of the bauxite deposit. At the end of 1956 Consolidated Zinc formed a new company called Commonwealth Aluminium Corporation (Comalco) to develop the deposit. The first shipments of bauxite were made to Japan, Europe and Bell Bay, Tasmania in 1961 and 1962 after which exports have risen to a current 11 million tonnes per year. In the period from 1970 to 1972 mining was extended to a site approximately 19 km north of Weipa known as Andoom. Today, bauxite mined at Andoom amounts to 70% of the total mined in the area, with the rest supplied from the Weipa Peninsula (from *Weipa, The Mine and its People*; Comalco Aluminium Limited publication, 1991).

CLIMATE

Weipa experiences a hot climate with a temperature always above 18°C and a small annual temperature range of less than 5°C from winter to summer. Maximum monthly temperatures range from 35°C in November to just under 30°C in July. Weipa has a mean annual rainfall of between 1611 and 1728 mm, of which over 90% of it falls during the months from November to April inclusive. Occasionally, the monsoons arrive early during October and may extend into May resulting in an increase in the mean monthly rainfall for these months. Winter in Weipa is very dry, with less than 8 mm to as low as 1 mm of rain falling during the months of June to September. Potential evaporation exceeds the mean annual rainfall at a total of 1880 mm per annum (Specht *et al.*, 1977).

1.7.2 The Gove bauxite deposit

The lateritic bauxite at Gove extends over an area of 60km². The top part of the profile is similar to a typical one at Weipa, however the bottom part is quite different. Below the loose pisolithic bauxite, exists a cemented zone of pisolitic bauxite where small pisoliths are welded together at their points of contact imparting a dense, compacted appearance to the material. Beneath the cemented pisolitic bauxite is a massive concretionary zone containing numerous tubular cavities. Within this zone, disseminated nodules and pisoliths are scattered throughout an abundant and well cemented kaolinitic matrix. The concretionary zone passes into a hard, vesicular laterite zone. Abundant cemented nodules and vesicular cavities exist in the upper part, passing downward into red clay containing intermittent layers of gravel and ironstone in the lower part. A mottled kaolinitic zone exists below this layer.

Over part of the area, an unusually sharp and irregular contact exists between the pisolithic bauxite horizon and the tubular concretionary zone. This led Grubb (1970) to believe that an erosional unconformity exists over the area, possibly resulting from a marine transgression shortly after the main period of bauxitisation. The observation of sedimentary layering in the pisolithic zone by Somm (1975), added weight to his theory.

The distribution of minerals within the weathering profile at Gove is similar, but more variable to that at Weipa. Kaolinite is dominant in the lower part of the profile whilst gibbsite is the most abundant mineral in the upper pisolithic zone. In the soil and pisolithic zones, boehmite and hematite are more concentrated. Goethite is more abundant than hematite in the lower kaolinitic zone. The concentration of quartz increases markedly in the upper pisolithic and soil zones despite it being virtually absent in the lower zones. This distribution of quartz is another piece of evidence supporting Grubb's marine transgression theory. (Loughnan & Sadleir, 1984)

1.7.3 The Darling Range bauxite deposit

The Darling Range bauxites have a prominent hardcap of 1 to 2 metres thickness beneath the overlying soil cover. The hardcap is composed of pisoliths and angular to subrounded nodules set in a finer grained matrix and cemented by goethite and hematite. Underlying the hardcap is an earthy nodular zone of 2 to 3 metres thickness. This zone consists of nodules and scattered oöoliths in a friable, earthy matrix. The nodular zone is underlain by a transitional zone which is somewhat mottled and pale in colour. The transitional zone varies from being clayey if developed upon metadolerite, to sandy if the parent material is gneissic granite.

The mineralogy of the weathering profile developed on metadolerite is significantly different to that of the profile formed on the gneissic granite. The succession developed on metadolerite contains abundant goethite and hematite, whereas the one developed on gneissic granite contains a high proportion of sand-size quartz. Both profiles contain appreciable quantities of gibbsite, mainly in the upper nodular zones. Kaolinite is most abundant in the lower transitional zones, particularly in the transitional zone developed upon the metadolerite.

The Darling Range bauxites are unusual in that very little boehmite exists in the ore zones. As well, the presence of unaltered muscovite in association with gibbsite in the nodular zone is enigmatic.

Because of the extreme lateral variability of the bauxite, ore of economic grade tends to be restricted to small isolated deposits rarely exceeding 1 km² in area. (Loughnan & Sadleir, 1984)

PART TWO

Methodology and Results

Chapter 2

Optical microscopy

2.1 Introduction

A number of people have attempted to classify bauxitic pisoliths from Weipa in the hope of understanding their evolution. Bryce (1989) undertook a detailed hand specimen study of bauxitic pisoliths, from which she developed a classification system. As an extension of this study, Campbell (1990) constructed a similar classification system based on his observations of pisoliths in thin-section.

One of the aims of this project was to develop an evolutionary model for bauxitic pisoliths, therefore obviating the need to categorise them. The following chapter details the structure visible in pisoliths using an ordinary light microscope and puts forward a theory to explain these features in the context of an evolutionary model.

The bauxitic pisoliths of Weipa may be divided into two main groups. Over 95% of pisoliths are single and average 5 mm in diameter. The remainder are compound; that is roughly elliptical hollow bodies, 20 to 50 mm in diameter, with single pisoliths inside.

2.2 Method

2.2.1 Single pisoliths

Bauxite samples from sixteen drill-holes were selected from Comalco's auger-drilling reserve collection. Eight of the drill-holes were located at Weipa and eight at Andoom (Figures 2.1, 2.2 and Appendix 1). Polished thin-sections of pisoliths, mounted in polyester resin, were made from samples obtained from the top, middle and bottom part of the bauxite horizon from each of the different localities. The examination of approximately 500 individual pisoliths revealed many similarities and possible evolutionary pathways. During the study, the model was continually updated and refined to take into account these similarities as well as the numerous variations. Mineral characterisation techniques were employed (see later chapters), so that the observed processes could be validated.

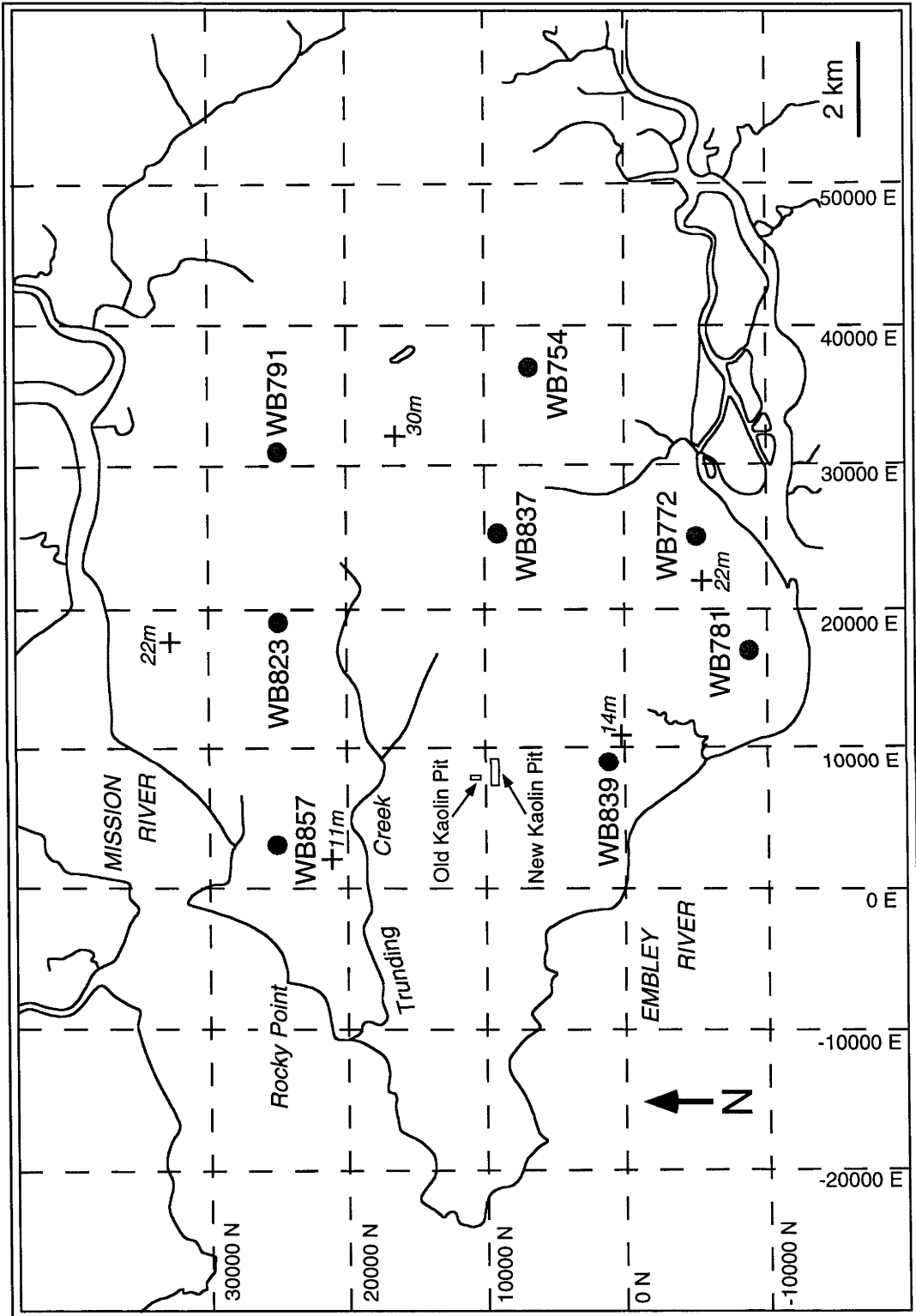


Figure 2.1

Mine-coordinate map of the Weipa area showing the location of the selected drill-holes.

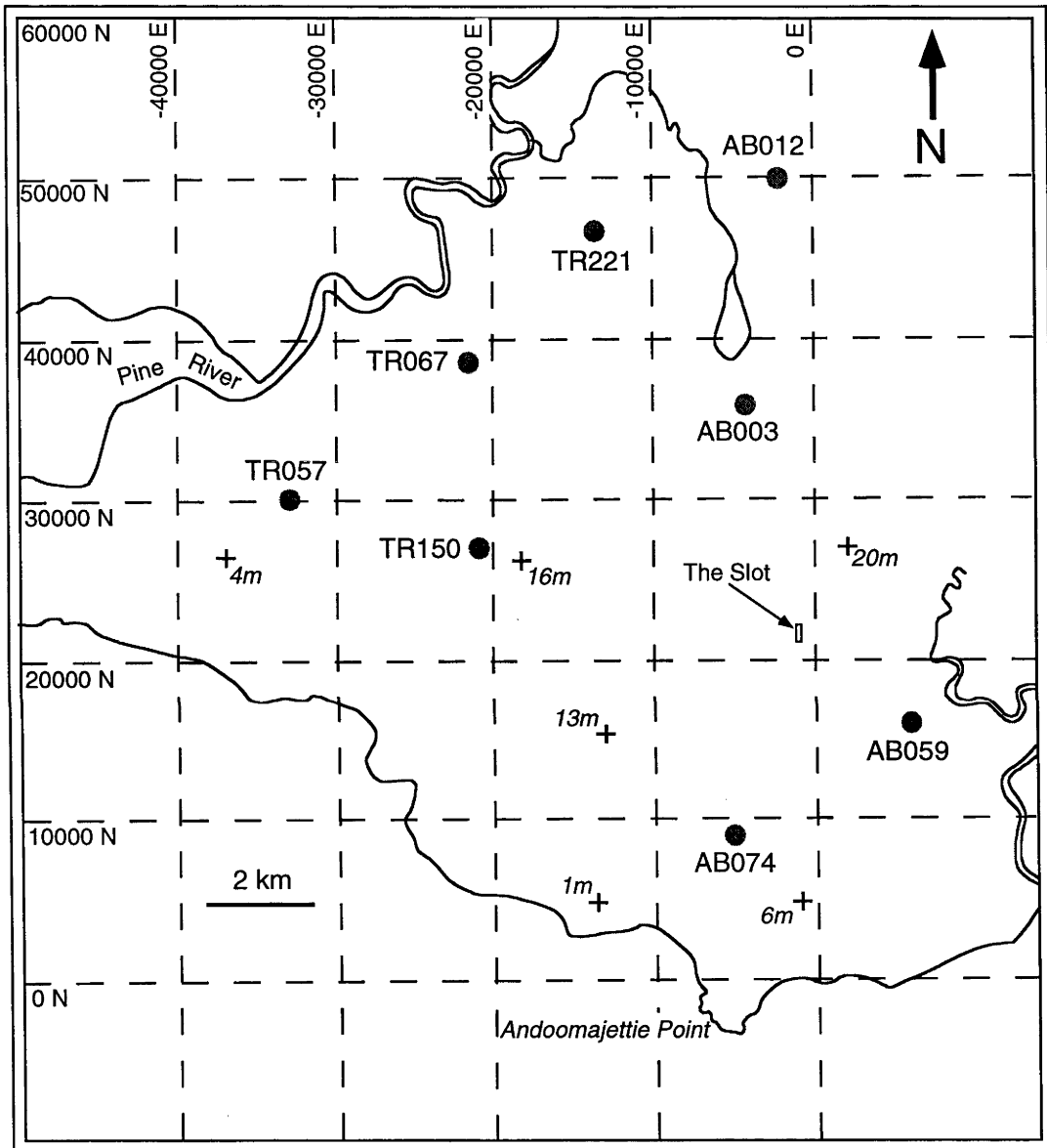


Figure 2.2
Mine-coordinate map of the Andoom area
showing the location of the selected drill-holes.

2.2.2 Compound pisoliths

Using the principles of geological mapping; textural and mineralogical maps of compound pisoliths were constructed. Firstly, a compound pisolith was cut in half. A thin-section was made from one of the halves, while the other half was retained for X-ray diffractometry. The thin-section was examined using an ordinary light microscope. To maintain observational accuracy an enlarged contact print of the thin-section was used as a base for mapping. Boundaries of major textural and colour differences were recorded directly onto an overlay.

2.3 Results

2.3.1 Single pisoliths

Any given pisolith may contain up to a maximum of three discrete sets of cortical layers. Two intervening quartz-rich zones may or may not be present (Figure 2.3). Where a quartz-rich zone is absent between two cortical layers, there is invariably evidence for a hiatus in the form of truncated cortical banding or radial cracks.

The cortical layers are characterised by the presence of fine sub-parallel banding. Broad, iron-rich bands are commonly superimposed upon these (Figure 2.4).

The quartz-rich zones are generally not layered and are characterised by higher concentrations of quartz and minerals such as zircon, rutile and tourmaline. Fine cortical banding is absent from quartz-rich zones, however broad iron-rich banding may sometimes be present. The quartz within the quartz-rich zones of bauxitic pisoliths has undergone varying degrees of dissolution and replacement by gibbsite (Figure 2.5).

The *inner cortical layer* is generally dense, well indurated and commonly has a vitreous lustre. Cracks, if they are present, may be infilled with either boehmite or poorly-diffracting material (see chapter 6, "Quantitative X-ray diffraction" for the definition of poorly-diffracting material). The *inner cortical layer* is commonly found in the core of well-developed, concentrically-banded pisoliths.

The *1st quartz-rich zone* is usually dense, well indurated and may also have a vitreous lustre. If the quartz has been dissolved, infilling by gibbsite, boehmite or poorly-diffracting material (PDM) generally occurs. Boehmite or PDM may infill any cracks which are present. The *1st quartz-rich zone* is commonly found as the core of well-developed pisoliths.

The *middle cortical layer* is commonly quite dense and well indurated. The outer edge of this layer is commonly hematite and boehmite-rich. Cracks may or may not be infilled.

The 2nd quartz-rich zone is commonly porous. Infilling of voids is usually lacking. Cracks are usually not as well-developed and are generally not infilled.

The outer cortical layer is typically porous and friable. This layer is pale-coloured due to its low iron concentration and high gibbsite or kaolinite content. The layer is devoid of cracks.

Idealised pisolith morphology

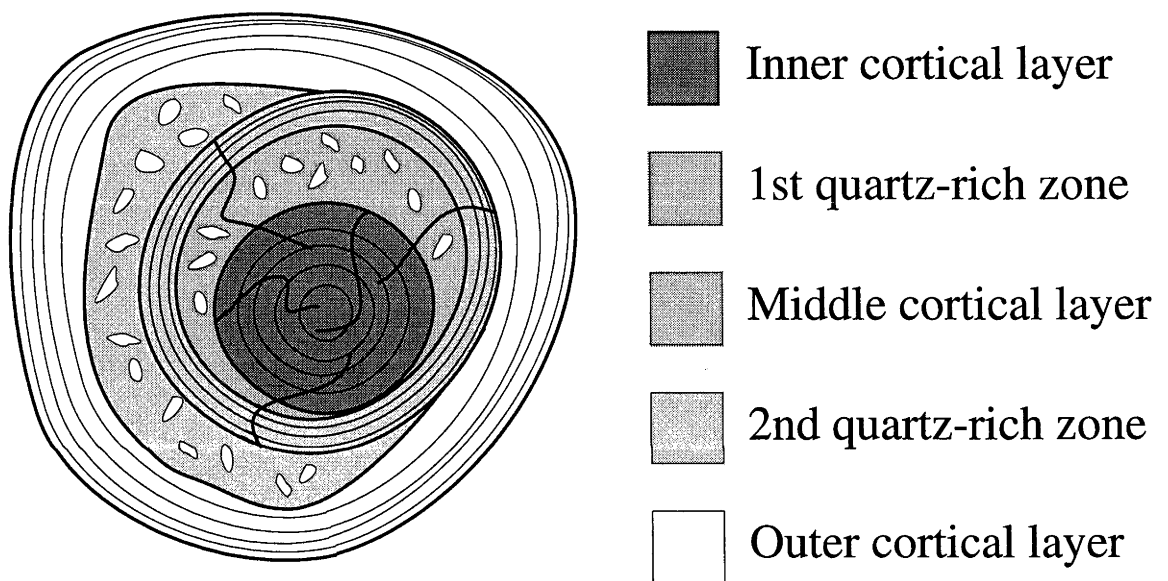


Figure 2.3

The figure depicts a pisolith with all five zones. A photo-micrograph of such a pisolith is shown in Figure 2.6.2. The presence of both quartz-rich zones is infrequently observed in pisoliths.

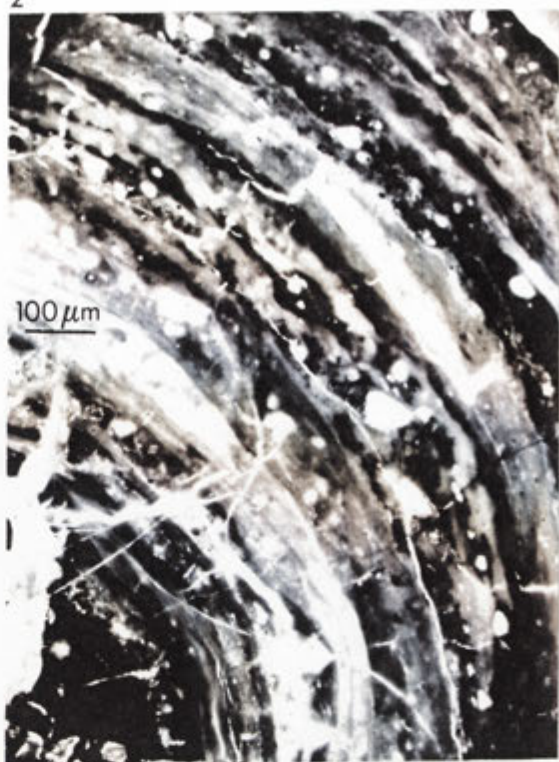
Figure 2.4

- Figure 2.4.1 A pisolith from drill-hole WB772EH (3.5-3.75 m) displaying cortical layers characterised by the presence of fine sub-parallel banding. Scale bar = 100 μm .
- Figure 2.4.2 A pisolith from drill-hole WB857EH (2.5-3 m) displaying cortical layers characterised by the presence of fine sub-parallel banding. Scale bar = 100 μm .
- Figure 2.4.3 A pisolith from drill-hole WB837EH (3.25-3.5 m) displaying broad, iron-rich banding. Some of the edges of the bands are quite gradational, indicating a diffusion boundary. Scale bar = 100 μm .
- Figure 2.4.4 Another section of the same pisolith (WB837EH (3.25-3.5 m)) displaying broad, iron-rich banding. Some of the edges of the bands are quite gradational, indicating a diffusion boundary. Scale bar = 100 μm .

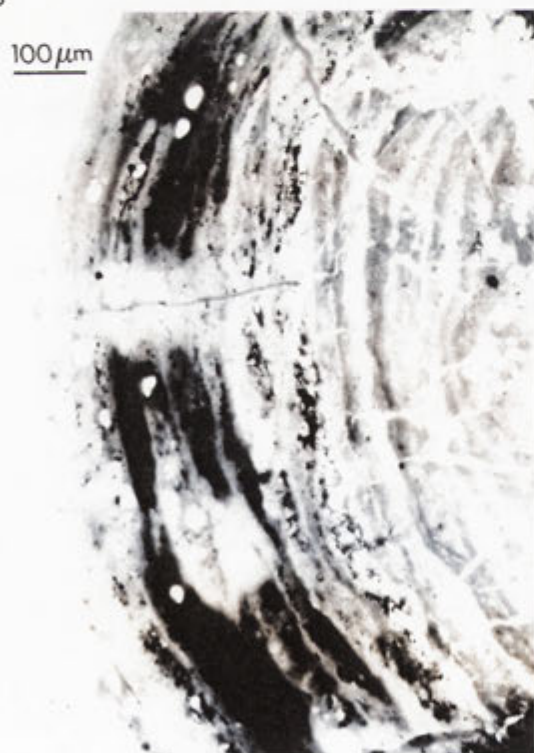
1



2



3



4



Figure 2.5

Figure 2.5.1 A void with gibbsite crystals projecting inwardly away from the void wall, in a pisolith from drill-hole WB781EH (4-4.25 m).
Scale bar = 100 μm .

Figure 2.5.2 A void with gibbsite crystals (arrowed) projecting inwardly away from the void wall, in a pisolith from drill-hole WB839EH (2.5-2.75 m).
Scale bar = 100 μm .

Figure 2.5.3 A void lined with gibbsite crystals (arrowed), in a pisolith from drill-hole WB839EH (2.5-2.75 m). Scale bar = 100 μm .

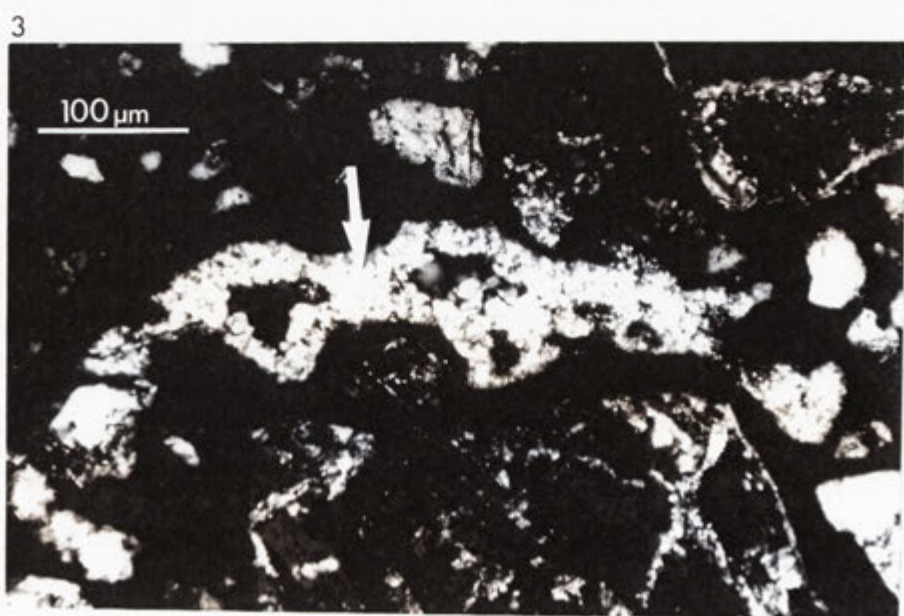
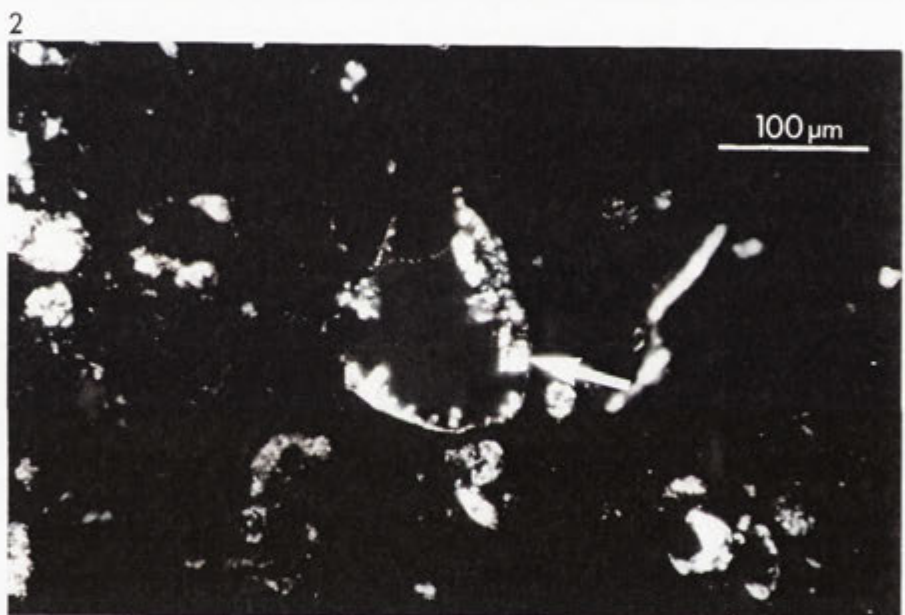
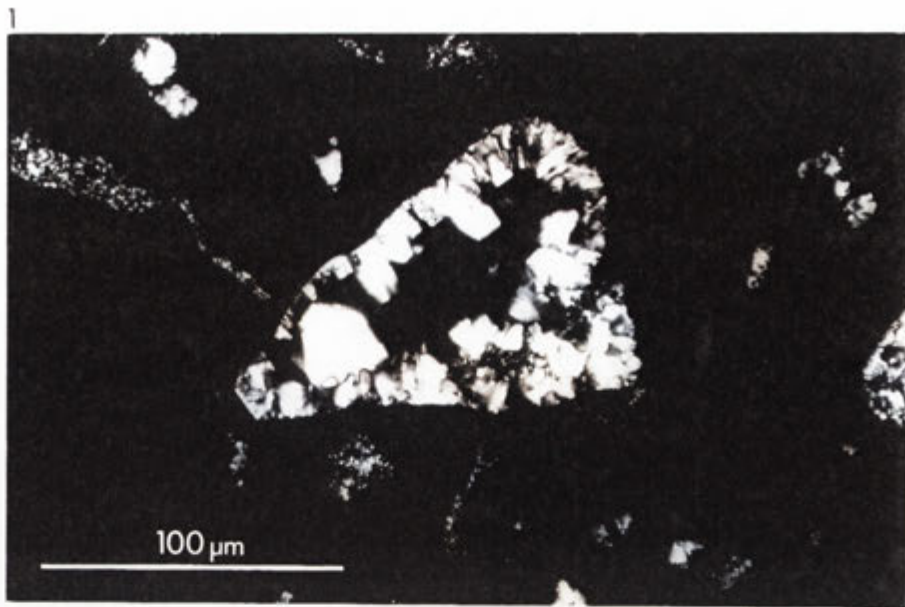


Figure 2.6

- Figure 2.6.1 A pisolith from drill-hole WB791EH (3.00 - 3.25 m depth) displaying 4 distinct zones (2-5). The *1st quartz-rich zone* (2) is surrounded by the *middle cortical layer* (3). Partially surrounding the *middle cortical layer* (3) is the *2nd quartz-rich zone* (4). Enveloping zones 2-4 is the *outer cortical layer* (5). Scale bar = 1 mm.
- Figure 2.6.2 A pisolith from drill-hole WB823EH (3.00 - 3.25 m depth) displaying all 5 zones. The arrows mark the boundary between the *inner cortical layer* (1) and the *1st quartz-rich zone* (2) defined by the truncation of cracks. The *1st quartz-rich zone* (2) has a higher quartz content compared to the adjacent zones and encompasses the *inner cortical layer* (1). Surrounding the *1st quartz-rich zone* (2) is the *middle cortical layer* (3). Partially surrounding the *middle cortical layer* (3) is the *2nd quartz-rich zone* (4). Enveloping zones 1-4 is the *outer cortical layer* (5). Scale bar = 1 mm.
- Figure 2.6.3 A section of a common compound pisolith from the Longtom mine, Weipa displaying all 5 zones as well as an outer quartz-bearing zone which merges with the surrounding matrix. This photograph shows that some pisoliths found within compound pisoliths are formed before the formation of the compound pisolith's shell. Scale bar = 1 mm.

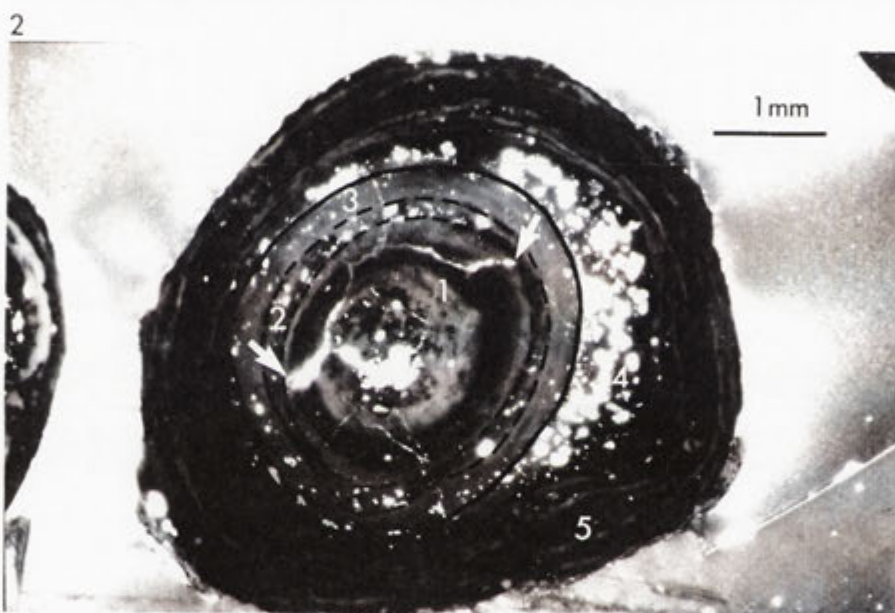
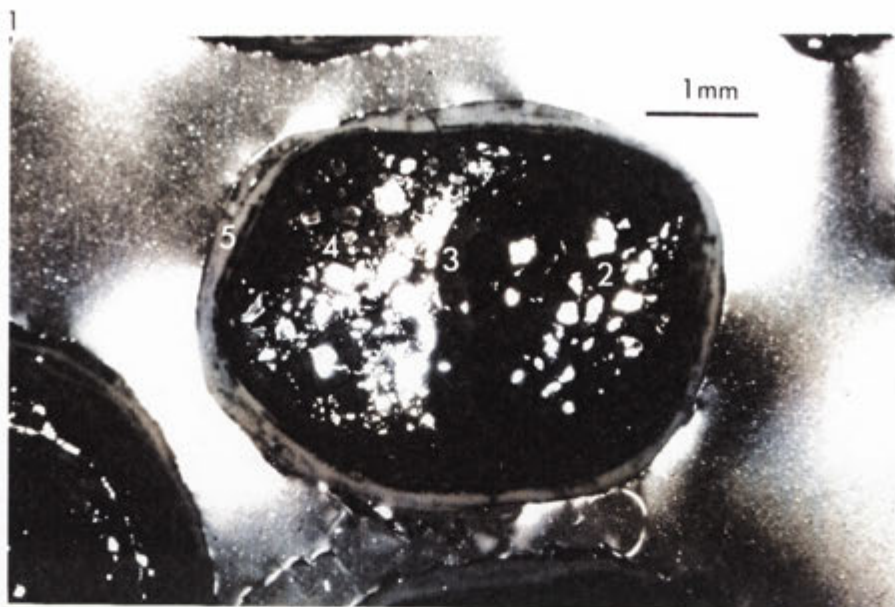
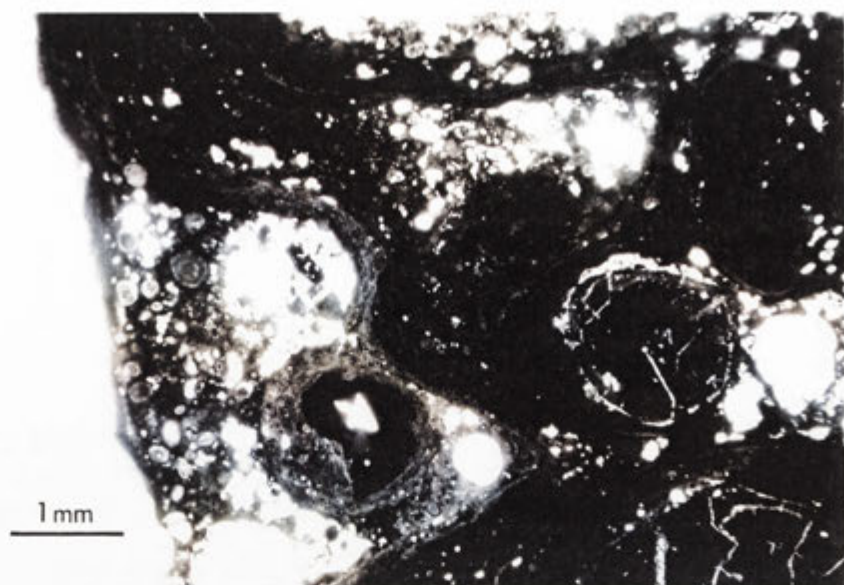


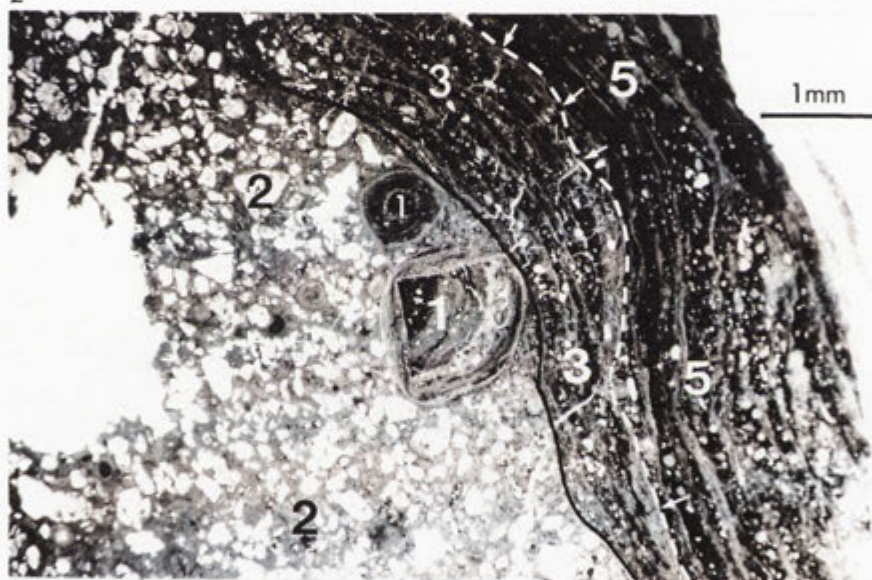
Figure 2.7

- Figure 2.7.1 Another section of the compound pisolith that was discussed in Figure 2.6.3. Scale bar = 1 mm.
- Figure 2.7.2 A section of a different compound pisolith from the Longtom mine, Weipa displaying 4 separate zones (see Figure 2.17). The *2nd quartz-rich zone* is missing in this part of the pisolith. The boundary between the *middle cortical layer* (3) and the *outer cortical layer* (5) is defined by the truncation of cracks (arrowed). Scale bar = 1 mm.
- Figure 2.7.3 Another section of the compound pisolith that was discussed in Figure 2.7.2 (see Figure 2.17). In this part of the pisolith, the *2nd quartz-rich zone* (4) is present between the *middle cortical layer* (3) and the *outer cortical layer* (5). The *middle cortical layer* (3) is severely truncated by the *outer cortical layer* (5) (arrowed). The *1st quartz-rich zone* (2) constitutes the "shell" of the compound pisolith. Scale bar = 1 mm.

1



2



3

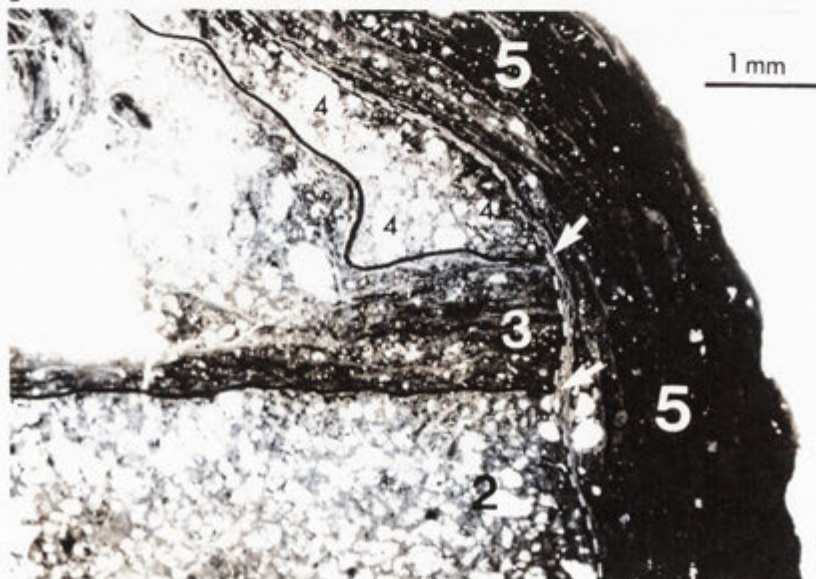


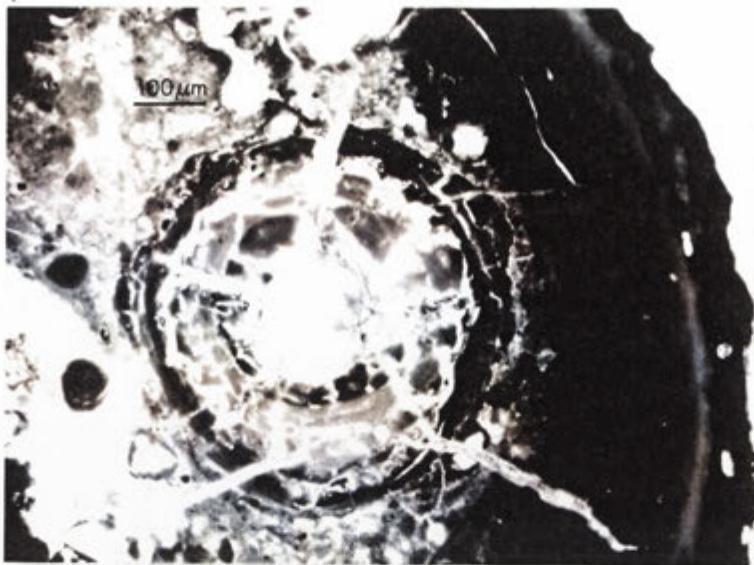
Figure 2.8

Figure 2.8.1 A pisolith from drill-hole WB823EH (3-3.25 m). The oöolith is ascribed to the *inner cortical layer*. The *1st quartz-rich zone* encompasses the oöolith which in turn is enveloped by the *middle cortical layer*. Radial cracks within this zone are truncated by the *outer cortical layer*. Scale bar = 100 µm.

Figure 2.8.2 A pisolith from drill-hole WB837EH (1-1.25 m). A broken oöolith (*inner cortical layer*) is supported in the *2nd quartz-rich zone*. The smaller oöoliths, contained within the *2nd quartz-rich zone* are ascribed to the *middle cortical layer*. Enveloping the *2nd quartz-rich zone* is the *outer cortical layer*. Scale bar = 100 µm.

Figure 2.8.3 The inner part of a pisolith from drill-hole WB754EH (2.5-2.75 m) showing a fragmental remnant of the *inner cortical layer*. Iron has been mobilised from parts of the fragment (arrowed). Scale bar = 100 µm.

1



2



3

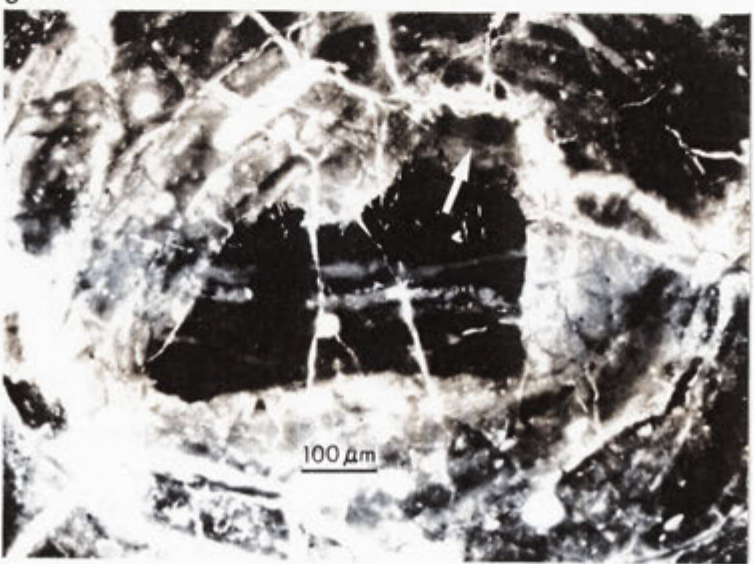


Figure 2.9

- Figure 2.9.1 A pisolith from drill-hole WB837EH (2-2.5 m). The oöolith is ascribed to the *inner cortical layer*. Partially surrounding the oöolith is the *1st quartz-rich zone*. The *middle cortical layer* encompasses the *1st quartz-rich zone*. Cracks are truncated (dashed line) by the *outer cortical layer*. Scale bar = 100 µm.
- Figure 2.9.2 A pisolith from drill-hole WB823EH (0.5-0.75 m). The pisolith is composed of a core consisting of the *1st quartz-rich zone*. A thin *middle cortical layer* surrounds the *1st quartz-rich zone*. A lens of material associated with the *2nd quartz-rich zone* lies between the *middle cortical layer* and the *outer cortical layer*. Scale bar = 100 µm.
- Figure 2.9.3 A pisolith from drill-hole WB839EH (2.5-2.75 m). The pisolith is composed of an oöolithic fragment (*inner cortical layer*) which is partially surrounded by the *1st quartz-rich zone* at the bottom of the micrograph. The *middle cortical layer* encompasses both the oöolith and the *1st quartz-rich zone*. Radial cracks are truncated by the *outer cortical layer*. Scale bar = 100 µm.

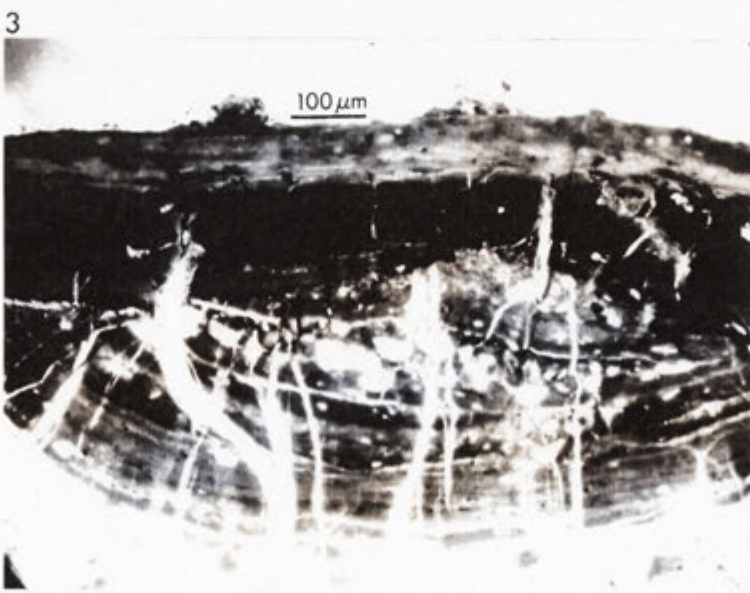
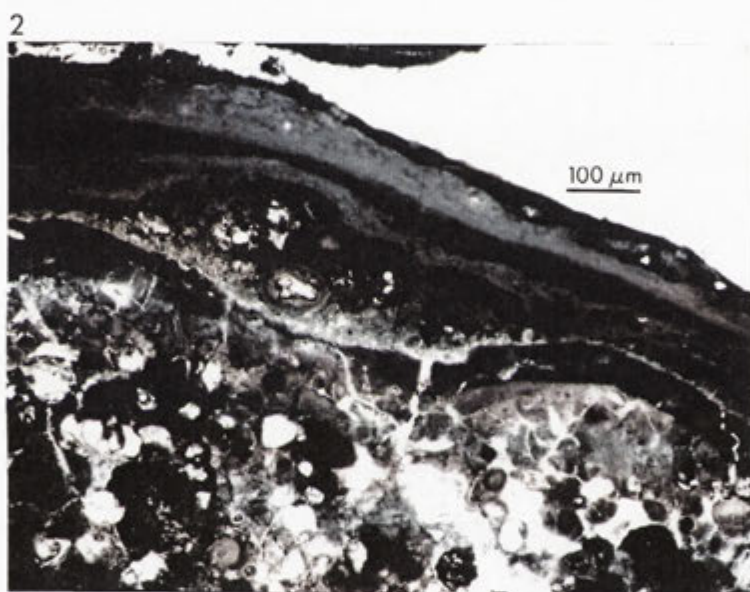
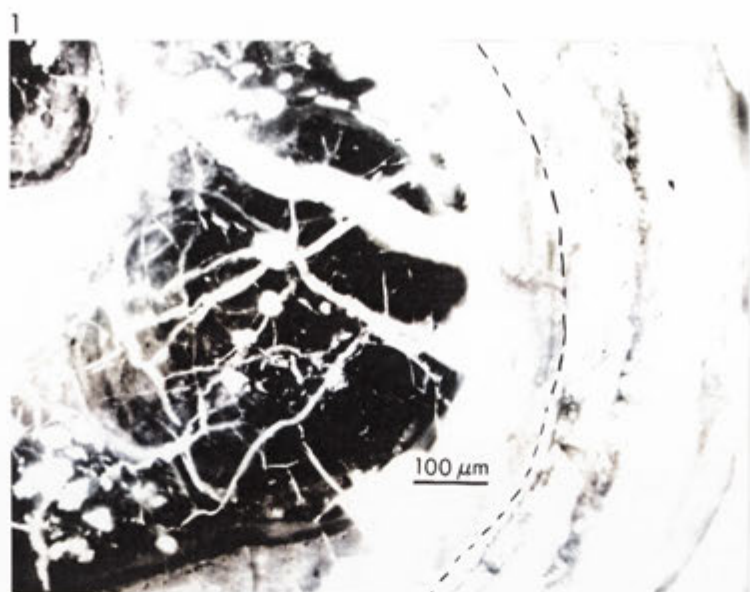


Figure 2.10

Figure 2.10.1 A pisolith from drill-hole WB781EH (2.75-3.25 m). Note the truncation of cracks at the boundary between two cortical layers. Scale bar = 100 μm .

Figure 2.10.2 Another view of the pisolith from drill-hole WB781EH (2.75-3.25 m). In this part of the pisolith a quartz-rich zone occurs between the two cortical layers. Scale bar = 100 μm .

Figure 2.10.3 A pisolith from drill-hole WB857EH (3.75-4 m). In this micrograph the inner cortical layers are "embayed" with a quartz-rich zone. Cracks are truncated by the quartz-rich zone. Scale bar = 100 μm .

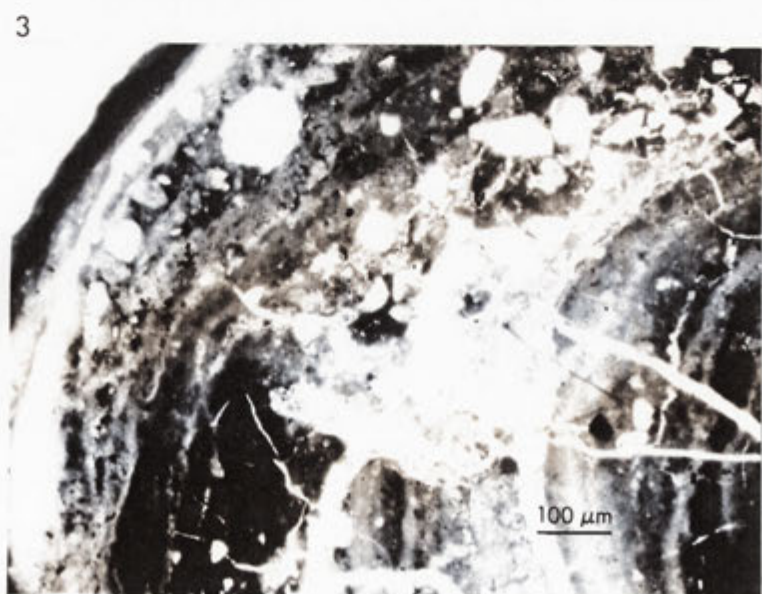
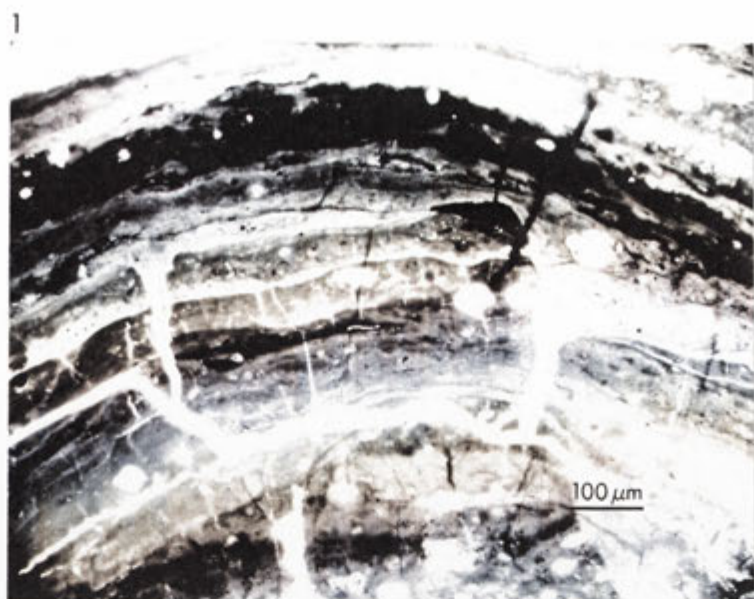


Figure 2.11

Figure 2.11.1 A pisolith from drill-hole WB823EH (2-2.25 m). The core of this pisolith consists of a pisolith fragment surrounded by a quartz-rich zone. Another cortical layer envelops these zones. Note also the truncation of cracks at the zone boundaries. Scale bar = 100 μm .

Figure 2.11.2 A pisolith from drill-hole WB754EH (2.5-2.75 m). This micrograph is particularly good in showing the truncation of cracks between two distinct cortical layers. Scale bar = 100 μm .

Figure 2.11.3 A pisolith from drill-hole WB857EH (1-1.25 m). The core of this pisolith consists of what appears to be the fragments of a brecciated pisolith. Surrounding each fragment is a quartz-rich zone. A cortical layer envelops these zones. Scale bar = 100 μm .

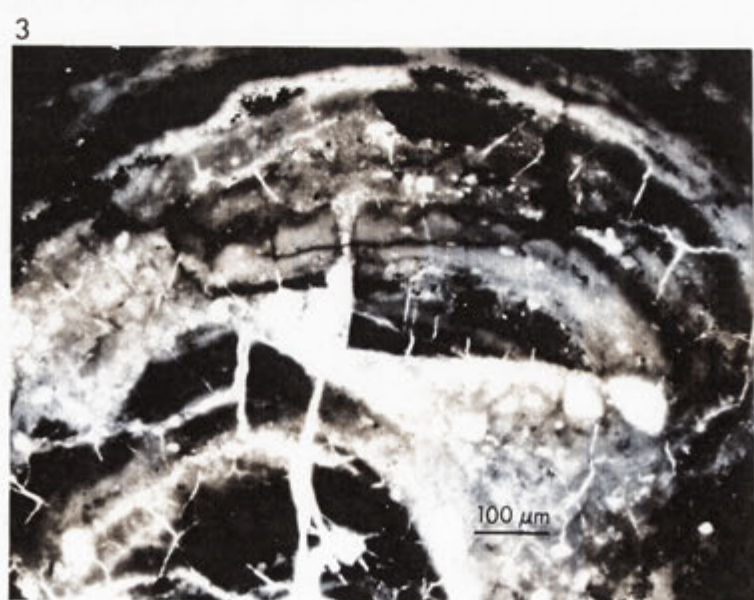
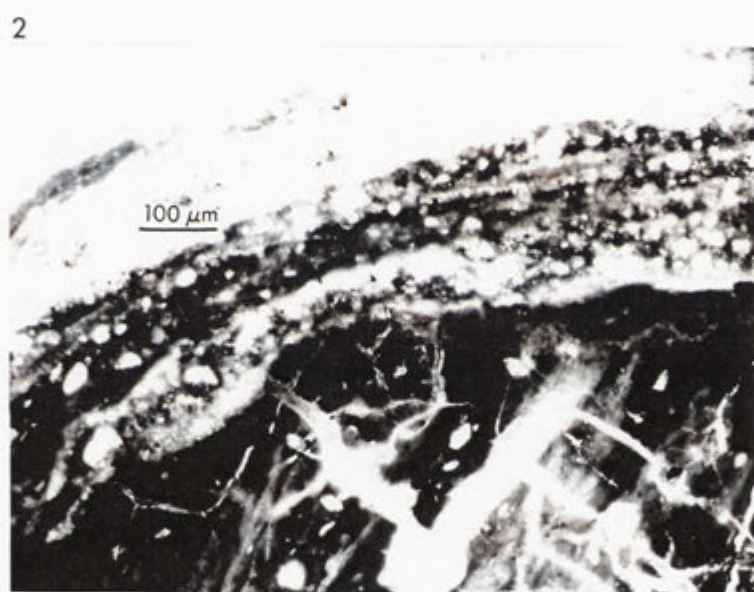
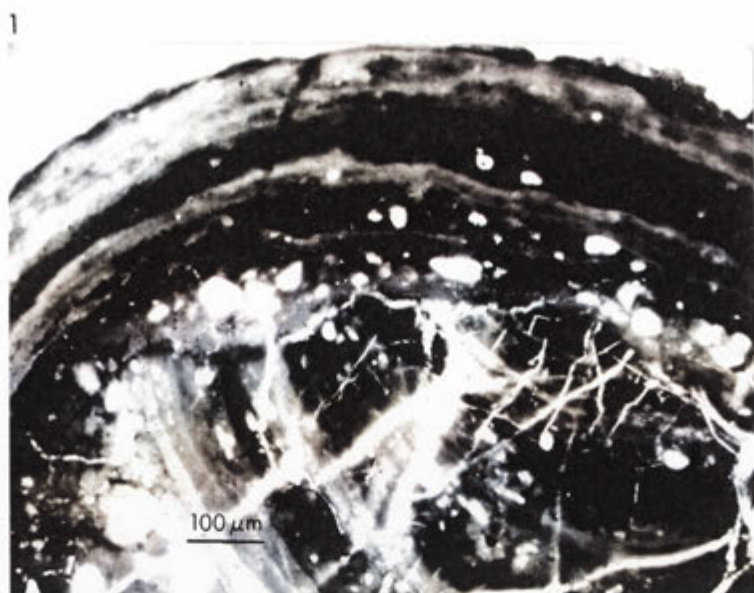


Figure 2.12

Figure 2.12.1 A pisolith from drill-hole WB839EH (2.5-2.75 m). The quartz-rich zone of this pisolith is embayed. The quartz-rich material infilling the embayment appears to have been overprinted by a diffuse cortical layering. Scale bar = 100 μm .

Figure 2.12.2 A pisolith from drill-hole WB781EH (1-1.5 m). The core of this pisolith is embayed by a quartz-rich zone. Suspended in the quartz-rich zone is a pisolith fragment. Scale bar = 100 μm .

Figure 2.12.3 A pisolith from drill-hole WB781EH (1-1.5 m). A very good example of cracks truncated at the boundary between two cortical layers. A quartz-rich zone is not present between the two layers. Scale bar = 100 μm .

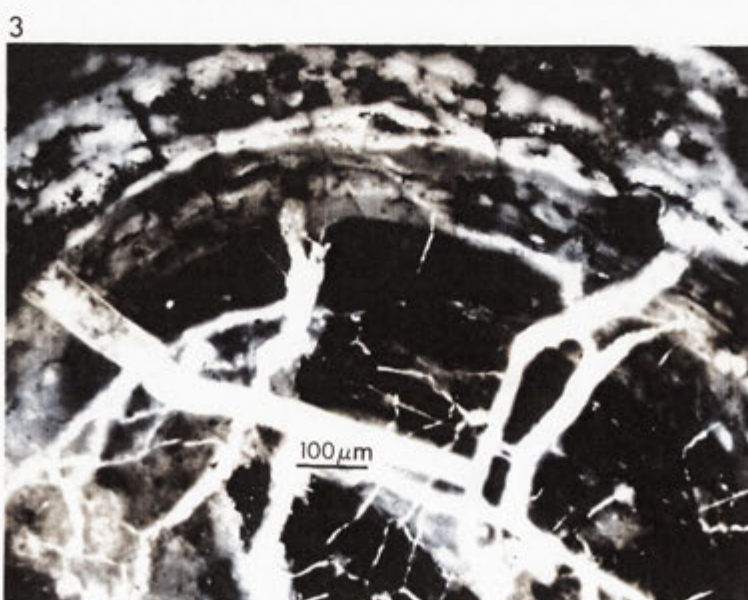
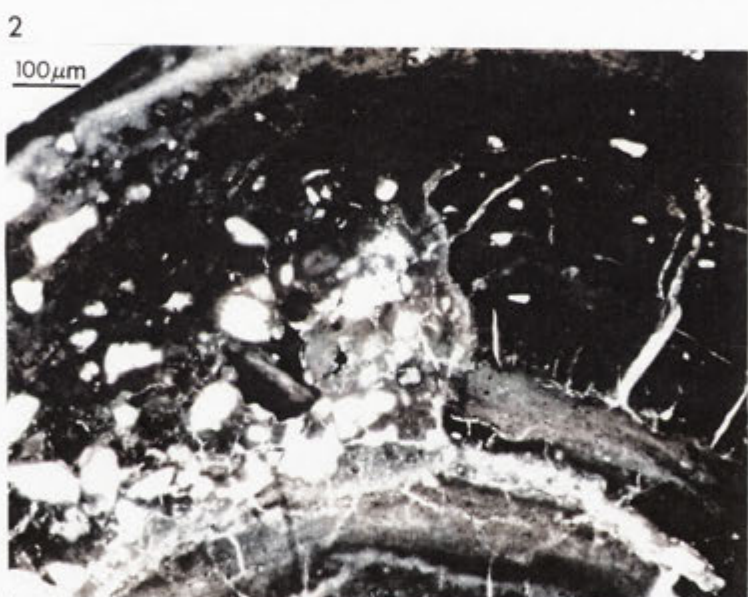
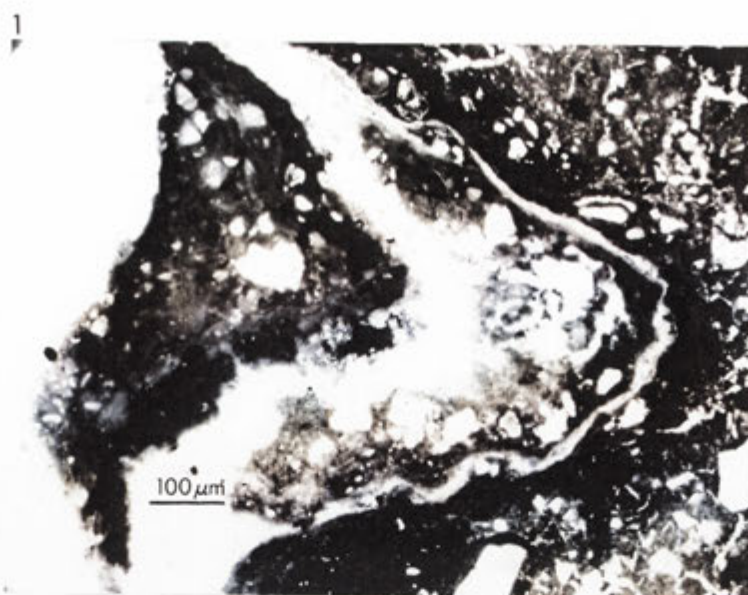


Figure 2.13

Figure 2.13.1 A pisolith from drill-hole WB791EH (1.5-1.75 m). The core of this pisolith consists of a quartz-rich zone with a whole oöolith suspended within it. A cortical layer surrounds the core. Scale bar = 100 μm .

Figure 2.13.2 A pisolith from drill-hole WB837EH (2-2.5 m). A small embayment is developed at the intersection of a tangential crack and the overlying cortical layer. Adjacent to the embayment the inner cortical layer appears somewhat "bleached". Scale bar = 100 μm .

Figure 2.13.3 A pisolith from drill-hole WB781EH (2.75-3.25 m). The outer surface of the core is embayed with quartz-rich material. Enveloping the core and the quartz-rich zone is a cortical layer. Scale bar = 100 μm .

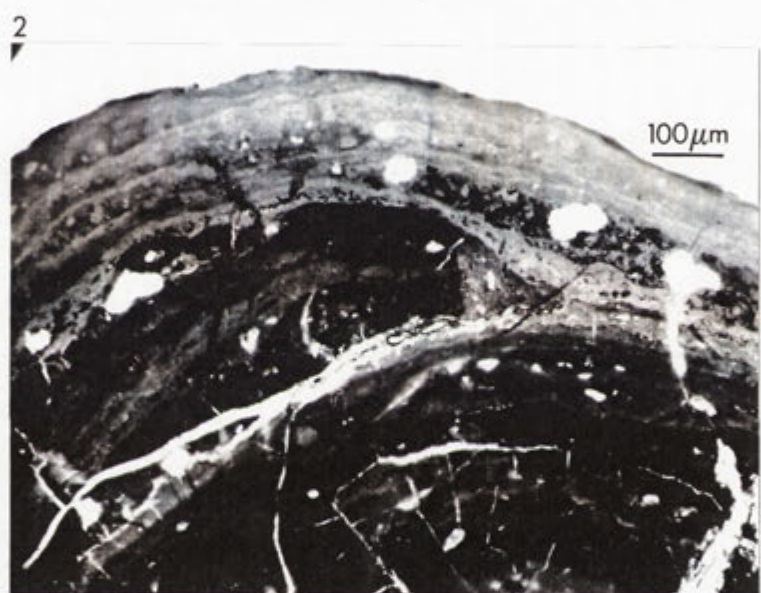


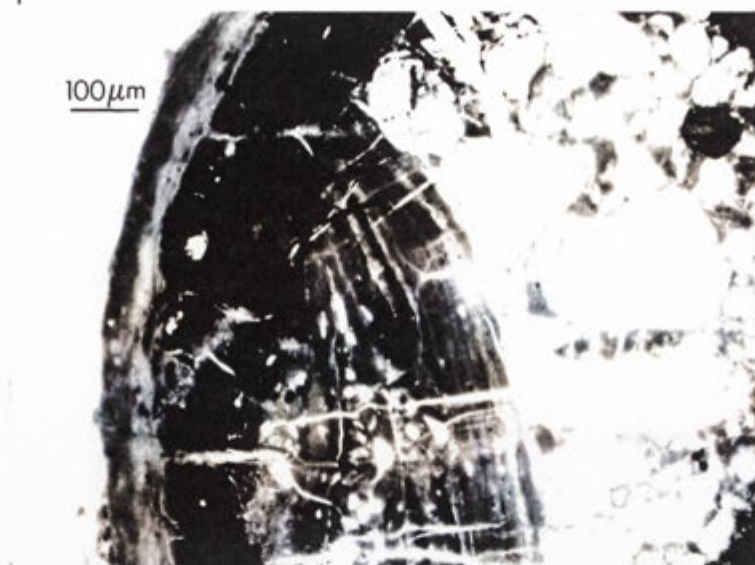
Figure 2.14

Figure 2.14.1 A pisolith from drill-hole WB839EH (2.5-2.75 m). The core of this pisolith is dominantly quartz-rich, with a pisolith fragment attached to the side of the quartz-rich zone. A dark hematite-rich layer surrounds the core and is overlain by a paler cortical layer. Scale bar = 100 μm .

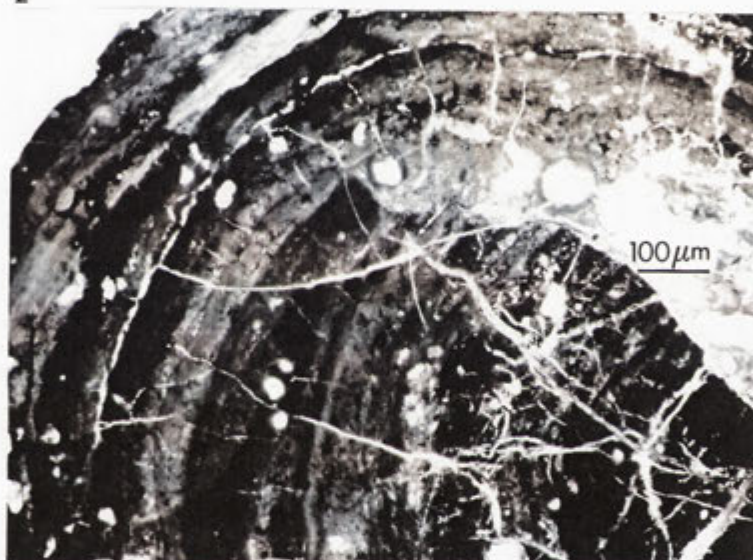
Figure 2.14.2 A pisolith from drill-hole WB857EH (2.5-3 m). One half of the core is composed of a pisolith fragment while a quartz-rich zone makes up the remainder. A cortical layer encompasses both zones. Scale bar = 100 μm .

Figure 2.14.3 A view of the cortical banding (left) in a common compound pisolith from the Longtom mine, Weipa. The right side of the micrograph shows the quartz-rich zone which makes up the "shell" of the compound pisolith. Scale bar = 100 μm .

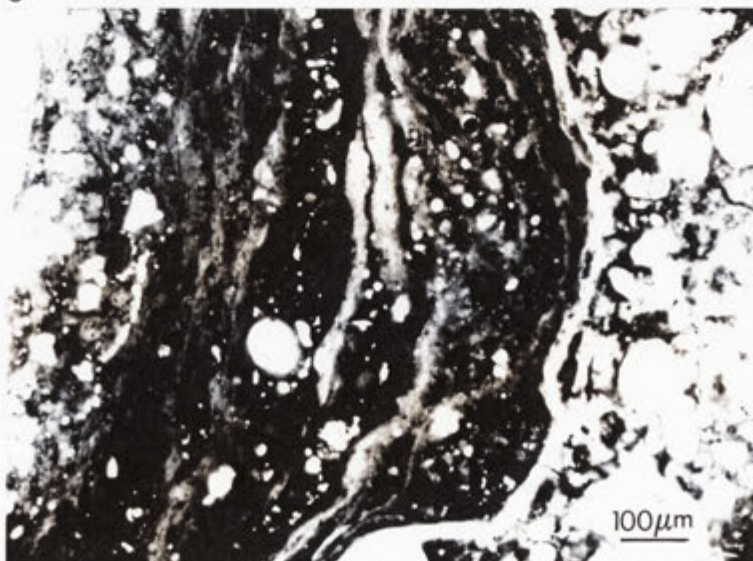
1



2



3



2.3.2 Compound pisoliths

Bauxitic compound pisoliths are tubular or egg-like structures composed of a shell which commonly encases single pisoliths (Figure 2.15). The shell contains around 66 wt.% gibbsite and has a quartz content of approximately 22 wt.% (Figures 2.16 and 2.17). The remaining 12 wt.% of the shell is composed of kaolinite (~ 6 wt.%), anatase (~ 3 wt.%), boehmite (~ 2 wt.%) and hematite (~ 1 wt.%). Generally, the main body of the shell is not layered but consists of a uniform distribution of medium-grained quartz grains within a bauxitic matrix. Broad diffuse banding or reddening which is commonly evident around the periphery of the shell is due to a concentration of hematite.

Surrounding the shell and in continuum with the matrix that surrounds the encased single pisoliths, is a gibbsite-boehmite-hematite layer. Overlying this layer is a boehmite-gibbsite-hematite layer forming the outermost skin of the compound pisolith. The boehmite content of this outer layer is around 38 wt.% while the gibbsite and hematite contents are respectively 34 and 12 wt.%. The outermost layer has a relatively high kaolinite content of approximately 11 wt.%. The remaining 5 wt.% of the layer is composed of anatase (~ 3 wt.%) and quartz (~ 2 wt.%). Both layers are strongly banded.

The pisoliths encased within the gibbsite-quartz shell are 2-3 mm in diameter and have a boehmite-gibbsite core with a kaolinite content of < 3 wt.%. Micro-sedimentological evidence indicates that the formation of the encased pisoliths predates the development of the gibbsite-quartz shell.

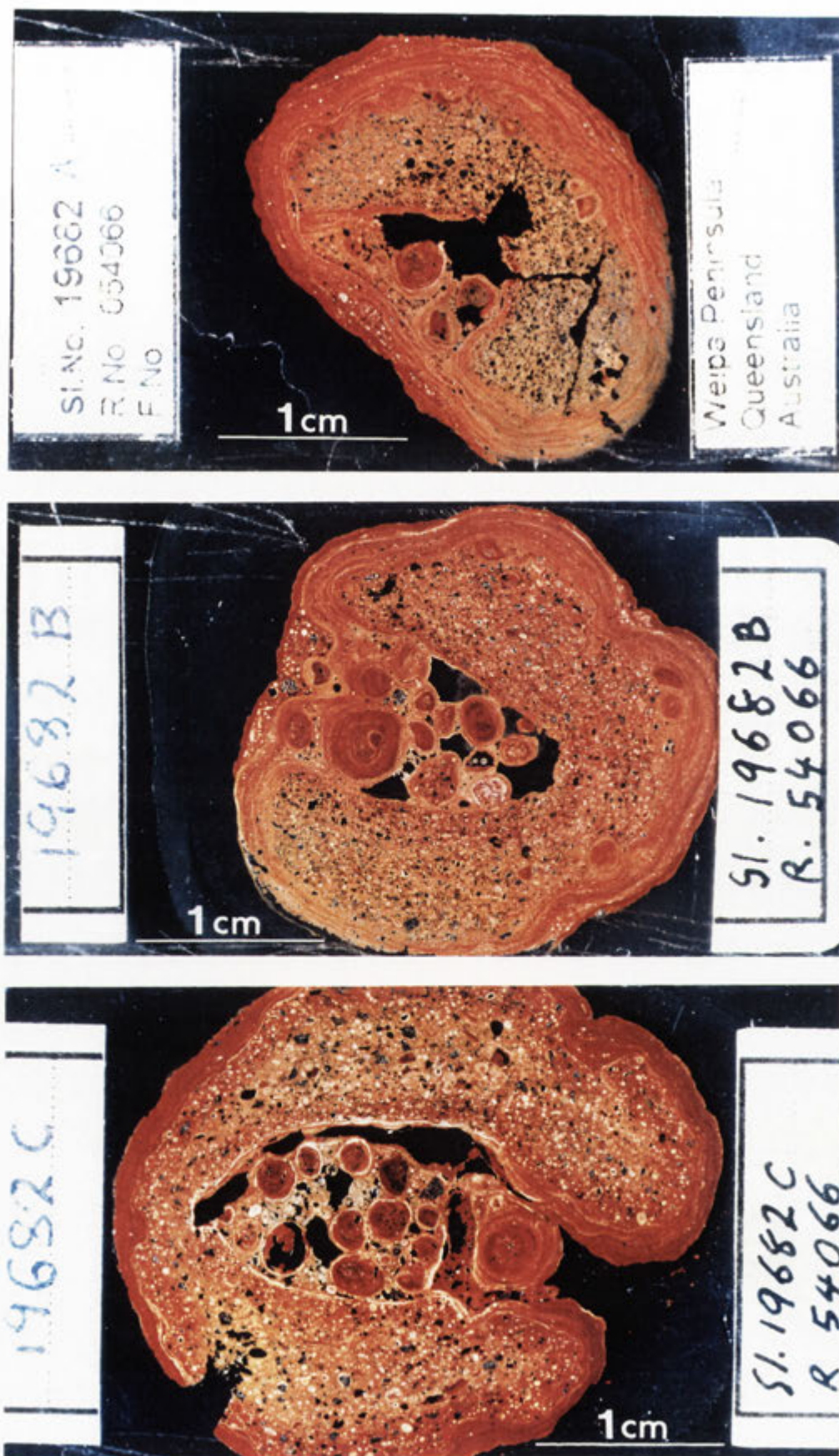
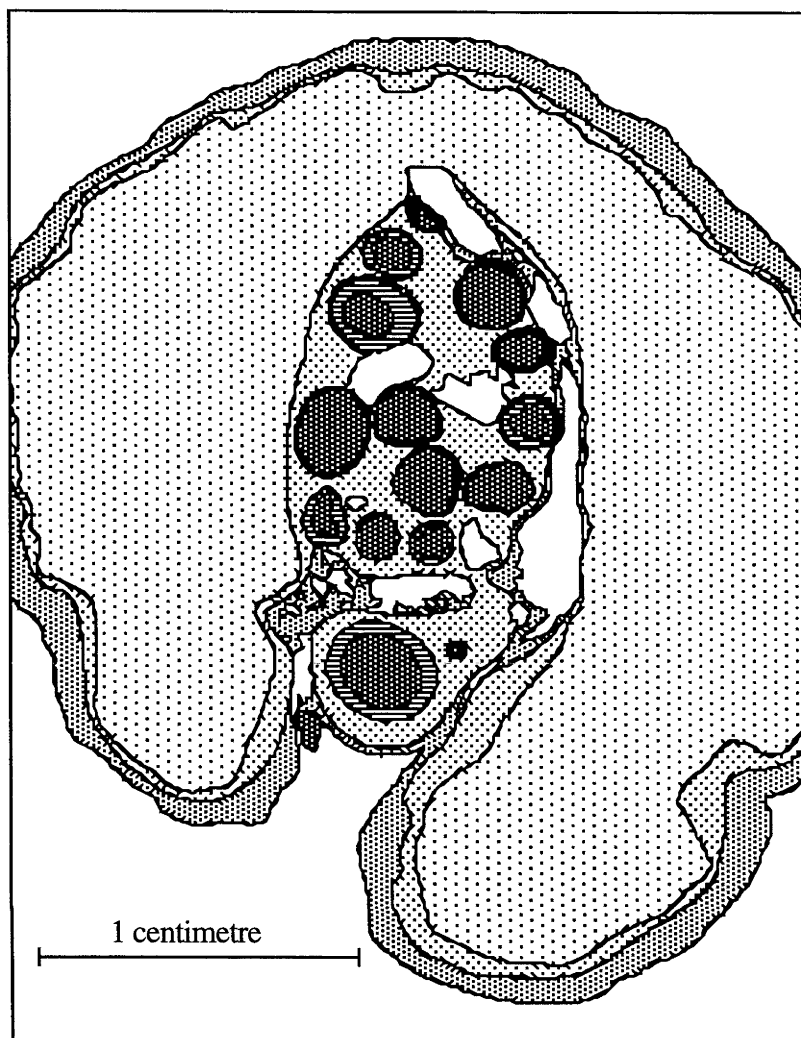


Figure 2.15

Sectioned common compound pisoliths from the Longtom mine, Weipa

Textural and mineralogical map of a common compound pisolith from the Longtom mine, Weipa.



SIROQUANT analyses of the individual zones
(Poorly diffracting material is not included)

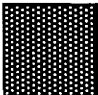
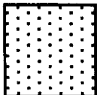
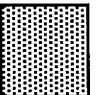
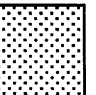

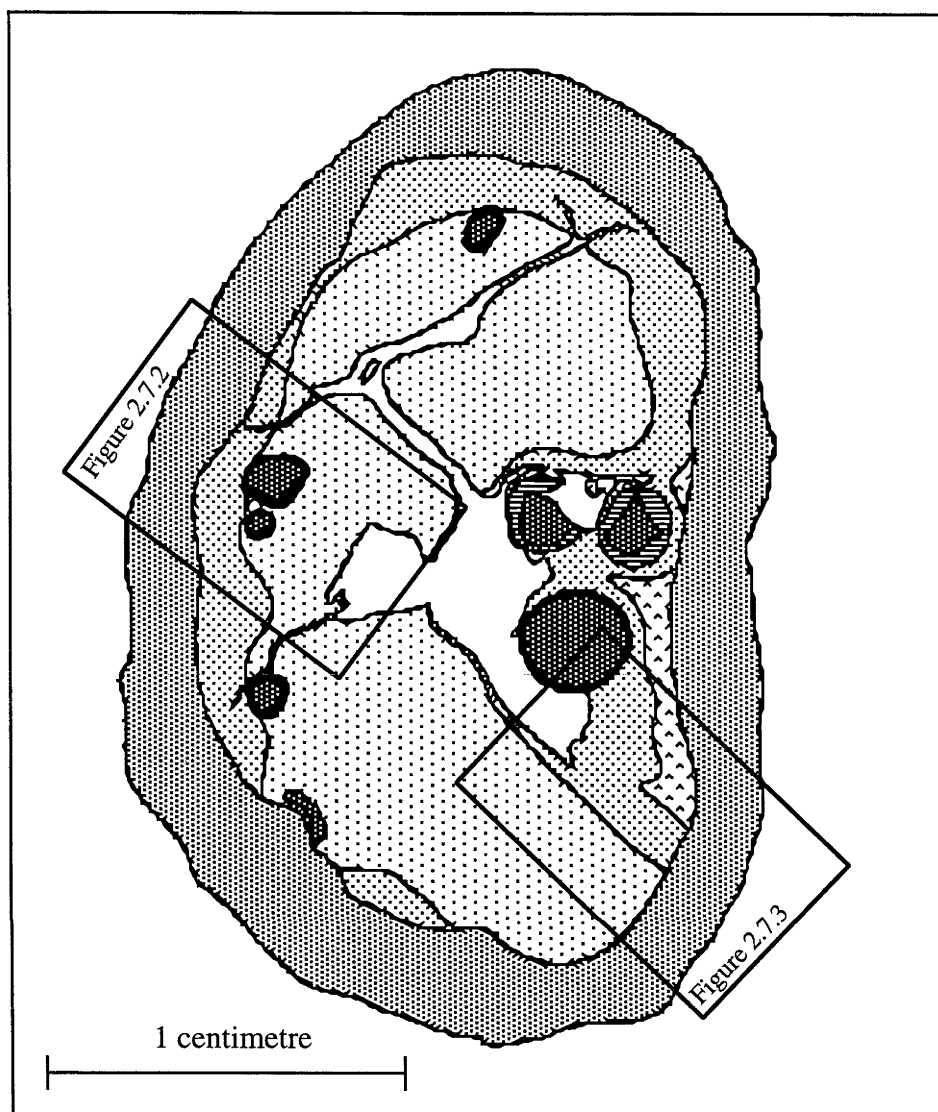
<u>mineral</u>	<u>weight%</u>				
					
gibbsite	33.1	68.1	34.3	65.5	47.6
quartz	1.5	19.5	1.3	0.4	0.0
boehmite	49.9	1.9	37.7	17.4	35.3
kaolinite	2.9	6.6	10.3	3.3	5.5
hematite	8.3	0.6	12.7	9.1	6.9
anatase	4.4	3.2	3.7	4.3	4.6

Figure 2.16

Textural and mineralogical map of a common compound pisolith from the Longtom mine, Weipa.



SIROQUANT analyses of the individual zones
(Poorly diffracting material is not included)

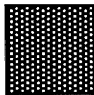
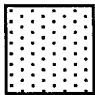
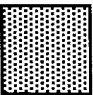
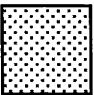

mineral	weight %				
					
gibbsite	60.4	63.4	34.4	58.8	79.6
quartz	2.3	24.1	2.5	7.1	4.9
boehmite	24.1	2.6	37.9	7.4	5.5
kaolinite	2.6	5.4	11.3	3.9	0
hematite	6.3	1.7	11.5	15.6	5.1
anatase	4.3	2.7	2.3	7.2	4.9

Figure 2.17

Chapter 3

Scanning Electron Microscopy

3.1 Introduction

Cambridge S360 and Jeol 6400 scanning electron microscopes were used in combination with energy dispersive X-ray analysis (EDXA) to identify some of the minerals contained within bauxitic pisoliths and ferruginous-kaolinite nodules.

Geochemical profiling across polished thin-sections of individual pisoliths was conducted using a Cameca electron microprobe, to study the variation in Al_2O_3 and Fe_2O_3 .

A back-scattered electron image of a thin-sectioned pisolith was analysed using the Apple Macintosh *Image* program. Correlation of radiation intensity with electron microprobe data, led to the production of a map showing the distribution of Fe_2O_3 within a pisolith.

3.2 Scanning electron micrography

3.2.1 Method

Individual pisoliths were split in half using a razor blade and mallet. As ferruginous-kaolinite nodules are somewhat larger than pisoliths, they were instead broken with a hammer. The pisolith halves and nodule fragments were mounted on aluminium stubs and a thin coating of gold (200Å) was applied to their surfaces. The scanning electron microscope was normally operated at 15kV unless charging was a problem, in which case the voltage was reduced. To identify zircon grains it was necessary to increase the voltage to 20 kV so that zirconium could be identified in the X-ray spectrum. To obtain high resolution images, a working distance of less than 12 mm and a lower than normal filament current was used.

3.2.2 Results

Many of the pisoliths examined, contain quartz grains which display unusual surface features (Figure 3.1). Their surfaces are commonly covered with either step-like features or what appear to be numerous crystal terminations, depending on the surface's crystallographic orientation. The surfaces may be dissected with deep chasms or pits. The nature and orientation of the observed features, appear to be crystallographically controlled. These features are indicative of an intense chemical weathering environment whereby the quartz has undergone dissolution by severe chemical etching (Krinley and Doornkamp, 1973). Such quartz grains generally occupy voids much larger than themselves. Elongate gibbsite crystals are commonly seen lining the void wall and projecting inwardly into the space surrounding a quartz grain. Gibbsite within these voids shows a variety of habits; hexagonal columns, tabular aggregates or groups of radiating needles (Figure 3.2). Some voids contain neither quartz nor gibbsite. The observations suggest that gibbsite nucleates on the void wall and grows into the space produced by the dissolution of quartz.

Boehmite is normally too small to image with a scanning electron microscope. However, sometimes the conditions are favourable for it to grow to a much larger size. Within cracks in the core of pisoliths, boehmite has been tentatively identified; the morphology of which is similar to synthetic boehmite (Figure 3.3.1 and 3.3.2)

Porous pisoliths commonly contain appreciable quantities of organic matter in the form of fungus (Figure 3.3.3 and 3.3.4). Dr. Graham Chilvers of the Department of Botany and Zoology, ANU examined the electron micrographs and believes that the branching filaments are fungal hyphae. The presence of a 'clamp connection' on one of the hyphae indicates that the fungus belongs to the class *Basidiomycetes*. The round objects in the micrographs may be teliospores, which are thick-walled resting spores.

Kaolinite within ferruginous-kaolinite nodules is usually too small to resolve well with a scanning electron microscope (i.e. $\ll 1 \mu\text{m}$). Quartz grains within the nodules display similar dissolution features to those found in bauxitic pisoliths. Aggregates of goethite and hematite can sometimes be seen resembling the inverted relief of quartz grains (Figure 3.3.5 to 3.3.8). This is interpreted to indicate that at one stage, goethite and hematite were growing on or in close proximity to the quartz grain. Subsequent removal of quartz by dissolution left a ferruginous mould of the quartz grain.

Figure 3.1

- Figure 3.1.1 A quartz grain displaying many deep dissolution pits. The grain occupies a void produced by the partial dissolution of quartz. Scale bar = 100 μ m.
- Figure 3.1.2 A close-up view of a dissolution pit. Scale bar = 1 μ m.
- Figure 3.1.3 Step-like features on the surface of a quartz grain. Scale bar = 10 μ m.
- Figure 3.1.4 The surface of a quartz grain dissected by deep dissolution chasms. Scale bar = 10 μ m.
- Figure 3.1.5 The surface of a partially dissolved quartz grain displaying numerous crystal terminations. Scale bar = 10 μ m.
- Figure 3.1.6 A quartz grain displaying step-like dissolution features and crystal terminations. Gibbsite crystals are visible in the top right-hand corner of the micrograph. Scale bar = 10 μ m.
- Figure 3.1.7 Well-defined crystal faces on a quartz grain that has undergone partial dissolution. A veinlet of gibbsite is draped over the quartz grain. Scale bar = 10 μ m.
- Figure 3.1.8 A close-up view of the gibbsite veinlet. The gibbsite may have originally nucleated on material within a crack in the quartz. Subsequent dissolution of the surrounding quartz allowed for further growth of the gibbsite crystals and the veinlet's isolation from the quartz. Scale bar = 1 μ m.

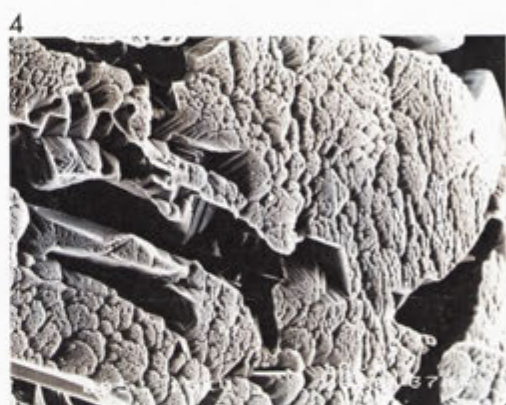


Figure 3.2

- Figure 3.2.1 Well-formed gibbsite crystals growing into a void. Scale bar = 1 μm .
- Figure 3.2.2 One of gibbsite's growth habits: a hexagonal column. Scale bar = 1 μm .
- Figure 3.2.3 Gibbsite crystals infilling a void which was produced by the partial dissolution of a quartz grain. The dark grey, featureless area at the bottom of the micrograph is quartz. Bauxitic material occupies a crack within the quartz grain (bottom centre). Scale bar = 10 μm .
- Figure 3.2.4 A close-up view of the previous micrograph showing well-formed gibbsite crystals displaying a columnar growth habit. Scale bar = 1 μm .
- Figure 3.2.5 A close-up view of a gibbsite crystal exhibiting a step-like growth pattern. Scale bar = 10 μm .
- Figure 3.2.6 The nucleation and growth of gibbsite on material that once occupied a crack in a quartz grain. Subsequent dissolution of the quartz enabled gibbsite to grow and fill the dissolution void. Scale bar = 10 μm .
- Figure 3.2.7 Gibbsite crystals growing as groups of radiating needles. Scale bar = 10 μm .
- Figure 3.2.8 Gibbsite crystals displaying a tabular growth habit. Scale bar = 5 μm .

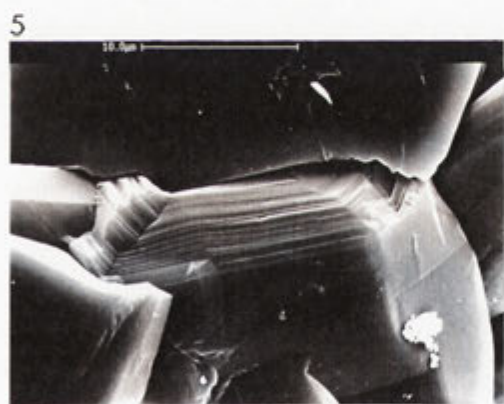
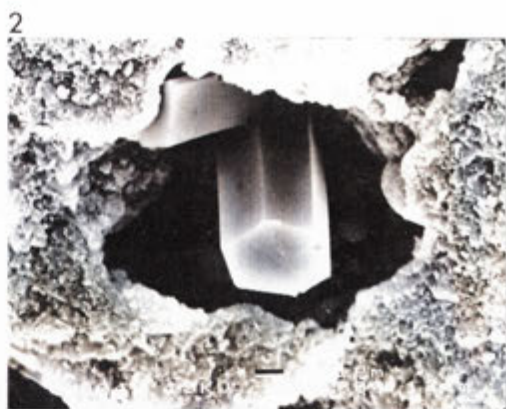
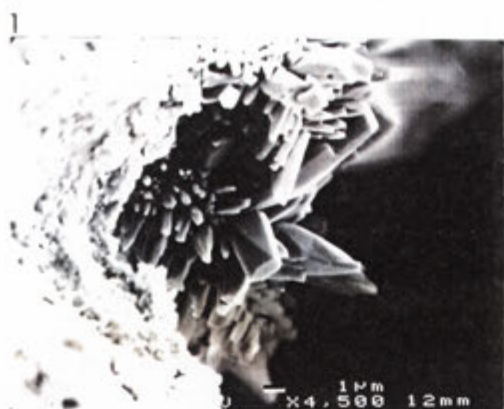
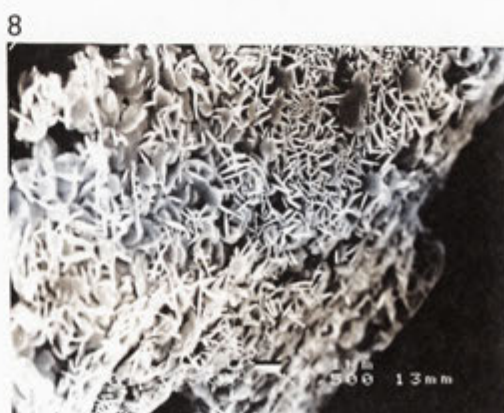
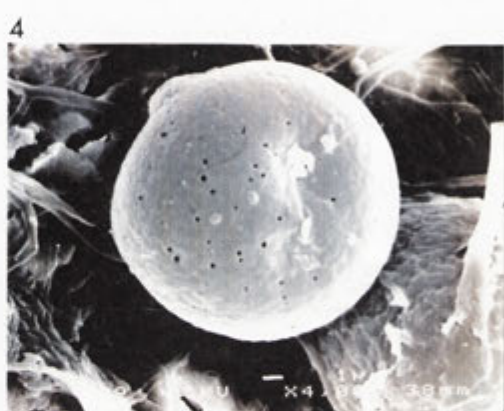
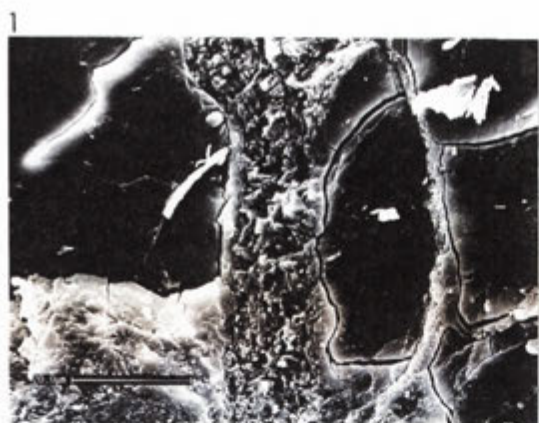


Figure 3.3

- Figure 3.3.1 Boehmite crystals growing within a shrinkage crack. Scale bar = 20 μm .
- Figure 3.3.2 A close-up view of the crack containing boehmite crystals. The morphology of the crystals is similar to that of synthetic boehmite (see figure 6.7). Scale bar = 5 μm .
- Figure 3.3.3 *Basidiomycetes* fungus growing within a porous bauxitic pisolith. Globular structures are teliospores and the filamentous strands are hyphae. Scale bar = 10 μm .
- Figure 3.3.4 A close-up view of a teliospore. Scale bar = 1 μm .
- Figure 3.3.5 A hematite-goethite mould of a quartz dissolution pit. The micrograph shows that hematite and goethite were at one stage growing on or in close proximity to a partially dissolved quartz grain. When the quartz grain completely dissolved, a mould was left behind. Scale bar = 10 μm .
- Figure 3.3.6 A close-up view of the mould displaying the constituent goethite (needle-like) and hematite (plate-like) crystals. Scale bar = 1 μm .
- Figure 3.3.7 A quartz dissolution void coated with a layer of goethite and hematite. "Curtains" of goethite and hematite drape into the void. The goethite and hematite may have previously coated the quartz grain as well as occupied cracks. When the quartz dissolved, the goethite and hematite became exposed. Scale bar = 100 μm .
- Figure 3.3.8 A close-up view of the goethite (needle-like) and hematite (plate-like) crystals. Scale bar = 1 μm .



At the old kaolin pit at Nanagai (near Weipa) exists a profile where pisoliths may be found within the mottled zone (Figure 3.4). These pisoliths consist of a bauxitic core surrounded by a kaolinitic cortex. The crystal habit of kaolinite is quite typical; consisting of foliated hexagonal plates. The X-ray spectrum shows that aluminium and silicon are in approximately equal abundance indicating the presence of kaolinite. Hematite found within the voids, is invariably aluminium-rich and has a wafer-like morphology. When there is unimpeded crystal growth, the hematite wafers commonly form rosettes (Figure 3.5).

Slightly rounded to well rounded zircon crystals are found within pisoliths (Figure 3.6). Like the accompanying quartz grains, zircons are believed to be of primary origin. There is a tendency for zircons to be more numerous in the quartz-rich zones of bauxitic pisoliths.

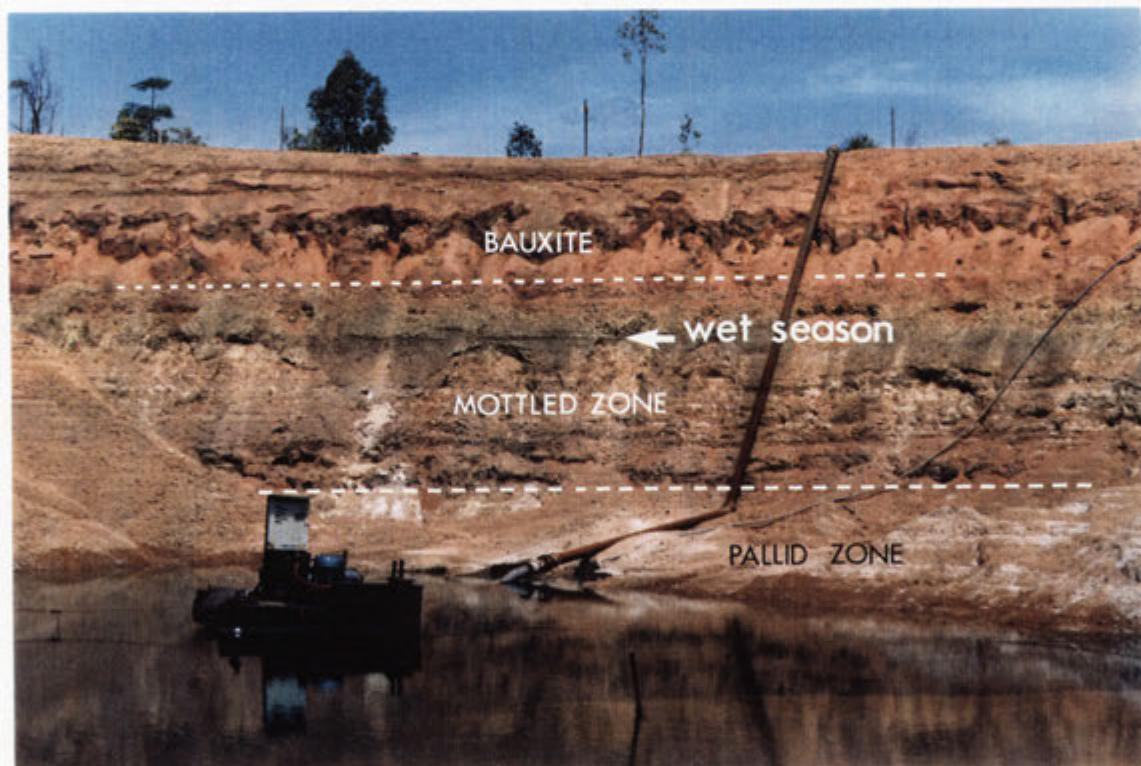


Figure 3.4

A photograph of the old kaolin pit at Nanagai, displaying three main zones in the weathering profile. The level of the pond is an expression of the water-table. The photograph was taken during the dry season (July). The height of the water-table during the wet season (January) is indicated. Between the wet season water-table level and the bauxite horizon lies the nodular ferruginous-kaolinite layer.

Figure 3.5

- Figure 3.5.1 Al-hematite wafers intermixed with gibbsite crystals, in a pisolith from the mottled zone at Nanagai, Weipa. Scale bar = 2 μm .
- Figure 3.5.2 Kaolinite crystals within a kaolinitic pisolith, from the mottled zone at Nanagai, Weipa. Scale bar = 2 μm .
- Figure 3.5.3 Al-hematite wafers forming a rosette within a void in a pisolith, from the mottled zone at Nanagai, Weipa. Scale bar = 5 μm .
- Figure 3.5.4 A close-up view of the Al-hematite rosette. Scale bar = 2 μm .
- Figure 3.5.5 Goethitic rods coated with gibbsite, growing within a void of a pisolith, from the mottled zone at Nanagai, Weipa. Scale bar = 10 μm .
- Figure 3.5.6 Goethitic rods without a coating of gibbsite. The large blocky mineral on the bottom and right-hand side of the micrograph is quartz. Scale bar = 1 μm .
- Figure 3.5.7 Columnar gibbsite growing within a void of a pisolith, from the mottled zone at Nanagai, Weipa. Some goethite needles are also visible in the micrograph. Scale bar = 10 μm .
- Figure 3.5.8 Ferruginous spherules, probably consisting of hematite, growing within a void of a pisolith, from the mottled zone at Nanagai, Weipa. Scale bar = 10 μm .

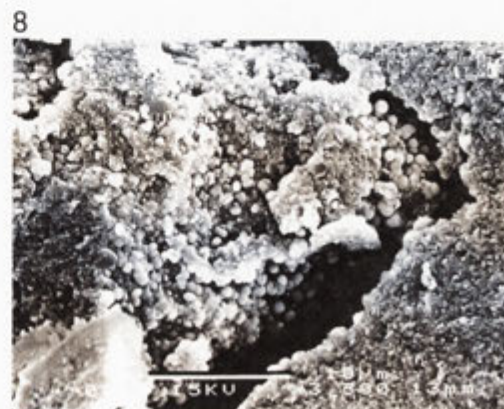


Figure 3.6

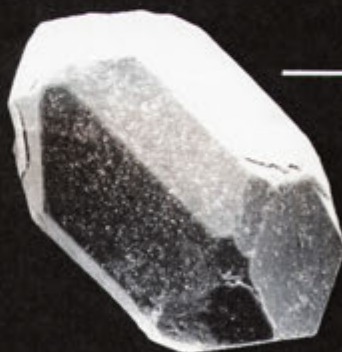
Figure 3.6.1 Zircons extracted from the shell of a common compound pisolith, Longtom mine, Weipa. Scale bars = 50 μm .

Figure 3.6.2 Zircons separated from the kaolinitic sands of the Bulimba Formation (8.5 - 8.75 m depth), Jewfish mine, Weipa. Scale bars = 50 μm .

1



2



3.3 Electron microprobe analysis

A Cameca electron microprobe operating at 15kV was employed in the study. Prior to analysis, a thin coating of carbon was applied to the polished surface of pisolith thin-sections. Energy-dispersive (EDS) point analyses were obtained at regularly spaced intervals across the surface of selected pisoliths. Initially, pisoliths were analysed at 400 μm intervals, however the resolution was found to be too coarse (Figure 3.7). Subsequent analyses were performed on pisoliths at 200 and 100 μm intervals (Figures 3.8 - 3.11). Those that were analysed at 100 μm intervals provided the most detailed profiles however they took a few hours to acquire.

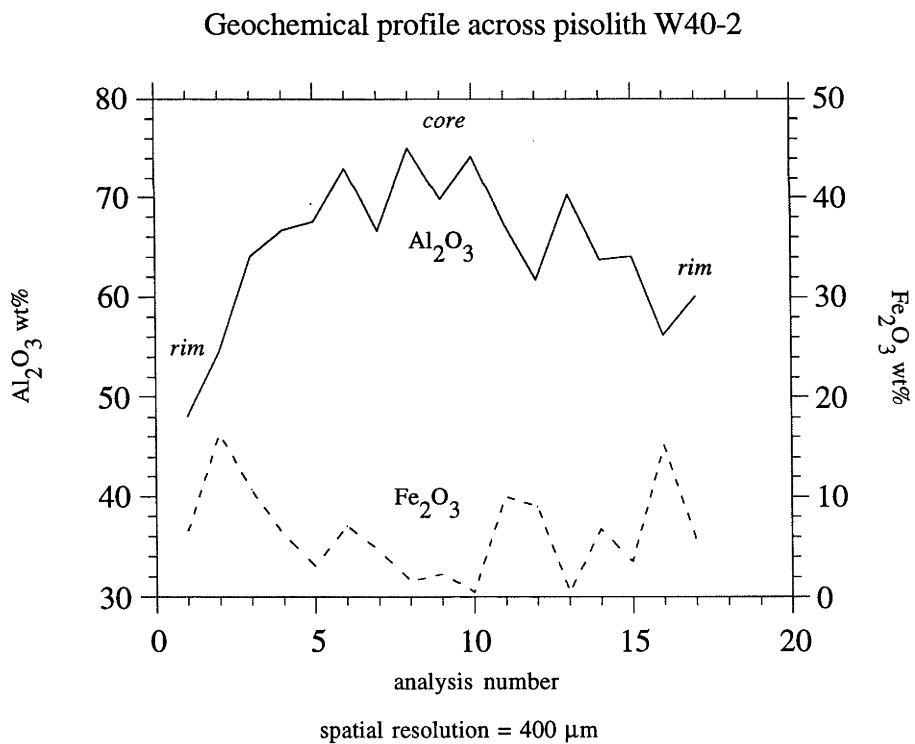


Figure 3.7

Geochemical profile across pisolite W40-6

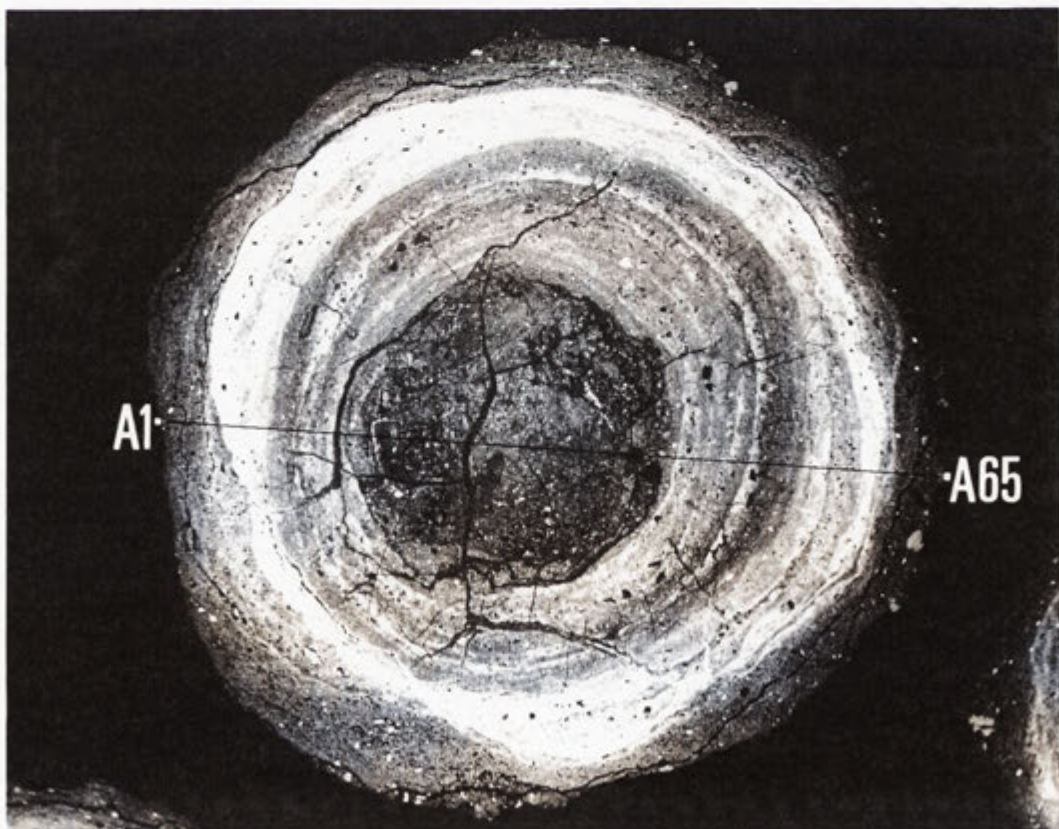
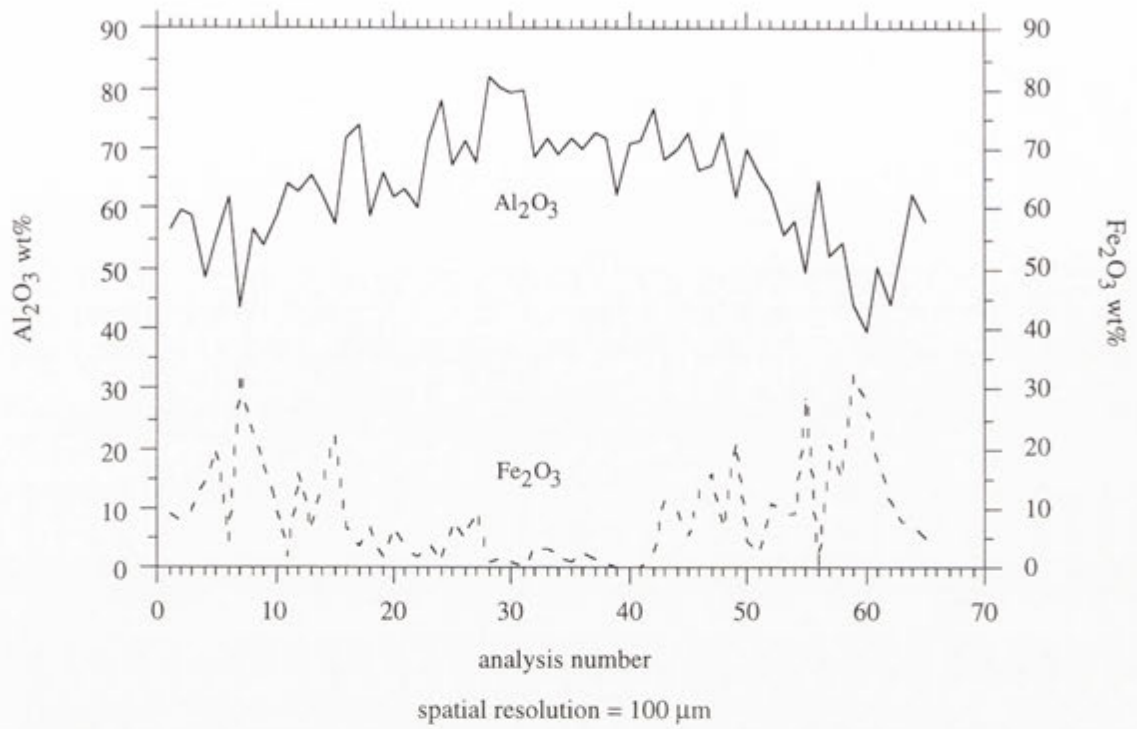
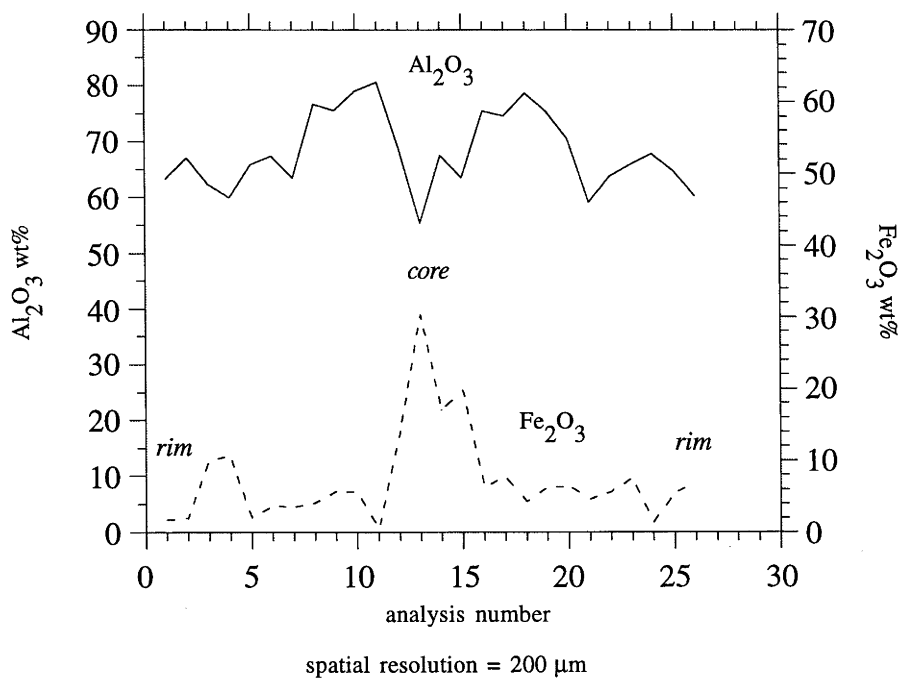


Figure 3.8

Geochemical profile across pisolith W3-5



Geochemical profile across pisolith W3-9

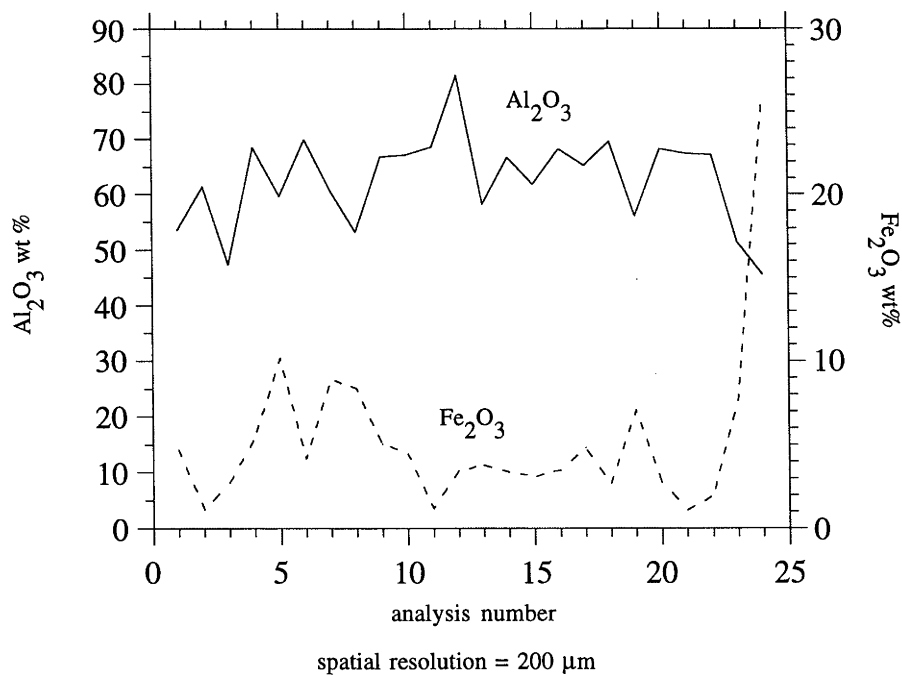


Figure 3.9

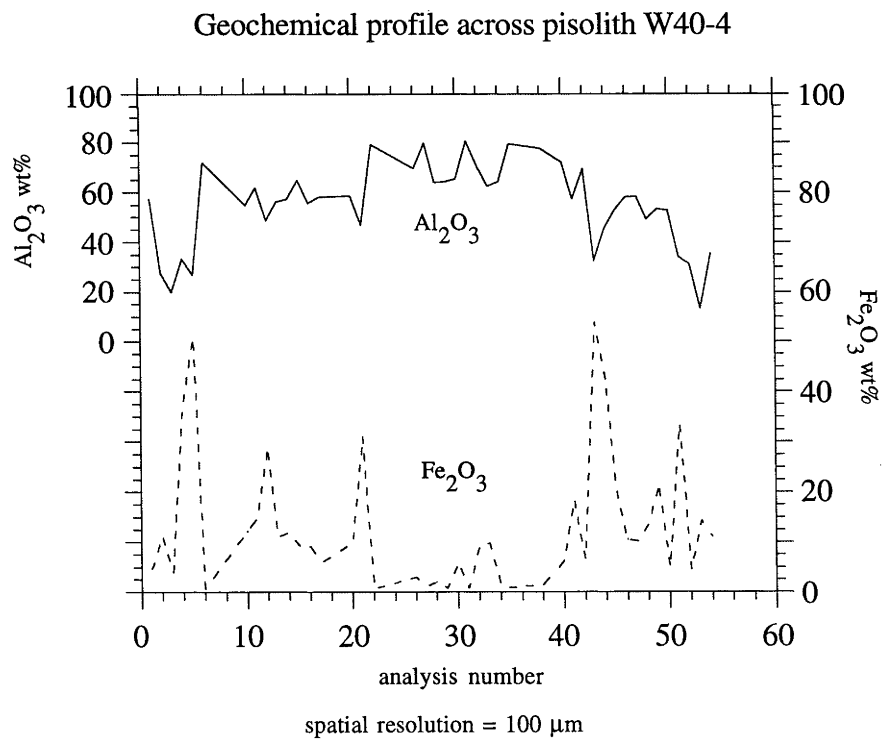
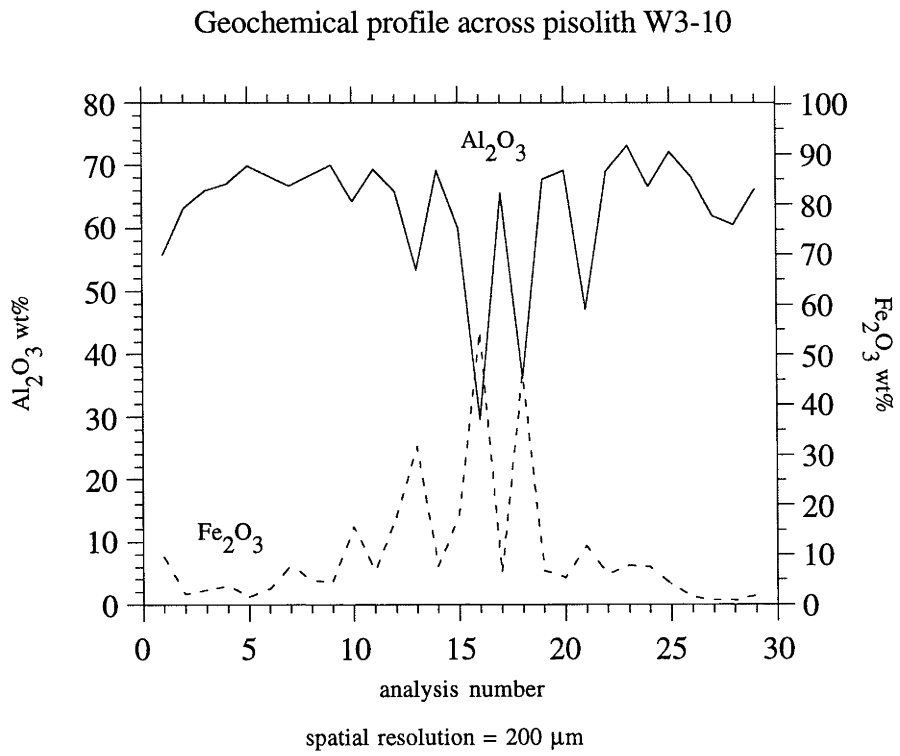
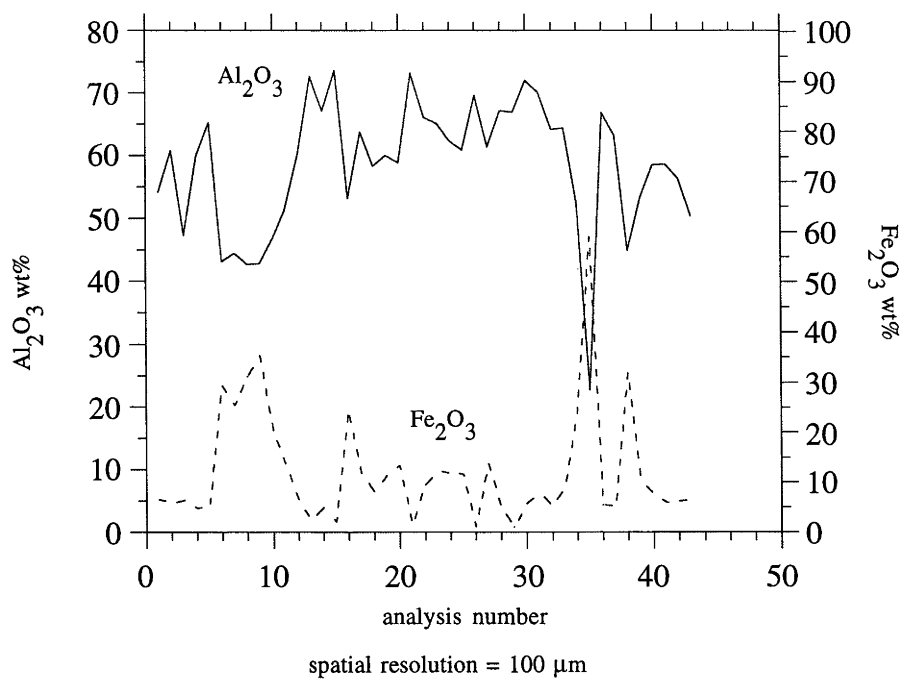


Figure 3.10

Geochemical profile across pisolith W40-11



Geochemical profile across pisolith W74-10

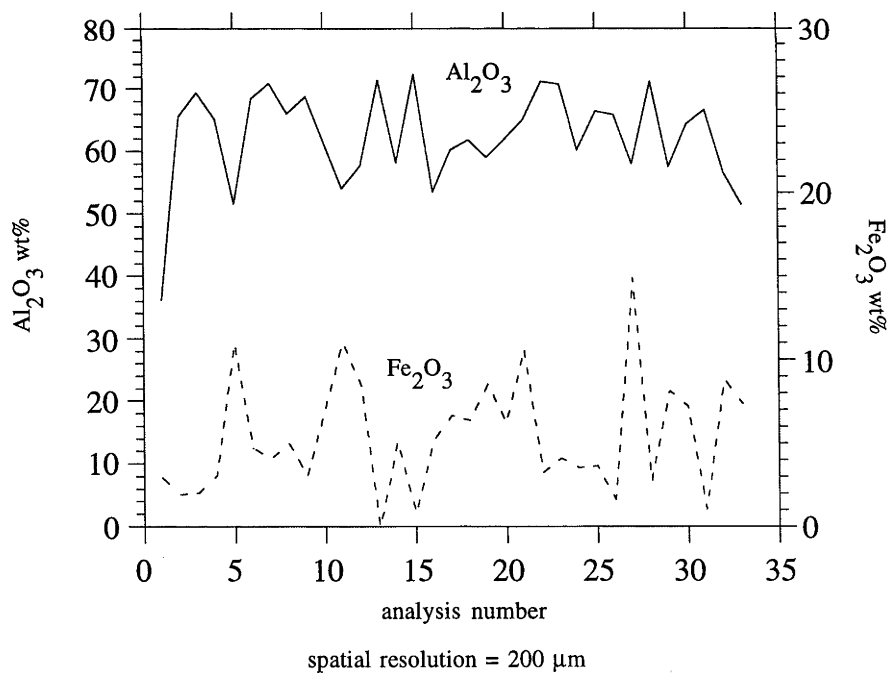


Figure 3.11

As well as supplying detailed geochemical information, the study also provided an insight into the mineralogy of pisoliths. When properly calibrated, the electron microprobe could discriminate between pure boehmite and gibbsite by the amount of alumina present with respect to water.

Localised heating by the electron beam commonly causes dehydration of gibbsite resulting in an apparent increase in alumina concentration. Water has actually been observed boiling off at the site of electron bombardment. This effect is not normally seen in boehmite analyses as a much higher temperature (~500°C) is required for dehydration.

Electron microprobe analysis of the infilling material within some cracks, has shown that some contain pure boehmite. A typical analysis of the boehmite is outlined below.

ANALYSIS 20120

	wt%	M.W.	molar ratio	cation ratio	anion ratio	cations x R
SiO ₂	<0.1	60.1	<0.002	<0.002	<0.004	<0.001
TiO ₂	<0.1	79.9	<0.001	<0.001	<0.002	<0.001
Al ₂ O ₃	84.5	102.0	0.828	1.656	2.484	1.000
Fe ₂ O ₃	0.7	159.7	0.004	0.008	0.012	0.005
H ₂ O (assumed)	14.6	18.0	0.811	1.622	<u>0.811</u>	0.980
						3.313

Calculated on the basis of 2 oxygen atoms in the formula; $R = 2 / 3.313 = 0.604$

The formula for the crack infill is AlOOH (i.e. boehmite). The iron may be present as very minor isomorphous substitution for aluminium, or in the form of hematite staining.

An electron microprobe analysis of a gibbsite crystal was done for comparison.

ANALYSIS 21304

	wt%	M.W.	molar ratio	cation ratio	anion ratio	cations x R
SiO ₂	<0.1	60.1	<0.002	<0.002	<0.004	<0.002
TiO ₂	<0.1	79.9	<0.001	<0.001	<0.002	<0.001
Al ₂ O ₃	64.8	102.0	0.635	1.270	1.905	0.993
Fe ₂ O ₃	0.6	159.7	0.004	0.008	0.012	0.006
H ₂ O (assumed)	34.4	18.0	1.911	3.822	<u>1.911</u>	2.989
						3.834

Calculated on the basis of 3 oxygen atoms in the formula; $R = 3 / 3.834 = 0.782$

The formula for the mineral is Al(OH)₃ (i.e. gibbsite). The iron may be present as very minor isomorphous substitution for aluminium, or in the form of a thin hematite coating.

3.4 Image Analysis

The following section outlines the procedure for analysing back-scattered electron images of pisolith thin-sections.

There are three stages in the system for analysing images. The first stage involves the recording of the back-scattered electron images (Figures 3.12 and 3.13) onto S-VHS video tape. The video input level (contrast and brightness) must be correct to ensure that the image contains a complete range of grey tones. The second step requires the conversion of the video image to a digital form using the Macintosh *QuickImage 24* card and software. The last stage involves analysing the digital image using the public domain program *Image*.

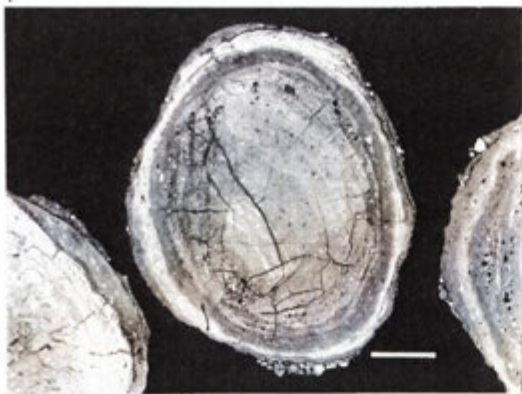
The digitised image consists of a range of optical densities grading from black which has a value of zero to white which is equivalent to 255. The digitised image is enhanced using a noise reduction function. An optical density profile across the image is acquired and is then correlated with the Fe_2O_3 percentages obtained from the electron microprobe. The colour scale consists of a spectrum of colours; violet representing the lowest radiation intensity while red representing the highest. A radiation intensity equal to zero is represented as black. Calibration of the colour scale to Fe_2O_3 percentages (Figure 3.14), enables a map to be drawn which depicts the percentage and distribution of Fe_2O_3 within a pisolith (Figure 3.15).

The presence of quartz grains within a pisolith is advantageous, as they can be used as an internal standard for optical density calibrations. The image of the quartz grains can be whitened, thereby distinguishing them from a particular percentage of Fe_2O_3 .

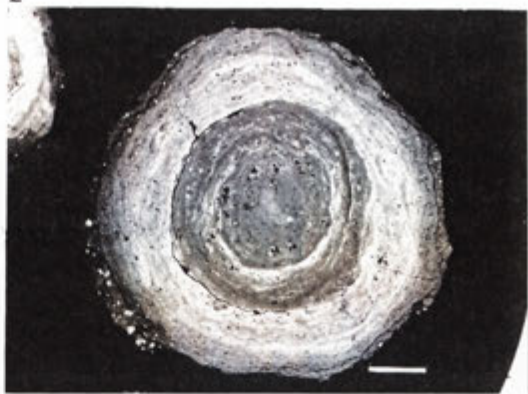
Figure 3.12

- Figure 3.12.1 A back-scattered electron image of pisolith W40-5.
Scale bar = 1 mm.
- Figure 3.12.2 A back-scattered electron image of pisolith W40-1.
Scale bar = 1 mm.
- Figure 3.12.3 A back-scattered electron image of pisolith W40-13.
Scale bar = 1 mm.
- Figure 3.12.4 A back-scattered electron image of pisolith W40-6.
Scale bar = 1 mm.
- Figure 3.12.5 A back-scattered electron image of pisolith W40-12.
Scale bar = 1 mm.
- Figure 3.12.6 A back-scattered electron image of pisolith W40-2.
Scale bar = 1 mm.
- Figure 3.12.7 A back-scattered electron image of pisolith W40-7.
Scale bar = 1 mm.
- Figure 3.12.8 A back-scattered electron image of pisolith W40-4.
Scale bar = 1 mm.

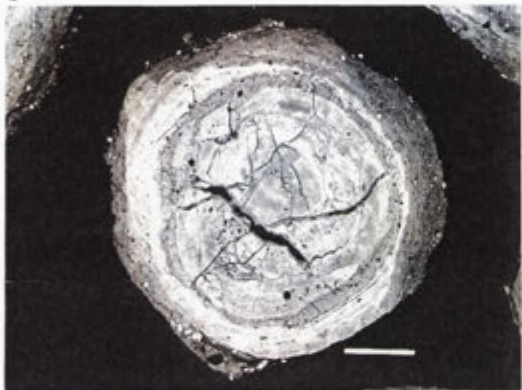
1



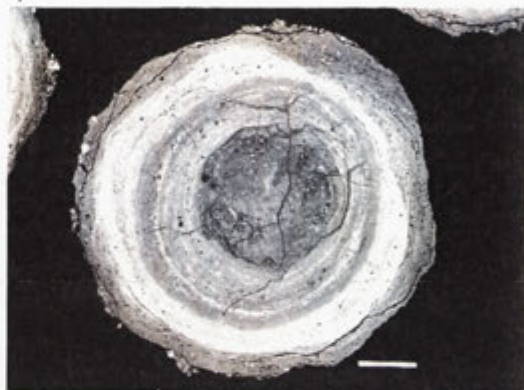
2



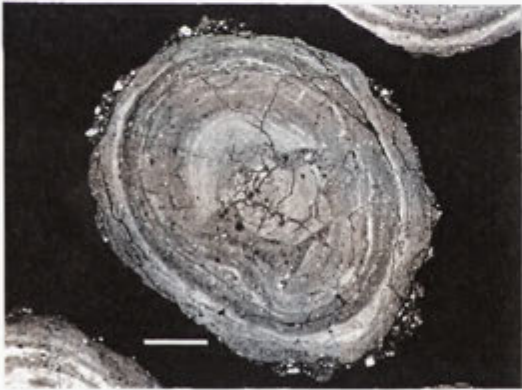
3



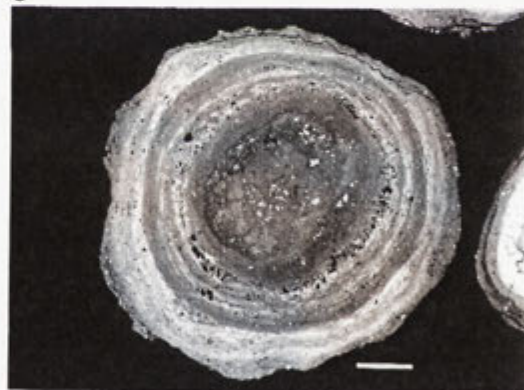
4



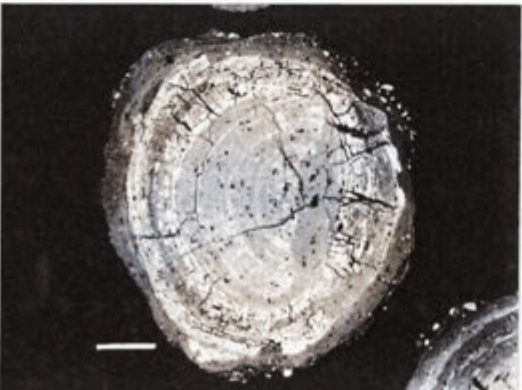
5



6



7



8

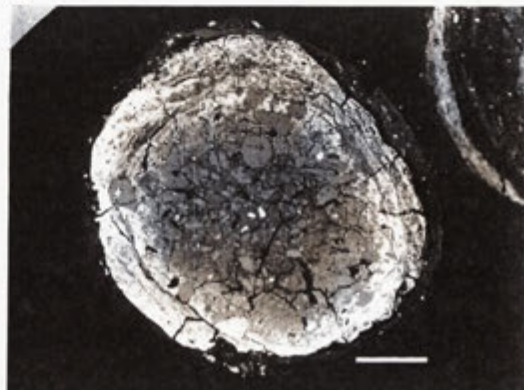
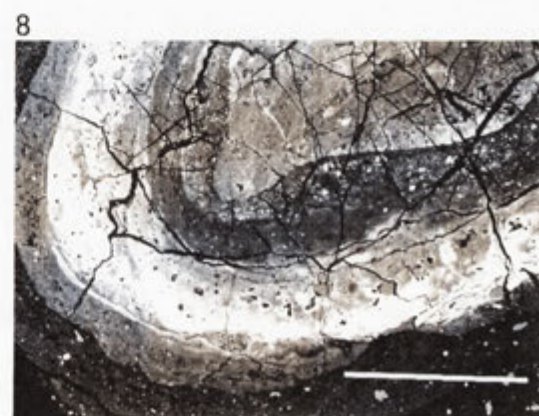
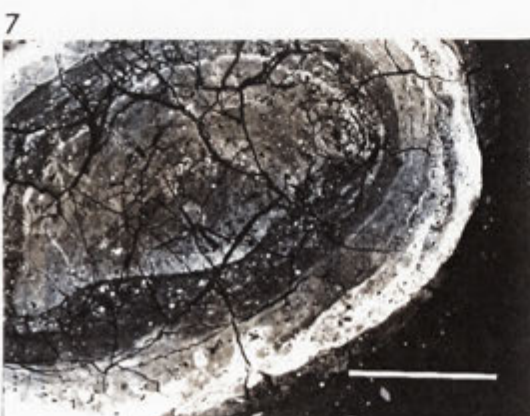
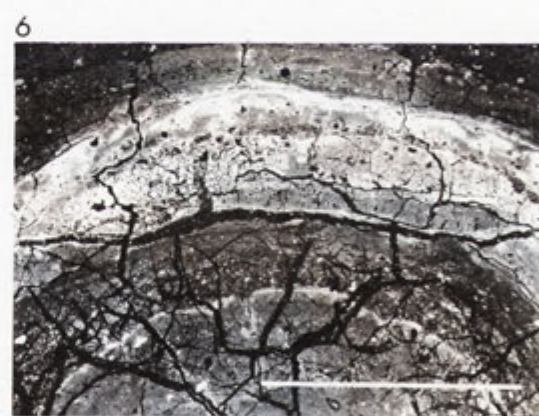
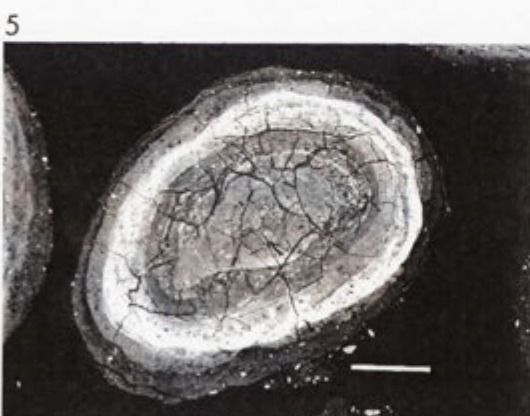
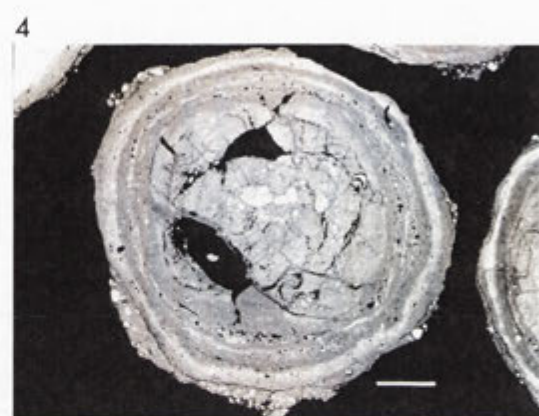
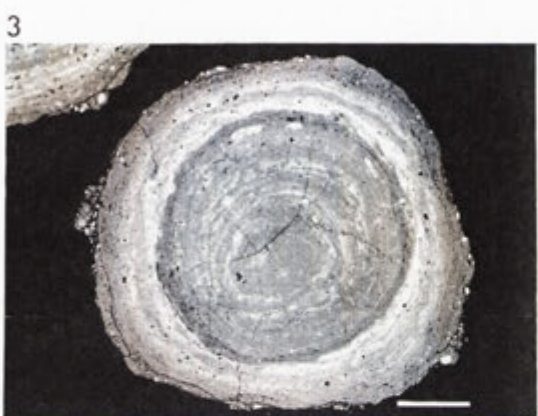
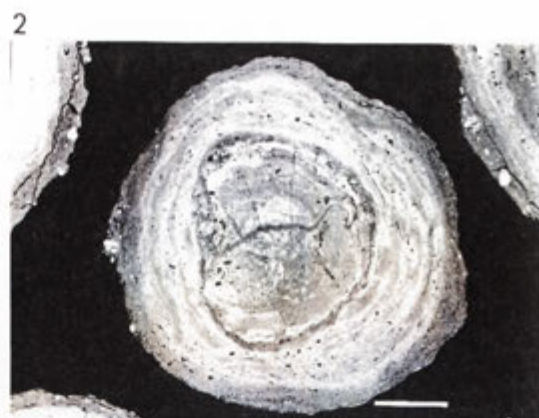
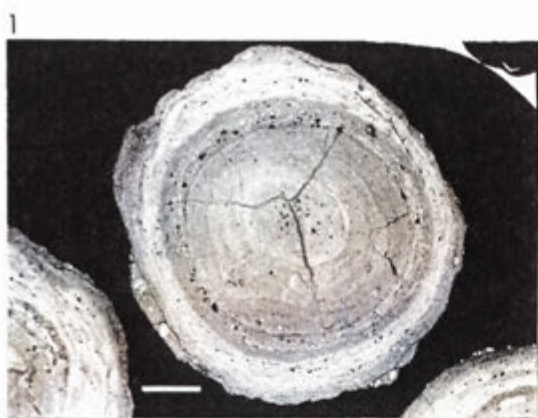


Figure 3.13

- Figure 3.13.1 A back-scattered electron image of pisolith W40-8.
Scale bar = 1 mm.
- Figure 3.13.2 A back-scattered electron image of pisolith W40-10.
Scale bar = 1 mm.
- Figure 3.13.3 A back-scattered electron image of pisolith W40-9.
Scale bar = 1 mm.
- Figure 3.13.4 A back-scattered electron image of pisolith W40-3.
Scale bar = 1 mm.
- Figure 3.13.5 A back-scattered electron image of pisolith W40-11.
Scale bar = 1 mm.
- Figure 3.13.6 A close-up view of pisolith W40-11. Scale bar = 1 mm.
- Figure 3.13.7 A close-up view of pisolith W40-11. Scale bar = 1 mm.
- Figure 3.13.8 A close-up view of pisolith W40-11. Scale bar = 1 mm.



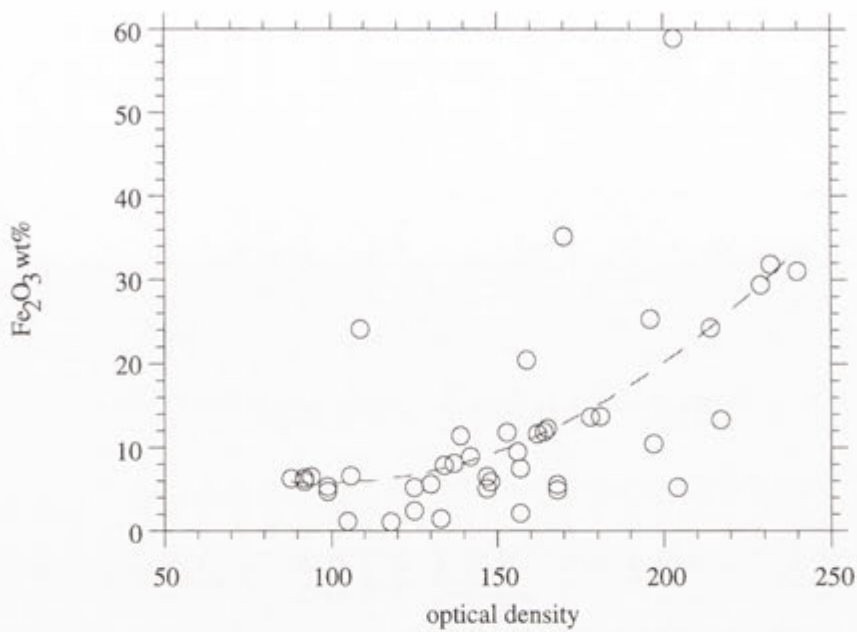


Figure 3.14

Correlation of Fe₂O₃ content with optical density
in a back-scattered electron image of a bauxitic pisolith (W40-11).

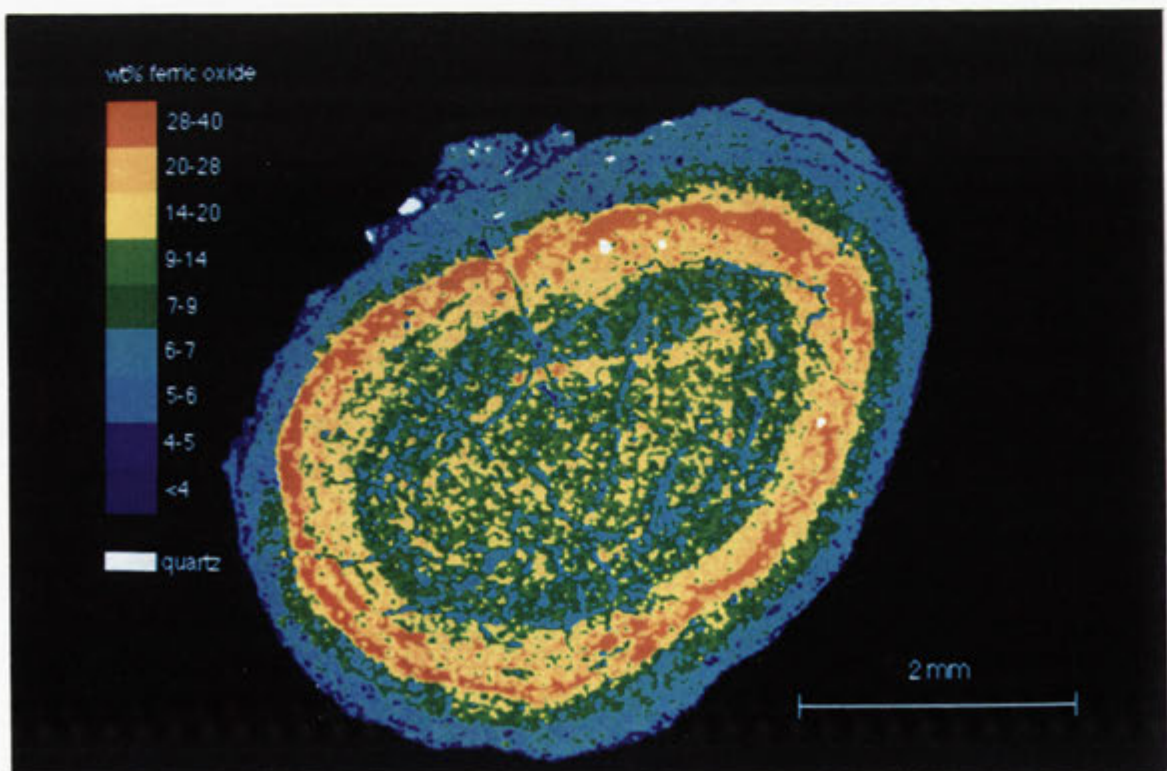


Figure 3.15

A map of pisolith W40-11 displaying the variation in Fe₂O₃ content.

Chapter 4

Fourier transform infrared spectrometry

4.1 Introduction

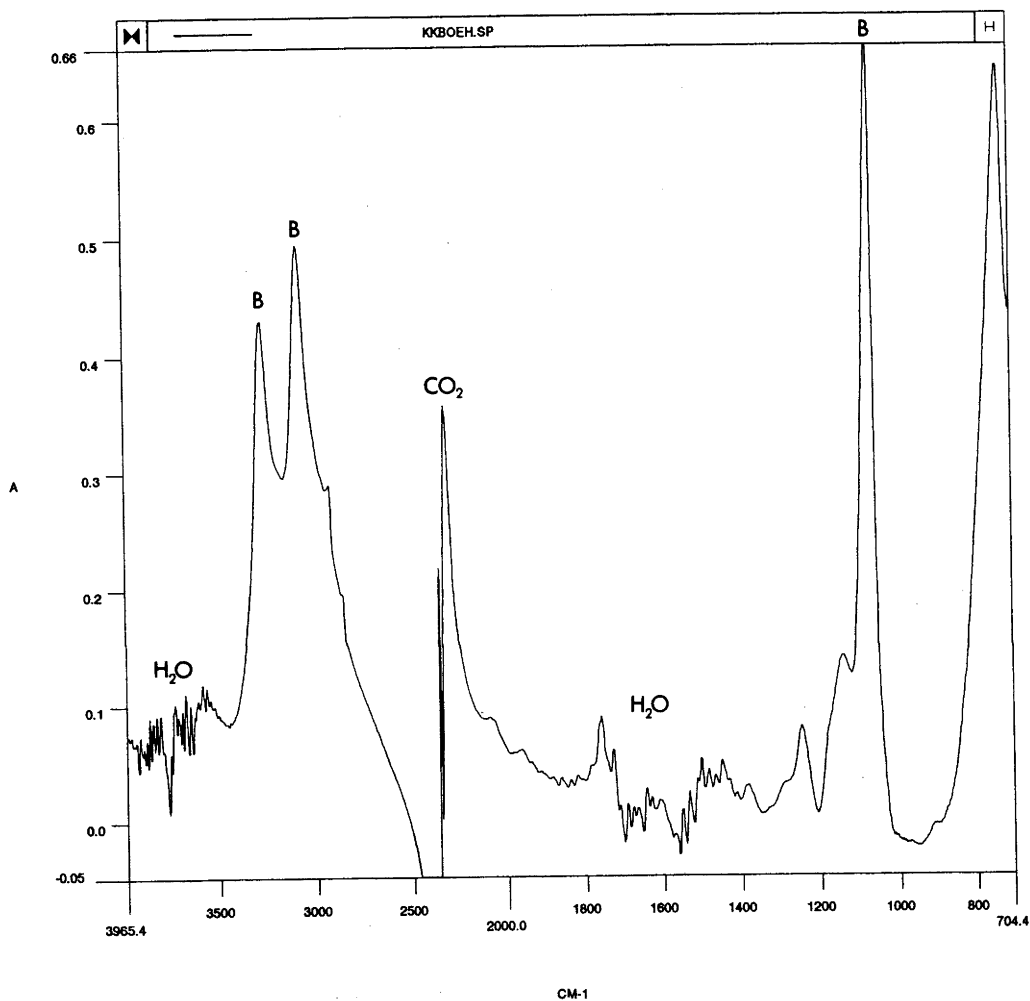
An infrared interferogram is obtained by the superposition of two infrared beams possessing variations in their optical path difference. The interferogram is expressed in terms of intensity *vs* path difference. Fourier analysis converts the interferogram into an intensity *vs* frequency (wavenumbers cm^{-1}) distribution (Möller & Rothschild, 1971). The spectroscopic technique is known as Fourier transform infrared (FTIR) spectrometry. Acquired spectra have a frequency range in the mid-infrared, from 700 to 4000 cm^{-1} , corresponding to wavelengths ranging from 14.3 to 2.5 μm . The highly sensitive FTIR spectrometers of today approach a spatial resolution close to the theoretical diffraction limit of 10 μm (Messerschmidt & Harthcock, 1988).

Using an attached microscope, a specular reflectance infrared spectrum of a 200 μm^2 area on the surface of a halved and polished pisolith is readily obtainable. Such spectra are highly distorted by anomalous dispersion effects and are normally difficult to interpret in their raw state. The distortion can be reduced significantly by calculating an absorbance spectrum from a specular reflectance spectrum, using the Kramers-Kronig transformation (Claybourn *et al.*, 1991) (Figure 4.1).

Qualitative analysis of the untransformed spectra is possible for boehmite, gibbsite and quartz as their spectra are quite different from each other (Figure 4.2 - 4.4). The specular reflectance spectrum of poorly-diffracting material (PDM), which sometimes becomes the dominant phase in the core of pisoliths (see Chapter 6, "Quantitative X-ray diffraction"), is relatively featureless apart from a broad feature around 3500 cm^{-1} associated with O-H stretching and a smaller feature around 1600 cm^{-1} possibly related to O-H bending (Figure 4.5).

When the minerals occur as a mixture, as in bauxitic pisoliths, their individual spectra are still quite recognisable (Figure 4.6). By measuring the intensity of particular vibrational bands, mineralogical maps showing the distribution of the respective minerals can be generated. The process lends itself to automation by using a programmable microscope stage as well as software for data handling and analysis.

Kramers-Kronig transformation

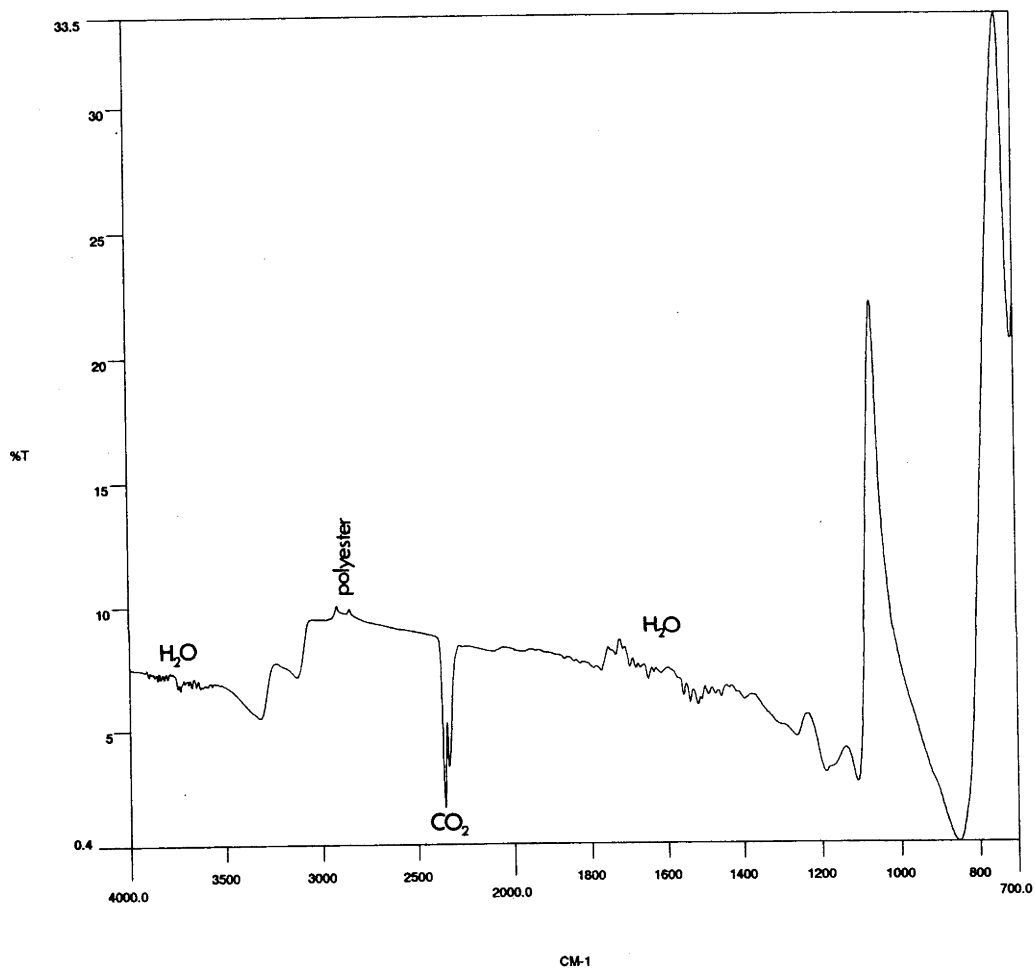


P-E 2000 Filename: KQBOEH.SP Date: 92/07/06 Time: 13:52:00.00
Scans: 64 Resolution: 8.00 Operator: DBT
Sample: 100% Boehmite synthetic RSES refl KK

Figure 4.1

A Kramers-Kronig transformed spectrum of boehmite.

Boehmite

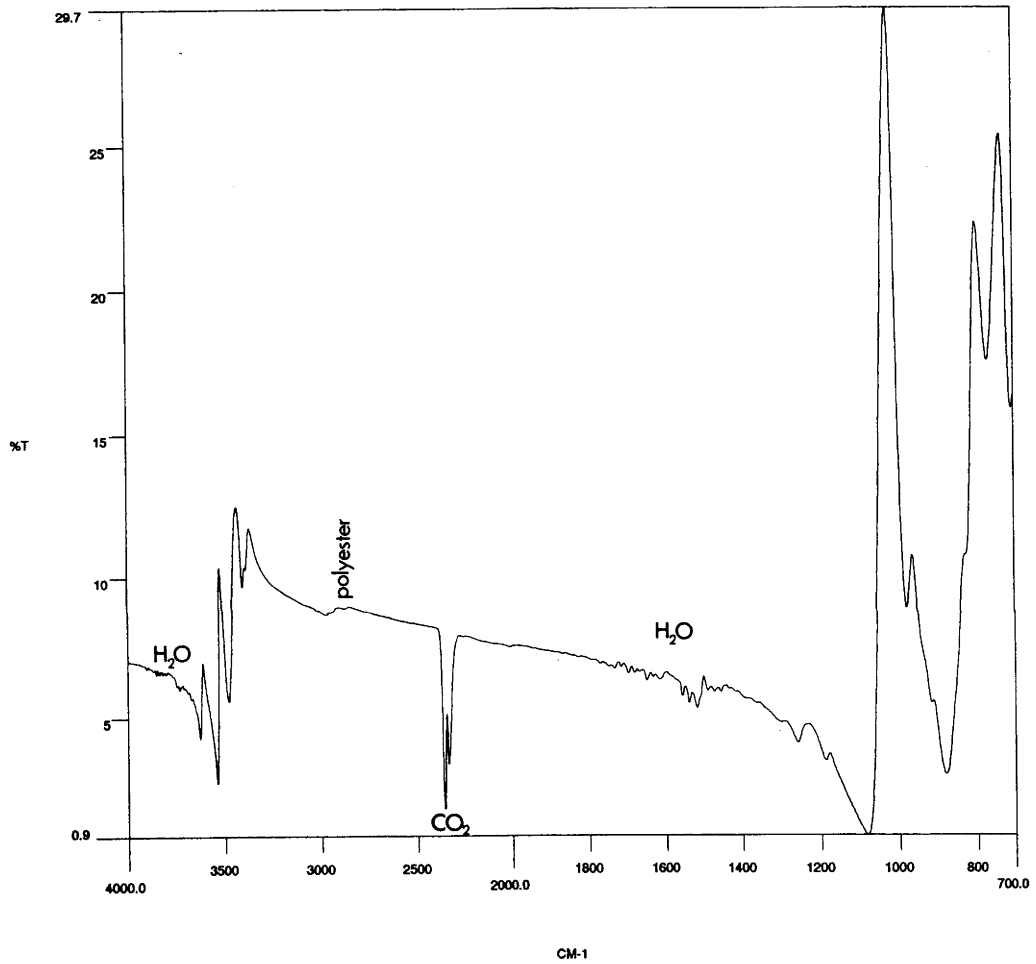


P-E 2000 Filename: BOEH.SP Date: 92/07/06 Time: 13:52:00.00
Scans: 64 Resolution: 8.00 Operator: Dbt
Sample: Boehmite 100% synthetic RSES refl

Figure 4.2

A specular reflectance spectrum (untransformed) of boehmite.

Gibbsite

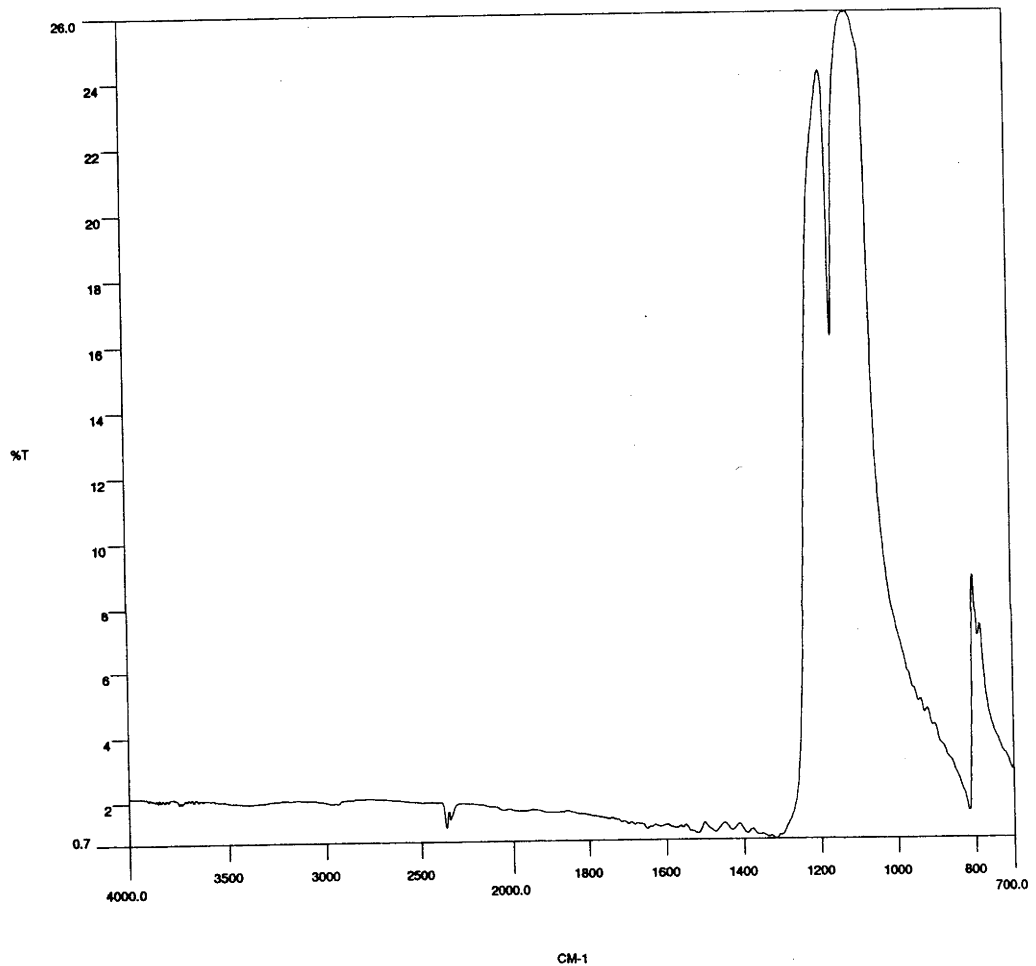


P-E 2000 Filename: GIBB.SP Date: 92/07/06 Time: 13:32:21.00
Scans: 64 Resolution: 8.00 Operator:
Sample: GIBBSITE 100% SHOWA DENKO REFL

Figure 4.3

A specular reflectance spectrum (untransformed) of gibbsite.

Quartz

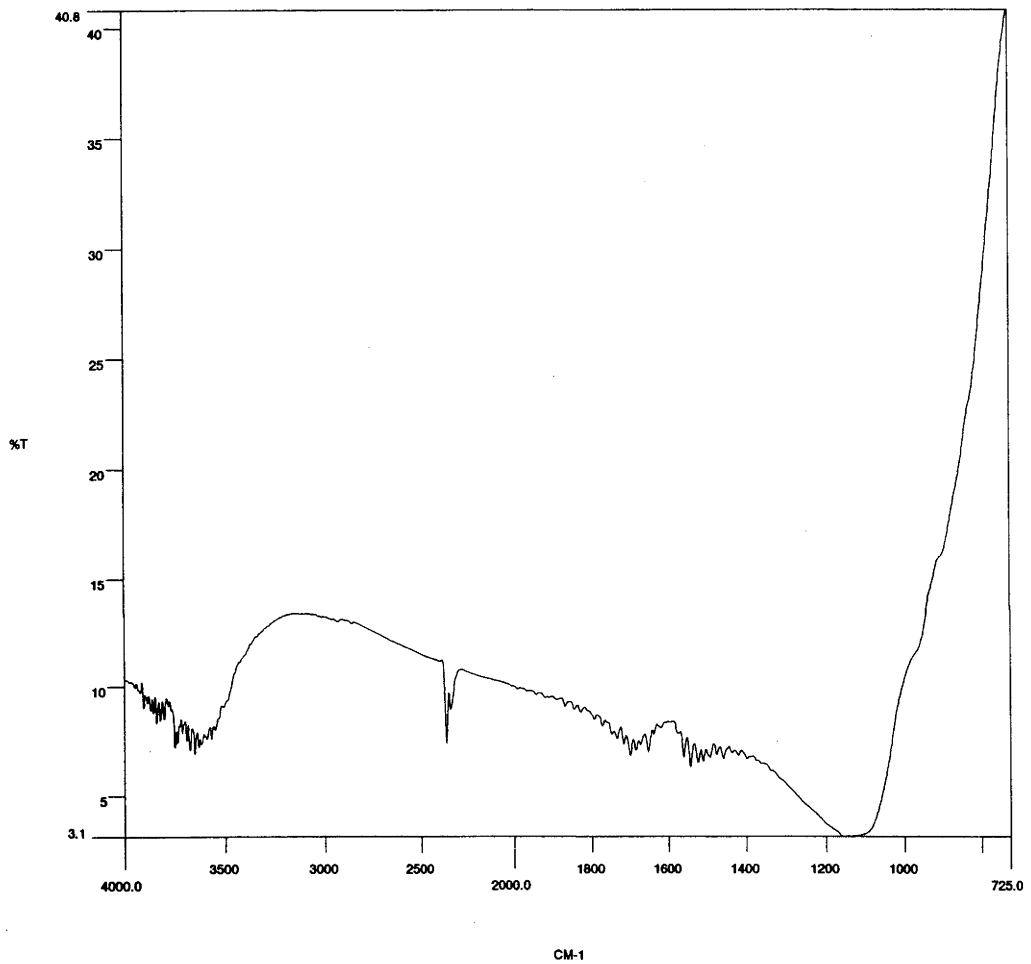


P-E 2000 Filename: QUARTZ1.SP Date: 92/07/08 Time: 09:14:08.00
Scans: 256 Resolution: 8.00 Operator: D.B.Tilley
Sample: Quartz longtom 1 run 1

Figure 4.4

A specular reflectance spectrum (untransformed) of quartz.

Poorly-diffracting material (PDM)

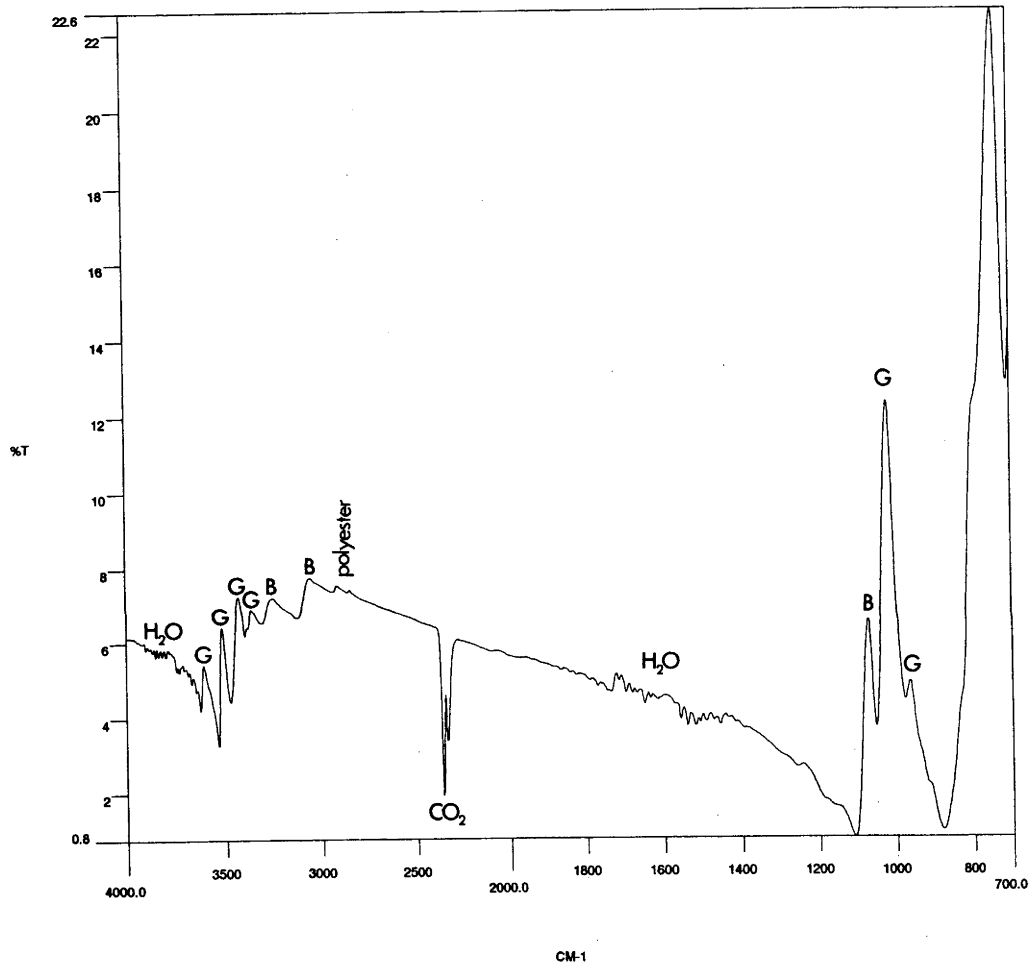


P-E 2000 Filename: B17.SP Date: 93/07/05 Time: 16:41:42.00
Scans: 32 Resolution: 8.00 Operator:
Sample: b17 19659.0

Figure 4.5

A specular reflectance spectrum (untransformed) of poorly-diffracting material.

Gibbsite and boehmite



P-E 2000 Filename: G-850%.SP Date: 92/07/06 Time: 14:12:39.00
Scans: 64 Resolution: 8.00 Operator:
Sample: none

Figure 4.6

A specular reflectance spectrum (untransformed) of a gibbsite-boehmite mixture.

Five vibrational frequencies are identifiable in the infrared spectrum of boehmite. The high frequency bands, 3267 and 3071 cm^{-1} correspond respectively to the $\nu_{\text{as}}(\text{O-H})$ and $\nu_{\text{s}}(\text{O-H})$ stretching vibrations (Kiss *et al.*, 1980). In the lower frequency part of the infrared spectrum, bending vibrations $\delta_{\text{as}}(\text{O-H})$, $\delta_{\text{s}}(\text{O-H})$ and $\gamma(\text{O-H})$ occur at 1147, 1071 and 744 cm^{-1} respectively (Kiss *et al.*, 1980).

Stretching vibrations of the hydroxyl group, $\nu(\text{O-H})$, in gibbsite (Kolesova & Ryskin, 1959) result in four maxima at 3609, 3526, 3432 and 3365 cm^{-1} . Bending vibrations of the hydroxyl group, $\delta(\text{O-H})$, in gibbsite (Kolesova & Ryskin, 1959) are exhibited in the spectrum at 1027, 972, 917, 800 and 734 cm^{-1} .

The spectrum of quartz is characterised by an intense absorption of infrared at the frequencies of 1186 and 1115 cm^{-1} associated with Si-O stretching. Between these two frequencies there is a decrease in absorption at 1159 cm^{-1} known as the *restrahlen* peak. The doublet at 800, 781 cm^{-1} is also characteristic of quartz.

The specular reflectance spectra of kaolinite and hematite were found to be relatively weak and had poorer signal to noise ratios than those of the above mentioned minerals (Frost *et al.*, 1993).

4.2 Experimental

4.2.1 Sample preparation

Bauxitic pisoliths are prepared for FTIR spectrometry by first mounting them in polyester resin. When the resin has set, the block is ground down, exposing the internal structure of the pisoliths. The surface is then smoothed with increasingly fine abrasives. When the surface has been flattened and smoothed it is impregnated with *Epo-tek* under a vacuum. Excess *Epo-tek* is removed using a razor blade and then allowed to cure for at least 24 hours. Using the finest abrasive, the block is cut back to expose the pisolith surface. Finally, the pisolith surface is polished on a soft lap using a diamond polishing compound.

Synthetically prepared samples of gibbsite and boehmite were used as standards because of their known purity and crystallinity. The gibbsite is commercially made by the alumina company, Showa Denko and is sold under the name *Higilite*. Boehmite was obtained by hydrothermally altering the synthetic gibbsite.

The standard mineral powders were pressed into small blocks using a hydraulic jack delivering a pressure of 350 bars. A very small amount of polyvinyl acetate (PVA) was needed during pressing to hold the block together after removal from the jack. The blocks were dried and impregnated with *Petropoxy*. The impregnated block was then mounted in polyester resin after which it was ground and polished in a similar manner to halved pisoliths.

Special care is required when mixing gibbsite and boehmite in known quantities so that homogeneity is attained. The best method for ensuring this is to mix and grind the two minerals together using a mortar and pestle. Acetone was added to aid in the mixing.

4.2.2 Mineralogical mapping

Spectra were obtained using a Perkin-Elmer 2000 FTIR spectrometer, equipped with an infrared microscope incorporating a mercury-cadmium telluride detector and a programmable stage. Reflectance spectra were collected at 8 cm^{-1} resolution and were composed of 16 separate scans added together. Acquisition of each spectrum takes less than 10 seconds. Even though a background spectrum was acquired, complete elimination of atmospheric H_2O and CO_2 from the spectrum was not possible due to their fluctuating concentrations. Fortunately, their vibrations did not coincide with the spectra of quartz, gibbsite or boehmite. If a 'clean' spectrum is required then the microscope stage can be purged with gaseous nitrogen.

Specific parts of the untransformed spectra were measured, to assess the quantity of minerals present, so that a map could be drawn showing their distributions. Quartz's relative concentration was determined by measuring the area of part of the quartz peak, formed by drawing a baseline from the restrahlen peak at 1159 cm^{-1} , to the normal baseline near 1280 cm^{-1} . The relative concentrations of gibbsite and boehmite were determined by measuring the areas of the O-H stretching bands at 3432 cm^{-1} and 3071 cm^{-1} respectively (Frost *et al.*, 1993). Mapping of pisoliths was accomplished by acquiring an array of spectra over the entire polished surface. Automation of the spectral acquisition stage was achieved by the application of a computer program. Maps were calculated using GRAMS 386 software (Galactic Industries Corporation, Salem, New Hampshire) (Figure 4.7).

As pisoliths are generally concentric in form and composition, a single traverse across the diameter of a pisolith should suffice for routine analyses (Figures 4.8 - 4.11)

In the absence of a motorised stage, a mineralogical map can still be produced if a grid is first etched onto the pisolith surface using a diamond scribe (Figure 4.12). This can be done using a scribe attached to the objective of a petrological microscope. A grid is drawn on the surface of the pisolith using a micrometer which is attached to the stage. A photograph of the pisolith surface displaying the grid ensures that observational accuracy is maintained.

Mapping of bauxitic pisoliths using FTIR spectrometry, has shown that minerals are generally distributed in concentric bands and are correlatable with specific zones identified with an optical microscope. The existence of variations in mineralogy at a spatial resolution of $200\text{ }\mu\text{m}$ is highlighted.

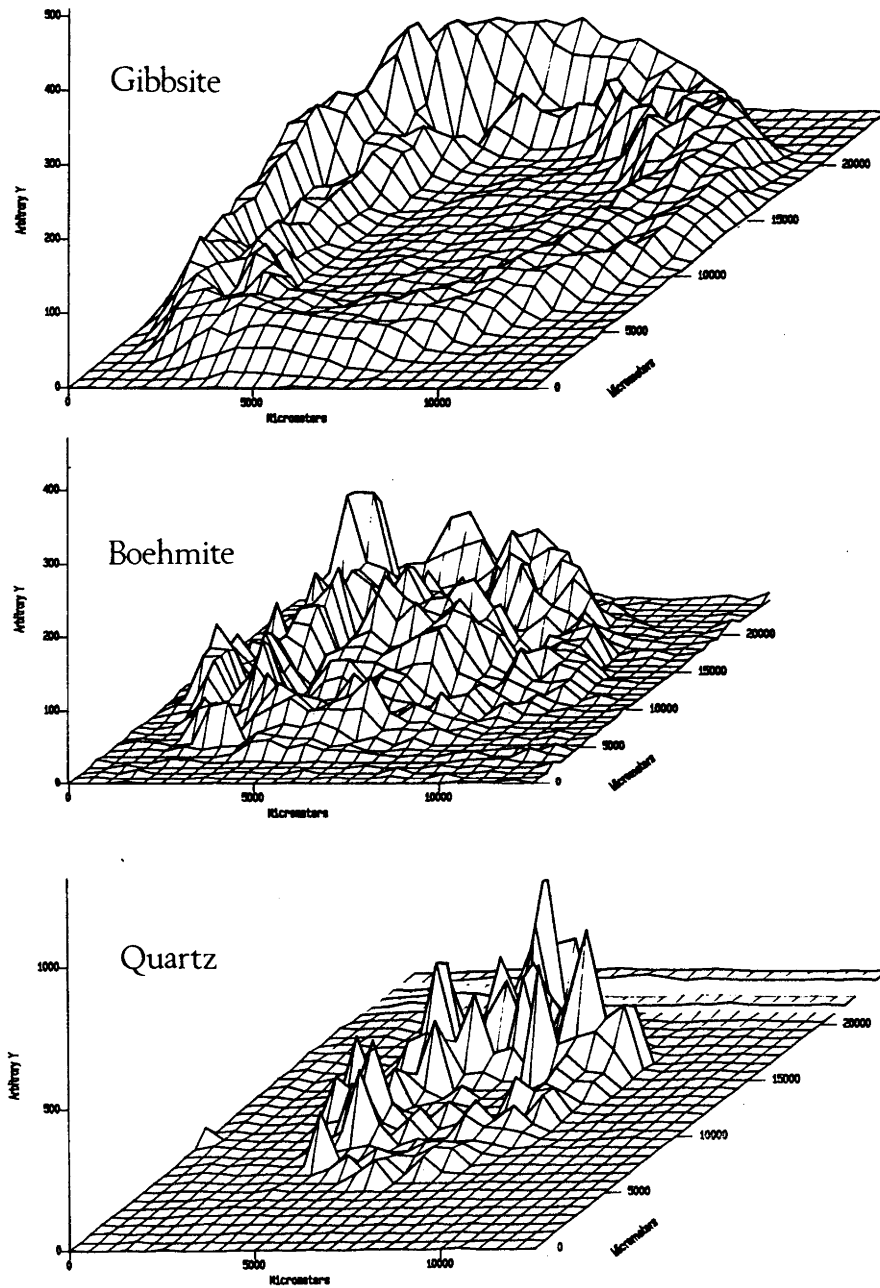


Figure 4.7

FTIR maps of a sectioned pisolith from Weipa showing the distribution of gibbsite, boehmite and quartz (after Frost *et al.*, 1993).

FTIR spectrometer traverses across pisolith W6-1
showing the distributions of gibbsite and quartz

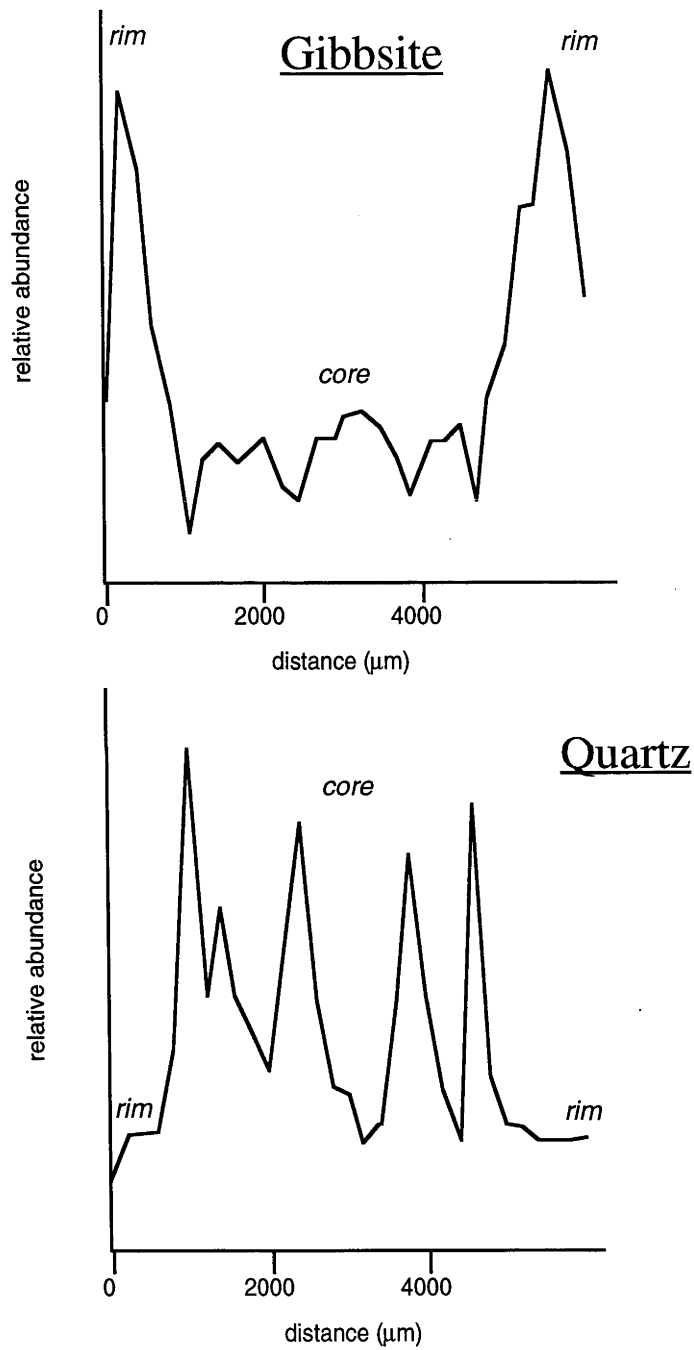


Figure 4.8

FTIR spectrometer traverses across pisolith W64-1
showing the distributions of gibbsite and quartz

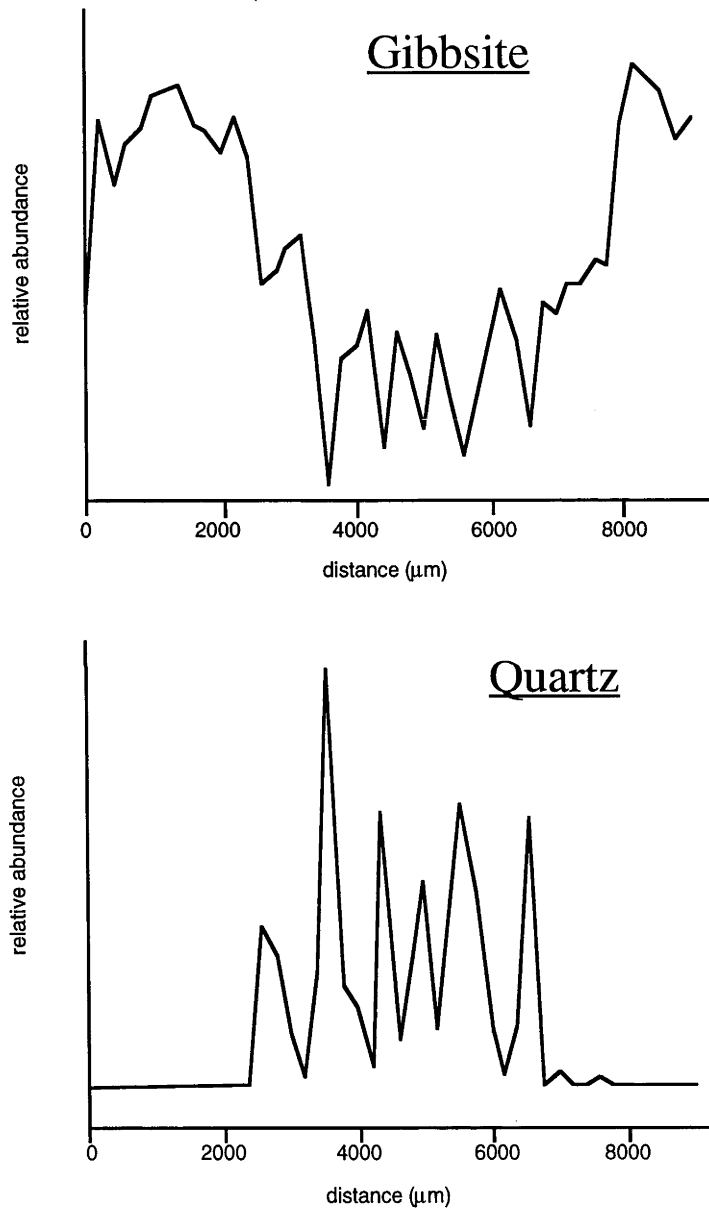


Figure 4.9

FTIR spectrometer traverses across pisolith A57-1 showing the distributions of gibbsite and boehmite

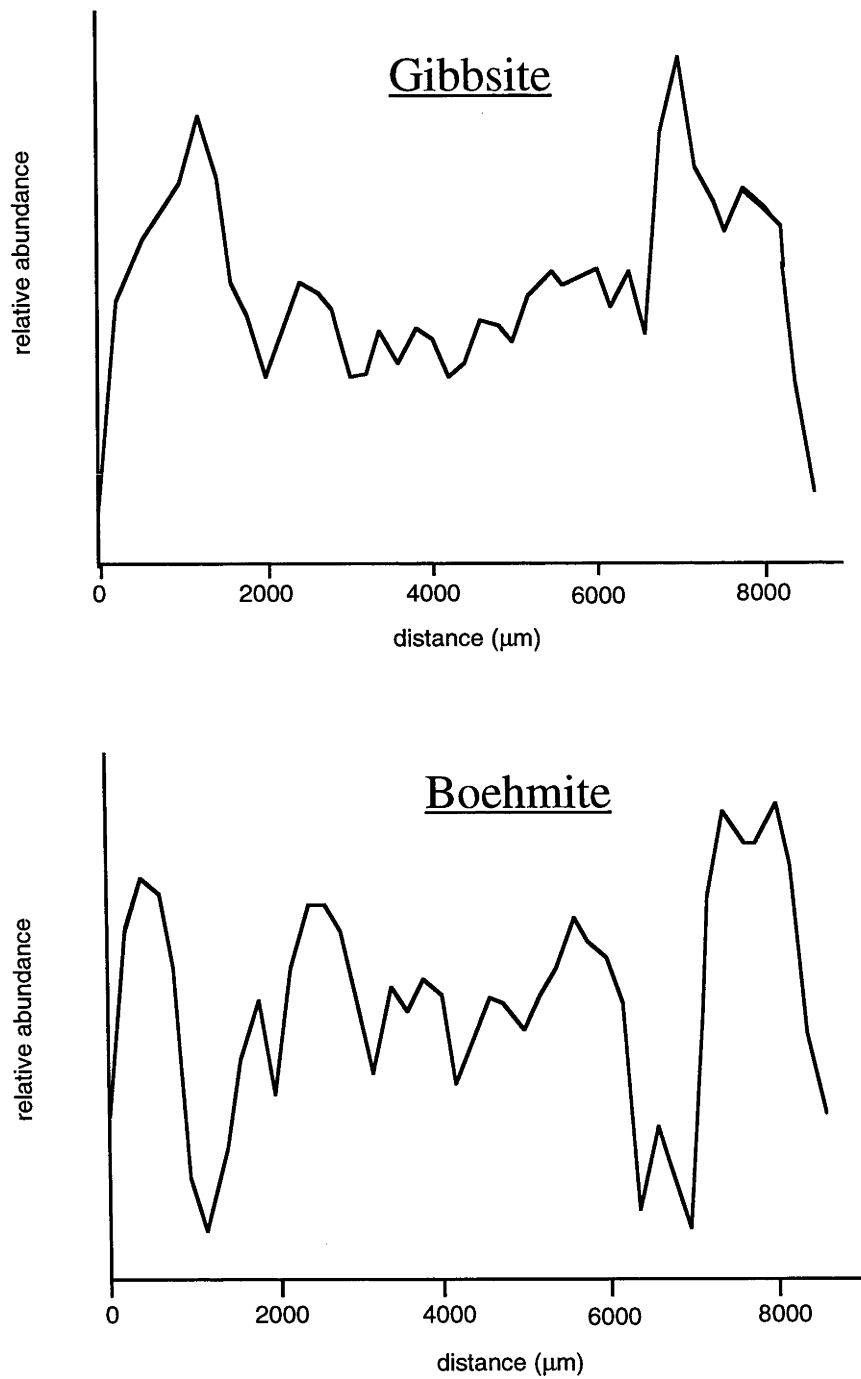


Figure 4.10

FTIR spectrometer traverses across pisolith A57-2 showing the distributions of gibbsite and boehmite

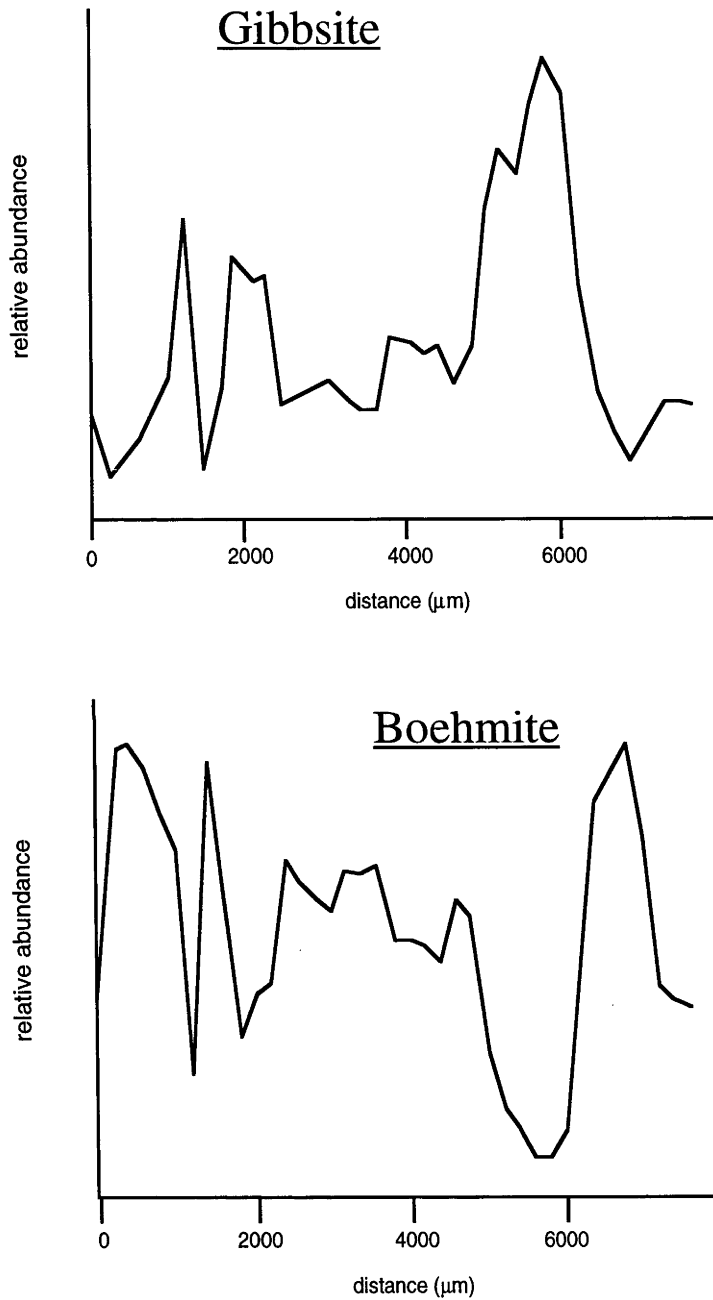
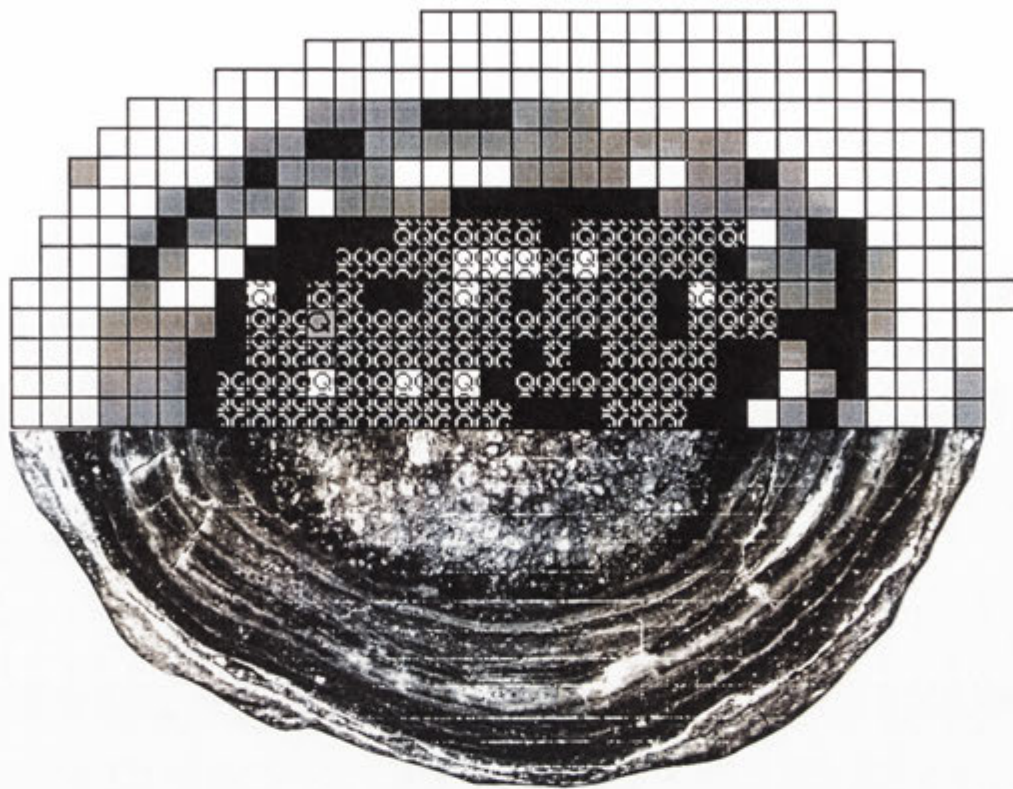








Figure 4.11



KEY

- | | |
|---|-------------------------------|
|  | gibbsite |
|  | gibbsite and boehmite |
|  | boehmite |
|  | quartz |
|  | boehmite and quartz |
|  | boehmite, gibbsite and quartz |

10 mm

Figure 4.12

FTIR map of a halved and polished sandy-core pisolith from Weipa.

The map does not take into account poorly diffracting material (PDM), which is often concentrated in the core of bauxitic pisoliths. The map only shows those mineral phases listed and their approximate relative abundance to each other.

4.2.3 Interference effect in thin-sections

It was found that thin-sections mounted on glass microscope slides are unsuitable for FTIR spectrometry due to an interference effect resulting in the superposition of a wave pattern upon the desired spectrum (Figure 4.13). This occurs when the infrared beam penetrates deeper than the thickness of the thin-section and is then reflected off the underlying bauxite-glue interface and subsequently interferes with the incident infrared beam. To verify that the interference pattern was produced in this manner, the thickness of the thin-section was calculated from the observed interference pattern.

$$\text{For films; } d = \Delta m / 2n (\nu_1 - \nu_2)$$

where d = thickness in centimetres.

ν_1 = frequency at which first maximum (or minimum) occurs, in wavenumber (cm^{-1}) units.

ν_2 = frequency at which last maximum (or minimum) occurs, in wavenumber (cm^{-1}) units.

Δm = number of complete fringe maxima (or minima) in the interval from ν_1 to ν_2 , a whole number.

n = index of refraction for the film ($n = 1.6$ for gibbsite).

$$d = \Delta m / 2n (\nu_1 - \nu_2)$$

$$d = 9 / 2 \times 1.6 (2723.5 - 1857.6)$$

$$d = 9 / 2770.9$$

$$d = 0.00325 \text{ cm} = 32.5 \text{ } \mu\text{m}.$$

The thickness calculated corresponds well with the 30 micron thickness technicians aim for when manufacturing thin-sections.

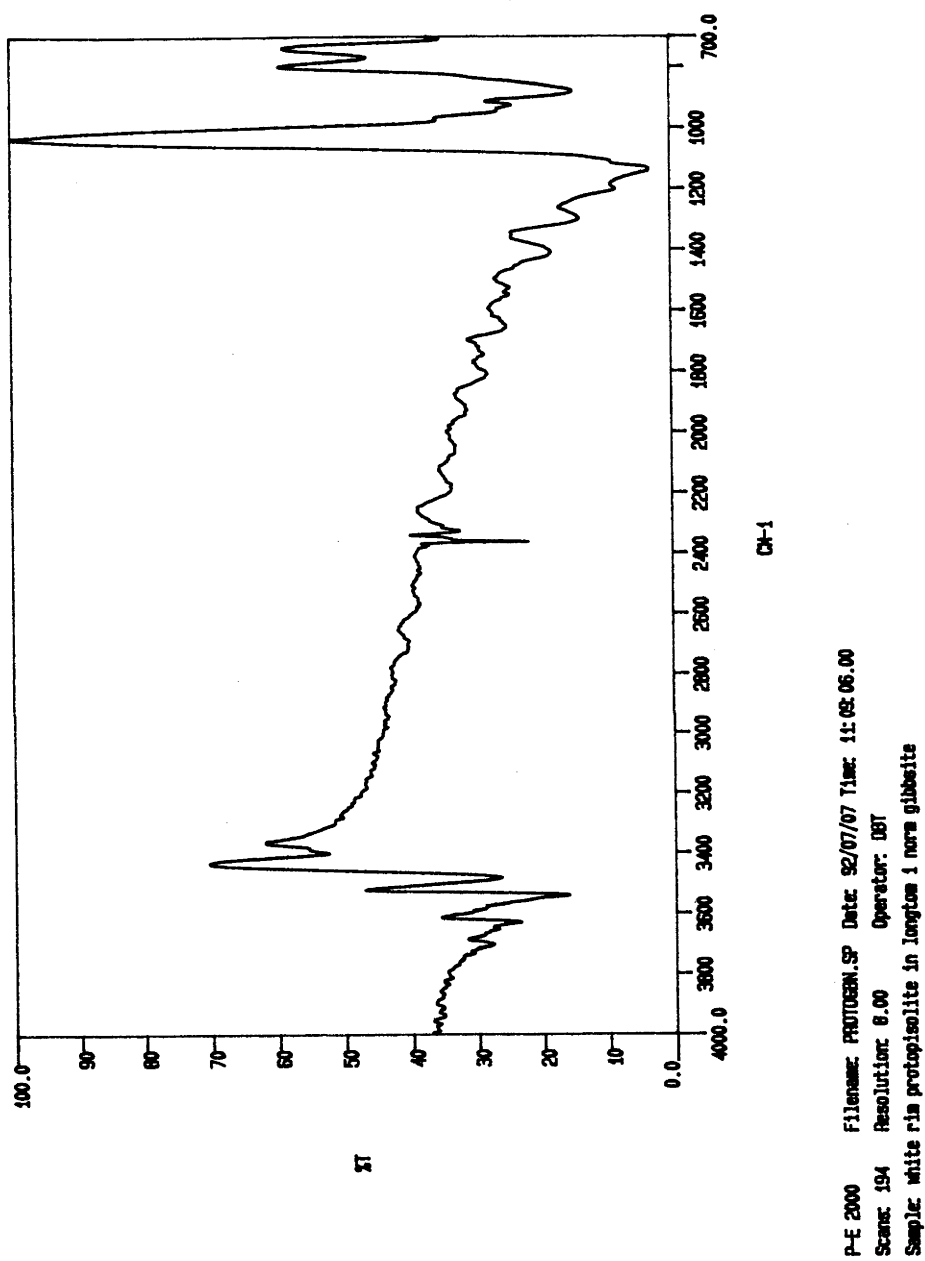


Figure 4.13

Interference effect in the specular reflectance spectra of pisolith thin-sections.

Chapter 5

Near-infrared reflectance spectrometry

5.1 Introduction

Since mining operations began at Weipa in the early 1960's, there has been the need for improved grade control at the mine site. Traditionally, grade control is accomplished by constructing a closely spaced array of drill-holes, with samples taken at regular intervals down to the nodular ferruginous-kaolinite layer ('ironstone'). Interpolation between the drill-holes is a requirement of this technique. The samples are analysed using XRF, after which the mineralogy is calculated using the so called CMP4 method devised by Comalco Mineral Products, Weipa. Calculation of the mineralogy by the CMP4 method, requires many assumptions which cannot be confidently relied upon. The assumptions include:

- a) the nature and chemical composition of the minerals present within the bauxite;
- b) the relative proportions of some of the minerals;
- c) the way in which the minerals react in the low and high temperature versions of the Bayer process (Morgan, 1992).

As there is often an abrupt change in the grade of ore at the bauxite/ferruginous-kaolinite layer interface, front-end loader drivers have been assigned the responsibility of ensuring that mining ceases when 'ironstone' is exposed (Figure 5.1). In some bauxite mines at Andoom, ferruginous-kaolinite nodules are similar in size to bauxitic pisoliths. In such cases, sighting of "ironstone" from the cabin of the front-end loader can become very difficult. Significant amounts of high grade ore may be left behind if the depth of mining is under-estimated. Alternatively, high grade ore that has been previously mined can become contaminated with ferruginous-kaolinite if the depth of mining is over-estimated.

*Pima III*¹, a compact hand-held infrared spectrometer, can provide the mine geologist with a tool for analysing bauxite at the mine site. *Pima II* operates in the near-infrared wavelength interval between 1300 and 2500 nm (Figure 5.2).

¹*Pima II* is marketed and distributed by Integrated Spectronics Pty. Ltd.
P.O. Box 437, Baulkham Hills, N.S.W. 2153, Australia.



Figure 5.1

Bauxite being mined at the Jacaranda mine, Andoom. At present, the depth to which bauxite is mined is governed by the sighting of "ironstone". The use of an analytical instrument such as *Pima II* at the mine site could greatly improve grade control.



Figure 5.2

Pima II, a compact hand-held infrared spectrometer.

In this range, absorption by atmospheric water vapour is avoided. No sample preparation is required, however to ensure homogeneity, it is advisable to grind the sample in a mortar and pestle before analysis. The use of such an instrument at the mine site would overcome the subjectivity in determining the depth of mining. Furthermore, *Pima II* may be used during drilling to obtain rapid analyses of samples.

This chapter reports the results of a study showing that semi-quantification of bauxite mineralogy is possible, by measuring certain parts of the near-infrared spectrum. Although the technique at present is not sufficiently developed for direct application, the use of data processing techniques such as factor analysis and multiple linear regression (Fredericks *et al.*, 1987), may enable the routine quantitative analysis of bauxite to be performed at the mine-site.

5.2 Experimental methods and results

Bauxite samples from drill-holes WB754EH, WB837EH, TR221AB and TR067AB, were analysed using XRD and *Siroquant* to determine their mineralogy. Graphs depicting the variation in mineralogy down each drill-hole are presented in chapter 6, "Quantitative X-ray diffraction". A diffuse reflectance near-infrared spectrum was obtained for each sample using *Pima II* (Figure 5.3). The area of the 2212 nm peak that is associated with O-H vibrations in kaolinite, was then measured using the Siemens DIFFRAC-AT version 3.1 computer software (Figures 5.4 & 5.5). The data (Table 5.1) was plotted and the line of best fit having a correlation coefficient (R^2) of 0.867 was obtained (Figure 5.6.1). Using $y = 4.673x + 0.112$ as the equation for the line, predicted kaolinite contents were calculated. These values were plotted against the *Siroquant* determined values to assess the predictability of *Pima II* analyses (Figure 5.6.2). Residuals were plotted against the *Siroquant* determined values to gauge the randomness of the residuals (Figure 5.7). The standard error in predicting the wt.% of kaolinite by measuring the area of the 2212 nm peak is ± 2.4 wt.% (Table 5.2).

The same procedure was used on the 2270 nm peak associated with O-H vibrations in gibbsite (Table 5.3, Figures 5.8.1 and 5.8.2). The standard error in predicting the wt.% of gibbsite by measuring the area of the 2270 nm peak is ± 7.5 wt.% (Figure 5.9 and Table 5.4).

PIMA II spectra of bulk samples from drill-hole TR067AB, Andoom.

Bauxite bulk mineralogy (wt%) determined by Siroquant.

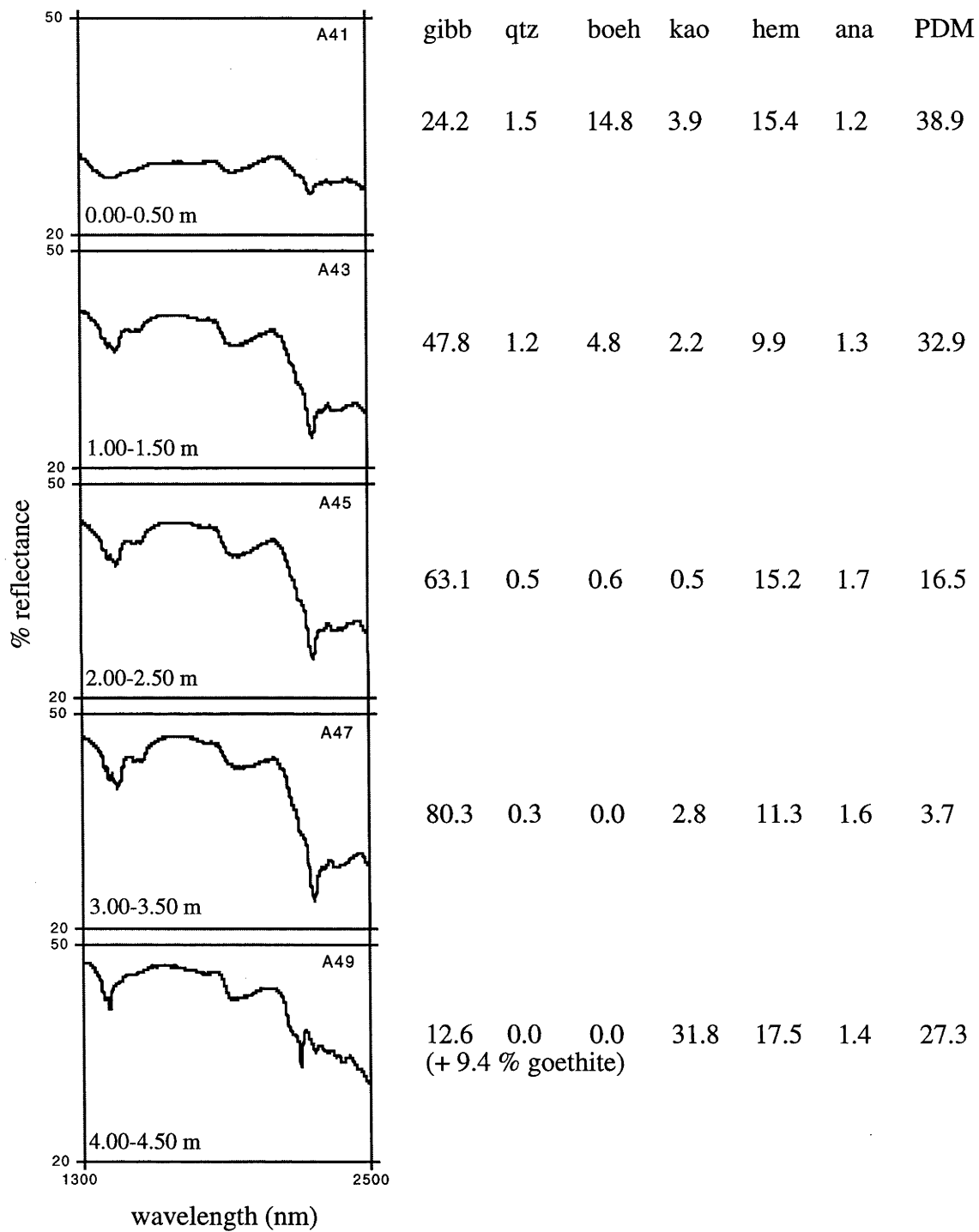


Figure 5.3

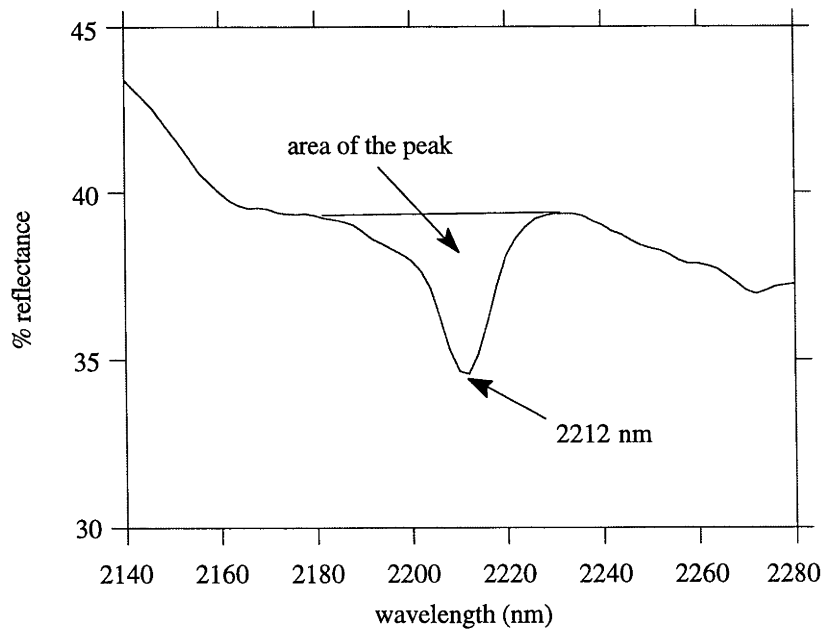
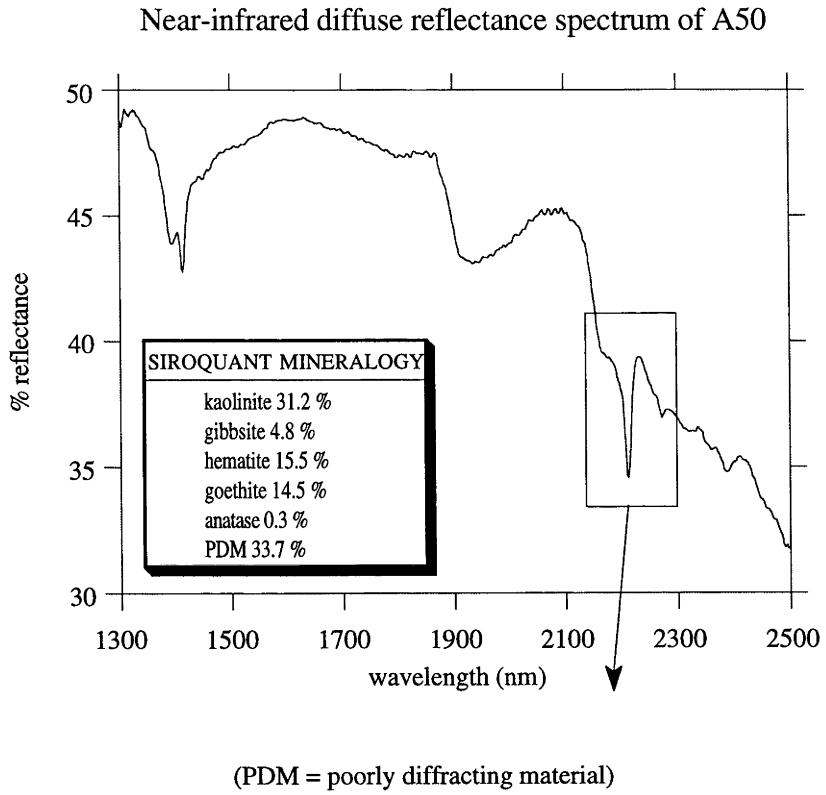


Figure 5.4

Near-infrared diffuse reflectance spectrum of A1

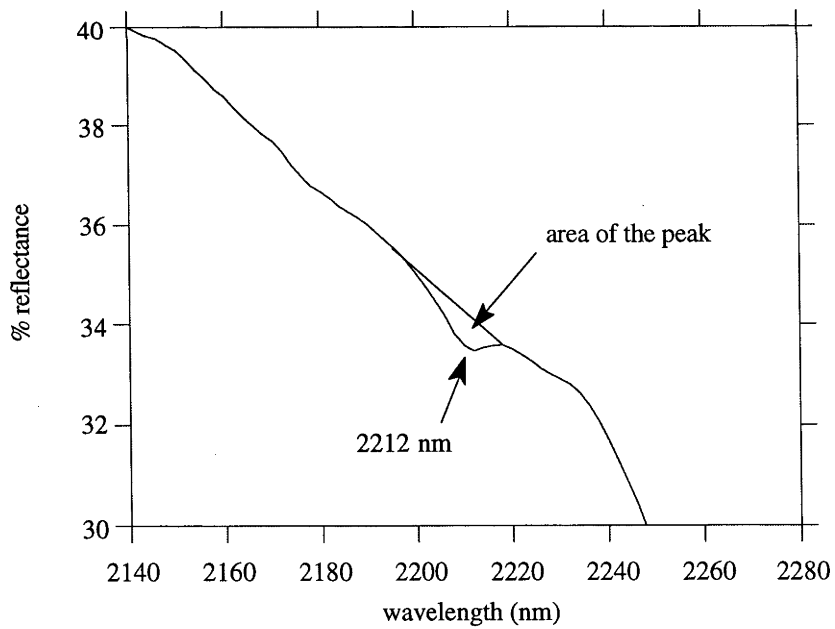
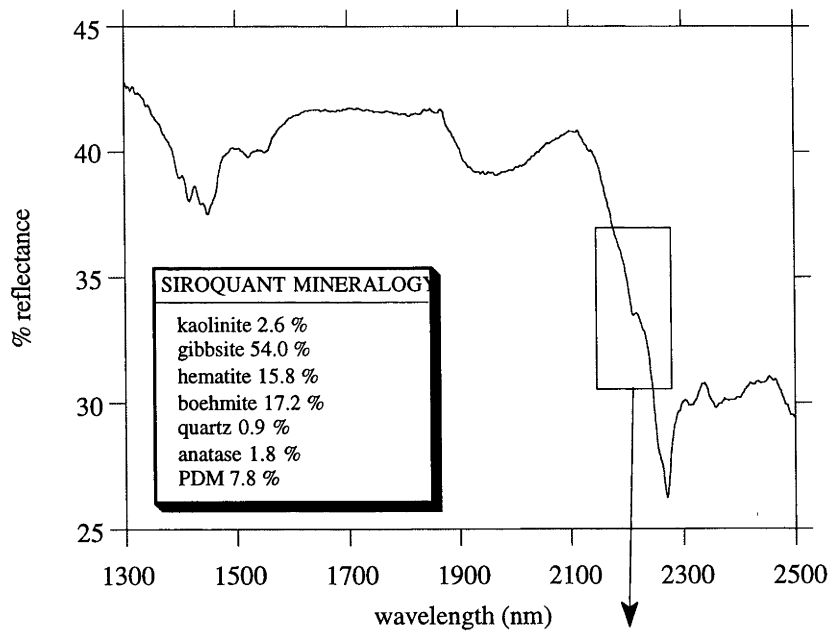


Figure 5.5

area of 2212 nm kaolinite peak (x)	wt.% kaolinite (SIROQUANT)	predicted wt.% kaolinite (PIMA) using $y=4.673x+0.112$
0.75	0.5	3.62
1.09	0.6	5.21
1.17	2.1	5.58
0.79	2.2	3.80
0.86	2.3	4.13
0.79	2.5	3.80
0.70	2.6	3.38
0.95	2.7	4.55
1.31	2.8	6.23
0.79	2.8	3.80
0.54	3.9	2.64
1.58	4.5	7.50
1.17	4.7	5.58
1.47	4.8	6.98
1.23	4.8	5.86
1.13	4.9	5.39
1.13	6.4	5.39
1.90	6.7	8.99
0.76	7.3	3.66
1.59	7.8	7.54
1.65	8.1	7.82
2.00	8.3	9.46
1.59	8.4	7.54
1.23	8.8	5.86
1.34	9.1	6.37
2.05	9.9	9.69
1.97	10.1	9.32
1.61	10.3	7.64
2.36	10.5	11.14
1.38	11.3	6.56
1.82	11.9	8.62
1.45	12.0	6.89
2.15	15.3	10.16
3.34	17.8	15.72
7.32	31.2	34.32
6.58	31.8	30.86

Table 5.1

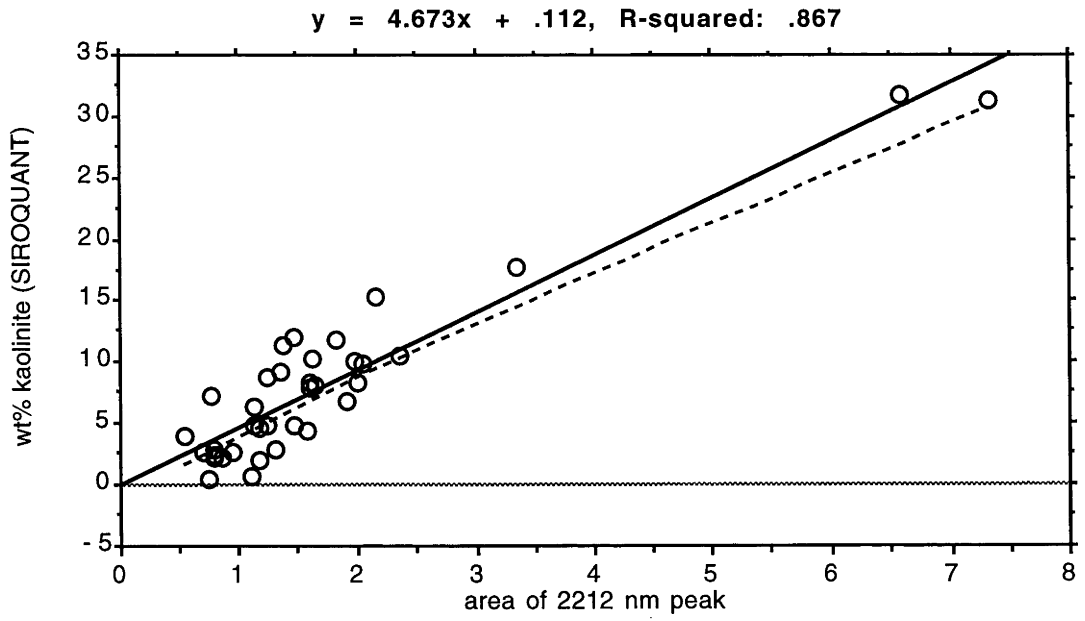


Figure 5.6.1

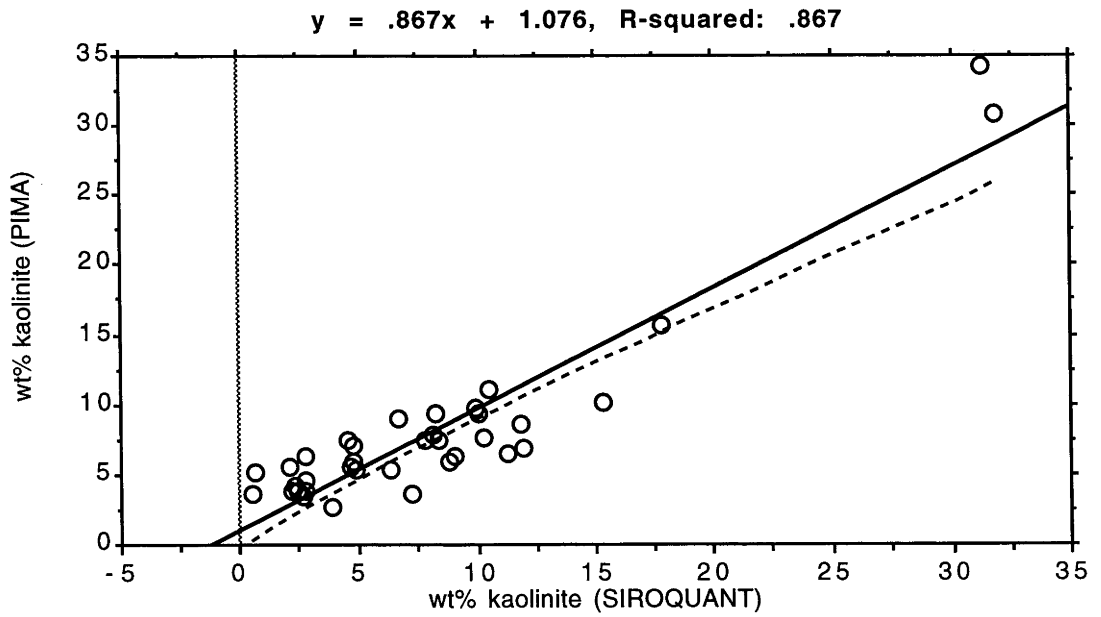


Figure 5.6.2

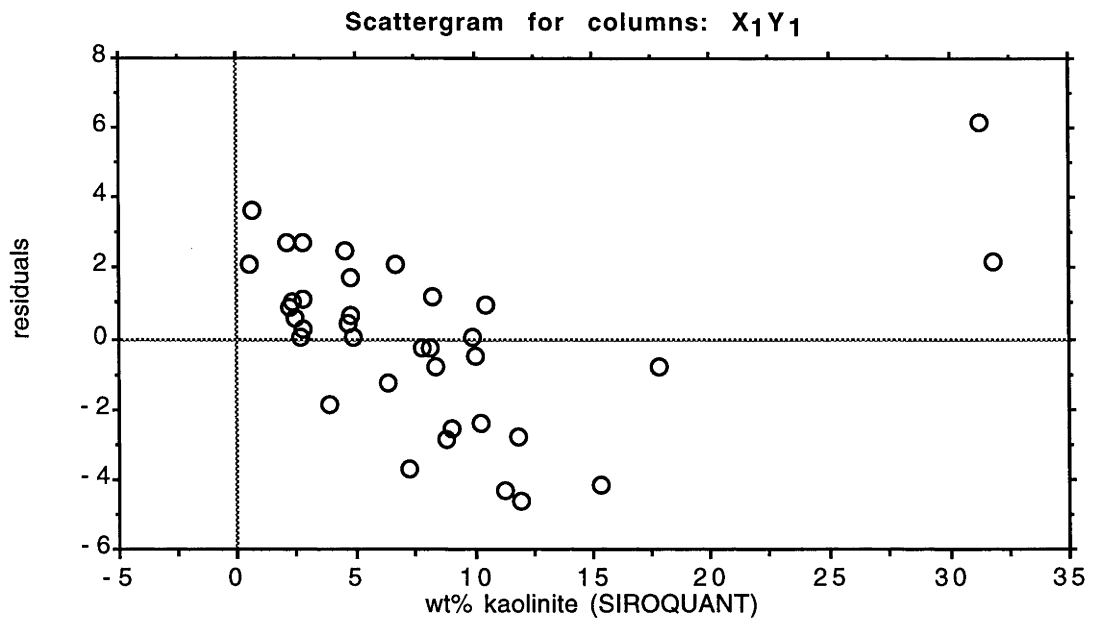


Figure 5.7

Simple Regression X 1 : wt% kaolinite (SIROQUANT) Y 1 : wt% kaolinite (PIMA)

DF:	R:	R-squared:	Adj. R-squared:	Std. Error:
35	.931	.867	.863	2.435

Analysis of Variance Table

Source	DF:	Sum Squares:	Mean Square:	F-test:
REGRESSION	1	1316.528	1316.528	222.028
RESIDUAL	34	201.605	5.93	p = 1.0000E-4
TOTAL	35	1518.134		

Residual Information Table

SS[e(i)-e(i-1)]:	e ≥ 0:	e < 0:	DW test:
248.074	21	15	1.23

Table 5.2

area of 2270 nm gibbsite peak (x)	wt.% gibbsite (SIROQUANT)	predicted wt.% gibbsite (PIMA) using $y=3.493x-3.35$
2.34	4.8	4.82
4.30	12.6	11.67
5.98	26.7	17.54
15.04	28.2	49.19
12.36	34.5	39.82
16.07	47.8	52.78
20.78	49.4	69.24
20.00	49.5	66.51
17.37	53.0	57.32
18.97	53.8	62.91
16.49	54.0	54.25
18.59	57.9	61.59
16.77	58.3	55.23
17.72	59.2	58.55
19.49	59.3	64.73
17.29	59.7	57.04
20.70	60.1	68.96
17.58	60.7	58.06
20.34	61.4	67.70
16.68	61.9	54.91
17.65	63.1	58.30
18.50	64.6	61.27
20.47	64.7	68.15
17.99	64.9	59.49
21.42	65.9	71.47
19.06	67.0	63.23
21.19	69.5	70.67
21.36	71.7	71.26
19.83	72.5	65.92
20.51	74.2	68.29
20.50	75.7	68.26
22.96	76.9	76.85
20.78	77.1	69.24
21.40	78.1	71.40
18.73	78.6	62.07
20.22	80.3	67.28
27.22	100.0	91.73

Table 5.3

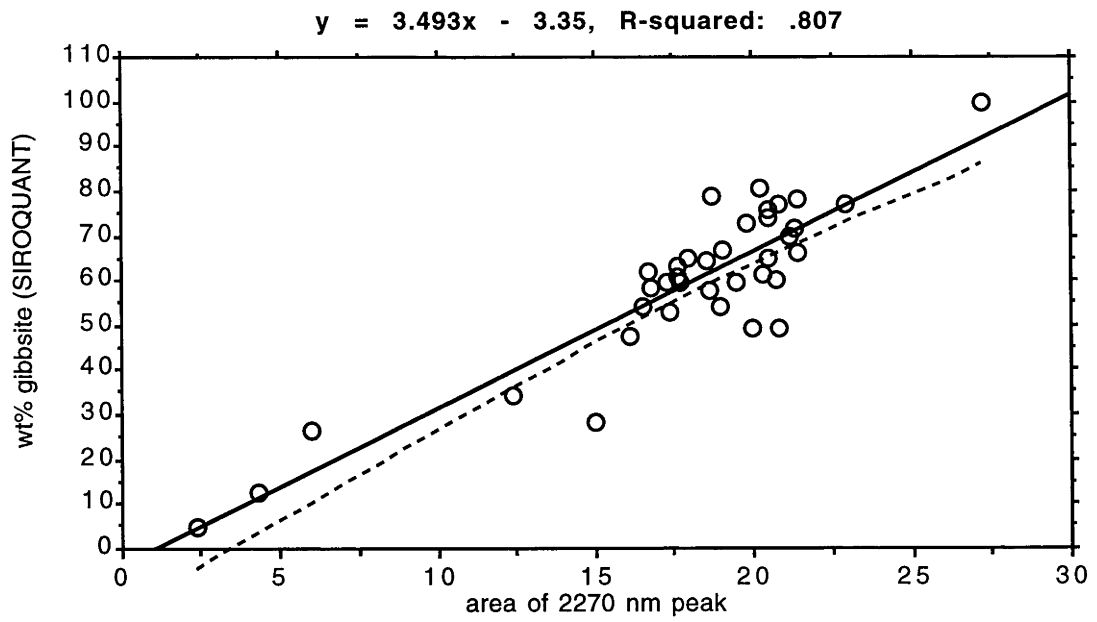


Figure 5.8.1

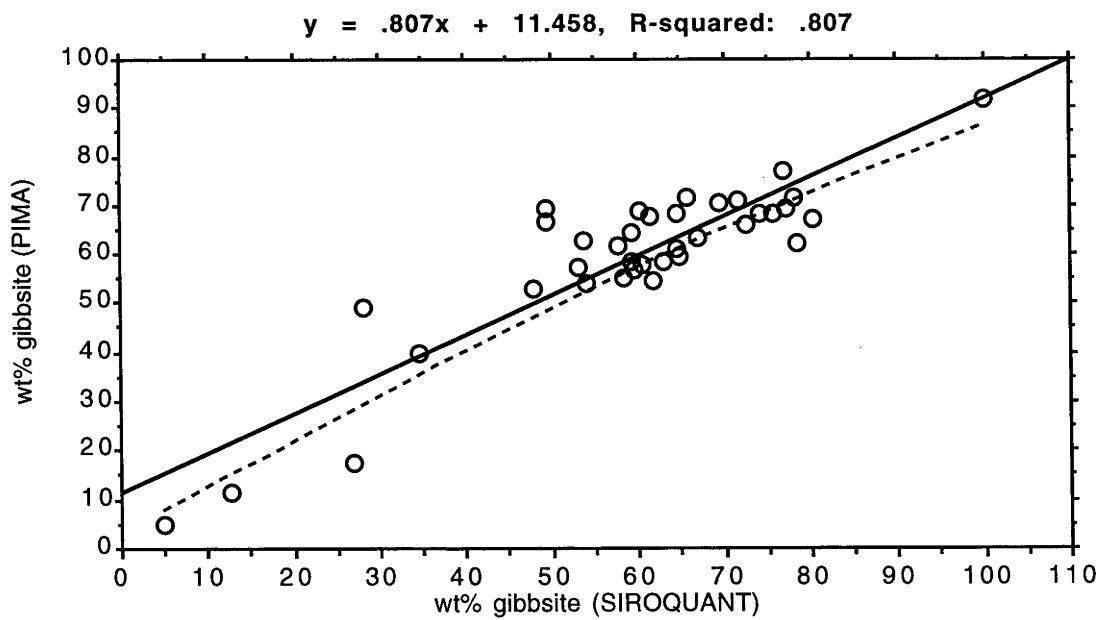


Figure 5.8.2

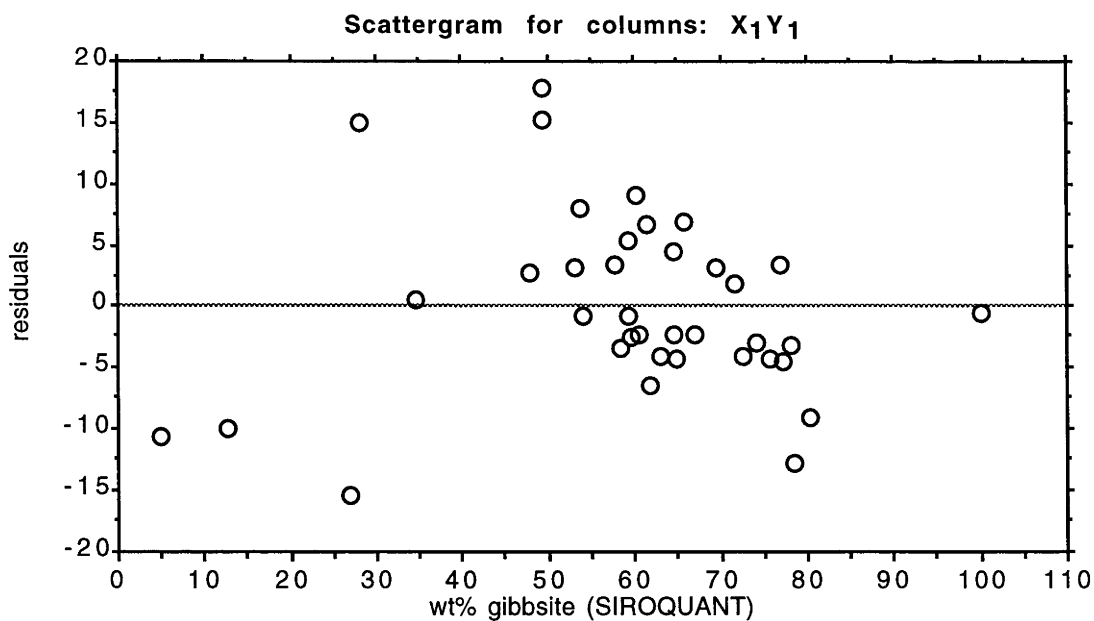


Figure 5.9

Simple Regression X 1 : wt% gibbsite (SIROQUANT) Y 1 : wt% gibbsite (PIMA)

DF:	R:	R-squared:	Adj. R-squared:	Std. Error:
36	.898	.807	.802	7.548

Analysis of Variance Table

Source	DF:	Sum Squares:	Mean Square:	F-test:
REGRESSION	1	8344.463	8344.463	146.447
RESIDUAL	35	1994.279	56.979	p = 1.0000E-4
TOTAL	36	10338.742		

Residual Information Table

SS[e(i)-e(i-1)]:	e ≥ 0:	e < 0:	DW test:
3058.293	16	21	1.534

Table 5.4

Hematite does not contain any O-H bonds therefore no distinct absorption bands occur in the near-infrared wavelength range between 1300 and 2500 nm (Figure 5.10.1). However, a general decrease in reflectance towards the shorter wavelength end of the spectrum is clearly visible when spectra from the Weipa bauxite samples are superimposed on top of those from Andoom (Figure 5.10.2). The negative correlation between the infrared reflectance at 1300 nm and the hematite content was used in a prediction test (Table 5.5, Figures 5.11.1 and 5.11.2). The standard error in predicting the wt.% of hematite by measuring the reflectance at 1300 nm is ± 2.9 wt.% (Figure 5.12 and Table 5.6).

Boehmite exhibits two rather broad and shallow absorption features in the near infrared wavelength range with their maxima occurring at 1670 and 2320 nm. The near infrared spectra displayed in Figure 5.13.1 show the effect of mixing boehmite with gibbsite.

Like hematite, quartz has a relatively featureless infrared spectrum (Figure 5.13.2), however ground quartz is somewhat more reflective than finely powdered hematite. The broad diffuse maxima, shared in both spectra, may be due to a small amount of moisture in the samples.

Figures 5.14.1 and 5.14.2 show infrared spectra of bauxite containing a high proportion of poorly diffracting material (PDM). Quantitative XRD analysis using *Siroquant*, showed that the Weipa sample (Figure 5.14.1) contained 62 wt.% PDM and the one from Andoom (Figure 5.14.2) contained 78 wt.% PDM. In both cases, absorption occurs at 1420 nm and 1950 nm associated with stretching and bending vibrations within water molecules (Drennen & Lodder, 1993). As the samples were air dried prior to spectra acquisition, the water must be strongly bound.

Thermogravimetric (water) analyses of the samples were carried out by the Australian Geological Survey Organisation (Figures 5.15 and 5.16). The analyses also showed the presence of strongly bound water, indicating PDM has a strong attraction for water and/or has a high surface area per unit volume. The peaks observed between 244°C and 266°C are associated with the thermal decomposition of gibbsite (Inoue, et al., 1989). The series of peaks up to ~200°C in both samples, are due mainly to the loss of molecular water adsorbed onto the surface of PDM. The presence of 4 thermogravimetric peaks associated with the PDM suggests that more than one phase of PDM may be present.

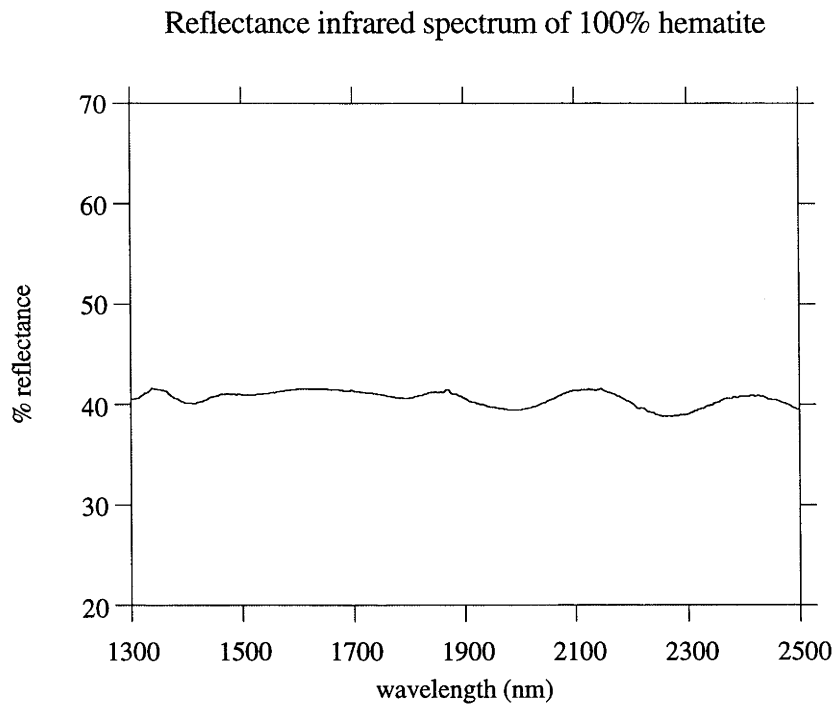


Figure 5.10.1

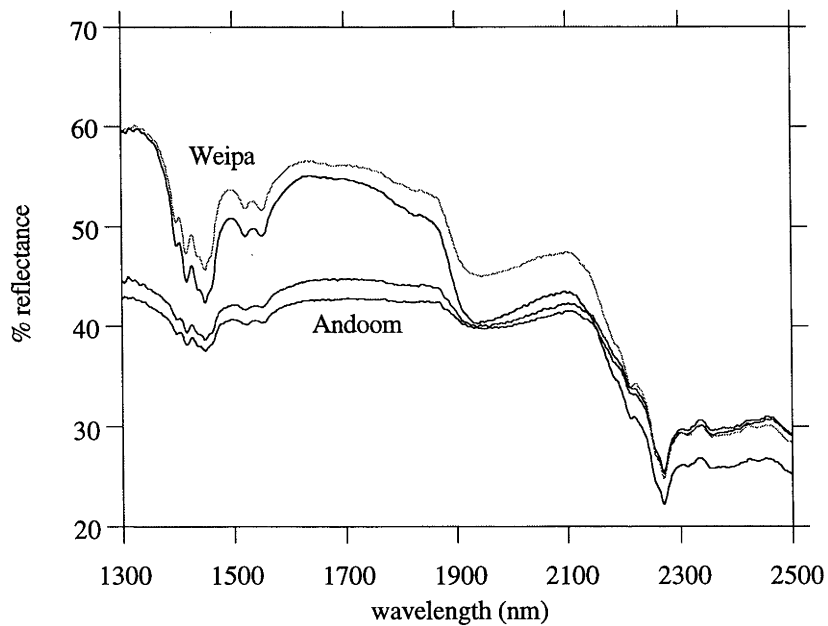


Figure 5.10.2

Typical diffuse reflectance infrared spectra of bauxite from Weipa and Andoom. A reduction in reflectance occurs in the shorter wavelengths for samples from Andoom due to their high hematite content.

wt.% hematite (SIROQUANT)	reflectance at 1300 nm (x)	predicted wt.% hematite (PIMA) using $y=-0.662x+42.117$
1.4	58.80	3.19
1.5	61.05	1.70
1.5	61.68	1.28
1.7	59.35	2.83
1.9	56.72	4.57
1.9	58.88	3.14
2.0	62.47	0.76
2.0	59.43	2.77
2.1	57.25	4.22
2.1	60.87	1.82
2.3	64.39	-0.51
2.4	59.37	2.81
2.6	57.46	4.08
2.7	56.98	4.40
3.4	53.13	6.94
3.4	59.33	2.84
4.6	45.21	12.19
5.1	51.74	7.87
6.0	42.99	13.66
6.5	56.99	4.39
9.9	41.88	14.39
11.2	44.79	12.47
11.3	46.41	11.39
13.4	43.97	13.01
14.4	44.90	12.39
14.8	42.77	13.80
15.2	44.41	12.72
15.2	43.99	13.00
15.5	48.97	9.70
15.8	42.72	13.84
16.1	42.74	13.82
17.1	31.19	21.47
17.5	47.14	10.91
17.5	48.00	10.34
17.6	42.25	14.15
18.0	41.77	14.47

Table 5.5

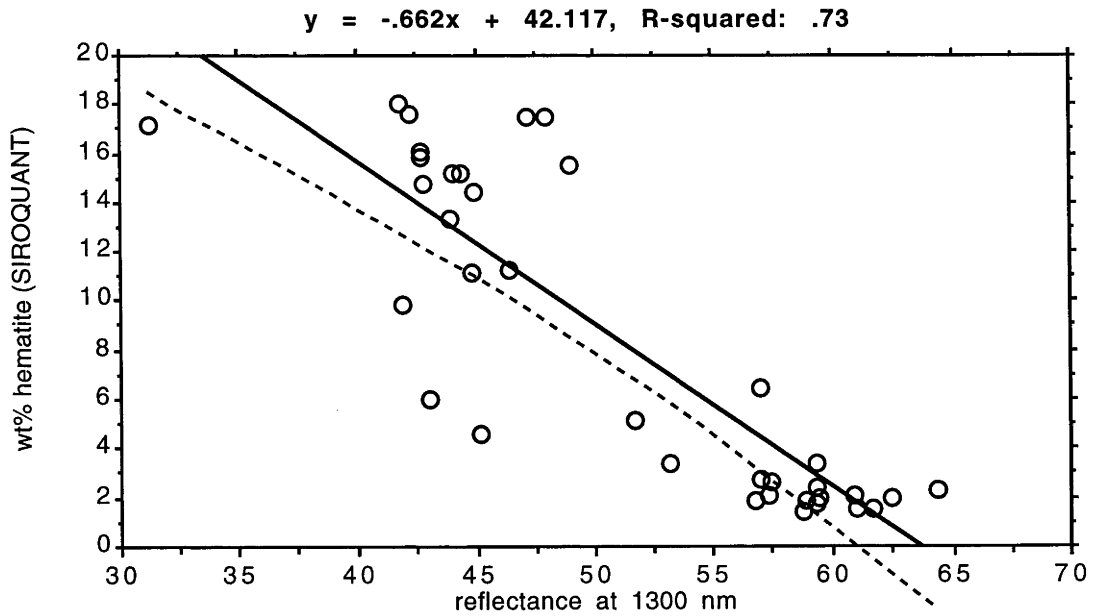


Figure 5.11.1

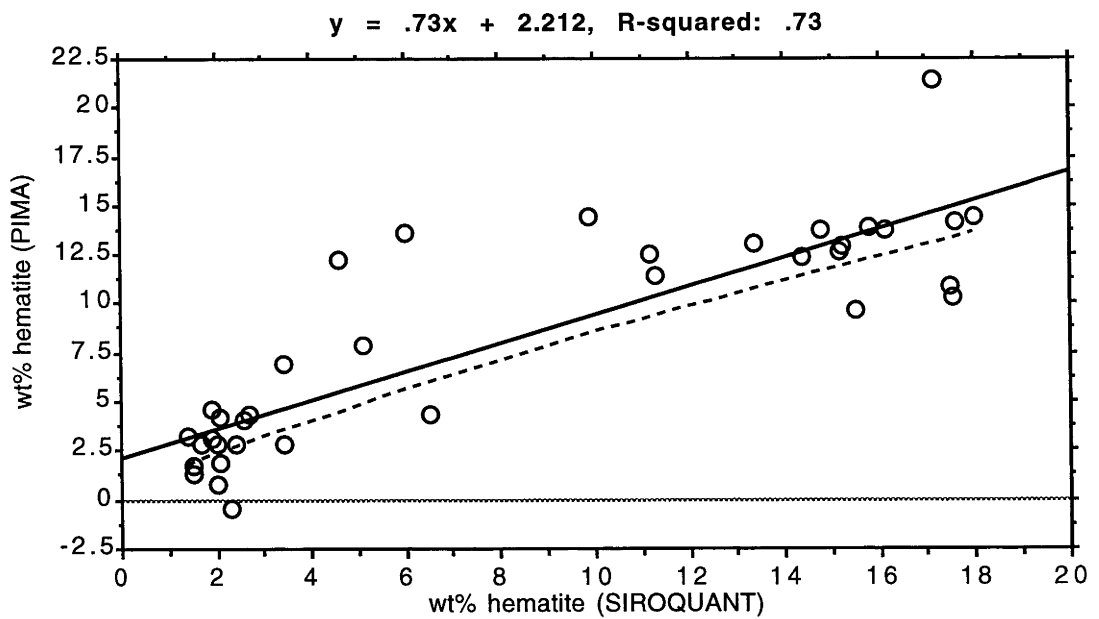


Figure 5.11.2

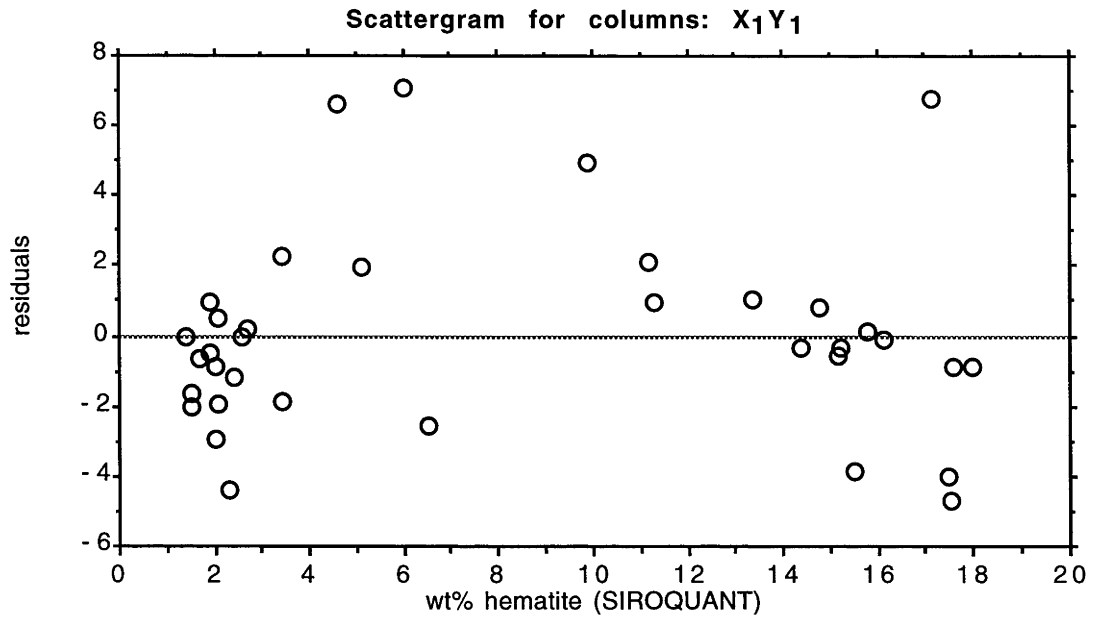


Figure 5.12

Simple Regression X x_1 : wt% hematite (SIROQUANT) Y y_1 : wt% hematite (PIMA)

DF:	R:	R-squared:	Adj. R-squared:	Std. Error:
35	.854	.73	.722	2.906

Analysis of Variance Table

Source	DF:	Sum Squares:	Mean Square:	F-test:
REGRESSION	1	774.439	774.439	91.726
RESIDUAL	34	287.06	8.443	$p = 1.0000E-4$
TOTAL	35	1061.499		

Residual Information Table

SS[e(i)-e(i-1)]:	$e \geq 0$:	$e < 0$:	DW test:
556.875	14	22	1.94

Table 5.6

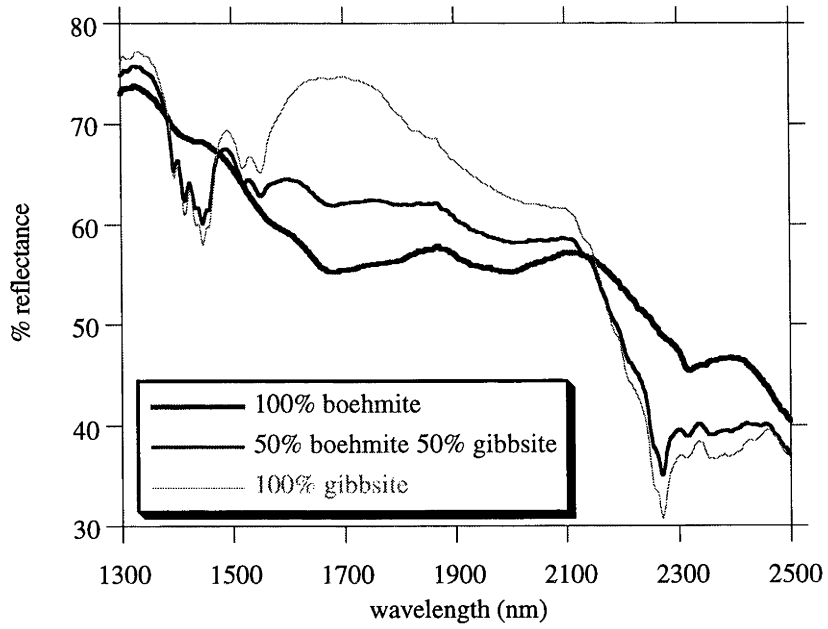


Figure 5.13.1

Near infrared spectrum of 100% quartz

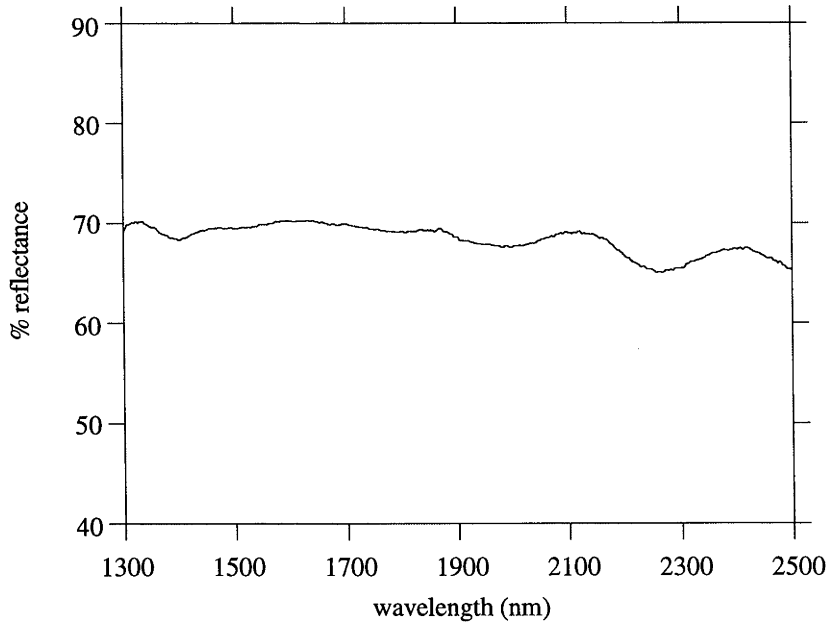


Figure 5.13.2

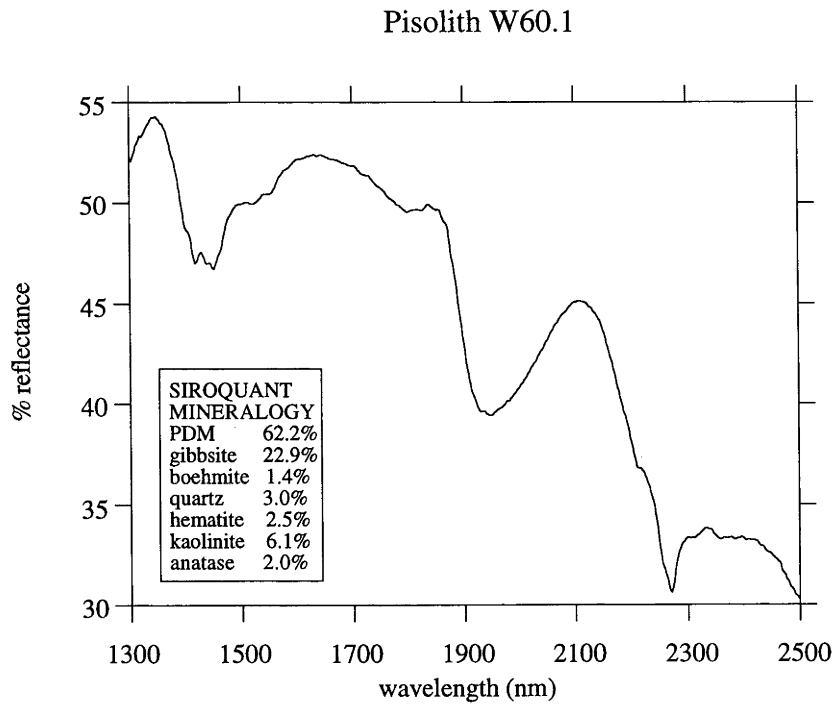


Figure 5.14.1

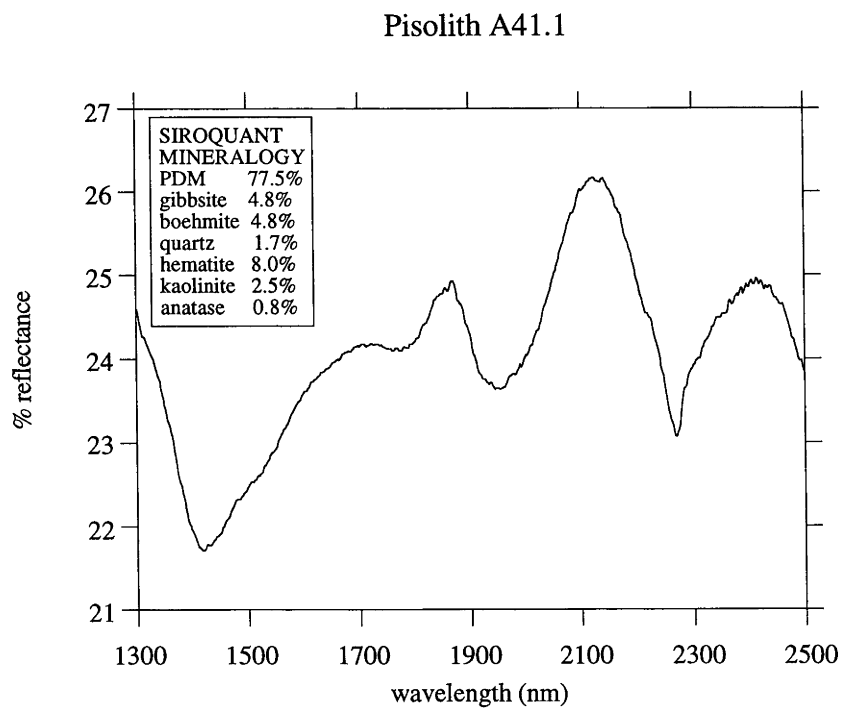


Figure 5.14.2

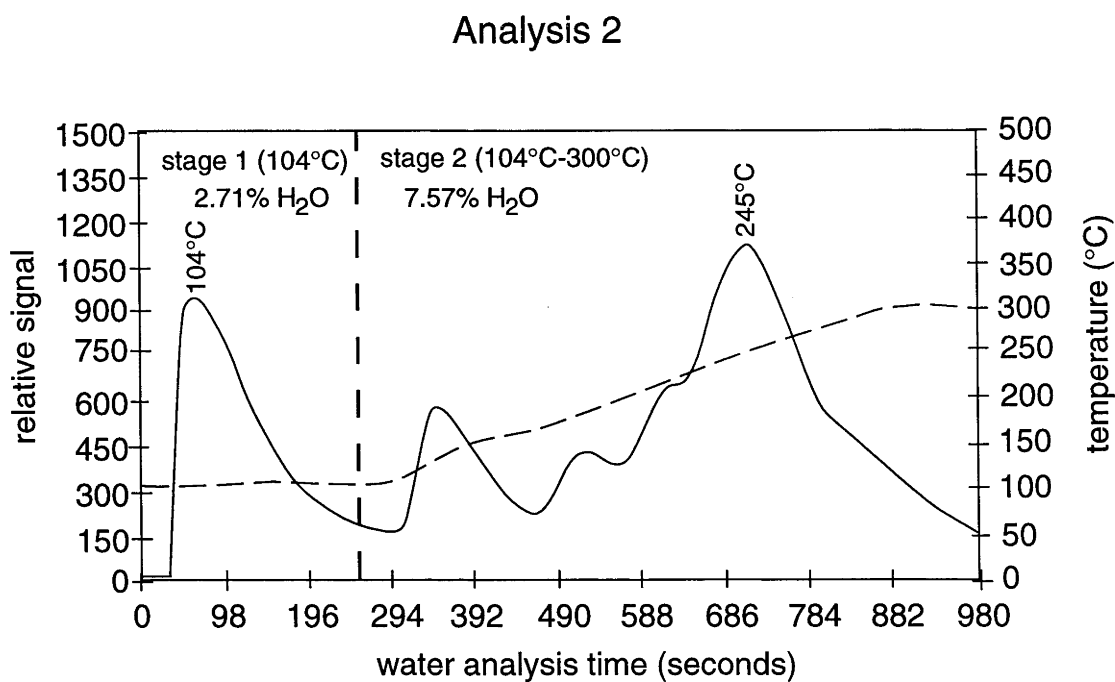
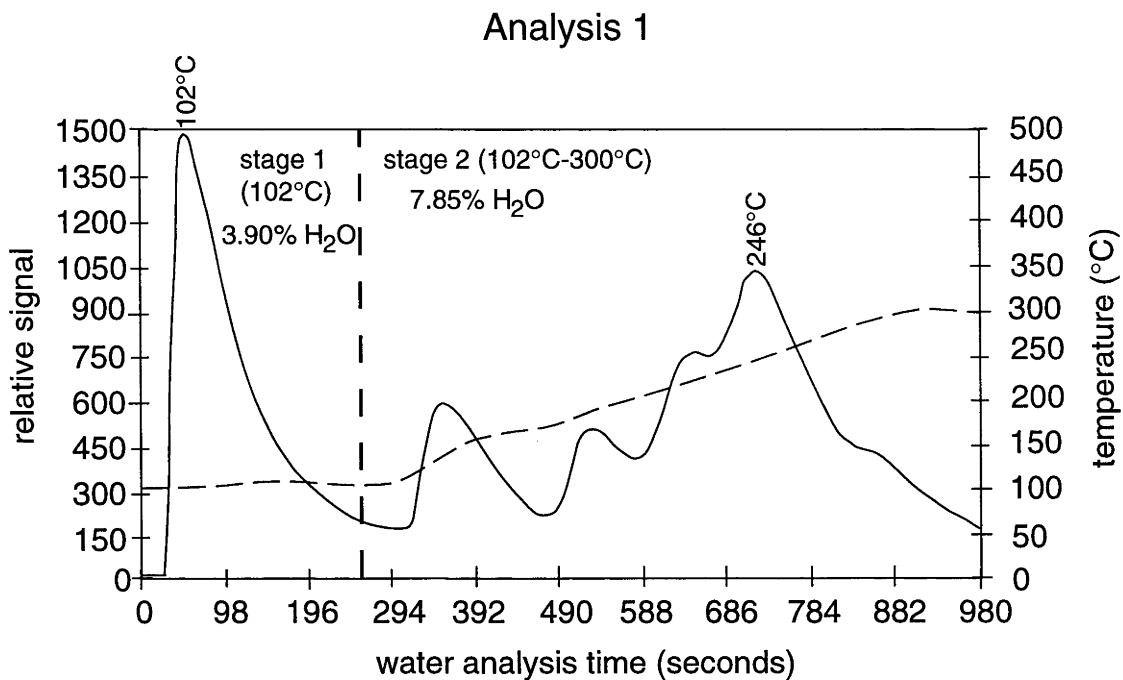
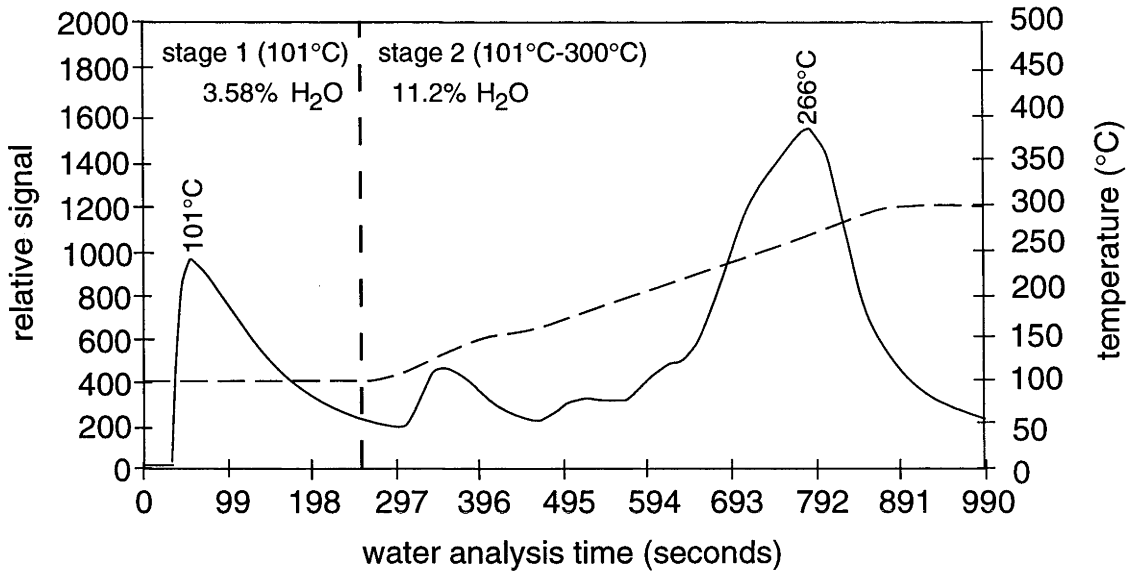


Figure 5.15

Thermogravimetric analyses of pisolith A41.1
obtained at the Australian Geological Survey Organisation.

Analysis 1



Analysis 2

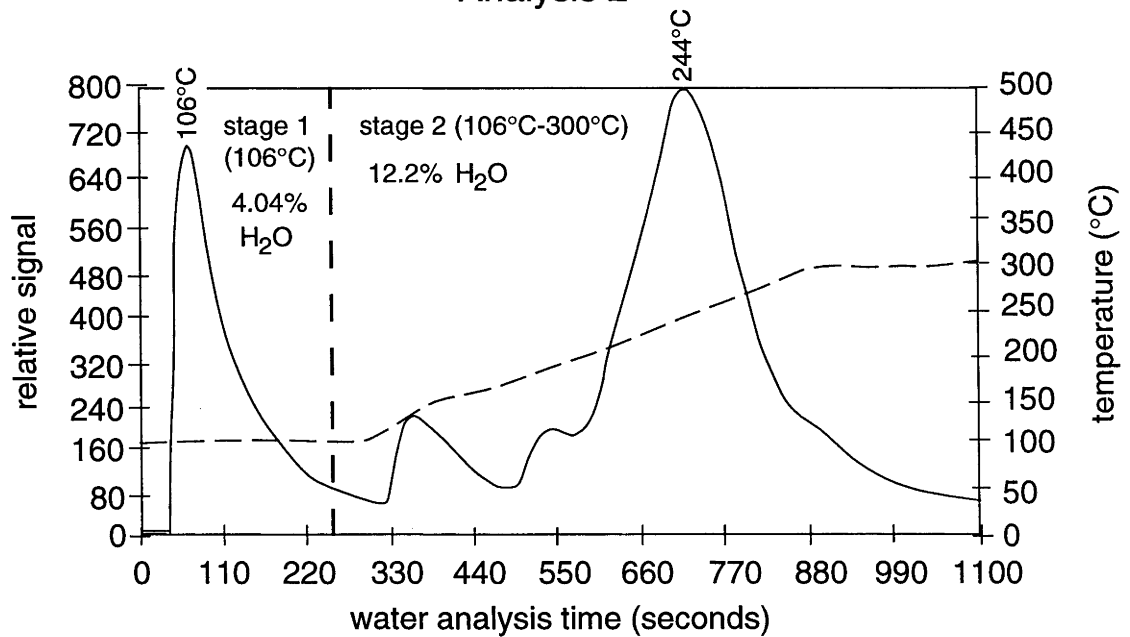


Figure 5.16

Thermogravimetric analyses of pisolith W60.1
obtained at the Australian Geological Survey Organisation.

Chapter 6

Quantitative X-ray diffraction

6.1 Introduction

X-ray diffraction (XRD) studies for this work were done on a Siemens D501, θ - 2θ powder diffractometer using $\text{CuK}\alpha$ radiation and a graphite post-sample monochromator, collimated by 1° divergence slits. For quantitative analysis, samples were usually run from 6 - 66° at steps of 0.02° 2θ and a counting time of 1.2 seconds/step. Figure 6.1 shows a typical XRD scan of bauxite, with major peaks indexed for the six main minerals that may be present.

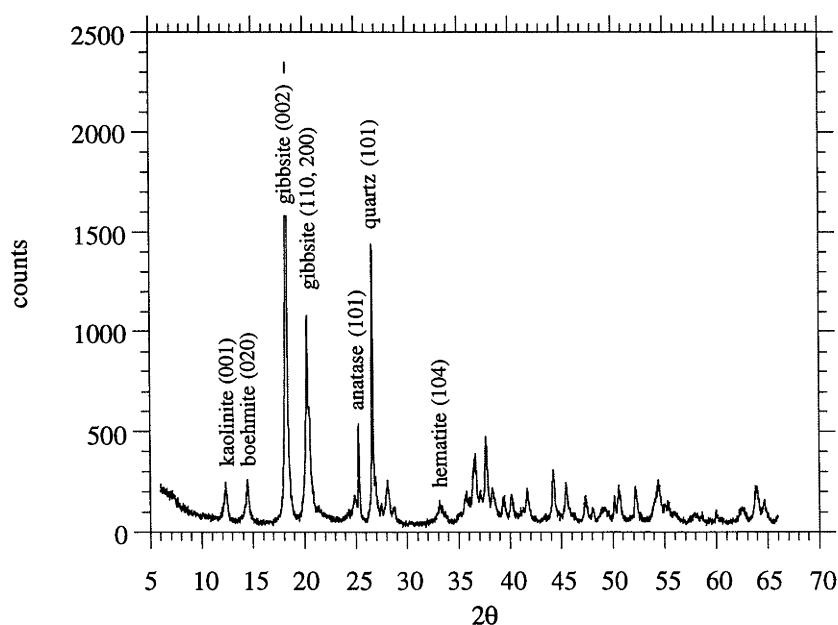


Figure 6.1

A typical X-ray diffractogram of bauxite. Major peaks have been indexed for the six main minerals generally found in the bauxite of Weipa and Andoom.

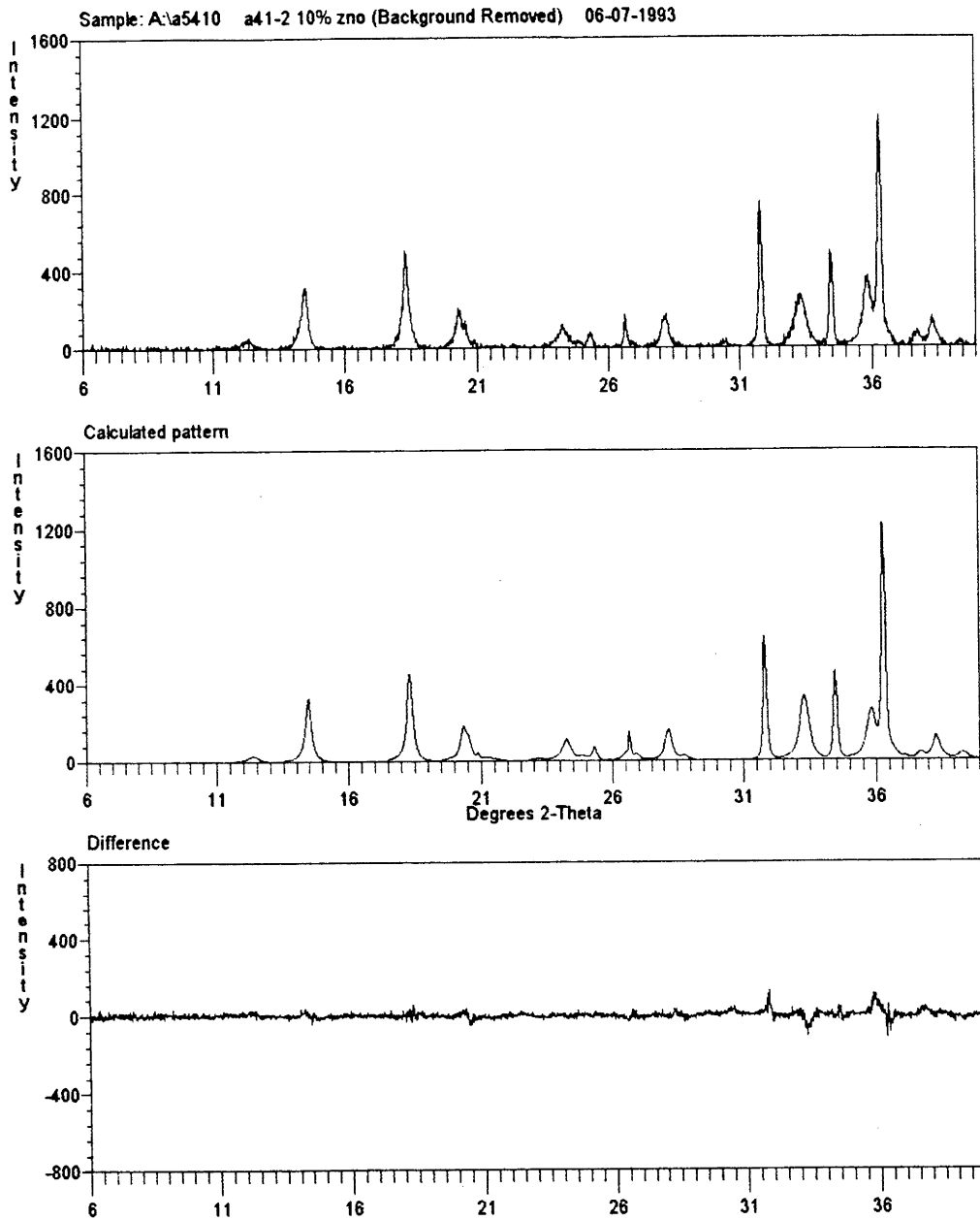
Quantitative X-ray diffraction techniques traditionally involved the measurement of the intensity of chosen peaks and subsequent comparison with those in standard calibration mixtures. However, these methods were tedious, as standards needed to be made up for a variety of situations and intensity anomalies caused by angular dependent aberrations such as preferred orientation often made the method unreliable.

The foundations for multiphase profile analysis of the complete powder diffraction pattern were first laid down by Rietveld (1969). He showed that it was possible to replicate a measured diffraction profile with a calculated pattern. The advantage of full profiling is that residual errors caused by intensity aberrations inherited from the sample preparation stage or from using imperfect structural models tend to be positive and negative over the full diffraction profile leaving the Rietveld phase scaling factors largely unaltered (Taylor, 1991). Other workers including; Hewat (1973), Wiles & Young (1981), Will, Huang & Parrish (1983), Hill & Howard (1986) and (Taylor, 1991) have since refined the technique, culminating in the writing of *Siroquant*².

Siroquant is a Rietveld-type multiphase analysis program which replicates a measured diffraction pattern by employing a least-squares fitting routine which adjusts the scaling factors until the calculated profile best approximates the measured one (Figure 6.2). In the process, a differential pattern is produced which indicates the degree to which the calculated pattern replicates the measured one. As an additional means of determining the degree of fit, the statistical parameter, χ^2 (chi-squared), is displayed after each least-squares fitting routine. Ideally, a perfect match is attained when $\chi^2 = 1$, however this seldom occurs. Generally, a good fit is indicated when the χ^2 -value is less than 3. The quantity of individual minerals present within a sample is calculated from their respective scaling factors and absorption coefficients.

Siroquant has the provision for quantifying the amorphicity of a sample. The presence of poorly-diffracting material (PDM) in a sample causes a reduction in the diffracted intensity of the crystalline phases. The amorphicity of a sample may be due to a number of reasons. Minerals that are composed of particles smaller than several hundred Å, have broad diffraction patterns. The diffraction lines may be so broadened that they are lost in the background. Glassy materials have no three-dimensional periodicity and therefore give no diffraction lines. Disordered structures may have streaking in the reciprocal lattice, thereby contributing as well, to the poorly-diffracting material content of a sample (*pers. com.* John C. Taylor, 1993). Rietveld analysis alone cannot quantify amorphicity. However, the addition of an internal standard (ZnO or quartz are recommended by Taylor & Clapp, 1992) of known concentration, facilitates the quantification of the poorly-diffracting weight fraction.

²*Siroquant* is marketed and distributed by Sietronics Pty. Ltd.
P.O. Box 3066, Belconnen, A.C.T. 2617, Canberra, Australia.



<u>Phase</u>	<u>weight %</u>	<u>error %</u>
gibbsite	33.8	0.32
boehmite	20.4	0.26
quartz	1.8	0.13
hematite	21.0	0.22
kaolinite	5.9	0.45
anatase	1.5	0.12
ZnO	15.5	0.13

Figure 6.2

A typical *Siroquant* output showing the measured (background removed), calculated and difference patterns. In this case, 10 weight % of ZnO was added to the sample for the quantification of poorly-diffracting material. 39.6 weight % PDM must be present to account for the discrepancy between the known quantity of ZnO and that calculated.

Siroquant uses the following equations in the quantification of poorly-diffracting material (Taylor, J. C. *pers. com.*, 1993):

$$\begin{aligned} X_D &= 1 - Y_S / X_S \\ X_I &= X_D / (1 - Y_S) \end{aligned}$$

X_D = weight fraction of PDM in the sample containing an internal standard,

Y_S = weighed weight fraction of the internal standard,

X_S = *Siroquant* weight fraction of the internal standard.

X_I = weight fraction of PDM in the original sample containing no internal standard.

As the addition of an internal standard causes dilution of the sample and a subsequent loss in accuracy, it is preferable to run a sample without an internal standard, as well. This sample is used specifically for the purpose of quantifying well-crystallised phases while the sample containing the internal standard is used only for the amorphicity determination. To obtain the final quantification, the results from both samples are combined and normalised.

Chemical analyses using either X-ray fluorescence (XRF) or energy dispersive X-ray analysis (EDXA) show good agreement with *Siroquant* analyses when poorly-diffracting material is absent (Figure 6.3). When it is present, the chemical composition of the material is determinable by subtracting the *Siroquant* results from the chemical analyses. Chapter 7 deals with the composition of the poorly-diffracting material.

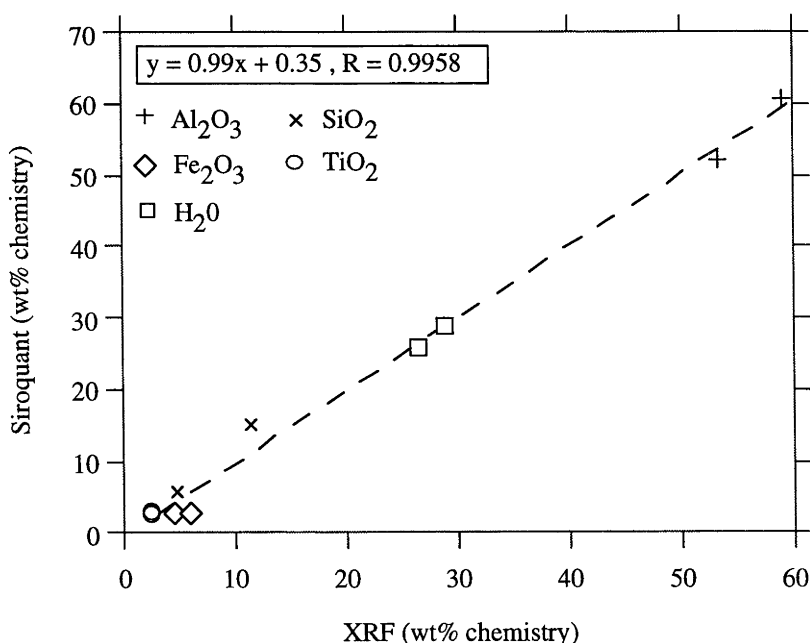


Figure 6.3

Correlation between the chemistry of bauxite analysed by XRF and that determined by *Siroquant*, when poorly-diffracting material is absent.

6.1.1 Creation and loading of a task file

An integral part of the *Siroquant* system is the concept of a hkl-file. Contained within a hkl-file, is data which enables the sub-program TRACSCAL, to calculate an XRD pattern for a particular mineral. Data contained within a hkl-file includes values for the intensity ($F_c(\text{hkl})$), multiplicity (M), d-spacing and orientation α -angle for each hkl powder diffraction line. A task file is created which consists of a collection of hkl-files of minerals to be quantified in the observed XRD pattern.

6.1.2 Background subtraction

After loading an observed XRD pattern into *Siroquant*, removal of the background is required before applying the quantification process. The background of an XRD pattern is composed of the low-angle scattering curve, ambient radiation and scattering bands associated with amorphous and poorly-diffracting material (Figure 6.4). Low-angle scattering is represented by an intensity curve which asymptotically approaches the ambient radiation level, as the 2θ -angle becomes larger. The presence of amorphous or poorly-diffracting material has the effect of introducing scattering bands into the XRD pattern. When quantification of such material is required, it is advisable to subtract the scattering bands during the background removal procedure, otherwise the quantity of well-crystallised material may be over-calculated. An apparent increase in the background level may be caused by peak overlap. In such cases, care must be exercised to ensure that not too much background is removed, otherwise phases associated with the peak overlap may be under-calculated.

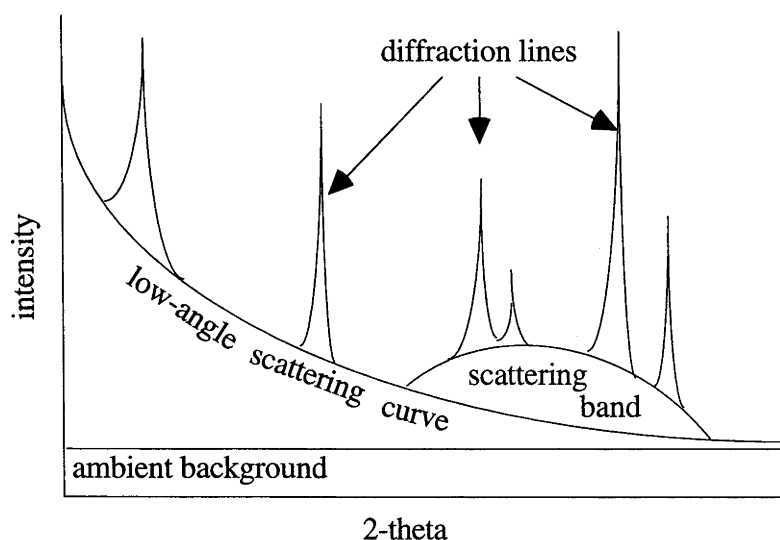


Figure 6.4

6.2 Experimental

6.2.1 Standards

Gibbsite ($\text{Al}(\text{OH})_3$) and boehmite ($\text{AlO}(\text{OH})$) are two minerals commonly found in bauxitic pisoliths. Synthetically prepared gibbsite and boehmite were combined in known quantities and analysed with *Siroquant* to gauge the program's accuracy (Figure 6.5).

The gibbsite that was used is commercially made by the alumina company, Showa Denko and is sold under the name *Higilite*. The grade H-43, has a mean particle size of $0.6 \mu\text{m}$ and a purity of 99.5 % (Figure 6.6). Boehmite was obtained by dehydrating gibbsite, hydrothermally:

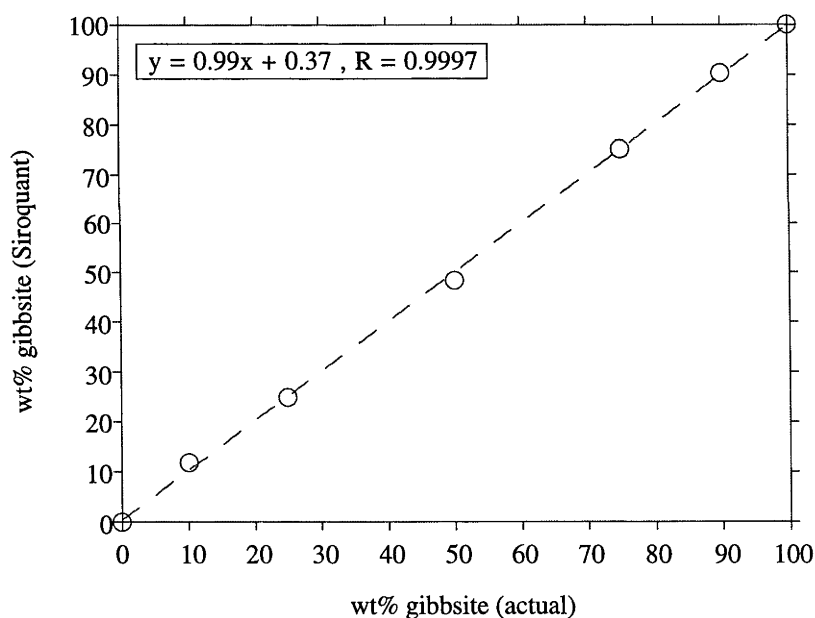
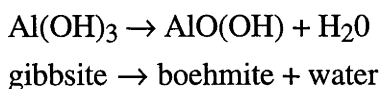


Figure 6.5

Correlation between the actual weight percent of gibbsite in a gibbsite-boehmite mixture and that determined by *Siroquant*.

One gram of *Higilite* and 1.4 ml of water were added to a 20 cm^3 Teflon™ autoclave liner. The liner was sealed within a steel casing and placed in an oven at $200 \text{ }^\circ\text{C}$. After 7 days the contents were removed and dried in an oven at $40 \text{ }^\circ\text{C}$. X-ray diffractometry and scanning electron microscopy (Figure 6.7 and 6.8) were undertaken on the resultant boehmite to ascertain its purity and crystallinity.

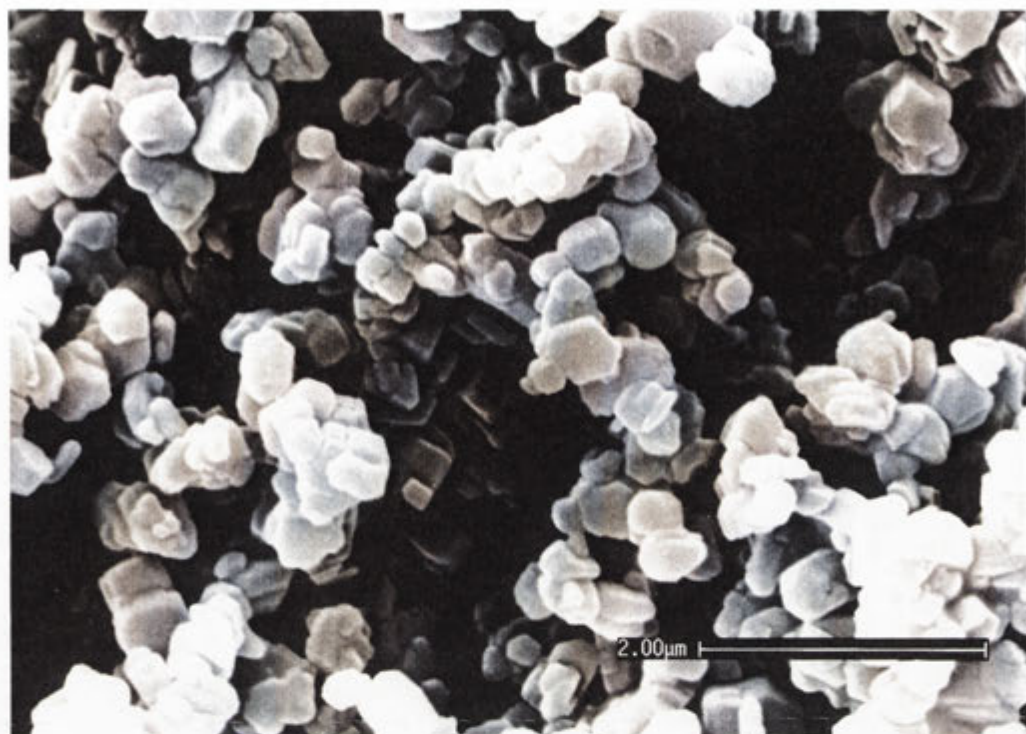


Figure 6.6

An SEM image of *Higilite* ; the gibbsite that was used as a standard and for the synthesis of boehmite.

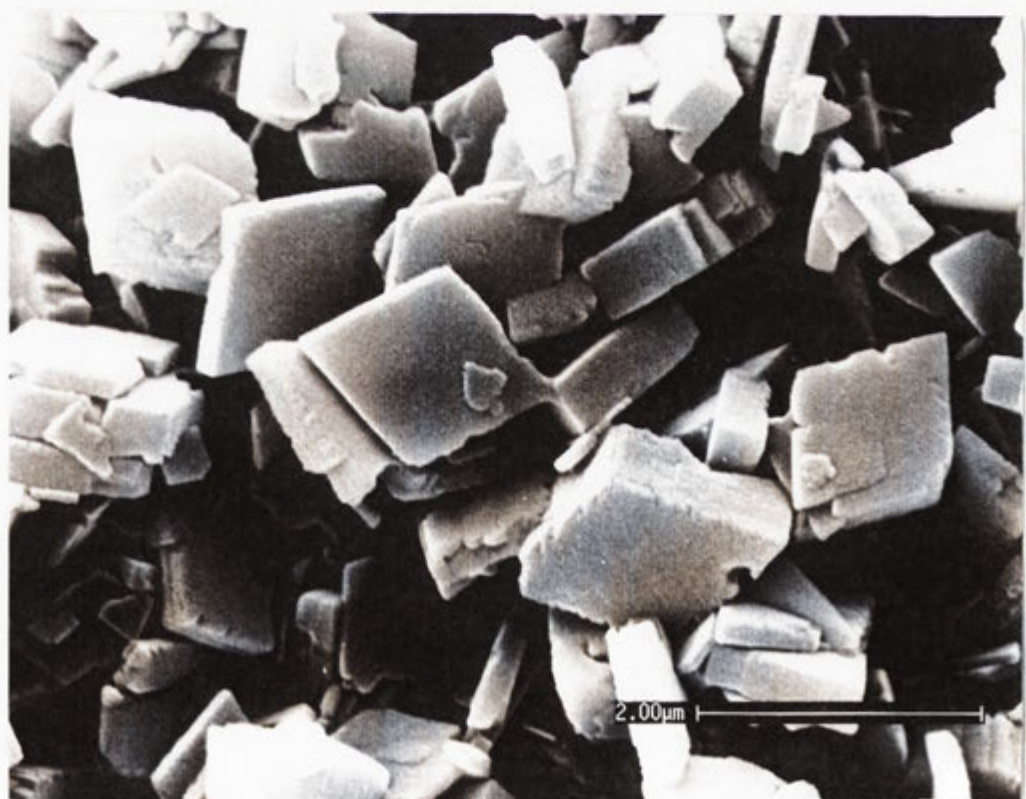
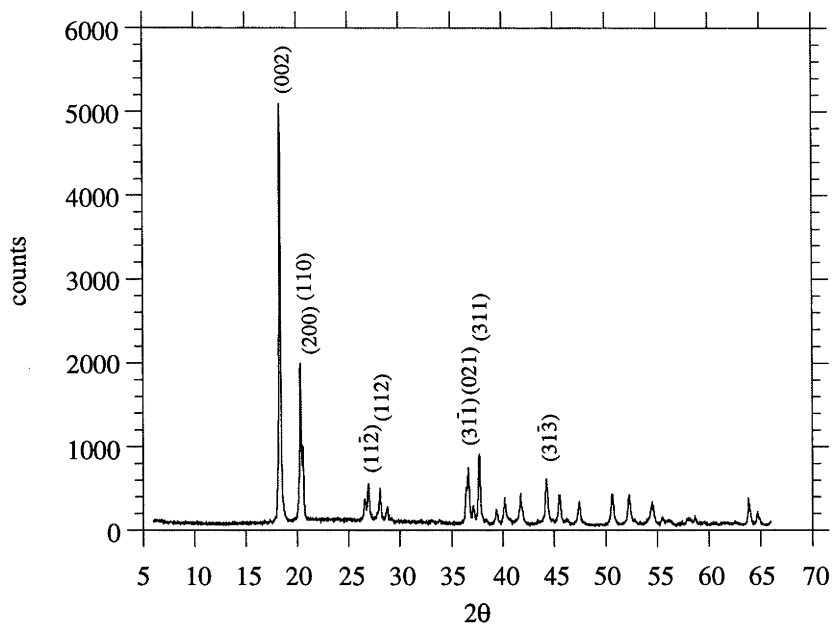


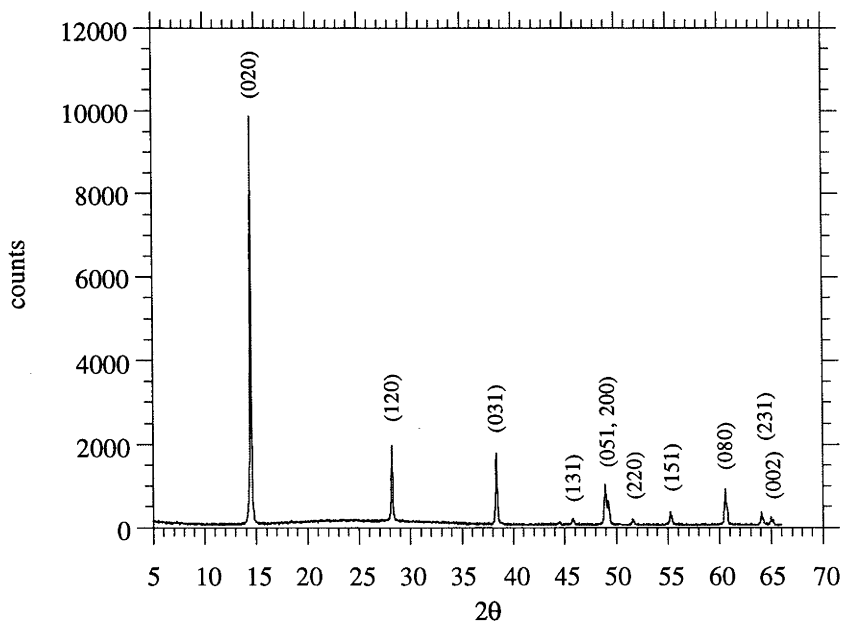
Figure 6.7

An SEM image of synthetic boehmite formed by dehydrating *Higilite* , hydrothermally.

X-ray diffractogram of Higilite (synthetic gibbsite)



X-ray diffractogram of synthetic boehmite

**Figure 6.8**

X-ray diffractograms of synthetic gibbsite and boehmite.

For clarity, only some peaks have been indexed in the gibbsite pattern.

To ascertain the accuracy of *Siroquant* in determining the poorly-diffracting material content of a given sample, varying quantities of ground glass and crystalline quartz were mixed together with a zinc oxide internal standard (see Table 6.1).

Table 6.1

Quartz (g)	Glass (g)	ZnO (g)	PDM content		actual wt% - calc. wt%
			actual wt%	calc. wt%	
0.10	0.00	0.10	0.00	0.40	-0.40
0.09	0.01	0.10	10.0	0.00	10.0
0.08	0.02	0.10	20.0	15.6	4.4
0.07	0.03	0.10	30.0	25.0	5.0
0.06	0.04	0.10	40.0	36.3	3.7
0.05	0.05	0.10	50.0	49.3	0.7
0.04	0.06	0.10	60.0	55.8	4.2
0.03	0.07	0.10	70.0	67.1	2.9
0.02	0.08	0.10	80.0	84.3	-4.3
0.01	0.09	0.10	90.0	86.6	3.4
0.00	0.10	0.10	100.0	99.8	0.2

A linear regression was performed on the data set, with the resultant graph (Figure 6.9) showing a reasonably good correlation. The results of the experiment revealed that ~90% of the *Siroquant* determined values fell within ± 5 wt.% of the actual PDM values. One of the test results (~10% of the data set) failed to detect 10 weight % PDM.

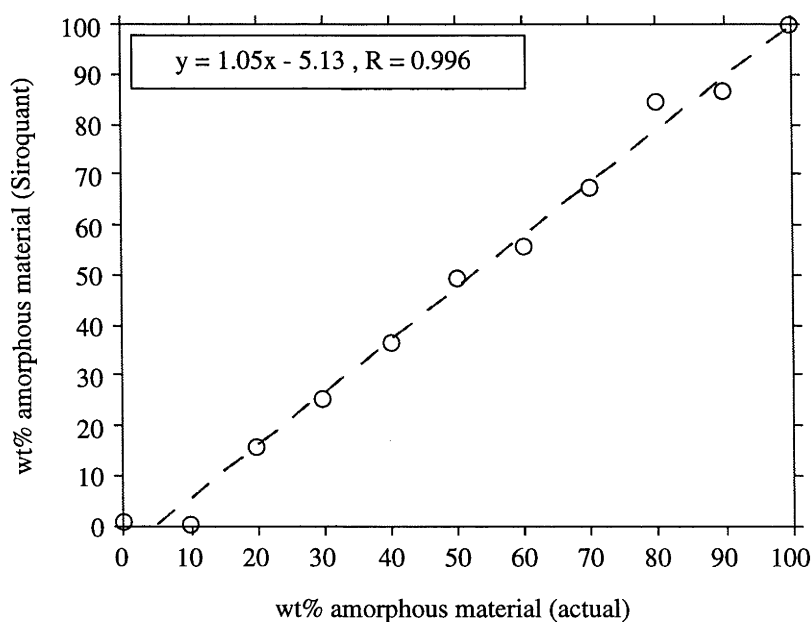


Figure 6.9

Correlation between the actual wt.% of glass and that determined by *Siroquant*.

6.2.2 Bulk analysis

The bulk mineralogical analysis of bauxite was performed to ascertain the distribution of minerals within the bauxite profile. Four sites were chosen, two from Weipa and two from Andoom. Fifteen pisoliths were selected randomly from each depth interval. Using a mortar and pestle they were ground and homogenised to a fine powder. A sub-sample was taken, to which a quantity of zinc oxide (usually 50 weight %) was added as an internal standard, for the quantification of poorly-diffracting material. The rest of the powder was packed against a ground glass tile in an aluminium holder for the determination of the crystalline phases. The mineralogy of both the sample containing the internal standard and the one without were determined, after which the results were combined and normalised. The mineralogy of the bauxite was expressed in terms of the weight % of individual crystalline phases plus the weight % of poorly-diffracting material. Graphs were constructed depicting the variation of mineralogy down the bauxite profile.

6.2.3 Analysis of individual pisoliths

The mineralogical analysis of 42 individual pisoliths was undertaken to ascertain the range and mean of pisolith mineralogy and to study the relationships that may exist between the different mineral species. From the Andoom collection, 21 pisoliths were randomly selected and another 21 were obtained from the Weipa collection. The pisoliths were ground to a fine powder in a mortar and pestle. To a portion of each pisolith sample, was added 33.3 weight % ZnO. The XRD patterns were analysed with *Siroquant* to determine their mineral and poorly-diffracting material contents.

6.2.4 Micro-sampling

Bauxitic pisoliths were mounted in resin and subsequently ground and polished to expose their inner structure. Three or four different zones were identified in each bauxitic pisolith with the aid of a binocular microscope. The boundaries of the zones were chosen on the basis of any obvious textural or colour changes. Following this, each zone was carefully separated using a dental drill. To facilitate the quantification of any poorly-diffracting phases, 33.3 % ZnO was added to each sample. As the samples were small, to obtain a diffractogram without the scattering bands associated with glass tiles, it was necessary to use a pure quartz crystal low background holder, which had been cut at such an angle as not to Bragg diffract X-rays. Quantitative analysis using *Siroquant* was performed on the resulting patterns. The results were later compiled into diagrams, showing the distribution of minerals across the selected pisoliths.

6.3 Results

6.3.1 Distribution of minerals within the bauxite profile

Several trends emerge when examining the mineralogical data of the four different bauxite horizons (Figures 6.10, 6.11, 6.12 & 6.13). The Weipa profiles (WB754EH and WB837EH) clearly display higher quartz contents than do the Andoom profiles (TR221AB and TR067AB), with the greatest concentration of quartz occurring at the top.

There is an overall tendency for boehmite to be concentrated at the top of the bauxite horizon. However, profile WB837EH has its boehmite-rich zone at a slightly deeper level of 1.4 metres.

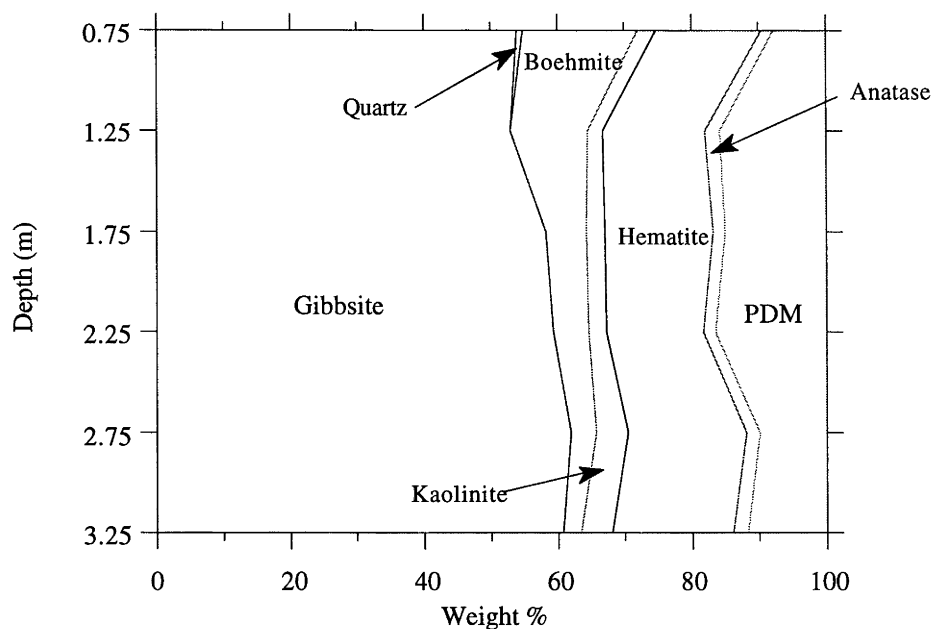
Apart from profile WB754EH, kaolinite content generally increases with increasing depth. No particular trend for kaolinite is observed in profile WB754EH.

In both Weipa profiles, hematite content decreases with increasing depth, while the Andoom profiles display no particular trends. Hematite is more abundant in the Andoom profiles than in the Weipa ones.

The gibbsite content of the four profiles show no distinct trends apart from the very top of the bauxite profiles generally having the lowest gibbsite concentrations. The bottom part of profile TR067AB includes the nodular ferruginous kaolinite layer and as such the gibbsite content is very low at this level. This profile also shows the abundance of kaolinite, hematite, goethite and poorly-diffracting material (PDM) within the top part of the nodular ferruginous kaolinite layer.

No consistent trends are apparent for the distribution of poorly-diffracting material within the four profiles. Anatase appears to be uniformly distributed throughout the individual bauxite profiles.

Mineral distribution within the bauxite horizon, TR221AB



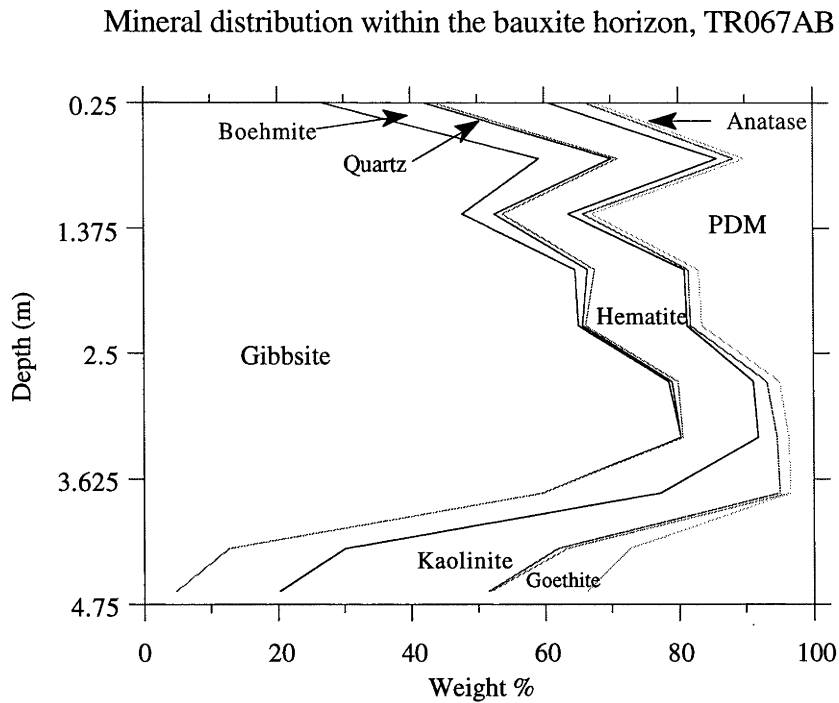
Bauxite bulk chemistry and mineralogy (wt%)

	Al ₂ O ₃	SiO ₂	Fe ₂ O ₃	TiO ₂	LOI	gibb	qtz	boeh	kao	hem	ana	PDM
A1	49.07	3.33	22.96	2.10	22.64	54.0	0.9	17.2	2.6	15.8	1.8	7.8
A2	48.06	3.18	23.17	2.25	23.40	53.0	0.0	11.5	2.3	15.2	2.2	15.9
A3	47.10	3.95	22.84	2.26	23.63	58.3	0.0	6.0	2.8	16.1	1.8	15.0
A4	48.05	3.52	20.83	2.46	24.86	59.3	0.0	5.3	2.7	14.4	1.8	16.5
A5	44.62	3.52	20.83	2.46	24.86	61.9	0.0	3.8	4.8	17.6	2.0	10.0
A6	45.18	4.73	23.69	2.39	23.75	60.7	0.0	2.7	4.7	18.0	2.2	11.6

XRF: Comalco Mineral Products, Weipa XRD: Geology Department, ANU

Figure 6.10

The distribution of minerals within the Andoom bauxite profile, TR221AB.



Bauxite bulk chemistry and mineralogy (wt%)

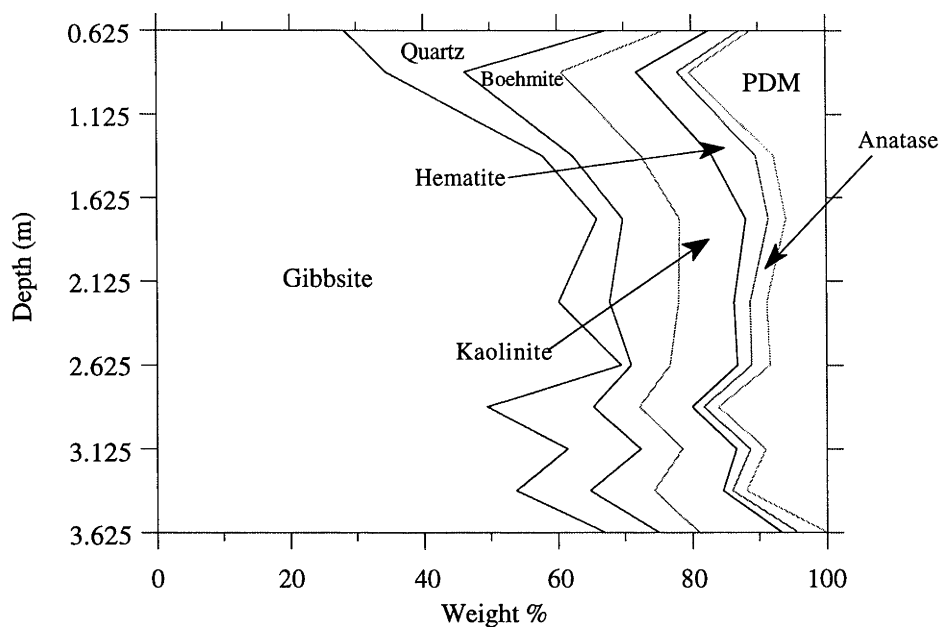
	Al ₂ O ₃	SiO ₂	Fe ₂ O ₃	TiO ₂	LOI	gibb	qtz	boeh	kao	hem	ana	PDM
A41	44.35	5.21	31.26	2.22	17.15	24.2	1.5	14.8	3.9	15.4	1.2	38.9
A42	48.05	3.42	22.22	2.30	24.11	59.2	1.0	10.8	2.5	14.8	1.6	10.1
A43	48.77	4.04	21.48	2.33	23.51	47.8	1.2	4.8	2.2	9.90	1.3	32.9
A44	47.52	2.94	22.07	2.39	25.09	64.6	1.1	1.9	0.6	13.4	1.5	17.0
A45	46.83	3.83	22.54	2.43	24.38	63.1	0.5	0.6	0.5	15.2	1.7	16.5
A46	48.47	4.47	19.14	2.52	25.34	78.6	0.9	0.5	2.0	11.2	1.8	5.0
A47	48.53	3.72	18.39	2.42	27.09	80.3	0.3	0.0	2.8	11.3	1.6	3.7
A48	42.30	11.03	22.85	1.90	22.12	59.7	0.0	0.0	17.8	17.5	1.6	3.4
A49	23.19	19.74	43.90	1.16	12.19	12.6	0.0	0.0	31.8	17.5	1.4	27.3
A50	20.45	18.91	48.38	0.98	10.82	4.8	0.0	0.0	31.2	15.5	0.3	33.7
						(+ 9.4 % goethite)						
						(+ 14.5 % goethite)						

XRF: Comalco Mineral Products, Weipa XRD: Geology Department, ANU

Figure 6.11

The distribution of minerals within the Andoom bauxite profile, TR067AB.

Mineral distribution within the bauxite horizon, WB754EH



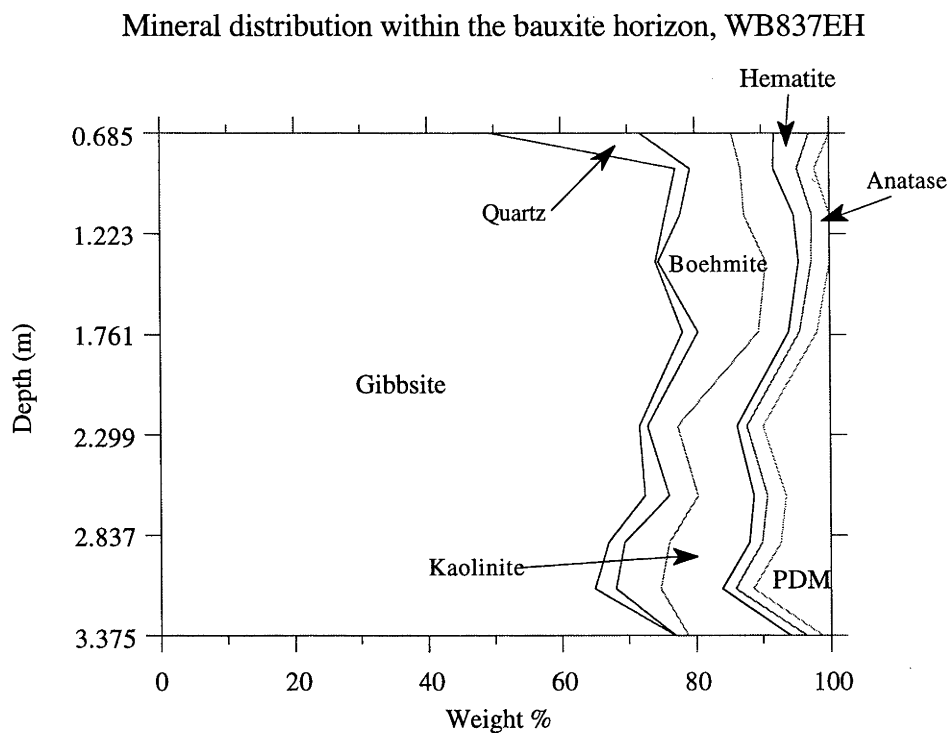
Bauxite bulk chemistry and mineralogy (wt%)

	Al ₂ O ₃	SiO ₂	Fe ₂ O ₃	TiO ₂	LOI	gibb	qtz	boeh	kao	hem	ana	PDM
W59	45.61	21.46	11.52	1.89	19.34	28.2	39.1	8.6	6.7	4.6	1.7	11.1
W60	49.14	15.57	13.18	2.08	19.86	34.5	11.7	14.4	11.3	6.0	1.8	20.2
W61	51.49	11.34	11.56	2.04	23.43	57.9	4.4	10.3	10.5	6.5	2.7	7.7
W62	55.64	9.13	6.74	2.38	25.89	65.9	3.9	8.4	9.9	3.4	2.6	6.0
W63	57.69	8.08	5.51	2.58	25.99	60.1	7.7	10.2	8.3	2.4	2.5	9.0
W64	58.16	7.87	5.65	2.58	25.91	69.5	1.5	5.7	10.1	2.1	2.8	8.5
W65	56.58	11.04	4.70	2.45	25.14	49.5	15.8	6.9	7.8	1.7	2.2	16.2
W66	57.13	8.66	5.12	2.55	26.43	61.4	11.0	6.1	8.1	2.1	2.3	9.0
W67	57.55	10.40	4.40	2.49	25.06	53.8	11.0	9.5	10.3	1.4	2.1	11.7
W68	54.20	11.42	6.71	2.44	24.98	64.7	9.6	5.7	11.9	2.6	2.9	2.6

XRF: Comalco Mineral Products, Weipa XRD: Geology Department, ANU

Figure 6.12

The distribution of minerals within the Weipa bauxite profile, WB754EH.



Bauxite bulk chemistry and mineralogy (wt%)

	Al ₂ O ₃	SiO ₂	Fe ₂ O ₃	TiO ₂	LOI	gibb	qtz	boeh	kao	hem	ana	PDM
W1	48.78	16.67	10.05	2.17	22.10	49.4	22.5	13.6	6.4	5.1	3.1	0.0
W2	56.54	6.06	7.57	2.39	27.47	77.1	2.2	7.6	4.9	3.4	2.6	2.2
W3	59.96	4.85	5.03	2.40	27.63	75.7	2.1	9.6	7.3	2.7	2.6	0.0
W4	61.59	4.42	4.83	2.47	26.64	74.2	0.4	16.0	4.8	1.9	2.7	0.0
W5	59.06	5.24	4.51	2.55	28.66	78.1	2.3	9.1	4.5	1.5	2.6	1.9
W6	58.01	6.46	3.65	2.37	29.60	71.7	1.2	4.5	8.8	1.5	2.4	9.8
W7	58.79	7.31	4.62	2.49	26.86	72.5	3.6	4.2	8.4	2.0	2.8	6.5
W8	59.01	8.10	4.28	2.49	25.93	67.0	2.4	6.6	12.0	1.9	2.8	7.3
W9	59.93	7.38	4.24	2.47	25.88	64.9	3.2	6.7	9.1	2.0	2.7	11.3
W10	55.04	7.25	7.58	2.21	27.92	76.9	0.0	1.9	15.3	2.3	2.4	1.2

XRF: Comalco Mineral Products, Weipa

XRD: Geology Department, ANU

Figure 6.13

The distribution of minerals within the Weipa bauxite profile, WB837EH.

6.3.2 Mineralogical composition of bauxitic pisoliths

The results from the mineralogical analysis of 42 individual pisoliths, selected randomly from the Andoom and Weipa collections, is presented in Table 6.2. Figures 6.14 and 6.15 display the average pisolith mineralogical composition for each locality, while the accompanying tables outline the range, mean weight % and standard deviation of minerals present in the pisoliths.

Some noticeable differences occur between the pisoliths of Andoom and those of Weipa. Andoom pisoliths generally contain more hematite and boehmite, whereas pisoliths from Weipa are typically more kaolinite and quartz-rich. The poorly-diffracting material, gibbsite and anatase contents of Weipa pisoliths are similar to those of Andoom pisoliths.

The strong negative correlation between the poorly-diffracting material and gibbsite+boehmite content of pisoliths (Figure 6.16) is due largely to a mathematical artefact where (for the well-crystallised components);

$$\begin{aligned} \text{gibbsite+boehmite} &= 100 - (\text{hematite+kaolinite+quartz+anatase}) \\ &\approx \text{constant.} \end{aligned}$$

Plotted on the same graph are examples of bauxitic oolites (micro-bauxite) from WB772EH and ferruginous-kaolinite nodules from the base of AB003BF, TR067AB and AB012BF. The oolites and in particular the nodules, do not lie on the same trend line as do the pisoliths because of their high kaolinite contents.

The graph depicting the anatase vs gibbsite+boehmite content of pisoliths, shows a positive correlation ($r = 0.45$).

A relationship exists between the quartz and hematite content of pisoliths. The concentration of hematite is at its greatest, when the concentration of quartz is at its lowest. At hematite concentrations of less than 8 wt.%, the quartz content varies between 0 and 6 wt.%, while above 8 wt.% the quartz content only fluctuates between 0 and 0.5 wt.%. A partial separation of the Andoom data from the Weipa data occurs in this graph.

In the quartz vs boehmite graph, boehmite content is at its greatest (i.e. >25 wt.%) when the quartz content is below 0.5 wt.% (Figure 6.17). No clear relationships occur in the quartz vs PDM and the quartz vs gibbsite graphs.

Table 6.2

Weipa pisoliths

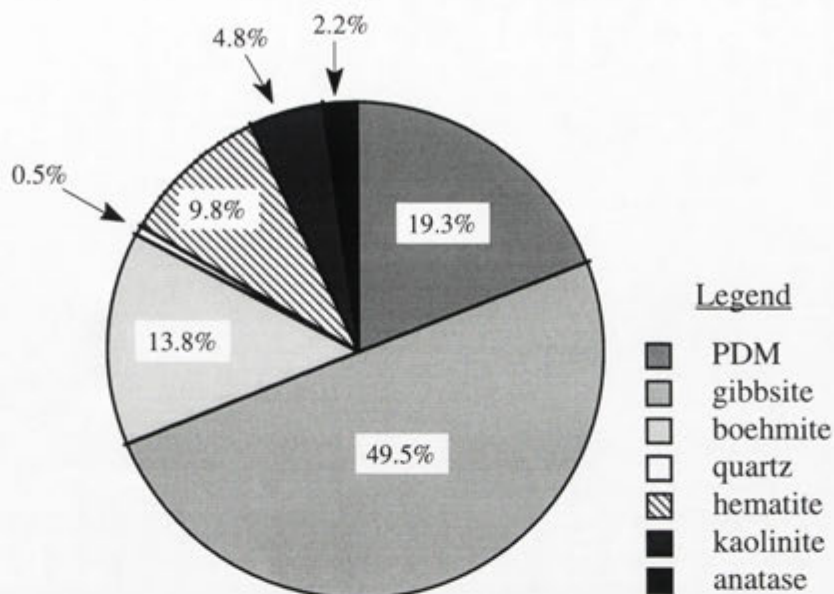
	PDM	gibb	boeh	qtz	hem	kao	ana (wt%)	comments
W3	18.46	49.63	17.53	1.60	1.66	8.94	2.17	
W6	18.71	60.13	8.55	3.56	0.85	5.83	2.37	
W10	37.30	49.20	0.00	0.39	4.72	7.07	1.32	
W11	26.35	32.15	21.61	1.43	6.78	9.78	1.89	
W15	37.37	40.72	6.53	0.93	3.06	9.40	1.99	
W19	25.48	56.30	2.33	0.97	1.89	11.05	1.97	
W20	45.49	11.12	27.08	0.28	6.51	7.76	1.77	
W24	0.00	81.90	1.90	5.10	2.20	6.50	2.50	
W28	0.00	87.33	1.64	0.00	4.02	4.02	2.98	
W32	4.56	43.35	2.27	8.98	6.59	32.26	1.99	oolith (microbauxite)
W34	22.66	22.32	27.72	0.21	4.21	20.98	1.91	oolith (microbauxite)
W38	15.24	40.33	4.73	1.72	4.99	30.41	2.58	oolith (microbauxite)
W40	0.00	73.62	4.78	1.01	5.07	12.61	2.90	
W44	38.96	39.61	1.16	4.22	0.97	12.82	2.27	
W48	0.00	86.41	0.15	0.15	1.62	8.71	2.95	
W50	35.40	26.27	15.39	1.71	6.38	13.36	1.50	
W54	54.03	35.52	0.98	0.90	0.71	6.23	1.65	
W58	9.09	68.45	7.48	2.63	2.13	8.14	2.08	
W60	62.22	22.86	1.42	2.98	2.53	6.05	1.96	very high PDM content
W64	46.17	36.41	1.38	5.02	1.25	7.86	1.92	
W68	0.00	67.60	12.72	5.62	1.04	10.36	2.66	
W70	29.13	47.49	15.30	0.00	2.07	4.27	1.74	
W74	19.96	67.76	1.05	1.06	1.26	6.71	2.19	
W78	0.00	64.82	19.46	0.90	1.95	10.03	2.84	

Andoom pisoliths

	PDM	gibb	boeh	qtz	hem	kao	ana (wt%)	comments
A1	57.01	18.52	8.86	0.07	12.12	2.15	1.28	
A4	7.72	64.43	3.42	0.49	17.81	4.27	1.85	
A6	3.32	71.44	2.63	0.00	14.99	5.29	2.34	
A7	34.28	40.70	12.03	0.39	8.95	2.20	1.45	
A11	0.00	85.49	0.00	0.15	11.32	0.29	2.76	
A15	6.99	77.44	0.78	0.00	12.46	0.00	2.34	
A16	20.45	51.62	12.62	3.91	5.39	3.76	2.26	
A21	15.05	61.25	6.24	0.00	11.64	3.60	2.23	
A25	43.00	41.41	0.42	2.93	3.63	5.59	3.02	
A26	20.32	2.95	55.45	0.32	9.29	10.10	1.57	
A28	14.06	56.80	16.60	0.00	7.47	2.69	2.37	
A30	33.87	0.00	0.31	0.00	6.39	58.11	1.31	nodule ("ironstone")
A31	5.47	69.49	9.98	0.00	8.02	4.28	2.77	
A36	18.64	61.25	3.69	0.00	4.48	9.16	2.78	
A40	21.26	6.10	50.56	0.21	10.80	9.17	1.91	
A41	77.48	4.76	4.81	1.66	7.97	2.52	0.80	very high PDM content
A46	5.86	73.30	0.23	0.00	14.39	4.23	1.99	
A50	34.45	0.00	0.00	0.02	16.02	42.29	1.02	nodule (+ 6.20 % goethite)
A51	29.15	43.81	9.95	0.81	7.23	6.93	2.13	
A53	7.21	65.93	4.67	0.00	13.27	6.80	2.11	
A55	9.27	0.00	0.00	0.00	7.05	82.08	1.61	nodule ("ironstone")
A56	7.55	0.13	69.57	0.18	13.35	7.33	1.90	
A60	10.48	65.66	13.30	0.00	6.04	2.12	2.40	
A63	0.00	78.03	4.48	0.00	4.78	9.27	3.44	

(Mineralogical analyses by *Siroquant*)

Average mineralogical composition of 21 pisoliths from Andoom.

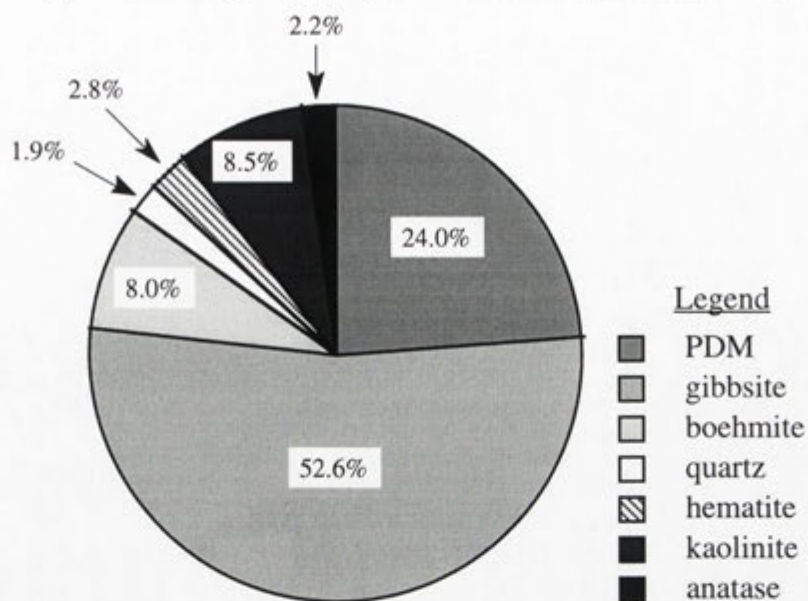


<u>mineral</u>	<u>min. (wt.%)</u>	<u>max. (wt.%)</u>	<u>mean (wt.%)</u>	<u>std. dev.</u>
gibbsite	0.1	85.5	49.5	27.4
boehmite	0.0	69.6	13.8	19.5
quartz	0.0	3.9	0.5	1.1
hematite	3.6	17.8	9.8	3.9
kaolinite	0.0	10.1	4.8	3.0
anatase	0.8	3.4	2.2	0.6
PDM	0.0	77.5	19.3	19.7

Figure 6.14

Pie diagram displaying the average mineralogical composition of pisoliths from Andoom. Mineralogical analyses of 21 pisoliths were performed using *Siroquant*.

Average mineralogical composition of 21 pisoliths from Weipa.



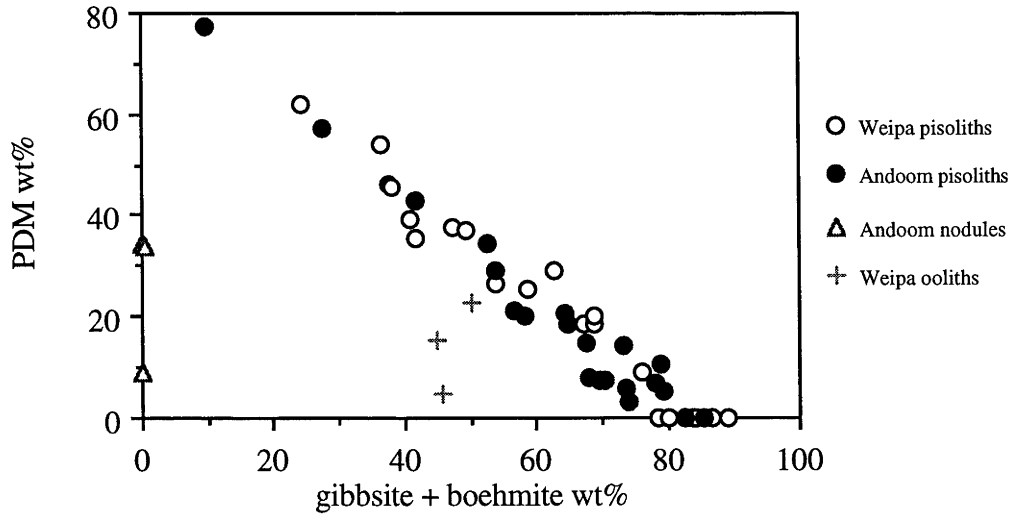
mineral	min. (wt.%)	max. (wt.%)	mean (wt.%)	std. dev.
gibbsite	11.1	87.3	52.6	21.5
boehmite	0.0	27.1	8.0	8.3
quartz	0.0	5.6	1.9	1.8
hematite	0.7	6.8	2.8	2.0
kaolinite	4.0	13.4	8.5	2.7
anatase	1.3	3.0	2.2	0.5
PDM	0.0	62.2	24.0	19.8

Figure 6.15

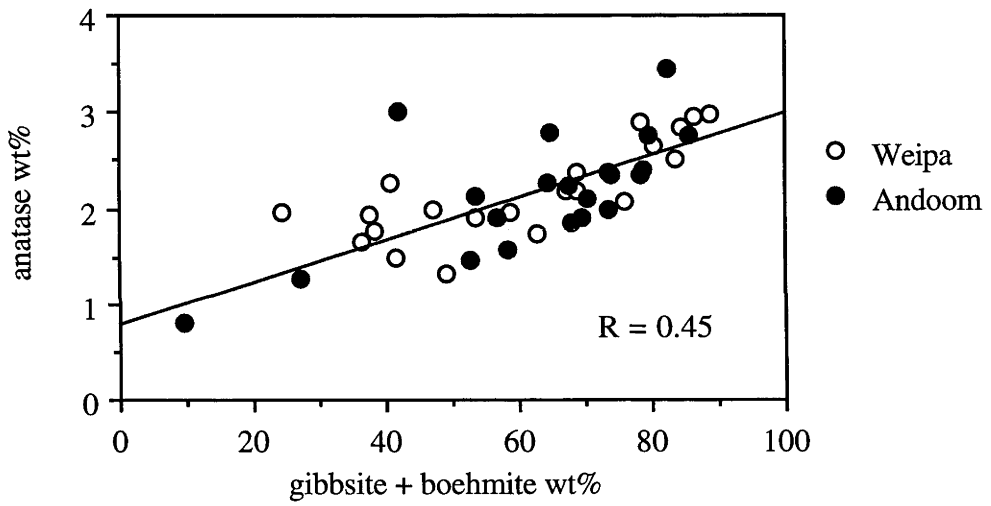
Pie diagram displaying the average mineralogical composition of pisoliths from Weipa.

Mineralogical analyses of 21 pisoliths were performed using *Siroquant*.

Relationship between gibbsite+boehmite and PDM in pisoliths, ooliths and nodules



Relationship between gibbsite+boehmite and anatase in pisoliths



Relationship between hematite and quartz in pisoliths

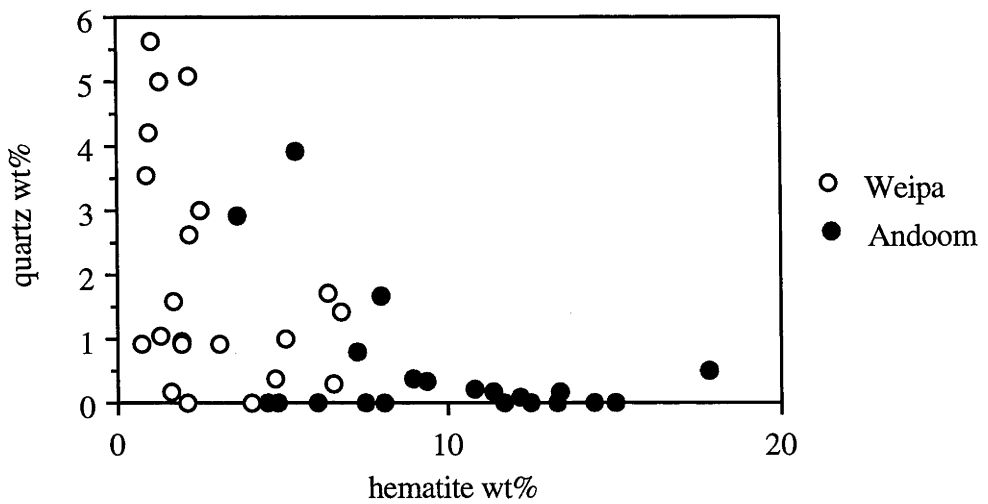


Figure 6.16

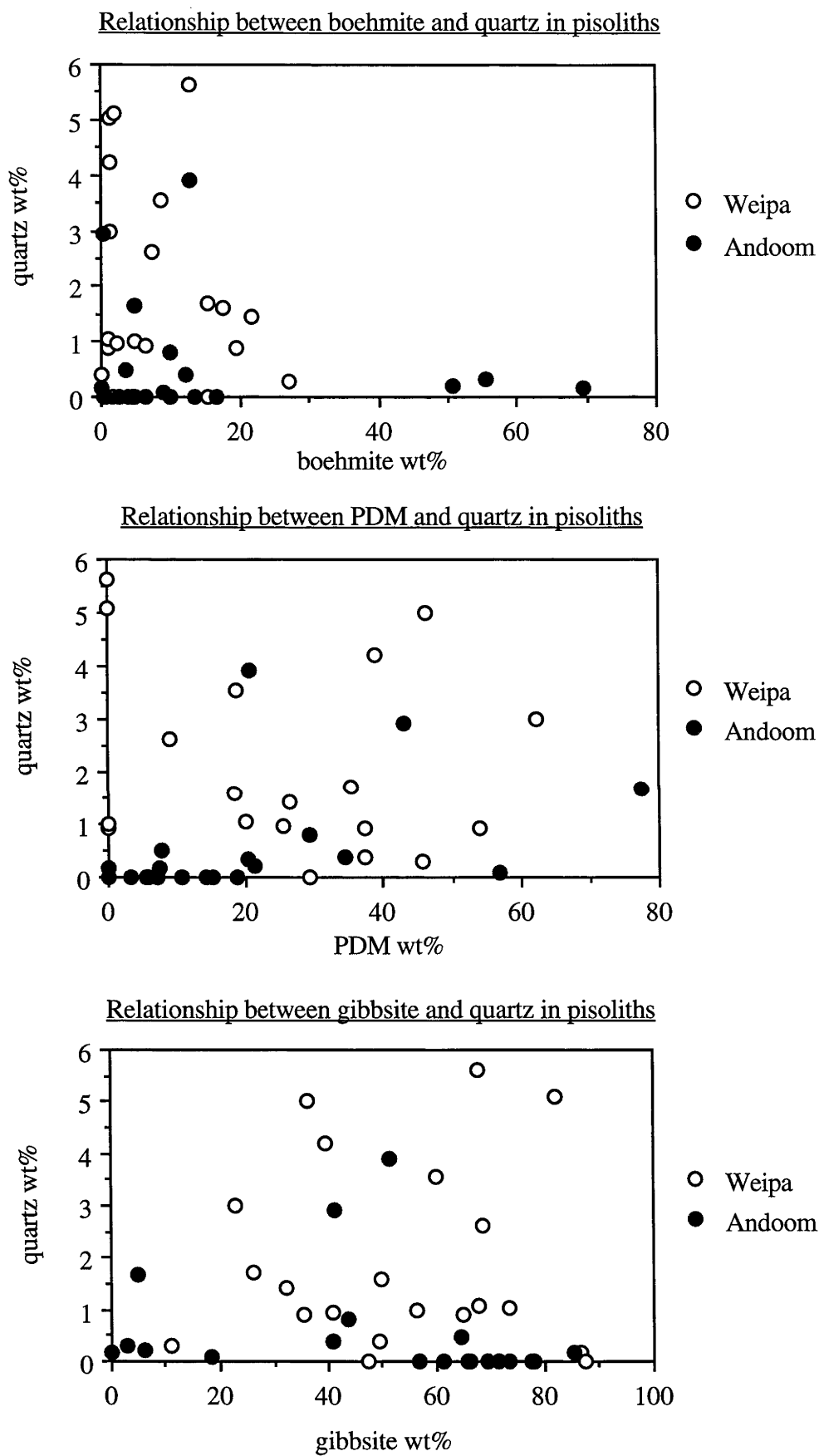


Figure 6.17

6.3.3 Distribution of minerals within bauxitic pisoliths

The microsampling and XRD analysis of discrete zones in bauxitic pisoliths demonstrated a radial variation in mineralogy (Table 6.3 & 6.4 and Figures 6.18, 6.19, 6.20 & 6.21).

Bauxitic pisoliths tend to have high amounts of poorly-diffracting material in their cores. In general, pisoliths containing the greatest amount of poorly-diffracting material, usually contain a quartz-rich core. If quartz is present within pisoliths, it is generally concentrated in the core.

Bauxitic pisoliths from the same drill hole and same interval in the profile exhibit similarities or trends in their mineralogy. Pisoliths from drill hole WB837EH (3 - 3.25 m) tend to have a hematitic band between the core and the rim. The kaolinite increases from a minimum in the core to a maximum in the outer rim. The boehmite content of the pisoliths is very low, however there is a tendency for the boehmite to be of a higher concentration in the rim. Hematite is virtually absent from the outer rim.

Pisoliths from drill hole WB857EH (1 - 1.25 m) tend to have a boehmitic and hematitic rim. As with the previous pisoliths, the kaolinite content tends to increase outwards from the core. The boehmite content of the inner and outer core tends to be very low.

In the profile WB781EH at a depth of 1-1.5 m, pisoliths tend to have a boehmitic core. No quartz is evident in the pisolith that was analysed, even though the core contained up to 40% poorly-diffracting material.

The mineralogical data obtained in the experiment (Table 6.3) was plotted to ascertain any relationships which may exist between the different mineral phases. A negative correlation exists between the poorly-diffracting material content of bauxite and the gibbsite+boehmite percentage (Figure 6.22). A scatter-plot of boehmite versus quartz content revealed that these two minerals tend not to co-exist (Figure 6.23). A similar plot between gibbsite and quartz showed that when quartz is present in amounts greater than 1.5 wt %, the gibbsite content of bauxite tends to be less than 25 wt % (Figure 6.24). An opposite relationship exists between the percentage of poorly-diffracting material and quartz content. Here, the poorly-diffracting material content appears to be at its highest, that is greater than 50 wt %, when the percentage of quartz is greater than 1.5 wt % (Figure 6.25). The above relationships are only obvious in the data set used because the pisoliths were separated into their mineralogical distinct zones before analysis. Other data sets usually do not show these trends as the sampling is too coarse, for example as in bulk mineralogical analyses.

Table 6.3 The mineralogy of different zones within bauxitic pisoliths.

	gib	qtz	boe	hem wt. %	kao	ana	PDM
W70-1 core	33.8	0.0	18.2	1.5	7.5	0.8	38.2
inner cortex	40.3	0.0	6.9	3.3	5.2	3.0	41.3
outer cortex	74.5	0.0	5.1	1.4	6.9	2.7	9.4
W15-1 core	5.6	21.9	0.3	0.8	1.7	0.7	69.0
cortex	31.1	1.2	0.1	2.3	3.5	2.0	59.8
W40-1 core	5.1	6.8	0.0	1.0	0.9	2.3	83.9
inner cortex	60.5	0.0	0.8	3.4	7.3	2.8	25.2
middle cortex	37.2	0.0	10.6	7.9	13.8	2.4	28.0
outer cortex	47.8	1.0	7.8	4.7	13.6	2.2	22.7
W40-2 core	55.0	1.3	0.0	1.3	0.6	2.3	39.4
inner cortex	57.0	0.0	1.1	3.9	7.9	3.5	26.6
outer cortex	40.2	0.0	16.0	4.9	16.4	2.5	20.1
W9-1 core	75.3	0.0	0.0	1.9	2.4	2.7	17.8
inner cortex	83.8	0.0	1.6	5.6	5.9	3.1	0.0
outer cortex	84.6	0.0	2.0	0.3	10.4	2.8	0.0
W9-2 core	21.6	20.4	0.0	0.0	2.0	1.4	54.7
inner cortex	27.5	1.2	0.0	5.2	6.3	1.9	57.9
outer cortex	64.2	0.0	0.0	0.0	25.6	3.2	6.9

Analyses were performed using *Siroquant*.

Table 6.4 The chemistry of different zones within bauxitic pisoliths.

	SiO ₂	TiO ₂	Al ₂ O ₃	Fe ₂ O ₃
	wt. %			
W70-1 core	6.89	1.52	59.58	2.63
inner cortex	5.00	2.78	55.26	4.84
outer cortex	3.25	2.25	51.91	3.26
W15-1 core	25.27	0.97	55.54	2.14
cortex	2.63	2.34	51.42	6.77
W40-1 core	13.52	2.69	51.03	2.64
inner cortex	5.51	2.15	48.99	7.09
middle cortex	10.20	1.40	40.90	14.88
outer cortex	16.91	1.57	37.04	5.59
W40-2 core	2.92	2.34	50.76	3.49
inner cortex	2.91	2.75	49.58	6.33
outer cortex	11.23	1.84	46.51	9.93

Analyses were performed using EDXA

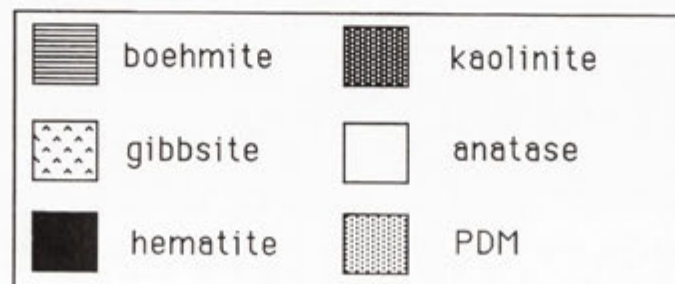
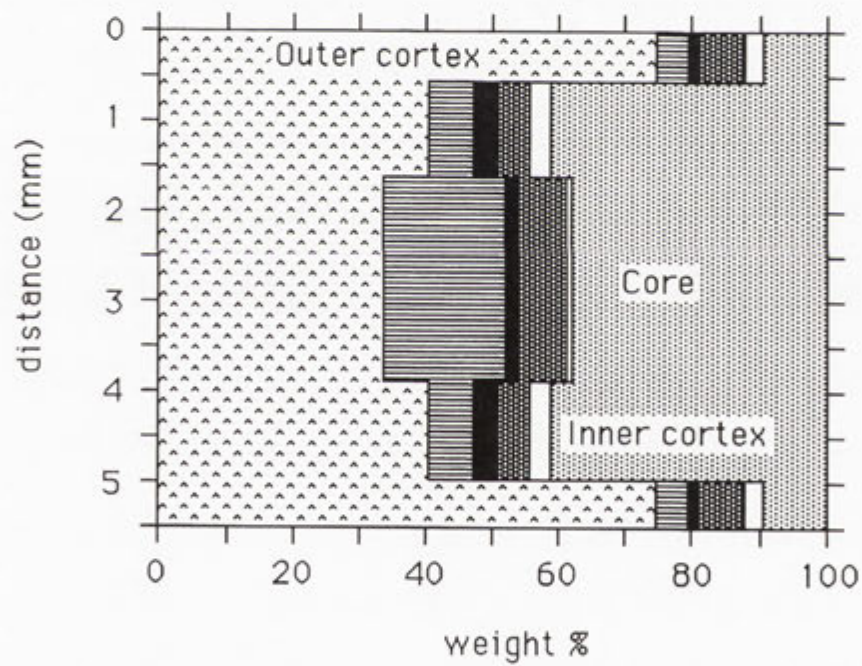
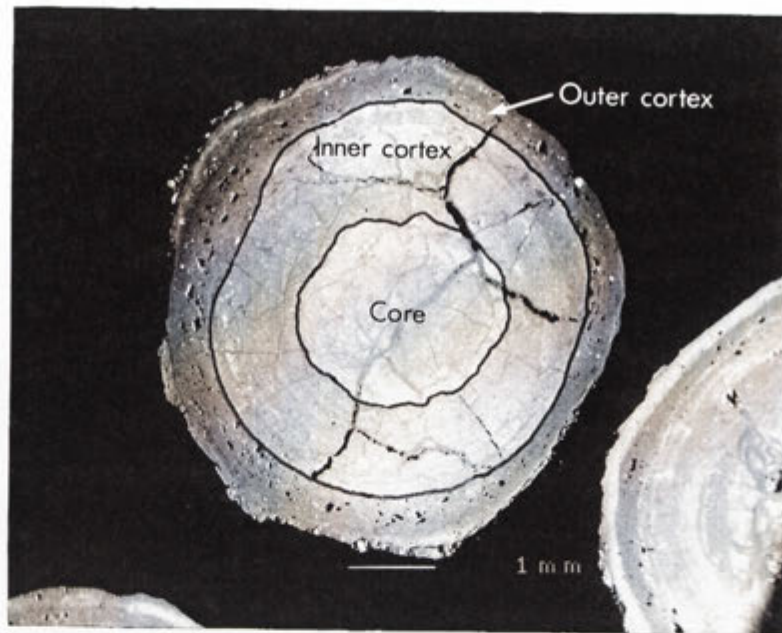


Figure 6.18

Mineralogical profile of a pisolith from drill hole WB781EH (1-1.5 m depth).

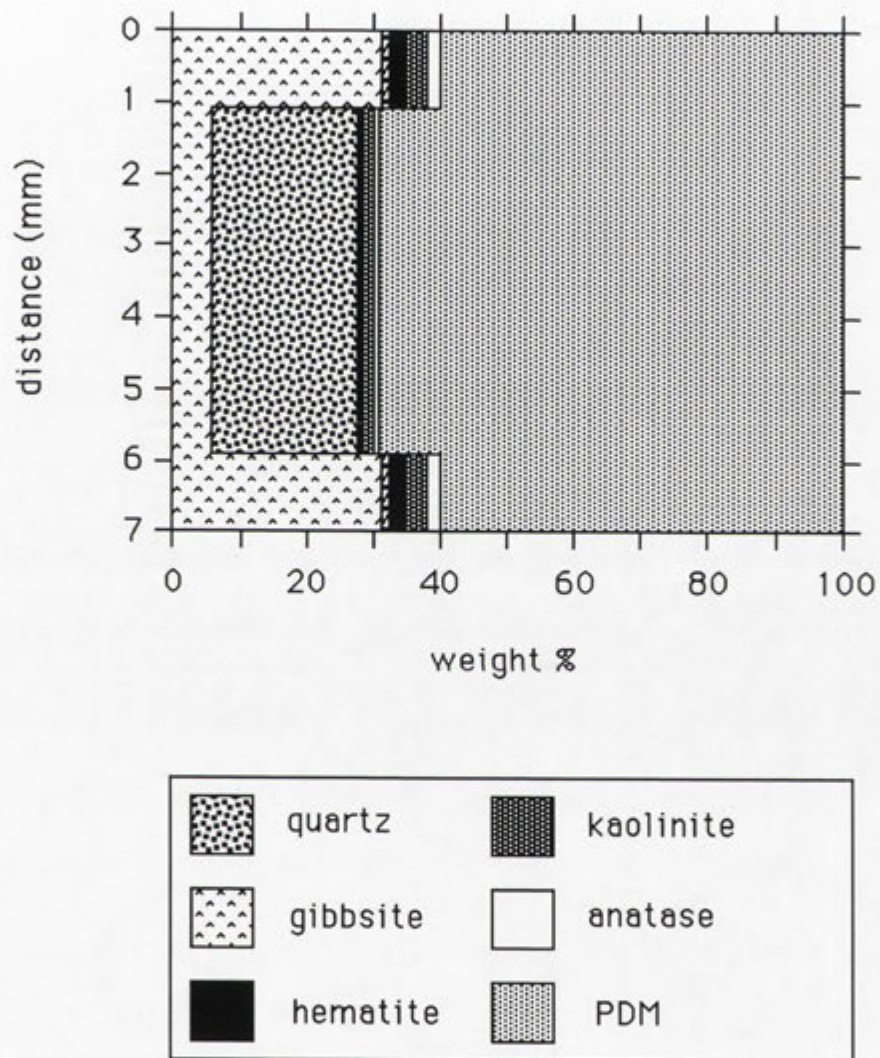


Figure 6.19

Mineralogical profile of a pisolith from drill hole WB823EH (2-2.25 m depth).

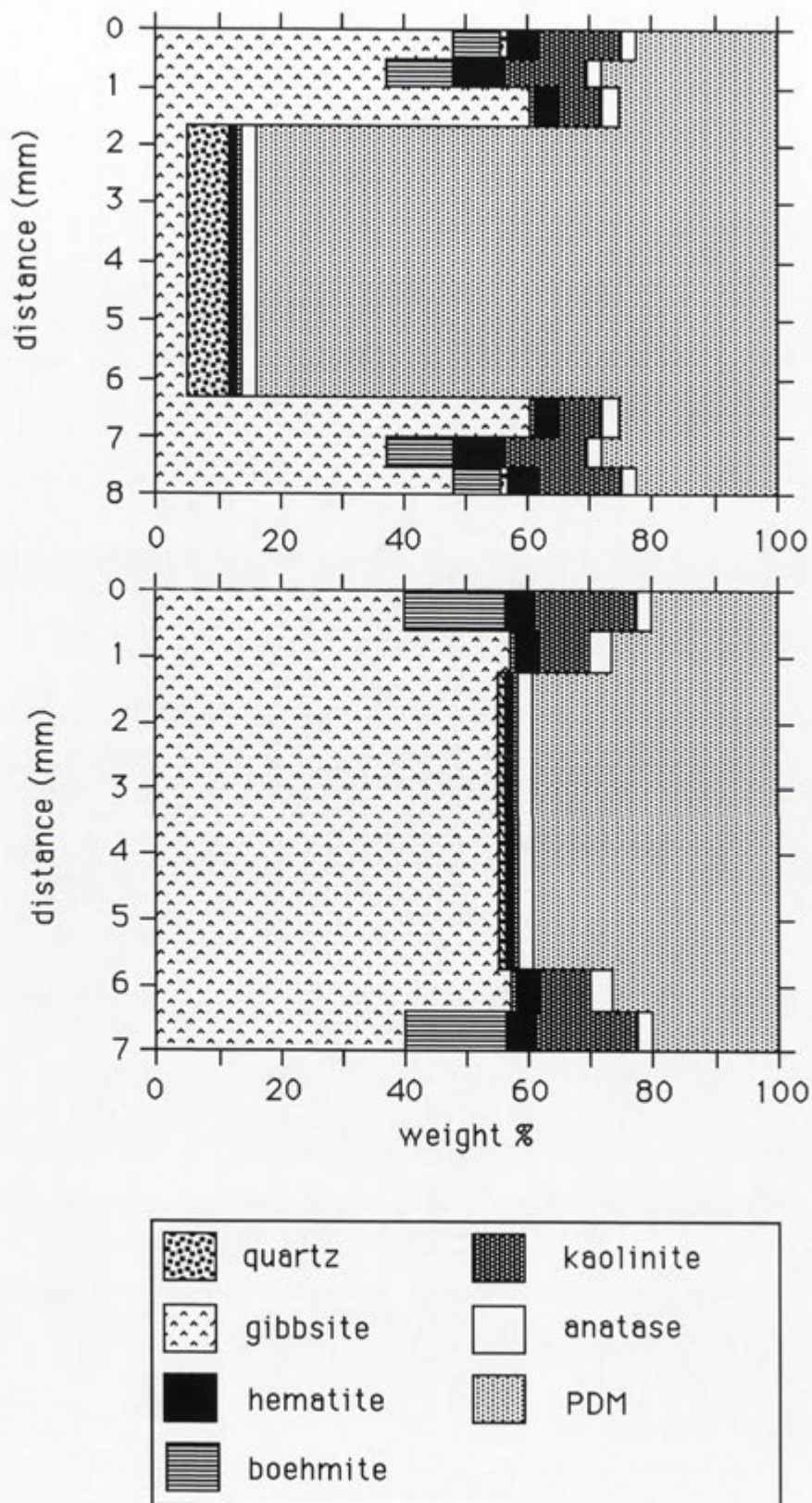


Figure 6.20

Mineralogical profiles of two pisoliths from drill hole WB857EH (1-1.25 m depth).

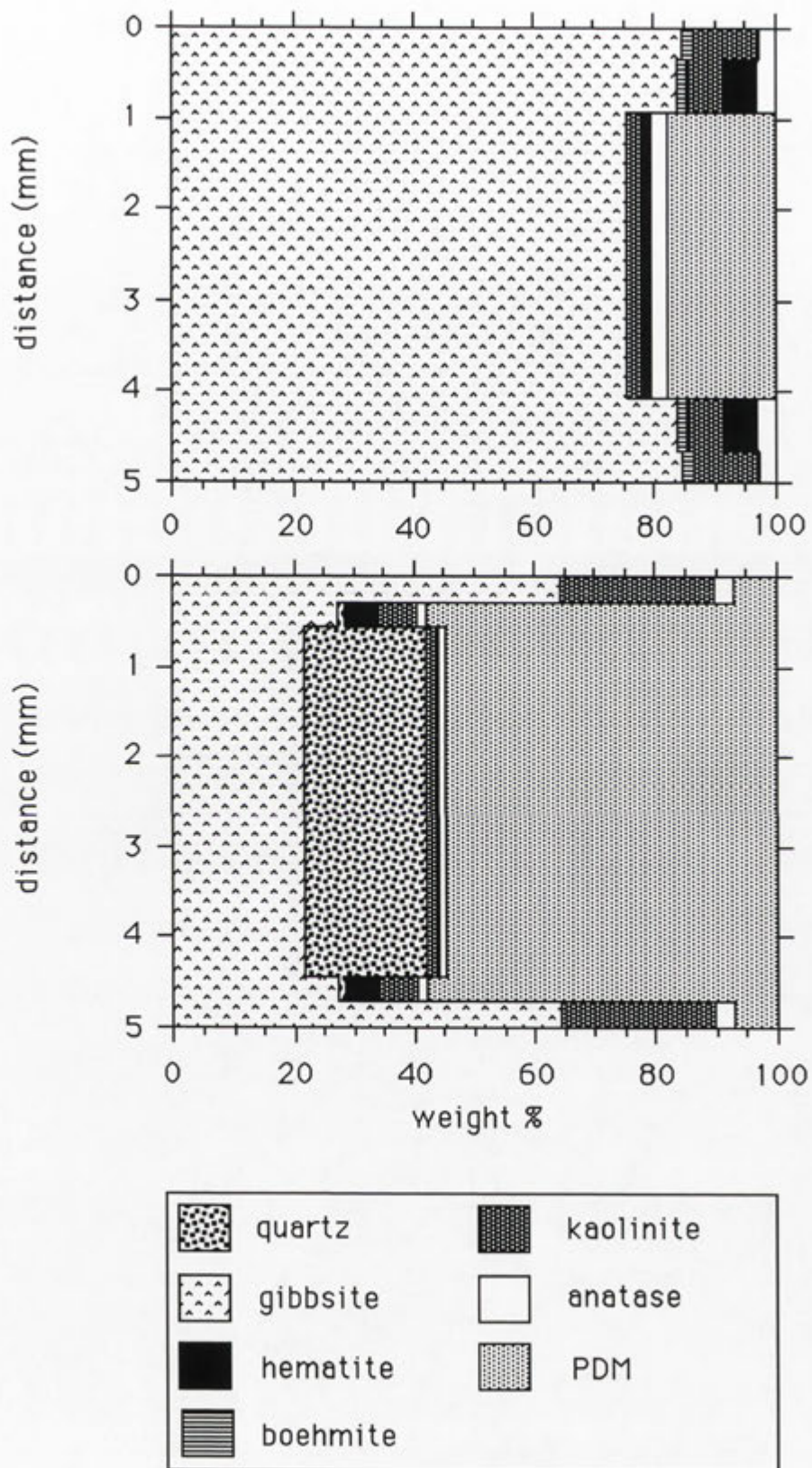


Figure 6.21

Mineralogical profiles of two pisoliths from drill hole WB837EH (3-3.25 m depth).

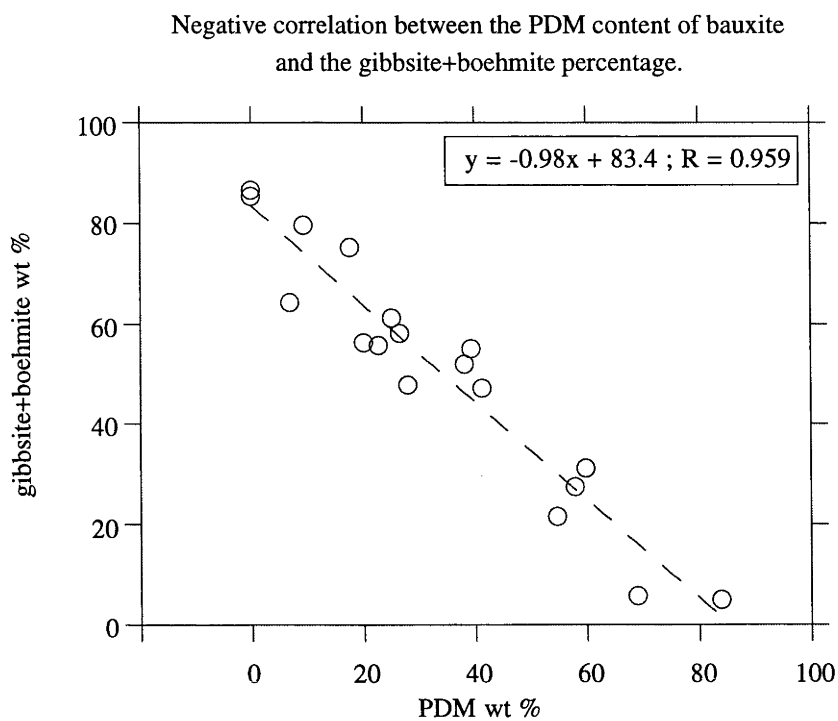


Figure 6.22

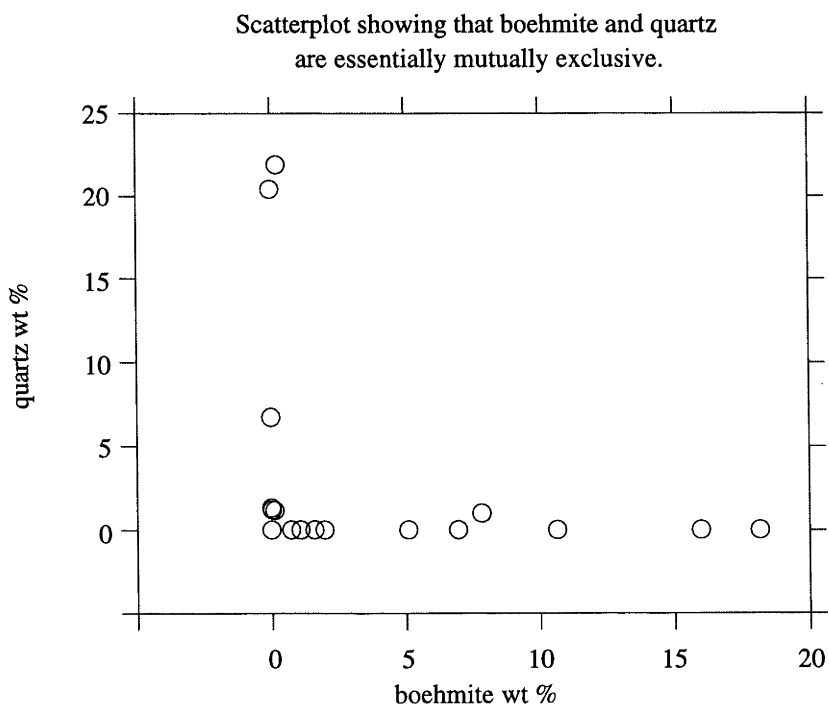


Figure 6.23

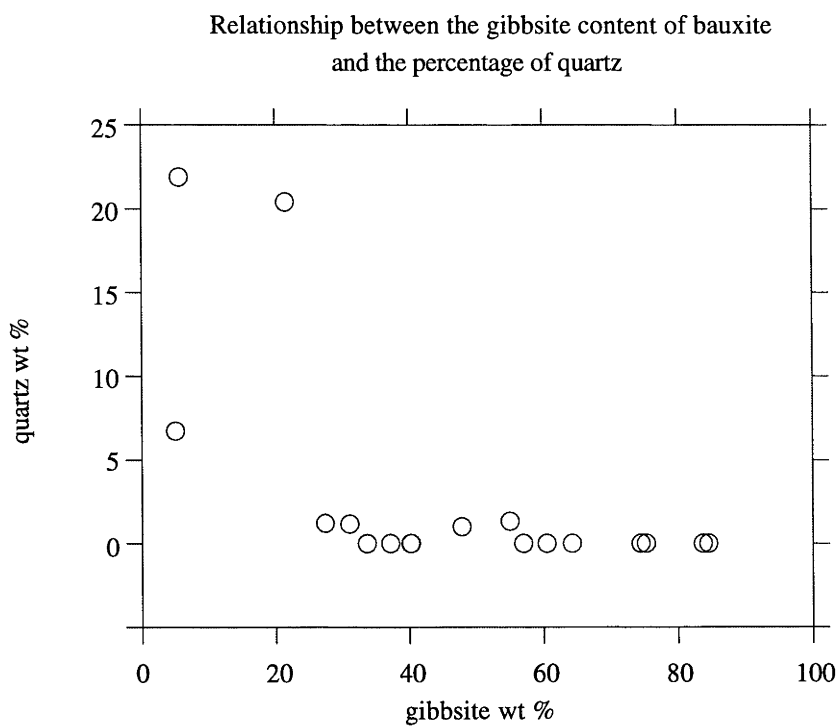


Figure 6.24

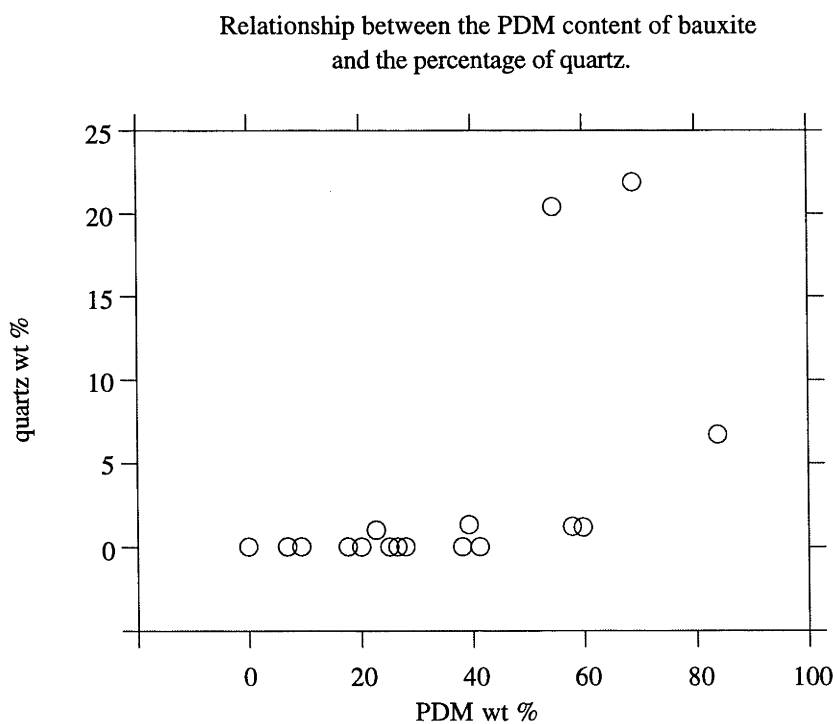


Figure 6.25

6.4 Determination of crystal sizes.

6.4.1 Experimental

The size of diffracting domains (which approximates the size of crystallites) of bauxitic minerals were determined using the Scherrer equation:

$$\varepsilon_i = \frac{1.04 \lambda}{(B_i - b) \cos \theta} \quad (\text{Klug \& Alexander, 1974}),$$

where;

- λ = 1.542 Å,
- ε_i = is an average crystallite thickness in Å,
- B_i = is an observed linewidth,
- b = is the instrumental linewidth in radians,
- θ = the angle of the line.

The instrumental linewidth (b), was found not to be a constant, but varied according to the 2θ angle (Figure 6.26). The full width at half maximum height (FWHM) was measured for the major peaks associated with minerals found in 8 bauxite samples from Weipa and 8 from Andoom, using the Siemens DIFFRAC-AT V3.1 software package. Average crystal thicknesses were calculated using the Scherrer equation (Table 6.5).

Relationship between instrumental linewidth (b) and 2-theta angle for three different standards

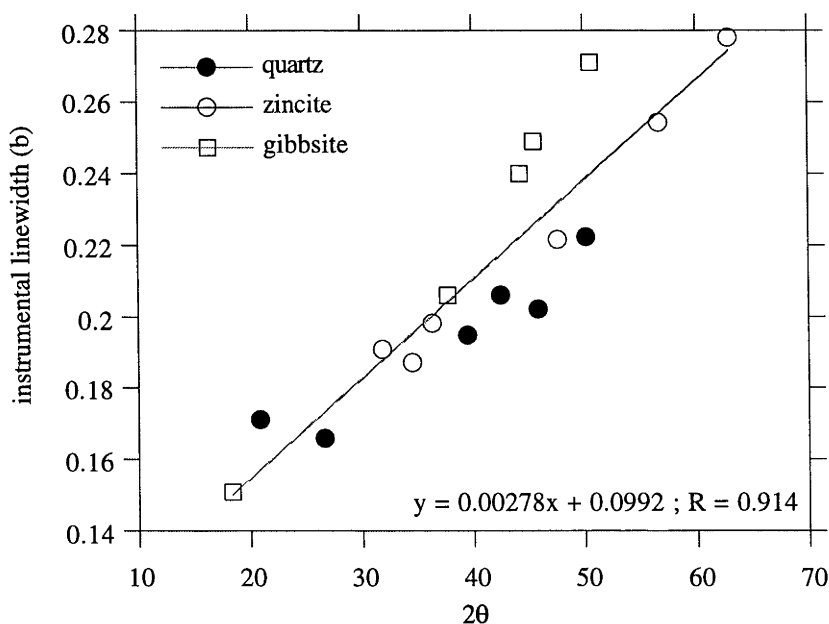


Figure 6.26

Table 6.5 Mean crystallite dimensions (nm) of minerals in bulk bauxite samples. Due to their coarseness (i.e. > 1 μ m), quartz and anatase are not included in the table as their size is governed by the degree of grinding.

Weipa						
	gibbsite	boehmite	kaolinite	hematite		
hkl	(002)	(020)	(001)	(104)		
d	4.8Å	6.1Å	7.1Å	2.7Å		
$^{\circ}2\theta$	18.3	14.5	12.3	33.2		
	(nm)	(nm)	(nm)	(nm)		
W6	402	47	46	96		
W15	136	60	38	81		
W24	208	43	69	126		
W34	178	44	35	27		
W44	142	43	56	41		
W54	246	39	51	53		
W64	224	36	51	187		
W74	147	38	49	106		
mineral (hkl)	min (nm)	max (nm)	points	mean (nm)	median (nm)	std dev (nm)
gibbsite (002)	136	402	8	210	193	87
boehmite (020)	36	60	8	44	43	7
kaolinite (001)	35	69	8	49	50	11
hematite (104)	27	187	8	90	89	52
Andoom						
	gibbsite	boehmite	kaolinite	hematite		
hkl	(002)	(020)	(001)	(104)		
d	4.8Å	6.1Å	7.1Å	2.7Å		
$^{\circ}2\theta$	18.3	14.5	12.3	33.2		
	(nm)	(nm)	(nm)	(nm)		
A4	187	103	68	26		
A11	154	47	-	23		
A21	137	54	81	29		
A28	205	70	32	27		
A36	187	63	45	30		
A46	200	38	40	23		
A53	195	109	59	27		
A60	210	87	90	36		
mineral (hkl)	min (nm)	max (nm)	points	mean (nm)	median (nm)	std dev (nm)
gibbsite (002)	137	210	8	184	191	26
boehmite (020)	38	109	8	71	67	26
kaolinite (001)	32	90	7	59	59	22
hematite (104)	23	36	8	28	27	4

6.5 Aluminium substitution in goethite.

6.5.1 Introduction

Schulze (1984) showed that the c unit cell dimension of synthetic goethites varied linearly with the amount of aluminium substitution in the range between 0 and 33 mole % aluminium. The formula used for calculating the c dimension of goethite uses the positions of the 110 and 111 diffraction lines: $c = (1/d_{111}^2 - 1/d_{110}^2)^{-1/2}$. An estimation of the aluminium substitution can be made from the relationship: mole % Al = 1730 - 572 c . Schulze (1984) indicated that this method may be used for determining the degree of substitution to ± 2.6 mole % Al with 95 % confidence.

Within different soil environments the amount of aluminium substitution in goethite varies. Therefore, our understanding of the pedogenic conditions which operated in the past as well at present may be greatly aided by determining the degree of aluminium substitution in natural goethites (Fitzpatrick and Schwertmann, 1982).

6.5.2 Method

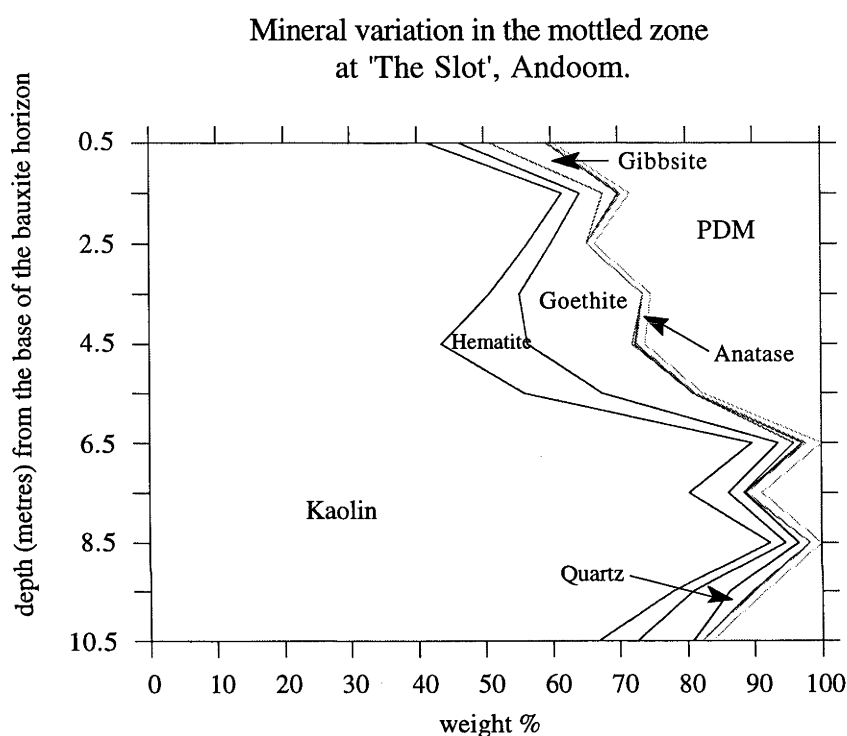
Samples were collected at intervals of 1 m from the base of the bauxite horizon (0 m) to a depth of 10.5 m in the mottled zone at a locality known as 'The Slot' near Andoom. A mottle or nodule was selected from each sample and ground to a fine powder using a mortar and pestle. To a portion of each sample was added 50 wt.% ZnO, for the quantification of poorly-diffracting material. The rest of the sample was packed in an aluminium holder against a ground glass tile for the quantification of the crystalline phases. The results were combined and graphed as a cumulative plot (Figure 6.27).

The degree of aluminium substitution in goethite was calculated from the XRD patterns which contained no internal standard. The results were displayed on a graph depicting the variation in Al-substitution. As a cross-check, the unit cell dimensions of goethite in the 3.5 m sample were determined by Rietveld structural refinement (Siroquant).

6.5.3 Results

The unit cell dimensions of goethite from the 3.5 m sample determined by Rietveld structural refinement are; $a = 4.598$, $b = 9.904$ and $c = 2.999$, indicating an aluminium substitution of 14 mole %. The aluminium substitution determined using the relationship $c = (1/d_{111}^2 - 1/d_{110}^2)^{-1/2}$ is 15 mole %.

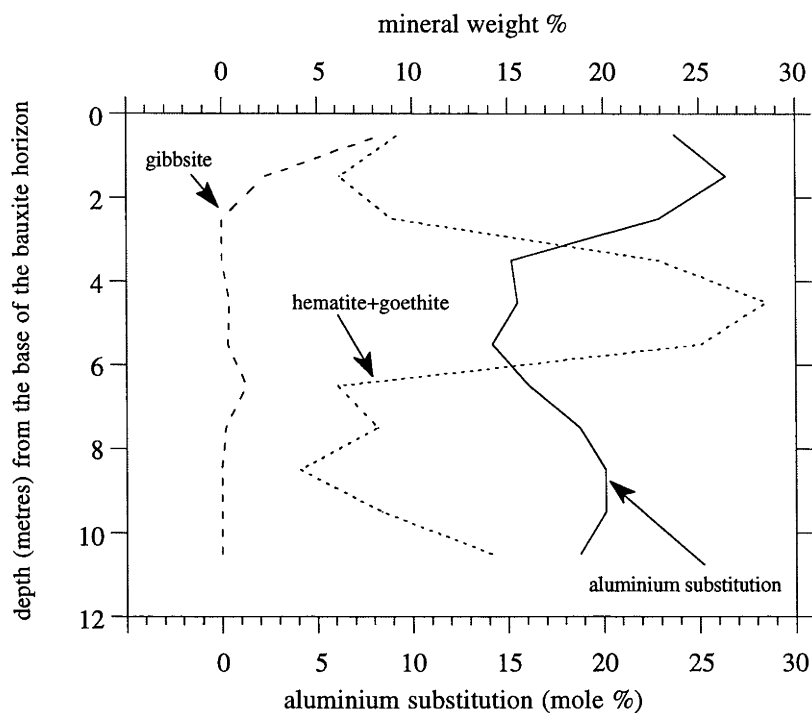
Figure 6.28 shows an abrupt increase in the Al-substitution from 15 mole % to 26 mole %, which appears to coincide with the onset of gibbsite crystallisation in the mottled zone. A minimum in the Al-substitution of goethite (≈ 15 mole %) occurs when the hematite+goethite content is at a maximum (≈ 30 weight %). There is a general rise in the poorly-diffracting material content towards the top part of the mottled zone, with a corresponding decrease in kaolinite.



Mineralogy (wt. %) of the mottled zone at "The Slot", Andoom

depth (cm)	kaol	hem	goeth	gibb	qtz	boeh	ana	PDM
50	41.5	4.8	4.5	8.5	0.0	0.2	0.8	39.7
150	61.6	2.7	3.5	2.3	0.0	0.4	1.3	28.2
250	56.4	3.5	5.4	0.0	0.0	0.0	1.1	33.5
350	50.8	4.5	18.4	0.0	0.0	0.0	1.3	25.1
450	43.6	12.9	15.6	0.4	0.0	0.2	1.3	26.0
550	55.9	11.7	13.4	0.3	0.0	0.1	1.2	17.4
650	89.8	3.9	2.2	1.3	0.0	0.5	2.3	0.0
750	80.4	5.9	2.3	0.2	0.1	0.1	2.3	8.8
850	92.5	2.2	1.9	0.0	1.7	0.0	1.7	0.0
950	77.8	3.0	5.4	0.0	3.6	0.3	1.6	8.4
1050	66.8	5.8	8.3	0.0	1.3	0.0	1.4	16.6

Figure 6.27



depth (m) from base of bauxite	mole % aluminium substitution
--------------------------------------	-------------------------------------

0.5	24
1.5	26
2.5	23
3.5	15
4.5	16
5.5	14
6.5	16
7.5	19
8.5	20
9.5	20
10.5	19

Figure 6.28

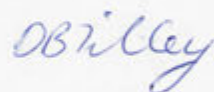
Aluminium substitution within the goethite of the mottled zone at "The Slot", Andoom. The weight percentages of gibbsite and hematite+goethite are superimposed.

PART THREE

Interpretation

Amendment

A recent letter dated 19th June 1995, from the International Mineralogical Association Commission on New Minerals and Mineral Names (CNMMN) discouraged the use of the name "tohdite" in any future publications due to it not being a valid mineral name. This ruling was received after publication of the following chapter, "Tohdite in bauxites from northern Australia". The name akdalaite ($4\text{Al}_2\text{O}_3 \cdot \text{H}_2\text{O}$) was approved by the CNMMN for the mineral corresponding to tohdite (due to their similarity) and as a consequence, Weipa tohdite should be referred to as akdalaite in any future publications.



13th December 1995

Chapter 7

Tohdite ($5\text{Al}_2\text{O}_3 \cdot \text{H}_2\text{O}$) in bauxites from northern Australia*

7.1 Introduction

Tohdite ($5\text{Al}_2\text{O}_3 \cdot \text{H}_2\text{O}$), is a synthetic phase described by Yamaguchi *et al.* (1964a) having hexagonal symmetry ($P6_3mc$) with $a=5.58 \text{ \AA}$ and $c=8.77 \text{ \AA}$. The structure of tohdite determined by Yamaguchi *et al.* (1964b) has four of the five aluminiums in octahedral coordination and the other in tetrahedral coordination, between four close-packed oxygen sheets (ABAC stacking). Shpanov *et al.* (1971) described akdalaite, a new mineral from a hydrothermal deposit, which they proposed was related to tohdite, but having a larger unit cell ($a=12.87 \text{ \AA}$, $c=14.97 \text{ \AA}$), slightly different composition ($4\text{Al}_2\text{O}_3 \cdot \text{H}_2\text{O}$), and minor amounts of Fe_2O_3 , BeO , ZnO and MgO .

Bauxitic pisoliths are concentrically zoned pea-sized particles common in deeply weathered aluminous rocks, and are the main components of bauxite ore-bodies. From any one particular locality, individual pisoliths vary widely in concentric structure and mineral distribution. The mineral composition of pisoliths is dominated by gibbsite ($\text{Al}(\text{OH})_3$) and boehmite ($\text{AlO}(\text{OH})$), with variable minor quartz (SiO_2), hematite (Fe_2O_3), kaolinite ($\text{Al}_2\text{Si}_2\text{O}_5(\text{OH})_4$) and anatase (TiO_2). Diaspore ($\text{AlO}(\text{OH})$), goethite ($\text{FeO}(\text{OH})$) and corundum (Al_2O_3) have also been reported from some bauxitic pisoliths. We report here evidence that tohdite constitutes an important component of some bauxitic pisoliths at Weipa, Cape York Peninsula, in northern Australia.

* "Tohdite ($5\text{Al}_2\text{O}_3 \cdot \text{H}_2\text{O}$) in bauxites from northern Australia" was received on the 22nd March 1994 by the editor of the journal *Clays and Clay Minerals* and was accepted for publication on the 3rd May 1994. The paper is presented here as a chapter, with only minor modifications.

7.2 Experimental

The bulk of pisoliths from Weipa are somewhat porous and soft enough to powder from a light hammer tap. Some, however, have a porous rim and a hard vitreous core, requiring a sharp blow to crack them. Examination by X-ray diffraction of 42 pisoliths selected randomly from 16 drill holes, showed that almost half contained more than 20 weight % of a material not accounted for, by identifiable well-crystallised minerals, and yielding very broad diffraction maxima. We refer to this material as poorly-diffracting material (PDM). A few pisoliths contained more than 50 weight % PDM. Pisoliths containing the highest percentage of poorly-diffracting material had a hard vitreous core surrounded by a softer porous rim. X-ray diffraction analysis of the vitreous core of such pisoliths was done using a Siemens D501 X-ray diffractometer, Cu $K\alpha$ radiation. Quantification of the mineralogy was determined on samples combined with 33.3 weight % ZnO as an internal standard, using the software package SIROQUANT. Differential XRD patterns were obtained by slow-scanning the sample without the standard, followed by subtraction of the calculated pattern for each of the well-crystallized components in proportion to their weight fraction. The bulk chemical composition of the pisolith cores was established by energy dispersive X-ray analysis (EDAX) in a JEOL 6400 scanning electron microscope operating at 15 kV. Transmission electron microscopy of one sample was performed on a crushed sample on a carbon support film in a JEOL 200CX TEM. Analytical TEM was carried out on the same crushed sample using a Philips 430EM transmission electron microscope operating at 300kV. An infrared spectrum of the PDM was obtained using a Perkin-Elmer 1800 FTIR spectrophotometer.

7.3 Results

The rim of vitreous-core pisoliths show clear concentric zoning, emphasised by a variation in iron content and therefore intensity in the back-scattered electron image (Figure 7.1). The core of such pisoliths display no zonation. Quantitative XRD examination of the pisolith depicted in Figure 7.1, revealed that the core contained 84 % poorly-diffracting material. Well-crystallized phases which yield sharp diffraction maxima included quartz, gibbsite, anatase, hematite, kaolinite and boehmite (Table 7.1).

TEM examination of the poorly-diffracting material revealed both structureless material and well-formed small crystals (6 nm diameter) with prominent 2.1 Å lattice fringes and less obvious fringes spaced at about 2.4 Å (Figure 7.2). The electron diffraction pattern from this material is: (relative intensity-d) 40-2.4 Å, 80-2.1 Å, 30-1.9 Å, 10-1.6 Å, 100-1.4 Å.

Table 7.2 shows the bulk composition of the core material, the calculated composition of the recognized well-crystallized minerals calculated from their ideal composition and phase weight percent (Table 7.1), and the composition of the poorly-diffracting material, established by difference.

A vitreous-core pisolith containing > 90 % PDM in its core, was selected to produce a differential XRD scan as shown in Figure 7.3. Broad peaks are evident, their peak width at half maximum of $1.6^\circ 2\theta$ indicates diffracting domains of the order of 7 nm. Relative intensity and d-spacings are shown in Table 7.3, and compared with the results for tohdite described by Yamaguchi *et al.*¹ Although the breadth of the XRD peaks introduces overlap and makes accurate measurement of 2θ difficult, refinement of the cell parameters for Weipa tohdite using uniquely indexable reflections clear of interference from other components yields $a=5.555$ and $c=8.968$, which are very close to those of synthetic tohdite.

Analytical TEM (AEM) of a PDM-rich sample highlighted the high aluminium content of the material (Table 7.4). Although a nano-probe (≈ 10 nm diameter beam) was used, the extremely fine crystal size of the PDM made it almost impossible to obtain analyses of single crystals without avoiding the possibility of contamination from adjacent dissimilar phases.

A transmittance infrared spectrum of the material containing > 90 % PDM, shows a broad absorption band at 3460 cm^{-1} associated with O-H stretching vibrations (Figure 7.4).

7.4 Discussion

The data presented here are consistent with the proposition that very fine-grained tohdite (or possibly akdalaite) is a major component of vitreous-cored pisoliths from Weipa, north Queensland. The differential XRD pattern provides the strongest evidence; the slightly greater d-spacings for the Weipa sample, particularly for hkl rather than 00l reflections, may be the result of lattice expansion from incorporation of Fe(III) in the Al sites, or be the result of displacement of peak maxima from the ideal Bragg position due to small crystal size effects. A chemical composition for Weipa tohdite cannot be established from the available data, as TEM and XRD evidence indicate other poorly-diffracting material may be present in the analysed samples.

The infrared spectrum of Weipa tohdite, is dissimilar to well crystalline gibbsite and boehmite. Between 2500 and 4000 cm^{-1} , the spectrum of gibbsite displays four absorption maxima associated with O-H stretching, whereas boehmite has two. The Weipa tohdite spectrum on the other hand, has a broad absorption band with a maximum at 3460 cm^{-1} associated with the O-H stretching vibrational mode. Another maximum occurring at 1630 cm^{-1} is related to O-H bending. The infrared spectrum of Weipa tohdite is indicative of a material containing a large amount of strongly bound water. This may account for the discrepancy between the theoretical water content of tohdite and that determined chemically.

Tohdite (ideal composition $96.6\text{ wt } \% \text{ Al}_2\text{O}_3$) is the most aluminium-rich mineral recognized in the Weipa bauxite, and its presence is significant for both extraction of alumina from bauxite and in interpreting the origins of bauxitic pisoliths. While it is not possible to determine if the mineral at Weipa is indeed tohdite and not akdalaite, this is the first reported occurrence of tohdite/akdalaite in bauxites, and may, depending on the equivalence or non-equivalence of tohdite and akdalaite, be a new mineral occurrence.



Figure 7.1

Back-scattered electron image of a vitreous-core pisolith displaying a concentrically banded rim and a fractured core devoid of zonation. Scale bar = 1 mm.

Quantitative XRD results from a vitreous-cored pisolith.

Phase	weight % excluding PDM	weight % including PDM
Gibbsite	31.47	5.06
Boehmite	0.06	0.01
Quartz	42.04	6.76
Hematite	6.34	1.02
Kaolinite	5.72	0.92
Anatase	14.37	2.31
PDM		83.92
Total	100.0	100.0

Table 7.1Composition of bulk core material,
crystalline components and composition of the
poorly-diffracting material determined by difference.

	bulk weight % (EDAX)	crystalline minerals (SIROQUANT)	PDM composition
SiO ₂	13.52	7.19	7.57
Al ₂ O ₃	51.03	3.68	56.65
TiO ₂	2.69	2.31	0.45
Fe ₂ O ₃	2.64	1.02	1.94
H ₂ O	29.79*	1.88	33.39
PDM		83.92	
Total	99.67	100.0	100.0

* H₂O by difference

Table 7.2

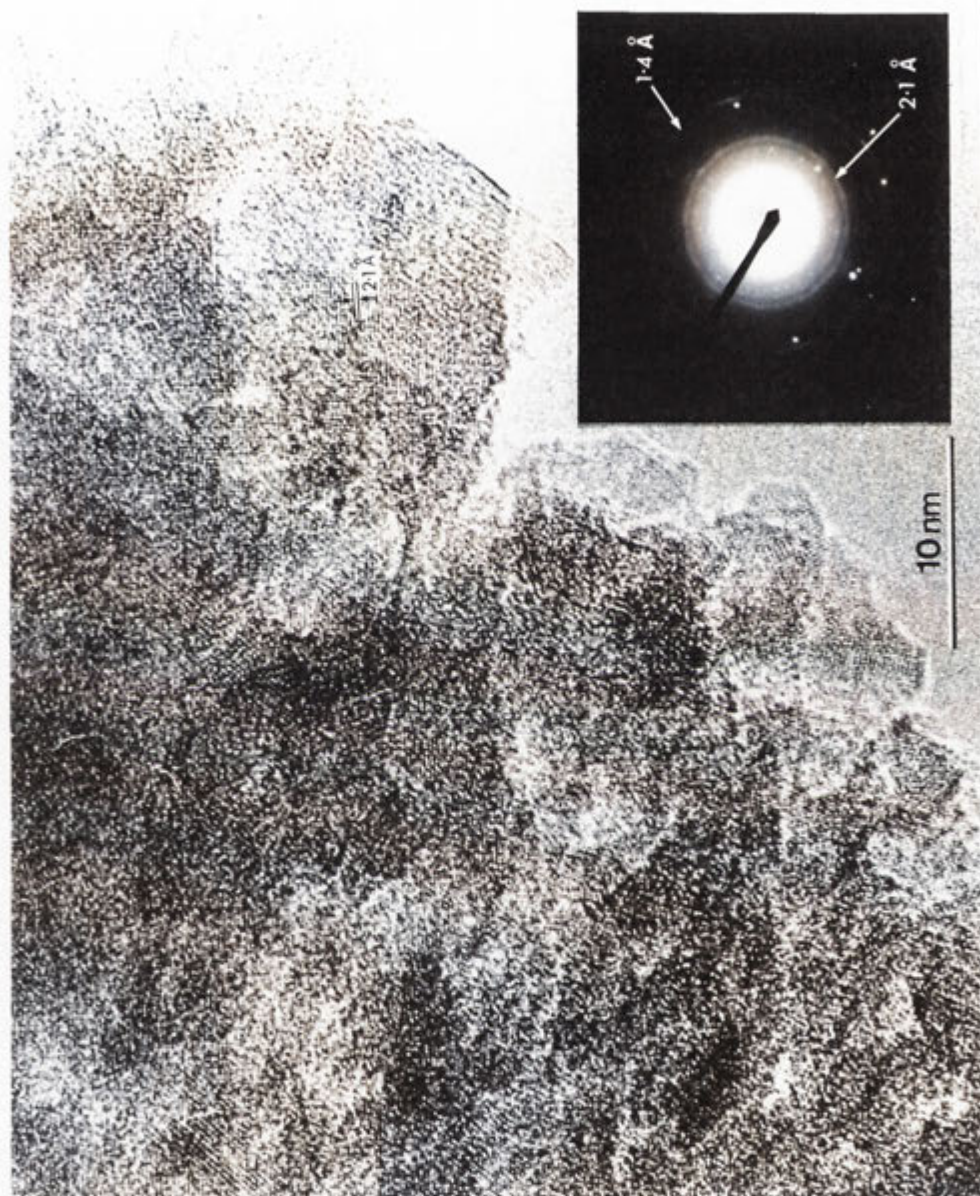


Figure 7.2

A TEM image of tohdite from Weipa bauxite showing small, well-formed crystals of 6 nm diameter and displaying prominent 2.1 Å lattice fringes and less obvious fringes spaced at 2.4 Å. The insert shows an electron diffraction pattern of the same material, displaying diffuse rings. The bright spots are associated with another well-crystalline phase. Scale bar = 10 nm.

XRD pattern for tohdite and differential XRD pattern of material from the core of a vitreous-core pisolith from Weipa.

<u>Tohdite*</u>			<u>Weipa</u>	
hkl	d(Å)	I	d(Å)	I
100	4.85	10	4.81	20
002	4.38	23	4.38	25
101	4.23	11	4.23	15
			3.68	10
102	3.25	60	3.33	50
110	2.79	12	2.82	40
103	2.50	54	2.53	60
200	2.42	12		}
112	2.35	77	2.37	}
201	2.33	38		}
202	2.11	100	2.12	75
			1.97	5
203	1.86	48	1.89	40
			1.76	5
			1.72	5
122	1.69	13	1.69	20
204	1.62	26	1.61	25
123	1.55	34	1.55	20
302	1.51	20	1.52	25
205	1.42	68	1.41	55
220	1.39	85	1.39	100

* Yamaguchi *et al.* (1964b) (only tohdite lines of relative intensity >10 are listed)

Table 7.3

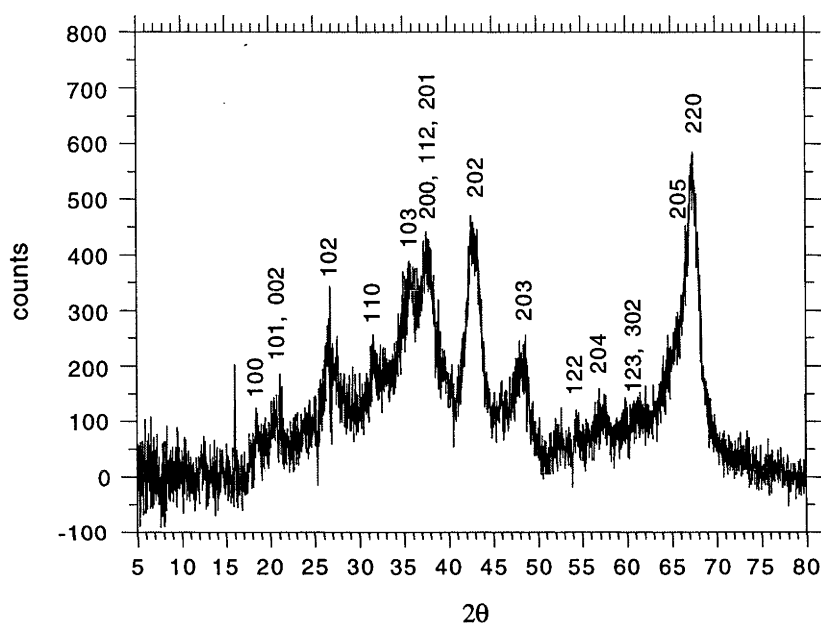


Figure 7.3

Differential XRD scan of tohdite from the core of a bauxitic pisolith. Broad peaks indicate extremely fine crystals of 7 nm diameter. The spike in the pattern at $16^\circ 2\theta$ is due to an unaccounted minor phase. Spikes observed in the region between 25 and $28^\circ 2\theta$ are artefacts caused by the incomplete subtraction of the (101) quartz peak.

Analytical TEM analyses* of a crushed sample
from a PDM-rich pisolith core.

elements	analysis 1	analysis 2	analysis 3	analysis 4
	(mole %)			
Al	78.4	84.6	95.2	93.7
Si	4.3	11.0	3.8	3.7
Ti	4.8	2.0	0.0	0.0
Fe	12.6	2.3	1.0	2.6

oxides	analysis 1	analysis 2	analysis 3	analysis 4
	(wt.%)			
Al ₂ O ₃	70.9	81.1	94.1	91.8
SiO ₂	4.6	12.5	4.4	4.3
TiO ₂	6.8	2.9	0.0	0.0
Fe ₂ O ₃	17.8	3.5	1.5	4.0

*all analyses are normalised to 100 wt.%

Table 7.4

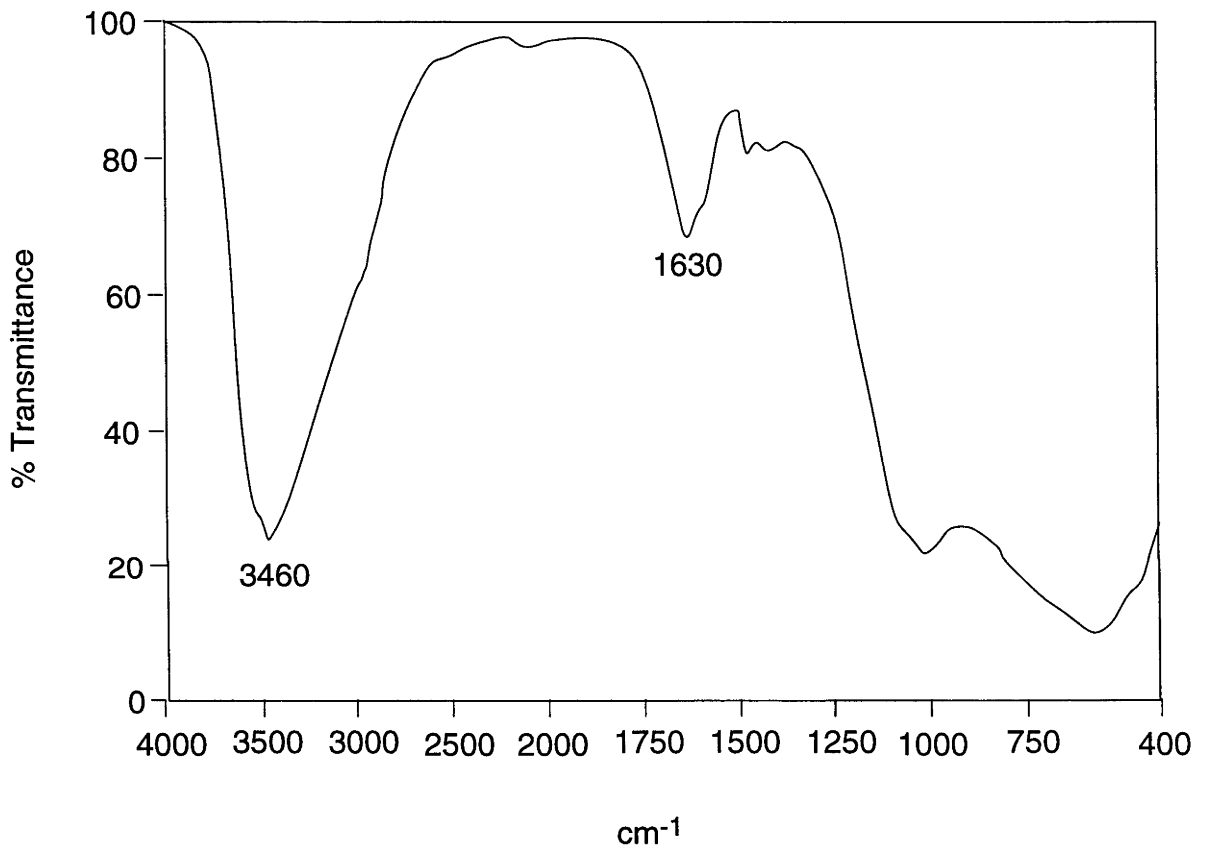


Figure 7.4

A transmittance infrared spectrum of tohdite, showing a broad absorption band at 3460 cm^{-1} associated with O-H stretching vibrations.

Chapter 8

Eta-alumina; a new bauxite mineral

8.1 Introduction

In the previous chapter it was reported that tohdite ($5\text{Al}_2\text{O}_3 \cdot \text{H}_2\text{O}$) may compose a significant proportion of the bauxite deposit at Weipa. Examination of pisoliths from Andoom (15 km north of Weipa) has revealed the presence of another poorly-diffracting phase, distinct from tohdite. Differential XRD and transmission electron microscopy (TEM) of the poorly-diffracting material (PDM) showed that the mineral has similar characteristics to that of eta-alumina ($\eta\text{Al}_2\text{O}_3$). Stumpf *et al.* (1950) described eta-alumina as having a cubic, spinel-type structure. They showed that eta-alumina is a transitional phase produced by the thermal decomposition of bayerite ($\beta\text{Al}(\text{OH})_3$). Further heating of eta-alumina leads to the formation of corundum ($\alpha\text{Al}_2\text{O}_3$).

8.2 Methods

The core of a bauxitic pisolith from Andoom (TR221AB: 1-1.5 m depth) was sampled using a dental drill. The extracted material was finely ground using a mortar and pestle and then applied to a low-background holder. An XRD pattern of the sample was obtained by slow-scanning over a period of 12 hours. A differential XRD pattern was produced by subtracting the calculated pattern for each of the well-crystallised components, in proportion to their weight fraction. The resultant differential XRD pattern was then indexed and compared with minerals and inorganic compounds in the powder diffraction file. When it was discovered that the d-spacings of the broadest peaks in the XRD pattern were similar to those of eta-alumina, quantitative analysis of the sample was performed using SIROQUANT.

The same powder that was used for XRD, was dispersed in ethanol using an ultrasonic bath and then pipetted onto a holey carbon-coated grid. TEM was performed on the sample using a Jeol 200CX transmission electron microscope, operating at 200 kV. Selected-area electron diffraction (SAED) patterns of bauxite particles were obtained at a camera length of 74 cm. A SAED pattern displaying a series of diffraction rings was indexed and compared to XRD and calculated d-spacing values.

Analytical TEM (AEM) was undertaken using a nano-probe in conjunction with energy dispersive X-ray analysis (EDXA) on a Philips 430EM transmission electron microscope, operating at 300kV. An infrared spectrum of the PDM was obtained using a Perkin-Elmer 1800 FTIR spectrophotometer.

8.3 Results

The raw XRD pattern is composed of relatively sharp peaks produced by hematite, gibbsite, quartz, anatase, rutile and kaolinite. The broadest peaks are due to the presence of a poorly-diffracting phase (Figure 8.1).

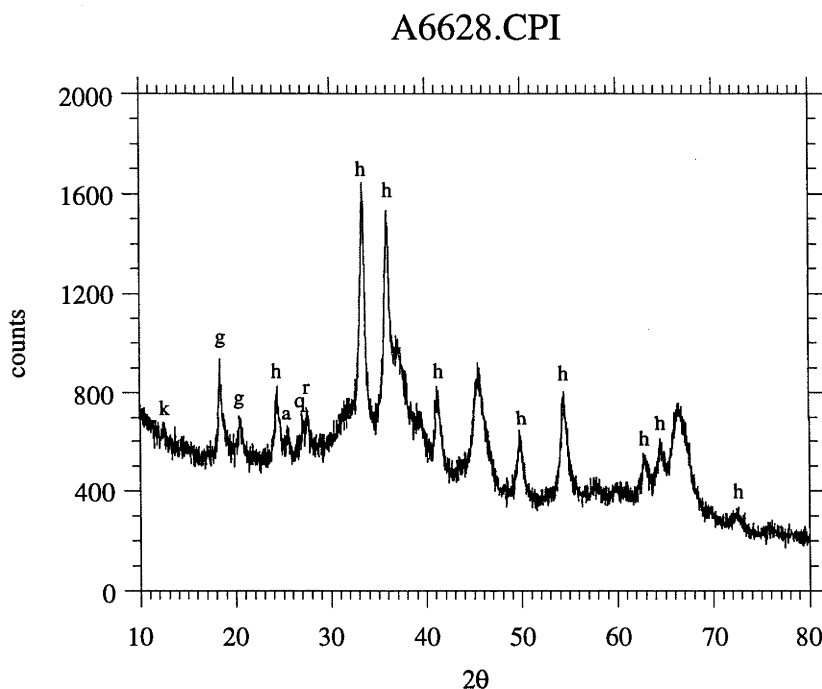


Figure 8.1

An X-ray diffractogram of PDM-rich bauxite extracted from the core of a pisolith from Andoom (TR221AB: 1-1.5 m depth), where g = gibbsite, h = hematite, k = kaolinite, a = anatase, q = quartz, r = rutile.

The procedure for obtaining a differential XRD pattern was reasonably effective in removing the well-defined peaks associated with gibbsite, hematite and other well-crystallised phases, even though some residual peaks are still evident (Figure 8.2). The differential XRD pattern displays a series of broad diffraction maxima, similar in intensity and breadth to Weipa tohdite, however the diffraction lines do not coincide with those of Weipa tohdite.

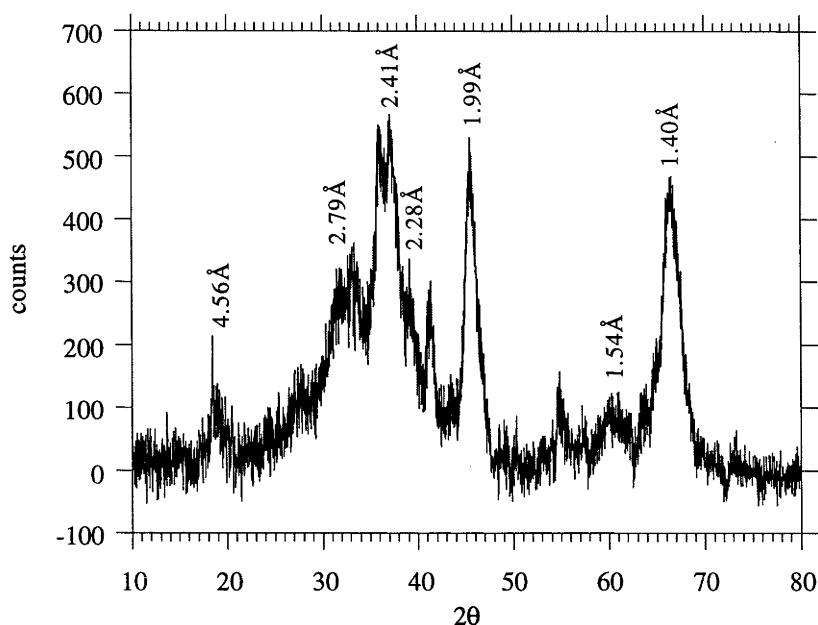


Figure 8.2

A differential XRD pattern of PDM obtained from the core of a pisolith from Andoom (TR221AB: 1-1.5 m depth).

The broad peaks have maxima which match well with those of eta-alumina (η - Al_2O_3) (Stumpf *et al.*, 1950) (Table 8.1). The 1.99 Å peak has a width (at half maximum) of $1.31^\circ 2\theta$ which gives a crystallite size of 9 nm when using the Scherrer equation. Quantitative XRD using SIROQUANT indicates that the core of the analysed pisolith contains greater than 70 weight % eta-alumina (Figure 8.3).

Extremely fine crystals of approximately 10 nm are evident in the TEM image (Figure 8.4) Those crystals which have lattice fringes of 2.0, 2.3 and 2.4 Å are associated with eta-alumina. The crystallite size of eta-alumina determined from the TEM image is close to that calculated using the Scherrer equation (\approx 9 nm) and is slightly larger than that of Weipa tohdite (\approx 6 nm). The d-spacing values obtained from the selected-area electron diffraction pattern (Figure 8.5) coincide well with the XRD pattern of the poorly-diffracting material, indicating that the finely crystalline material observed using TEM is the same material identified in the XRD pattern.

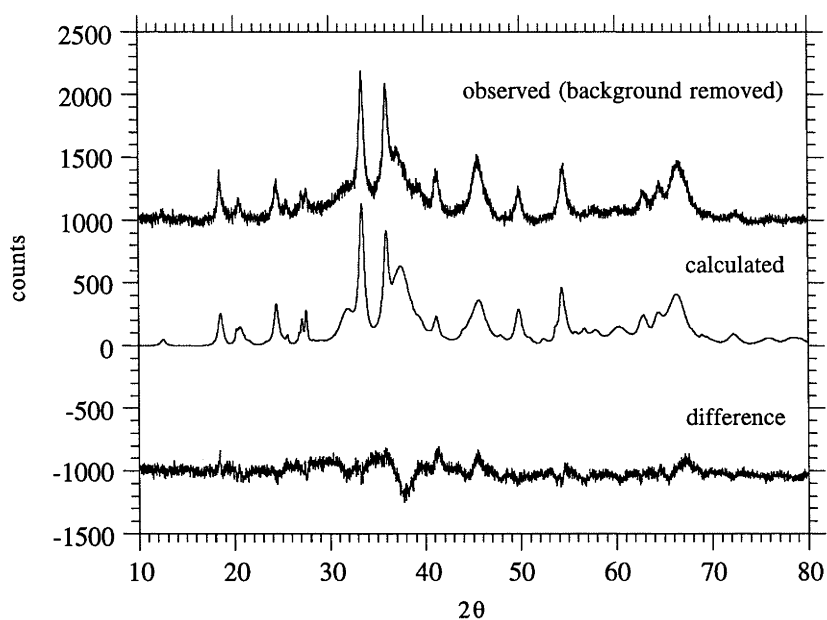
AEM of randomly selected crystals in the PDM-rich sample revealed the presence of two mineral phases; an aluminium-bearing ferruginous phase and an almost pure aluminous phase (Table 8.2 and Figure 8.6).

A transmittance infrared spectrum of the material containing approximately 70 % PDM, shows a broad absorption band at 3450 cm^{-1} due to O-H stretching and at 1630 cm^{-1} associated with O-H bending vibrations (Figure 8.7).

electron diffraction		differential XRD		η -alumina (Stumpf <i>et al.</i> , 1950)		
I/I ₁	d Å	I/I ₁	d Å	I/I ₁	d Å	hkl
		30	4.62	40	4.6	111
20	2.79	30	2.82	20	2.8	220
70	2.40	70	2.45	60	2.40	311
20	2.28	30	2.29	30	2.27	222
90	1.96	100	2.01	80	1.97	400
20	1.52	20	1.55	20	1.52	333
100	1.39	90	1.41	100	1.40	440
10	1.19			10	1.21	533
20	1.13			20	1.14	444
10	0.98			10	1.03	553
10	0.88					
10	0.80					

Table 8.1

Comparison between the d-spacing values of the poorly-diffracting material determined by electron diffraction, differential XRD and those calculated by Stumpf *et al.* (1950).



Siroquant Results

(global $\chi^2 = 7.28$)

<u>Phase</u>	<u>Weight %</u>	<u>Error</u>
eta-alumina	71.6	0.37
hematite	15.5	0.15
gibbsite	7.7	0.27
kaolinite	2.5	0.31
rutile	1.9	0.09
zircon	0.5	0.05
quartz	0.2	0.06
anatase	0.3	0.07

Figure 8.3

Quantitative analysis of the bauxite sample derived from the core of a pisolith from Andoom (TR221AB: 1-1.5 m depth).

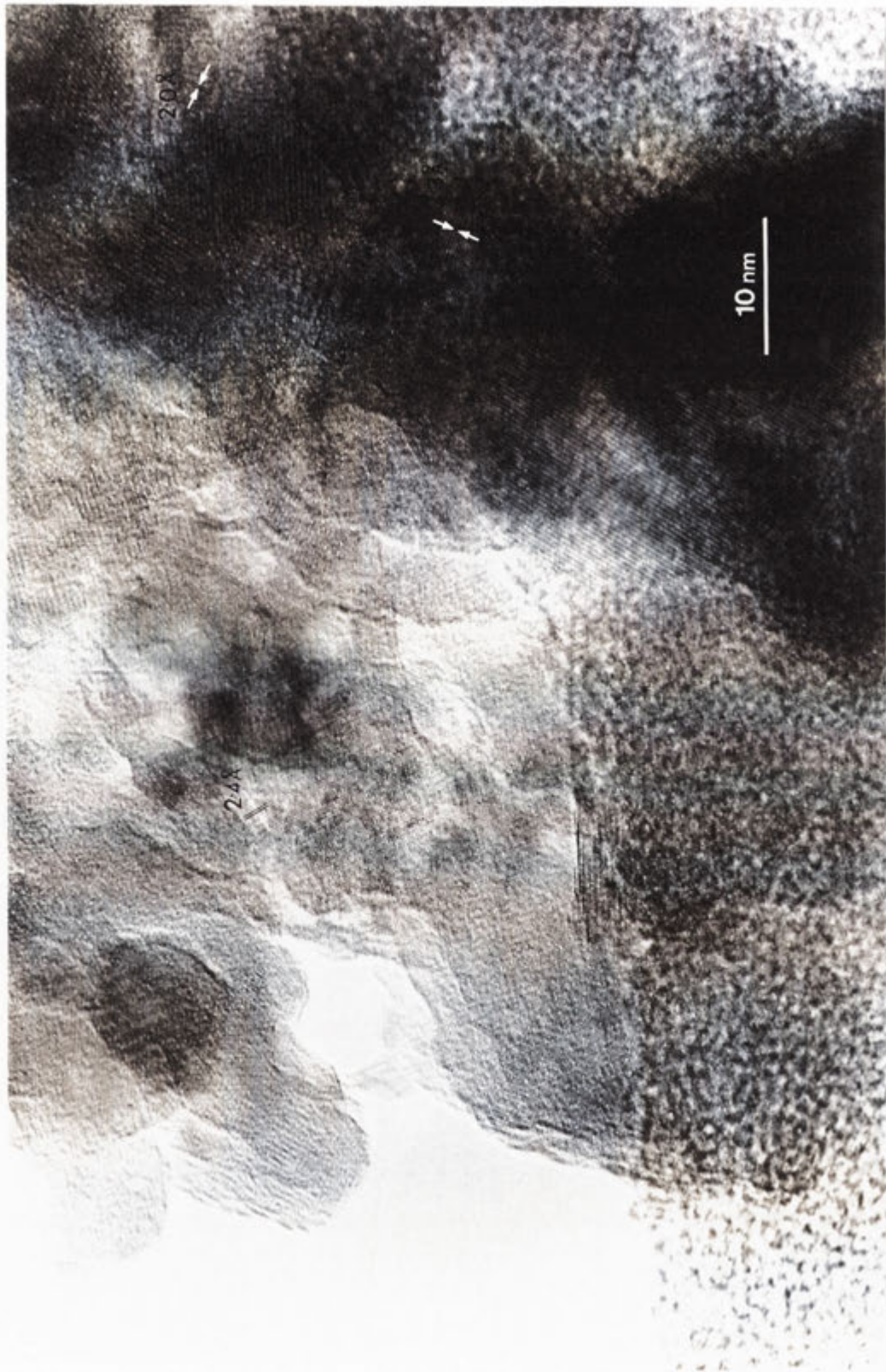


Figure 8.4

A transmission electron micrograph of one particular area in the poorly-diffracting material. The crystal size of the PDM is approximately 10 nm.

Lattice fringes of 2.0, 2.3 and 2.4 Å indicate eta-alumina.

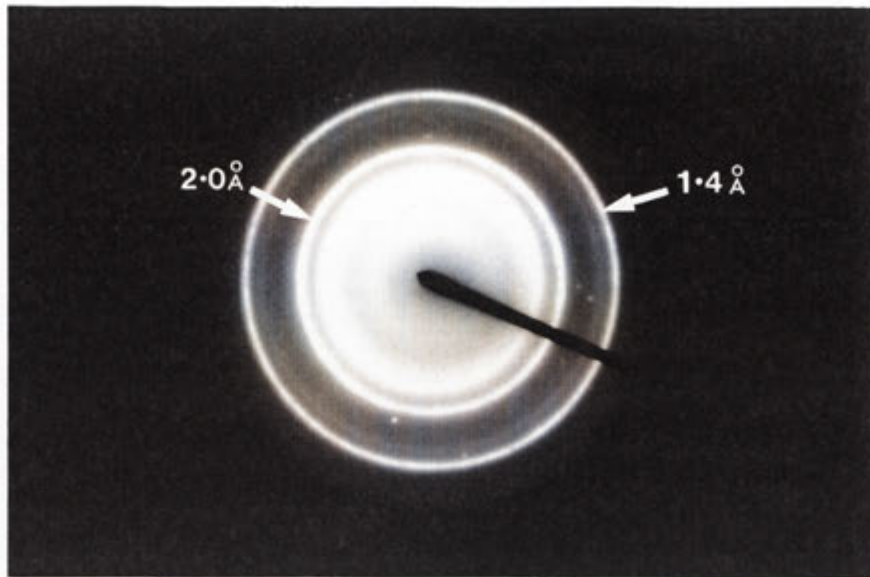


Figure 8.5

A selected-area electron diffraction pattern of eta-alumina.

analysis	Al_2O_3	Al	SiO_2	Si	TiO_2	Ti	Fe_2O_3	Fe
	wt.%	mole%	wt.%	mole%	wt.%	mole%	wt.%	mole%
1	95.5	96.8	1.4	1.2	0.9	0.6	2.2	1.4
2	15.4	22.2	0.0	0.0	2.4	2.2	82.3	75.7
3	18.6	26.4	0.0	0.0	2.4	2.2	78.9	71.4
4	29.8	39.9	0.6	0.7	2.6	2.2	67.0	57.3
5	95.7	97.0	0.8	0.7	1.1	0.7	2.4	1.5
6	95.1	96.6	0.8	0.7	1.0	0.6	3.1	2.0
7	23.0	31.9	0.3	0.4	2.2	2.0	74.4	65.8
8	36.3	47.2	0.0	0.0	1.3	1.0	62.5	51.8
9	96.4	97.6	0.6	0.5	0.7	0.4	2.3	1.5
10	88.5	92.1	0.9	0.8	0.0	0.0	10.6	7.1
11	91.1	94.1	0.0	0.0	0.1	0.1	8.8	5.8

Table 8.2

Nano-probe analyses of individual crystals in the PDM-rich bauxite sample.

The analytical total is not real but is recalculated to 100%.

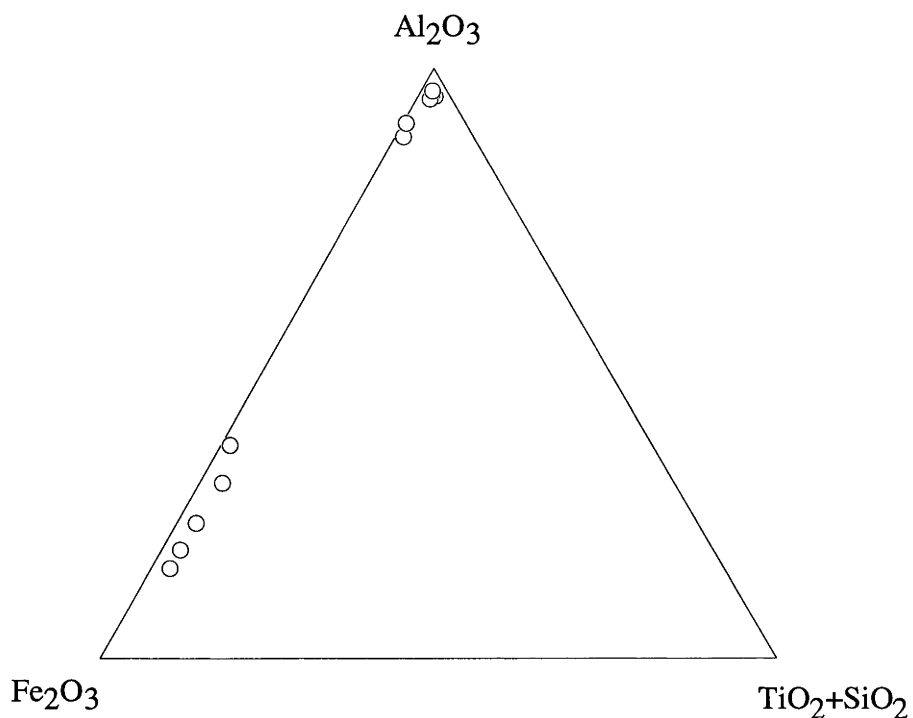


Figure 8.6

Tri-plot of the nano-probe analyses of individual crystals within a PDM-rich sample indicating the presence of an aluminium-bearing ferruginous phase (Al-hematite) and an almost pure aluminous phase (eta-alumina).

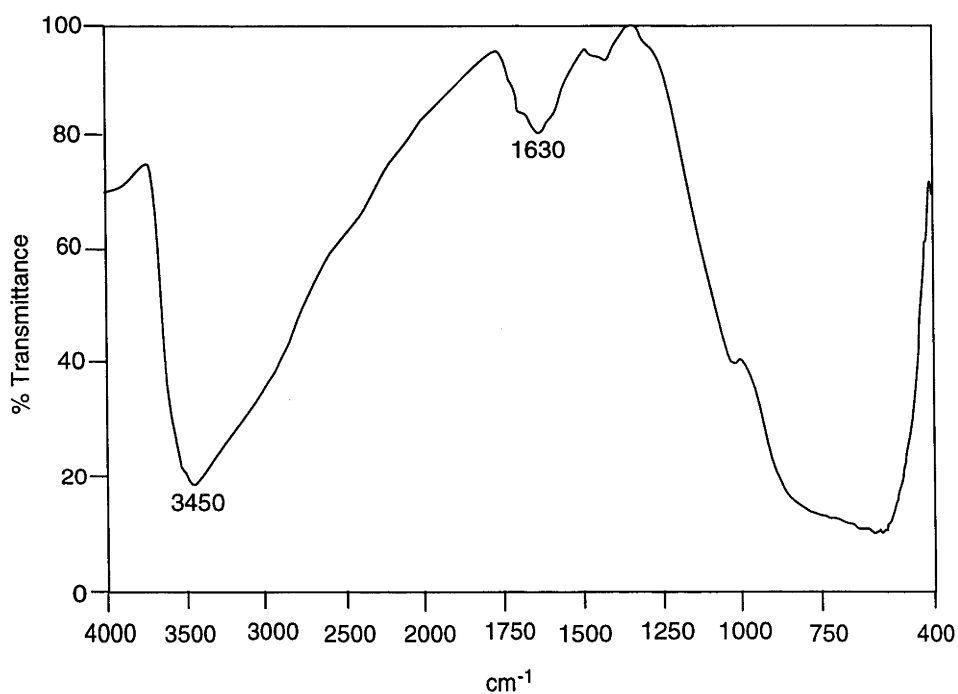


Figure 8.7

A transmittance infrared spectrum of bauxitic material containing approximately 70 wt.% eta-alumina, from the core of a pisolith from Andoom.

8.4 Discussion

Analytical TEM of the same PDM-rich material that had undergone XRD analysis, revealed the presence of an aluminium-bearing ferruginous phase which is ascribed to Al-hematite and an almost pure aluminous phase which is attributed to eta-alumina. As well as containing > 22 mole % Al, the hematite also contains 2 mole % Ti, while eta-alumina has < 1 mole % Ti and < 2 mole % Fe. Schwertmann (1988) reported that aluminium substitution in hematite can occur to a maximum of 18 mole % Al and that when hematite and goethite coexist, the Al-substitution in hematite is about half of that in goethite. Although every effort was made to ensure that the analyses were of individual crystals, contamination between the two phases may have still occurred resulting in an apparently higher than normal aluminium content for the hematite.

The water contained within the crystal lattices of gibbsite, boehmite and tohdite are respectively 34.6, 15.0 and 3.4 weight %. The theoretical crystalline structure of eta-alumina contains no chemically-bonded water. Both tohdite and eta-alumina contain appreciable amounts of strongly adsorbed water as evidenced by their transmittance infrared spectra however the actual amount is not determinable from the spectra alone. The reason for the large amount of adsorbed water is due mainly to their large surface areas. For example, the surface area of 1 gram of eta-alumina ($\rho = 3.63 \text{ g/cm}^3$) assuming it consists of an aggregate of cubic crystals is approximately 2200 m²/g.

The discovery of tohdite and eta-alumina in the bauxites of Weipa and Andoom has greatly expanded our knowledge and understanding of bauxite mineralogy and the role water activity plays in the evolution of bauxitic pisoliths (see Chapter 10). The occurrence of these minerals in the bauxite may also have implications in the Bayer refinery process and in grade control. The reactivities of tohdite and eta-alumina in the Bayer Process are not well understood, however it is hypothesised that their large surface areas may allow them to be easily dissolved in NaOH. The mineralogy of the Weipa and Andoom bauxites is currently calculated by Comalco from XRF chemical analyses using various assumptions. At present, tohdite and eta-alumina are not included in these calculations, hence the determination of the mineralogy by this method is in error.

Chapter 9

Compound pisoliths

9.1 Introduction

Constituting a minor part of the Weipa bauxite are shell and tube-like structures of bauxitic composition, ranging in length from 2 to 5 cm. The internal chamber of such structures commonly contain ordinary bauxitic pisoliths or oöoliths, however some are completely barren. Usually, there is at least one opening into the chamber. Openings may be partially or totally occluded with bauxite. These structures are designated *bauxitic compound pisoliths* and are known locally at Weipa as "mother pisolites" or "rattlers". Four different types of compound pisolith have been identified in the Weipa area. The *nodular* form externally resemble the underlying ferruginous-kaolinite nodules. *Common* compound pisoliths on the other hand, are smoother and more ellipsoidal in shape. Less common varieties are the root-like *tubular* compound pisoliths and the large *ovate* type. In general, compound pisoliths are poor grade ore because of their relatively high silica content. Their comparatively large size enables them to be easily discarded by sieving, during beneficiation. Very little research has been done on them, because of their uneconomic value. Evans (1965) first reported the existence of compound pisoliths in the Weipa bauxite. Grubb (1970) mentioned the existence of 'composite concretions' in the bauxite deposit of Gove, Northern Territory. He suggested that there were four stages in their development, but he did not elaborate. MacGeehan (1972) noted the presence of compound pisoliths at the base of the bauxite horizon and suggested they formed by the growth of gibbsitic membranes. In this chapter, compound pisoliths from Weipa are described in detail, and a hypothesis put forward to explain their formation, which in turn clarifies aspects of the evolution of the Weipa bauxite deposit as a whole.

During the dry season of 1992, Mike Morgan of Comalco Mineral Products, Weipa found nodules within a 1 metre interval at the base of the bauxite horizon, which varied in their internal morphology between ferruginous-kaolinite nodules (or 'ironstone') and nodular compound pisoliths. Superficially, nodular compound pisoliths resemble ferruginous-kaolinite nodules. When broken open, nodular compound pisoliths reveal an internal cavity, containing either pisoliths or oöoliths. Morgan hypothesised that compound pisoliths formed from the bauxitisation of 'ironstone' nodules.

Evidence genetically linking nodules and pisoliths has been uncovered at the Longtom, East Pike and Nanagai mines at Weipa, and along the Weipa to Andoom railway cutting. A compound pisolith similar in structure to those occurring at Weipa, has been found in the Wingello district on the Southern Tablelands of New South Wales, indicating the phenomenon may be quite widespread. Quantitative XRD has shown the existence of a mineralogical continuum between ferruginous-kaolinite nodules and nodular compound pisoliths, suggesting that nodules are precursory to the formation of pisoliths.

9.2 Nodular compound pisoliths

Nodular compound pisoliths are found scattered throughout a zone between the bauxite horizon and the underlying nodular ferruginous-kaolinite layer (Figure 9.1). The zone, having a thickness of approximately 1 m, has been observed at the Longtom and East Pike bauxite mines as well as the "old kaolin pit" at Nanagai. Examination of the Weipa to Andoom railway cutting and the road cutting between the East Weipa mine centre and Jewfish, also revealed the existence of such a zone. Externally, nodular compound pisoliths are similar in appearance to ferruginous-kaolinite nodules, however internally they display varying degrees of resemblance to common compound pisoliths (*pers. com.* Morgan, 1992) (Figure 9.2 and 9.3). Nodular compound pisoliths as with most types of compound pisolith, generally have at least one opening into the inside chamber. Unlike common compound pisoliths, it is quite normal for the nodular type to have more than one aperture. Those which least resemble common compound pisoliths, occur at the bottom of the zone, just above the nodular ferruginous-kaolinite layer. Such nodules contain a yellow inner zone surrounded by a dark red outer zone (stage 2). The inner zone is relatively soft and porous and is composed predominantly of oöoliths while the outer zone is hard and dense (Figure 9.4). Higher in the profile, the internal chamber of nodules become increasingly deficient in oöoliths while the number of pisoliths occupying the chamber generally increases.

Those which are most similar in morphology to common compound pisoliths, occur at the top of the zone. Such pisoliths vary from being irregular, to quite smooth and ellipsoidal in shape. The irregular ones tend to be slightly larger and heavier than common compound pisoliths (Table 9.1 and Figure 9.5), whereas the ellipsoidal shaped ones are similar in size. Cortical development is much less pronounced in nodular compound pisoliths than in common compound pisoliths.

The graphs (Figures 9.6 & 9.7) show a progressive decrease in the kaolinite content from about 70 to 15 wt %, as the nodules becomes more like compound pisoliths. Correspondingly, the gibbsite content increases from around 5 to 80 wt %. A reduction in the iron content of nodules occurs as they begin to resemble compound pisoliths.



Figure 9.1

The weathering profile exposed in the Weipa-Andoom railway cutting, Weipa. The head of the geological hammer marks the boundary between the bauxite horizon and the underlying nodular ferruginous-kaolinite layer. A 1m thick zone above this boundary contains nodular compound pisoliths.

	diameter (mm)
Minimum	22
Maximum	39
Mean	29.4
Std Deviation	3.86

Table 9.1

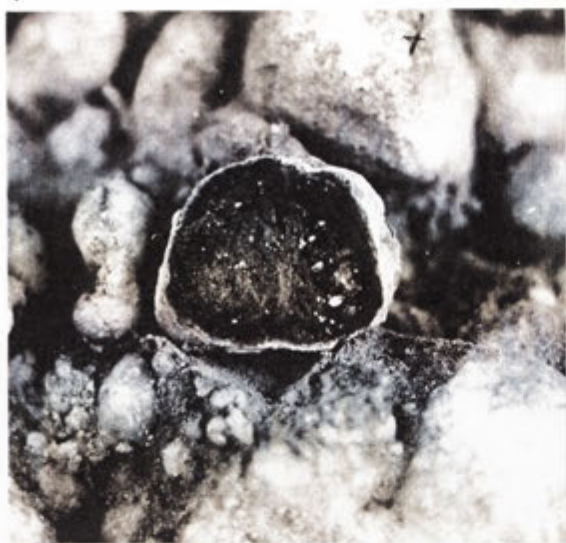
Dimensions of 56 nodular compound pisoliths from the Weipa-Andoom railway cutting.

Figure 9.2

Broken compound pisoliths and ferruginous-kaolinite nodules from the road cutting between the East Weipa mine centre and the Jewfish mine.

- Figure 9.2.1 A ferruginous-kaolinite nodule from the top of the mottled zone.
- Figure 9.2.2 A ferruginous-kaolinite nodule that has a friable, porous core surrounded by a hard, dense shell. The nodule came from the zone between the nodular ferruginous-kaolinite layer and the overlying bauxite.
- Figure 9.2.3 A nodular compound pisolith with a few loose particles occupying the chamber. No opening is evident in the shell of the compound pisolith.
- Figure 9.2.4 A nodular compound pisolith with single pisoliths occupying the chamber. An opening exists in the shell of the compound pisolith.
- Figure 9.2.5 A common compound pisolith which has a chamber devoid of material. No opening is evident in the shell of the compound pisolith. Note the presence of banding around the outside of the shell.
- Figure 9.2.6 A common compound pisolith having thicker banding around the outside of the shell. Pisoliths that once occupied the chamber fell out when the compound pisolith was broken with a hammer.

1



2



3



4



5



6

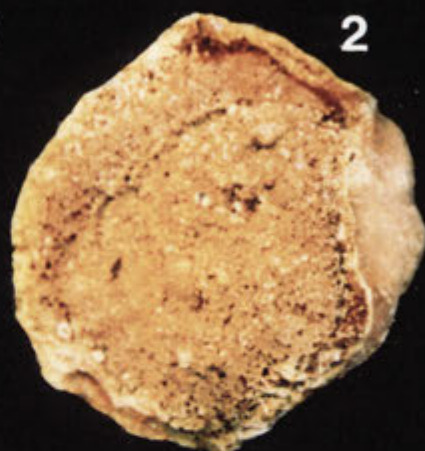
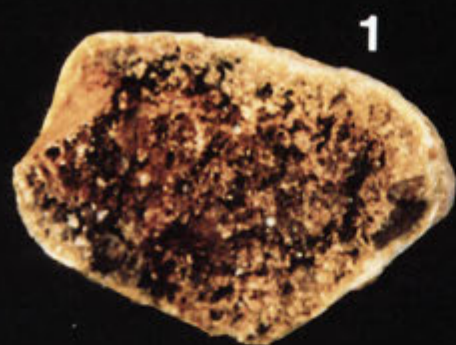


Figure 9.3

Four apparent stages in the evolution of nodular compound pisoliths. Externally, nodular compound pisoliths are similar in appearance to ferruginous-kaolinite nodules, however internally they display varying degrees of resemblance to common compound pisoliths.

The table below outlines the actual mineralogy of the depicted pisoliths.

mineral	stage 1 wt %	stage 2 wt %	stage 3 wt %	stage 4 wt %
kaolinite	62.1	15.2	12.5	13.7
hematite	4.5	0.7	1.1	0.7
goethite	5.0	0.9	0.5	0.6
gibbsite	8.5	80.5	75.2	81.5
quartz	0.4	0.0	0.0	0.0
boehmite	0.1	0.1	0.1	0.5
anatase	1.8	2.7	2.5	2.9
PDM	17.6	0.0	7.9	0.0



10 mm

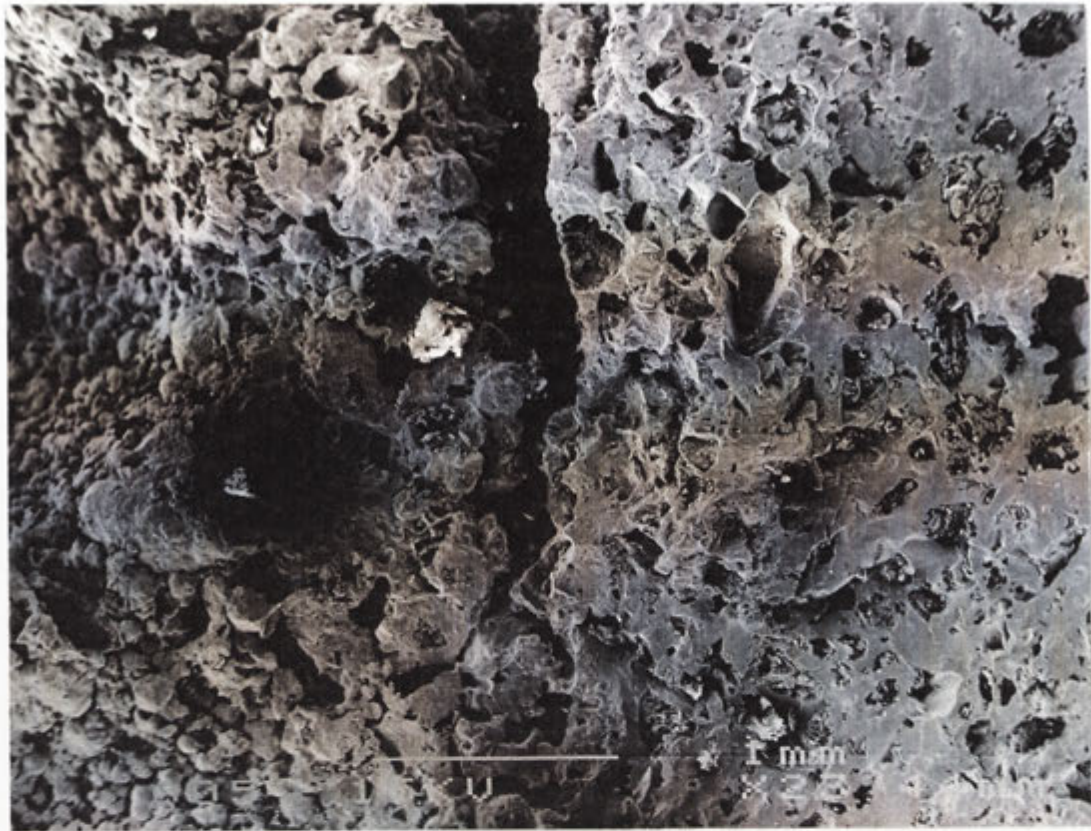


Figure 9.4.1

A zone of interconnected porosity is developed on the left-hand side of the micrograph as a result of the formation of oolites. Scale bar = 1 mm.



Figure 9.4.2

An oolite coated with gibbsite crystals. Scale bar = 10 μm .

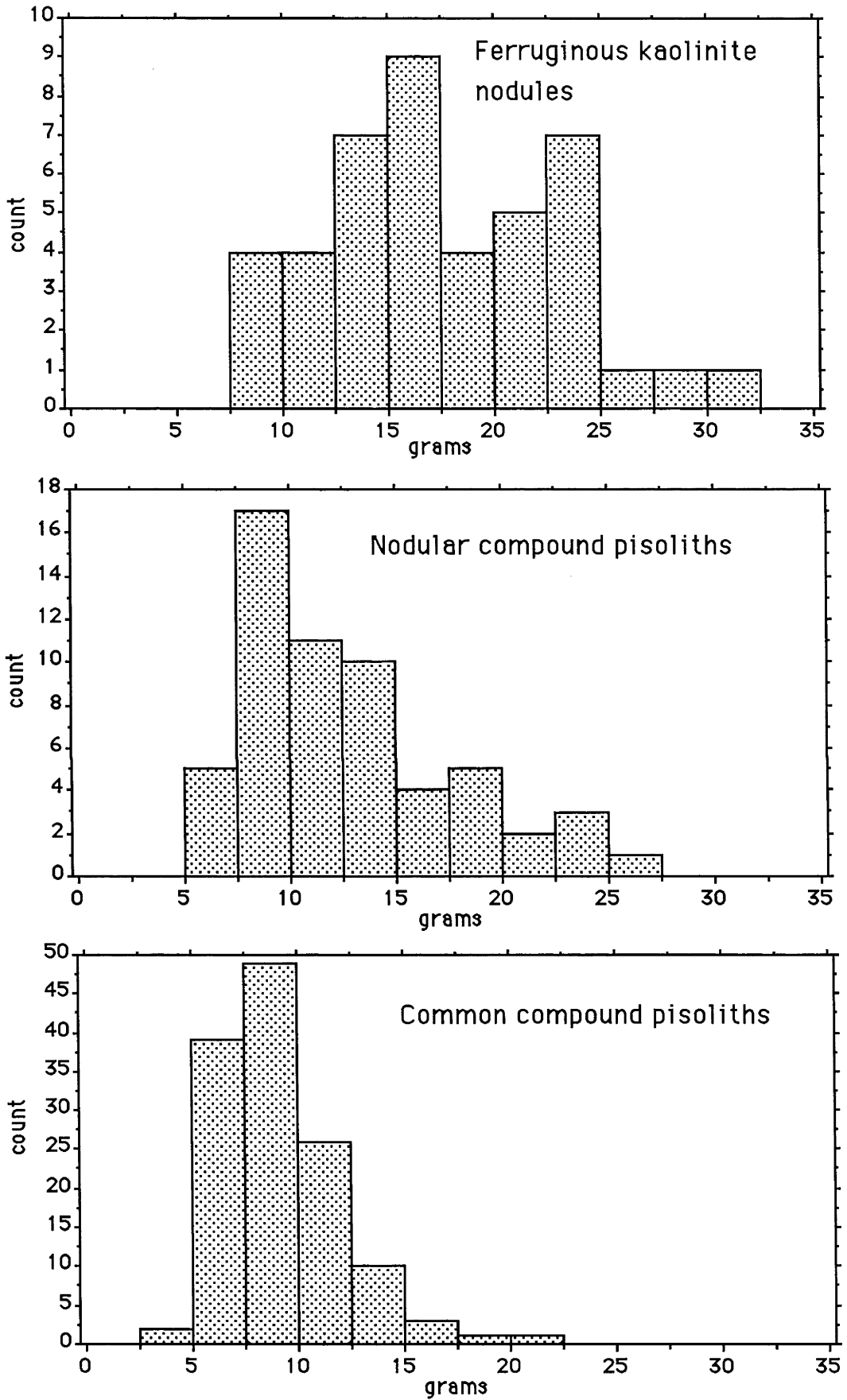
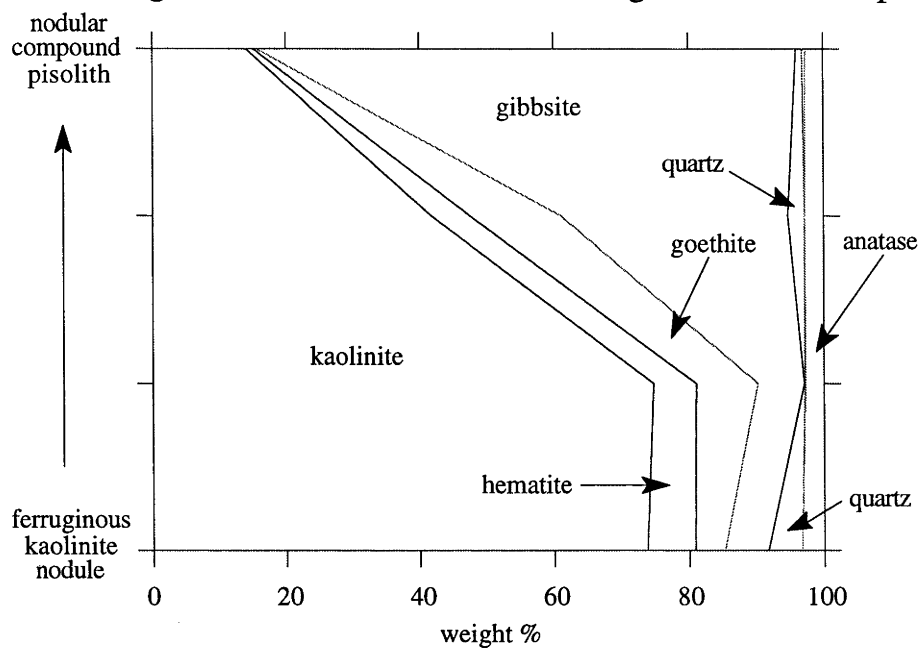


Figure 9.5

Frequency histograms of nodule and compound pisolith weights.

The evolution of compound pisoliths from
ferruginous kaolinite nodules at Longtom mine, Weipa.



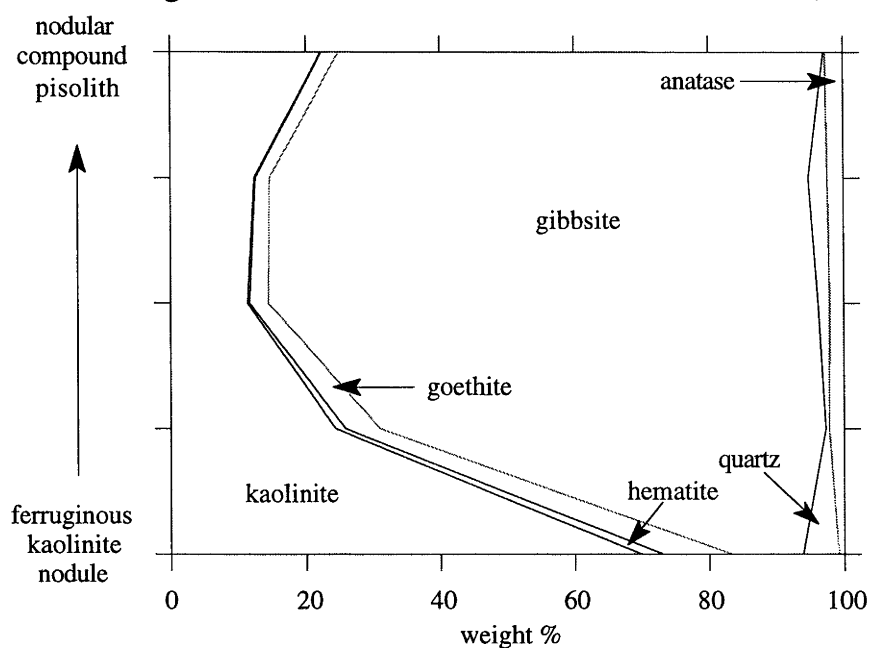
mineral	stage 1 wt %	stage 2 wt %	stage 3 wt %	stage 4 wt %
kaolinite	73.8	74.9	41.8	14.1
hematite	7.1	6.2	5.8	1.2
goethite	4.3	9.2	13.6	0.5
gibbsite	6.5	6.9	33.6	80.3
quartz	4.9	0.1	2.5	1.0
boehmite	0.0	0.2	0.0	0.4
anatase	3.3	2.6	2.7	2.6

Figure 9.6

The mineralogy of 4 apparent stages in the evolution
of nodular compound pisoliths from the Longtom mine, Weipa.

Poorly-diffracting material has not been taken into account.

The evolution of compound pisoliths from
ferruginous kaolinite nodules at East Pike mine, Weipa.



mineral	stage 1 wt %	stage 2 wt %	stage 3 wt %	stage 4 wt %	stage 5 wt %
kaolinite	69.8	24.4	11.4	12.4	22.3
hematite	3.2	1.5	0.3	0.3	0.1
goethite	10.3	5.1	2.8	2.1	2.6
gibbsite	10.6	66.3	81.7	80.2	72.2
quartz	5.4	0.5	1.7	2.8	0.2
boehmite	0.0	0.1	0.2	0.1	0.1
anatase	0.7	2.1	2.0	2.3	2.6

Figure 9.7

The mineralogy of 5 apparent stages in the evolution of nodular compound pisoliths from the East Pike mine, Weipa.

Poorly-diffracting material has not been taken into account.

9.3 Common compound pisoliths

Common compound pisoliths are the most numerous and have the widest distribution of all compound pisoliths. They are found in the top part of the bauxite horizon decreasing in frequency down the profile (Figure 9.8). The middle part of the bauxite horizon is much poorer in compound pisoliths.

Common compound pisoliths are approximately prolate spheroidal in shape and are typically 24 x 17 mm in size (Table 9.2 and Figure 9.9). Oblate spheroidal and spheroidal shapes are occasionally found. As a rule, common compound pisoliths which contain ordinary bauxite pisoliths within their shell, have an opening or evidence of one, into the internal chamber. Generally, the opening is close to one end of the compound pisolith and is sometimes occluded with bauxitic material. Those common compound pisoliths which have their internal chamber filled with oölitic material, do not possess any obvious opening. Similarly, those which are completely empty also lack any evidence for an opening.

	length (mm)	width (mm)	length/width
Minimum	16	10	1
Maximum	32	24	1.75
Mean	24.1	17.4	1.40
Std Deviation	3.1	2.2	0.16

Table 9.2

Dimensions of 99 common compound pisoliths from the Weipa-Andoom railway cutting.

The mineralogy of common compound pisoliths is quite complex (Figure 2.16 & 2.17). The shell is typically composed of gibbsite with variable quartz and accessory minerals such as zircon, rutile and tourmaline. The cortex which surrounds the shell, becomes more boehmitic and hematite-rich towards the periphery. The enclosed pisoliths usually have a boehmite-rich core surrounded by a gibbsitic rim.



Figure 9.8

The upper section of the weathering profile exposed in the Weipa-Andoom railway cutting, Weipa. The section consists of cemented bauxite containing scattered common compound pisoliths (arrowed) overlain by a friable soil layer.

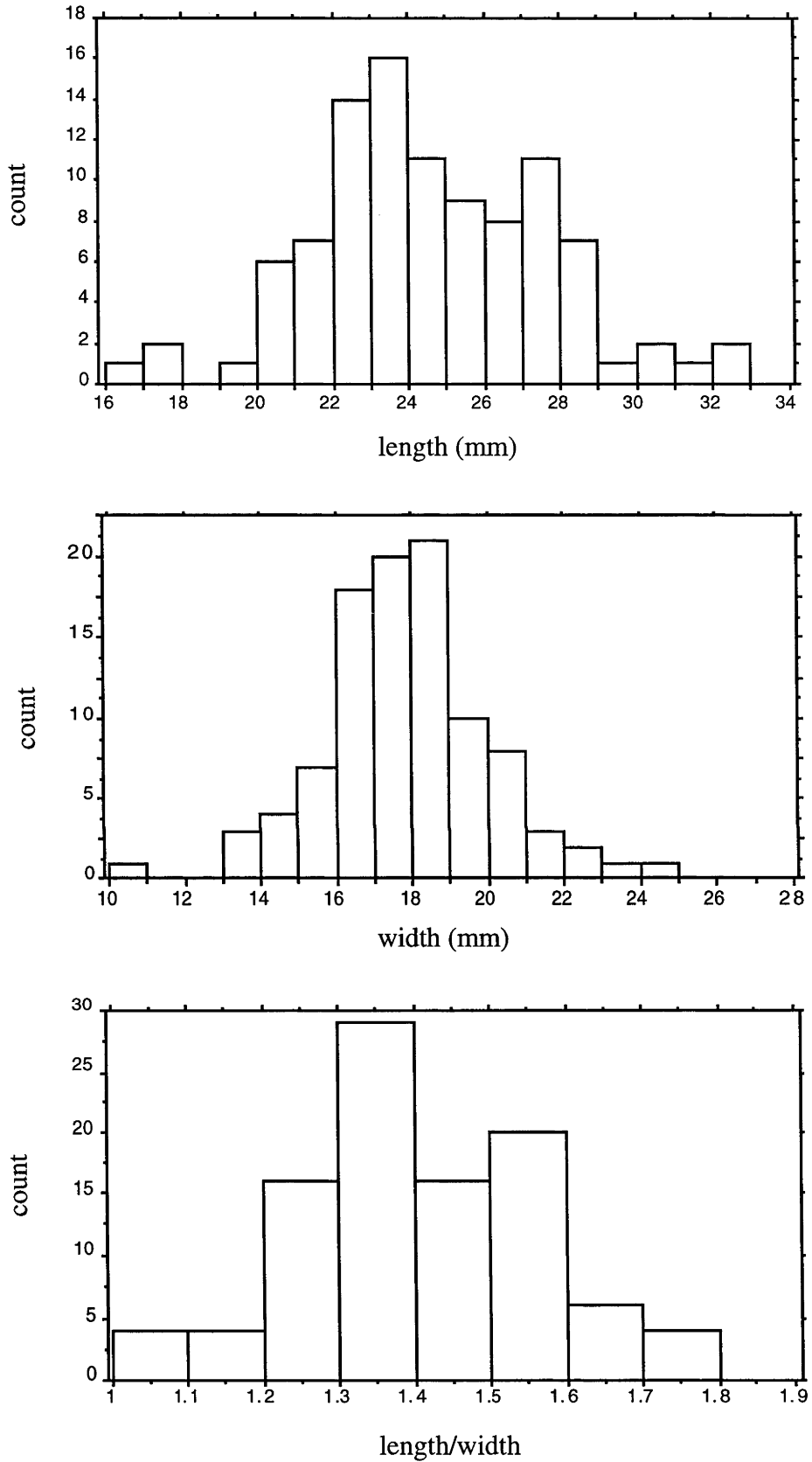


Figure 9.9

Frequency histograms of the dimensions of 99 common compound pisoliths from the Weipa-Andoom railway cutting, Weipa.

9.4 Other types of compound pisoliths

In addition to the compound pisoliths already described, two other varieties have been identified at Weipa and Andoom (Figure 9.10). The morphologically distinct families suggest that each group evolved in a different manner.

Tubular compound pisoliths are normally found near the base of the bauxite horizon. At the East Pike mine they are found at the top of the 1m transitional zone between the bauxite and the underlying ferruginous nodular kaolinite. Tubular compound pisoliths at the East Pike mine are approximately 23 x 12 mm in size (Table 9.3).

They have a short tube-like appearance and may have an opening at both ends or only at one end (Figure 9.11.1). Their shape suggests that they may have once been rhizoliths; root like concretions formed when a particular type of rainforest plant selectively extracted silica, leaving behind an encrustation of aluminium and iron-rich minerals. Rhizoliths can be found in many bauxite deposits and in some may constitute a significant portion of the ore (Butty & Chapallaz, 1984). At Weipa, tubular compound pisoliths may be the only surviving remnants of such concretions as a change in climatic and/or hydrological conditions resulted in the segmentation and bauxitisation of them. The climate and the vegetation type of today does not appear to promote rhizolith formation.

Ovate compound pisoliths are found in small groups, sporadically distributed throughout the bauxite deposit. They may be found at any level in the bauxite and soil horizons. They are the largest type of pisolith known in the Weipa area, averaging 49 x 30 mm (Table 9.4). Much smaller ovate compound pisoliths can be found, however their similar size and shape to common compound pisoliths, make them difficult to distinguish. A common feature to all ovate compound pisoliths, regardless of their size, is their thin shell. Often there is an opening or evidence for one, offset from one end of the compound pisolith. When such an opening is present, ordinary bauxitic pisoliths usually occupy the inside chamber. As with common compound pisoliths, when an opening is absent, the internal chamber is invariably devoid of material. As well as having only thin cortices, ovate compound pisoliths sometimes contain fragments of immature common compound pisoliths, suggesting that the ovate-type formed at a later date (Figure 9.11.2). Ovate compound pisolith shells are composed of material having a similar composition to that material which immediately surrounds them. Those which occur in the soil horizon are composed of soil material (Figure 9.12), while those that exist in the bauxite horizon are composed of bauxite.

Compound pisolith families

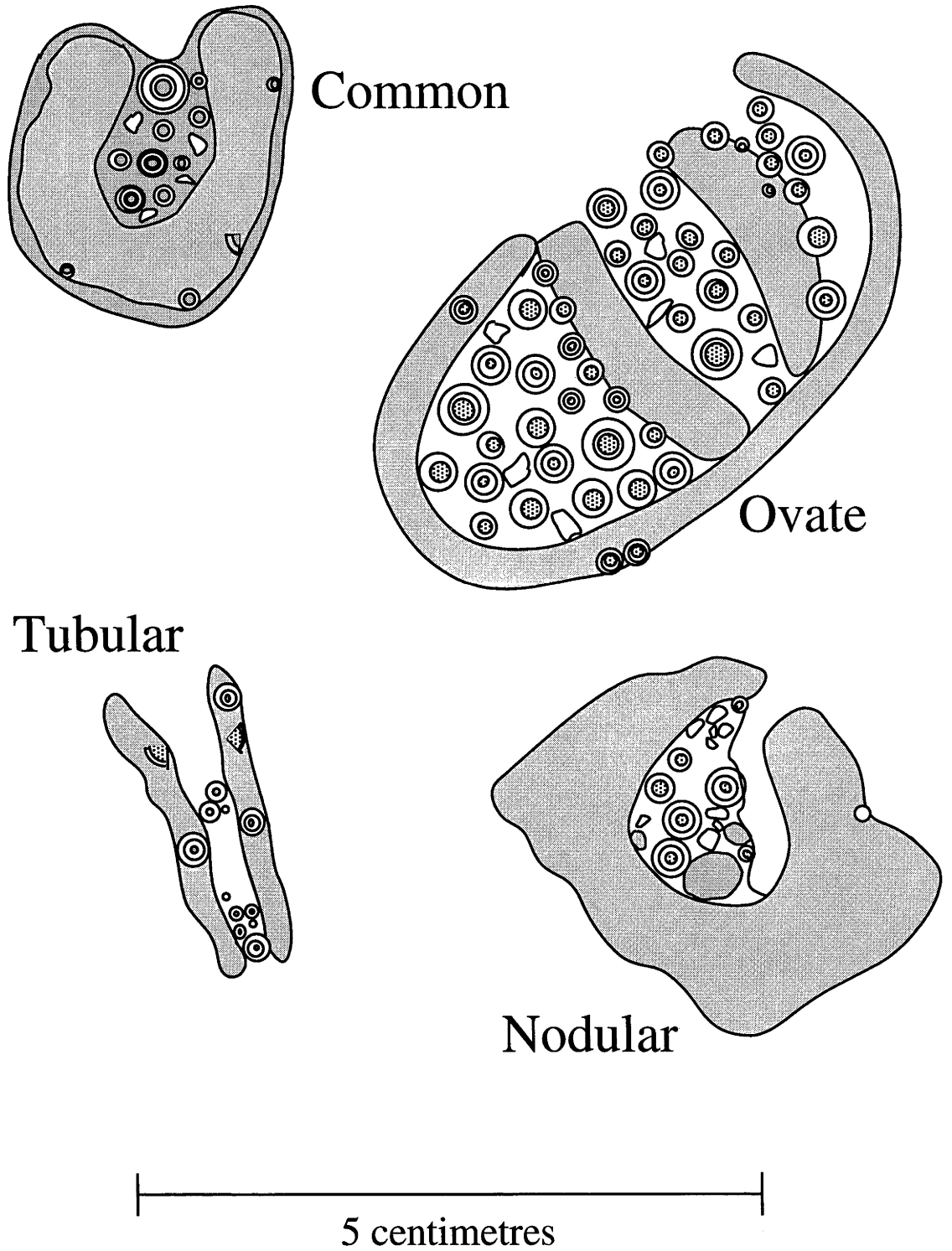


Figure 9.10

	length (l) (mm)	width (w) (mm)	l/w
Minimum	21	10	1.62
Maximum	25	13	2.40
Mean	22.9	11.8	1.95
Std. Deviation	1.38	1.08	0.21

Table 9.3

Dimensions of 11 tubular compound pisoliths from the East Pike mine, Weipa.

	length (l) (mm)	width (w) (mm)	l/w
Minimum	44	27	1.50
Maximum	59	32	1.84
Mean	49.3	29.9	1.65
Std. Deviation	3.8	1.8	0.09

Table 9.4

Dimensions of 17 ovate compound pisoliths
from Grunter, Ironbark and the Weipa-Andoom railway cutting.

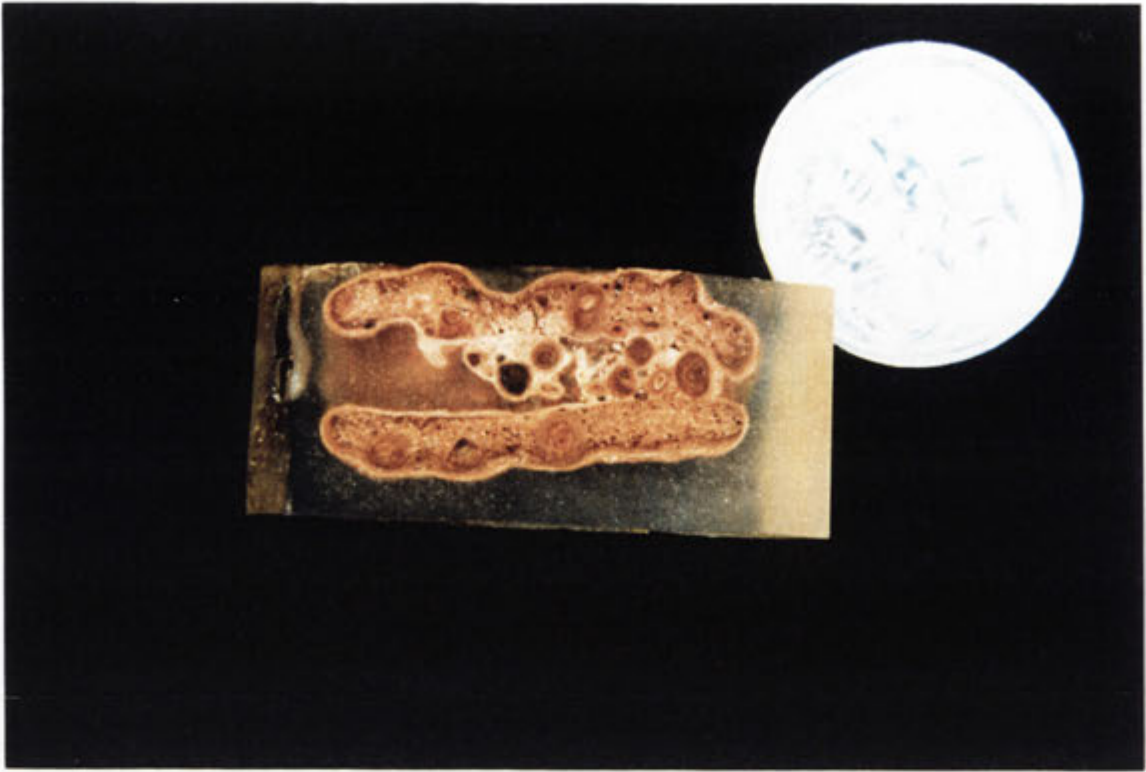


Figure 9.11.1

A sectioned tubular compound pisolith.



Figure 9.11.2

A sectioned ovate compound pisolith.

The remains of a broken common compound pisolith is evident in the internal chamber.



Figure 9.12

A broken ovate compound pisolith shell found in the soil horizon.

Similar, albeit calcareous structures, have been reported by Lea (1925) along a 500 kilometre stretch of the South Australian coastline, up to the West Australian border and for about 60 kilometres inland. These calcareous structures are believed to be constructed by the larval stage of the weevil, *Leptopius duponti* (Clog weevil) before undergoing pupation. *Leptopius duponti* belongs to the section of the weevil family called *Adelognatha*. Adult weevils in this section, possess a scar on the lower surface of the mandible where an accessory cusp was previously attached. Adult weevils are provided with the cusp to assist them during their emergence from the pupal cell (Zimmerman, 1994). Adult weevils inhabit the foliage of acacia trees while their larvae feed on the lower roots. The larva uses soil material to build its cocoon, usually quite close to the feeding area, 45 - 60 cm below ground level (Zimmerman, 1994). Normally, these cocoons are quite fragile until lime-rich water has infiltrated and hardened them.

The similar size and shape of ovate compound pisoliths when compared with the calcareous insect puparia indicate that *Leptopius duponti* or a similar species of weevil is responsible for the development of bauxitic ovate compound pisoliths. Within Australia, 82 species of *Leptopius* have been discovered, 35 of which inhabit Queensland (Zimmerman *pers. com.*, 1994). In the *Eucalyptus tetrodonta* forests of the Weipa area, *Acacia rothii* is the most common type of acacia tree growing (Specht, *et al.* 1977), which may provide a suitable food source for species of *Leptopius*.

Figure 9.13.1 is a photograph displaying the puparia of *Leptopius duponti* from the Elliston area, South Australia. The cocoons possess at least one opening into their inner chamber. Figure 9.13.2 is a photograph of ovate compound pisoliths from the Weipa-Andoom railway cutting, showing examples of both empty and infilled chambers. Lea (1925) explained the absence of large exit-holes in some of the puparia due to parasitism of the pupating weevil. After devouring the *Leptopius* larva the parasites leave the barren cocoon via small exit-holes. Such holes are much smaller than the escape-hole of the weevil, thereby leaving behind a shell which is less likely to be infilled.



Figure 9.13.1

Fossilised *Leptopius duponti* (Clog weevil) cocoons from the Elliston area, South Australia. Such cocoons are believed to be 100,000 years old and have become hardened by infiltrating lime-rich water.

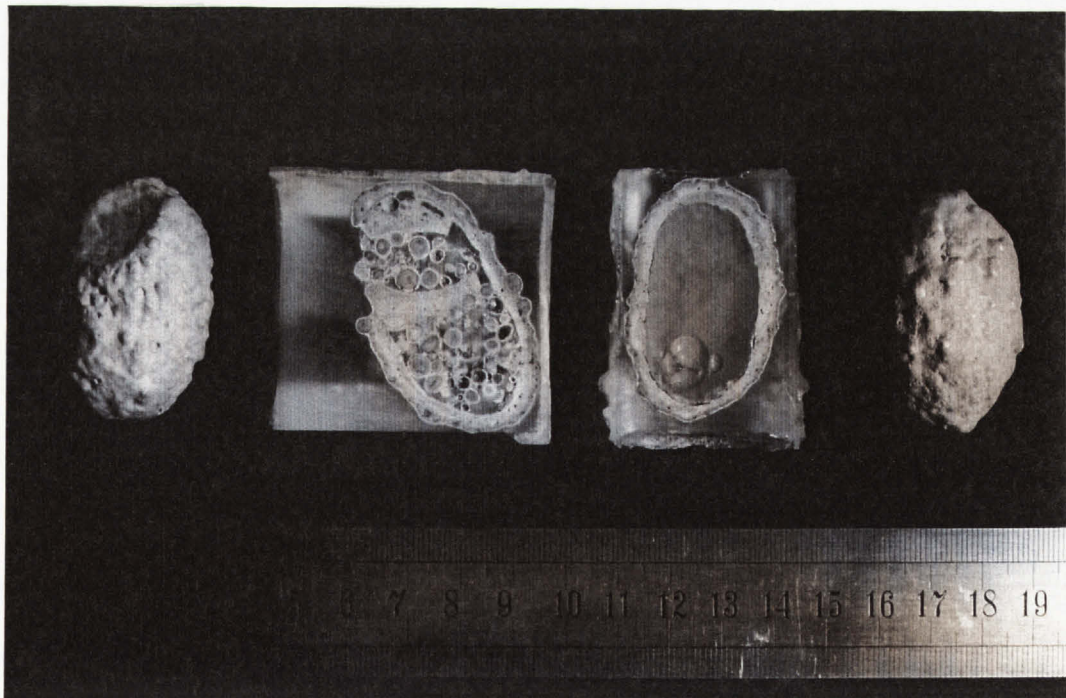


Figure 9.13.2

Ovate compound pisoliths from the Weipa-Andoom railway cutting, Weipa. Those shells which contain ordinary bauxitic pisoliths have an opening into the chamber, whereas those which are empty have no apparent opening.

9.5 Mass-balance

Field and laboratory investigations suggest that ferruginous-kaolinite nodules convert to common compound pisoliths by bauxitisation. To test this hypothesis, the mass change associated with bauxitisation was calculated and then compared with the morphology and densities of common compound pisoliths.

9.5.1 Density determination

The densities of ferruginous-kaolinite nodules and compound pisolith shells were determined using Archimedes Principle. Each sample was first weighed in air, after which it was suspended by a thread and weighed in a beaker of water. The ratio between the weight in air versus the weight in water gave the density of the sample. The principle was tested on quartz pebbles to determine the accuracy of the procedure. The technique gave values within $\pm 0.02 \text{ gcm}^{-3}$ of the actual density value of quartz (2.65 gcm^{-3}). Normally, density measurements of porous regolithic material are performed on wax-coated samples to minimise water absorption. As no air bubbles were evident escaping from the samples upon immersion in the water, it was decided not to coat them with wax. To be even more certain that water absorption did not significantly affect the measurements, the weight of the sample was recorded immediately after immersion in the beaker of water.

9.5.2 Results

The results of the density determinations are outlined in Table 9.5.

X₁ : ferruginous-kaolinite density					
Mean:	Std. Dev.:	Std. Error:	Variance:	Coef. Var.:	Count:
2.25	.105	.02	.011	4.652	27
Minimum:	Maximum:	Range:	Sum:	Sum Squared:	# Missing:
2.05	2.45	.4	60.74	136.927	0
X₁ : compound shell density					
Mean:	Std. Dev.:	Std. Error:	Variance:	Coef. Var.:	Count:
2.016	.069	.014	4.798E-3	3.436	23
Minimum:	Maximum:	Range:	Sum:	Sum Squared:	# Missing:
1.86	2.12	.26	46.362	93.559	0

Table 9.5

Samples from the Weipa-Andoom railway cutting, Weipa.

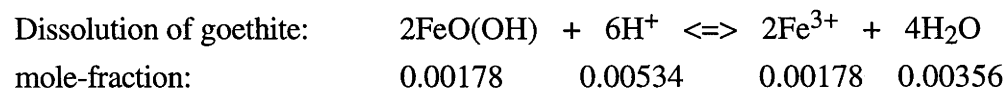
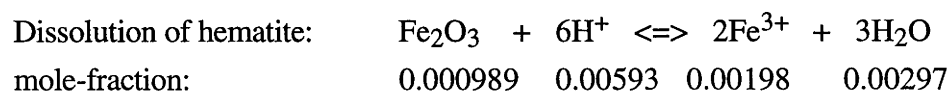
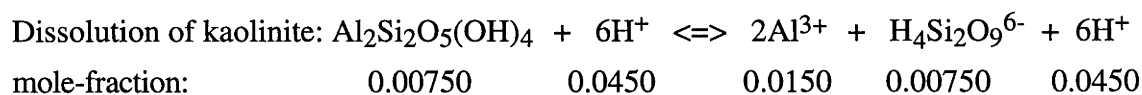
9.5.3 Calculations

A ferruginous-kaolinite nodule with an initial mineralogical composition of 86 wt.% kaolinite, 7 wt.% hematite and 7 wt.% goethite and a density of 2.25 gcm^{-3} would have a porosity of 22 % (see below). For simplicity, quartz, anatase and PDM were excluded from the calculations.

	$\rho \text{ (gcm}^{-3}\text{)}$	wt. %	$\rho\text{-fraction (gcm}^{-3}\text{)}$
Kaolinite	2.6	86	2.24
Hematite	5.2	7	0.36
Goethite	4.3	7	<u>0.30</u>
			2.90

$$\text{porosity} = 1 - 2.25 / 2.90 = 22 \%$$

	$\rho\text{-fraction (gcm}^{-3}\text{)}$	M (gmole ⁻¹)	mole-fraction
Kaolinite	1.935	258.14	0.00750
Hematite	0.158	159.70	0.000989
Goethite	<u>0.158</u>	88.85	0.00178
	2.251		

Mass loss during bauxitisation (per cm³)

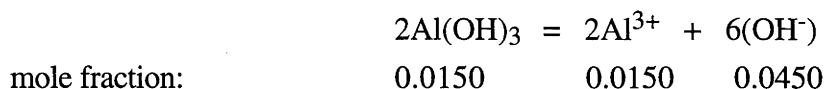
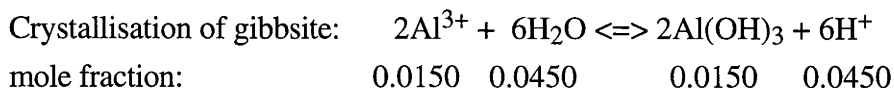
$$\text{mass (m)} = \text{moles (n)} \times \text{molecular weight (M)}$$

$$m_{\text{H}_4\text{Si}_2\text{O}_9^{6-}} = 0.00750 \times 204.18 = 1.531 \text{ g}$$

$$m_{\text{Fe}_2\text{O}_3} = 0.000989 \times 159.70 = 0.158 \text{ g}$$

$$m_{\text{FeO}(\text{OH})} = 0.00178 \times 88.85 = 0.158 \text{ g}$$

$$\text{total mass loss during bauxitisation} = 1.847 \text{ g}$$

Mass gain during bauxitisation (per cm³)

$$\text{mass (m)} = \text{moles (n)} \times \text{molecular weight (M)}$$

$$m_{\text{OH}^-} = 0.0450 \times 17 = 0.765 \text{ g (mass gained)}$$

$$\text{Net loss during bauxitisation (per cm}^3\text{)} = 1.847 \text{ g} - 0.765 \text{ g} = 1.082 \text{ g}$$

$$\therefore \text{density of the bauxitised nodule} = 2.251 \text{ gcm}^{-3} - 1.082 \text{ gcm}^{-3} = 1.17 \text{ gcm}^{-3}$$

However the mass is not evenly distributed within the bauxitised nodule but is concentrated in a shell. A compound pisolith shell with a mineralogical composition of 100 % gibbsite and a porosity of 22 % would have a density of 1.87 gcm⁻³.

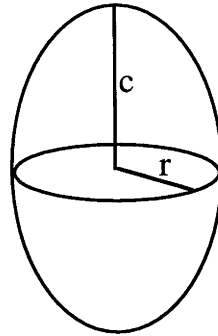
$$\text{porosity} = 1 - \rho_{\text{shell}} / \rho_{\text{gibbsite}} = 1 - 1.87 / 2.4 = 22 \%$$

\therefore the shell occupies: $1.17 / 1.87 = 0.63 = 63 \%$ of the total volume of the compound pisolith and the cavity occupies 37 %. In reality most common compound pisoliths contain some hematite, boehmite and anatase which increases the density to around 2.02 gcm⁻³ (see below).

Average common compound pisolith composition ($\rho=2.02 \text{ gcm}^{-3}$) from the Weipa-Andoom railway cutting, Weipa.

	$\rho \text{ (gcm}^{-3}\text{)}$	wt. %	$\rho\text{-fraction (gcm}^{-3}\text{)}$
Kaolinite	2.6	5.8	0.151
Hematite	5.2	2.2	0.114
Goethite	4.3	0.0	0.000
Gibbsite	2.4	81.4	1.954
Quartz	2.6	1.1	0.029
Boehmite	3.0	6.5	0.195
Anatase	3.9	3.0	<u>0.117</u>
			2.560

$$\text{porosity} = 1 - 2.02 / 2.56 = 21\%$$



$$\text{Volume of a prolate spheroid, } V = 4/3\pi r^2 c$$

Average length of common compound pisoliths = 24 mm

Average width of common compound pisoliths = 17 mm

$$\text{Total } V = 4/3 \pi (8.5)^2 \cdot 12 = 3632 \text{ mm}^3$$

$$\text{Chamber } V = 1344 \text{ mm}^3$$

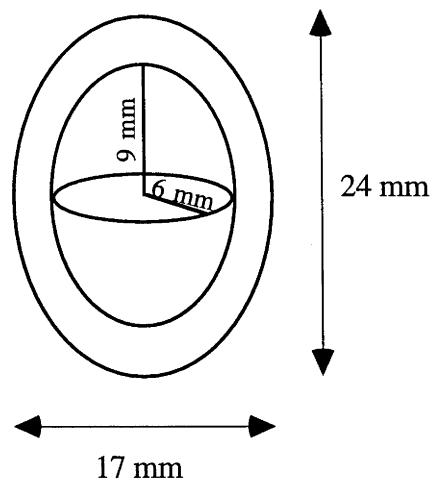
Length to width ratio of common compound pisoliths = 1.412

Length of chamber = 1.412r mm, Width of chamber = r mm

$$V = 4/3 \pi r^2 \cdot (1.412r)$$

$$r^3 = 3V / 5.648\pi$$

$$r = (227.24)^{1/3} = 6.1 \text{ mm, } c = 1.412r = 8.6 \text{ mm}$$



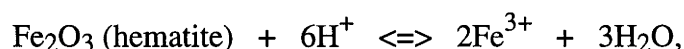
Comparison between the observed and calculated compound pisolith parameters:

	<u>observed #1</u>	<u>observed#2</u>	<u>observed#3</u>	<u>calculated</u>
cavity volume %	26	22	30	37
bulk ρ (gcm ⁻³) incl. cavity	1.51	1.61	1.43	1.17

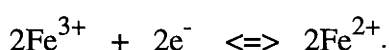
9.6 Discussion

Tardy (1993) believes that the development of bauxite is favoured over ferricrete formation, when the total annual rainfall exceeds about 1700 mm. Under such conditions, previously formed ferricrete undergoes dismantling while gibbsite accumulation takes place. Relative humidity and temperature are additional factors which control the development of either ferricrete or bauxite. Ferruginisation and the formation of ferricrete is favoured when the annual average relative humidity is around 60% and the temperature is about 28°C. Aluminium enrichment and bauxitisation on the other hand, develop at lower temperatures ($T > 22^\circ\text{C}$) and at relative humidities greater than 80% (Tardy, 1993). Taylor *et al.* (1992) showed that bauxite may even form under wet, cool to cold climatic conditions given sufficient time. The high temperatures, highly seasonal climate and fluctuating water table experienced at Weipa today, appear to be more conducive to ferricrete formation. These prevailing conditions have resulted in the chemical overprinting of the weathering profile by a mottled zone and a nodular ferruginous-kaolinite layer. The last bauxitisation episode was, and in some areas may still be, responsible for bauxitisation in the transitional zone. Ferruginous-kaolinite nodules are not stable in this zone and are in the process of transforming into bauxitic compound pisoliths (Figure 9.14). It appears that only nodules with a high percentage of kaolinite can transform to compound pisoliths during bauxitisation. Highly ferruginous nodules and those formed by the ferruginisation of bauxite, cannot transform to compound pisoliths due to them being deficient in kaolinite.

The transformation occurs when iron becomes mobilised and diffuses out of the nodule,



and



As well, kaolinite is dissolved, leaving behind bauxite minerals. The kind of bauxite mineral precipitated may depend on the thermodynamic activity of water in the immediate environment. For example, less hydrated minerals such as tohdite and eta alumina may only precipitate in micro-environments where the water activity is very low.

Evolution of compound pisoliths

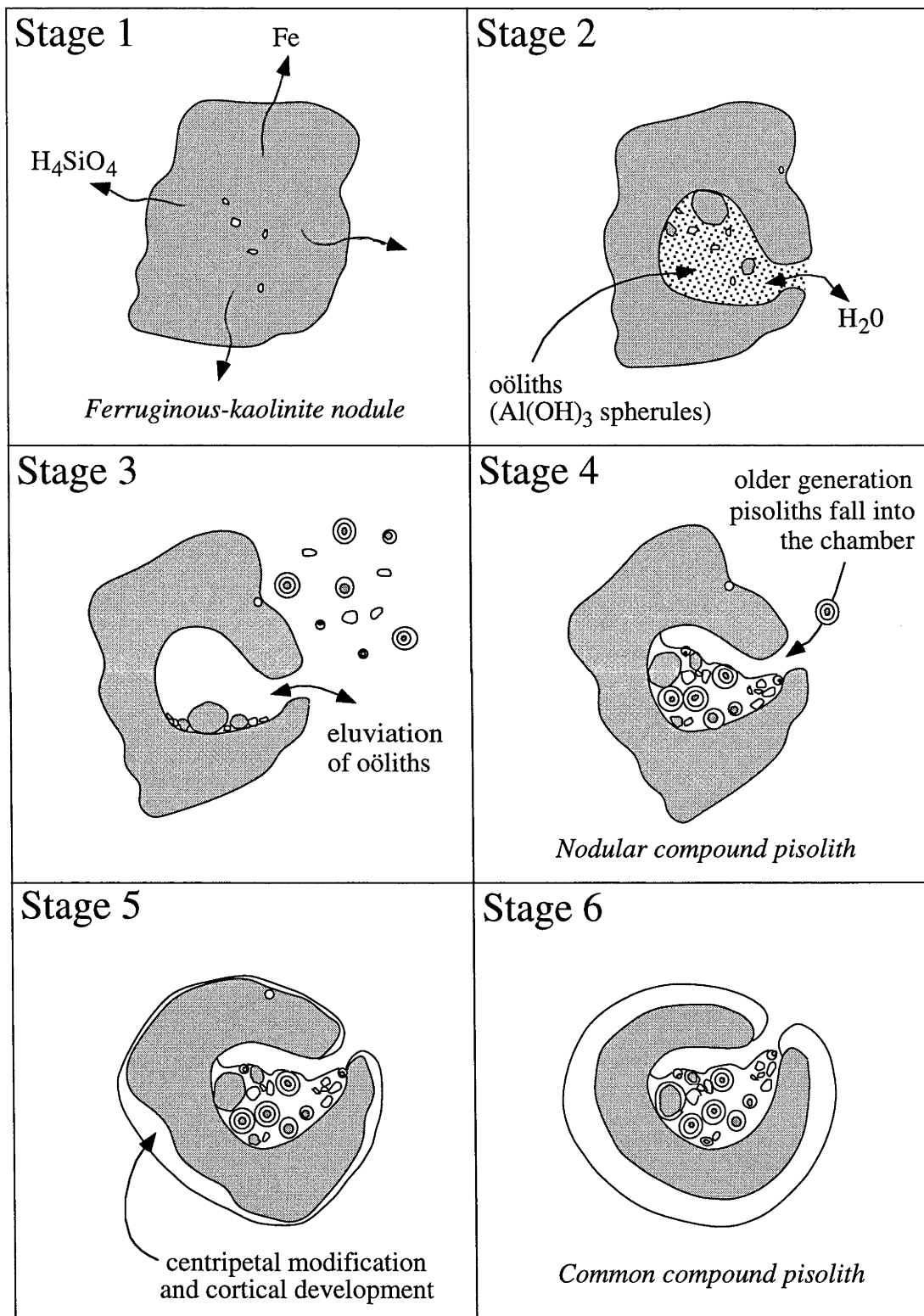
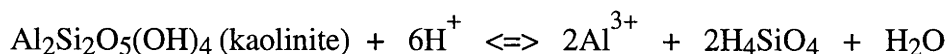


Figure 9.14



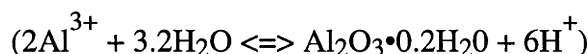
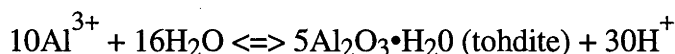
and



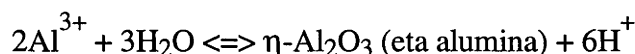
or



or



or



Mobilisation and diffusion is more pronounced along zones of pre-existing weakness resulting in an asymmetrical chemical gradient. A zone of enhanced permeability is created from the interior of the nodule to the outer surface when $\text{Al}(\text{OH})_3$ precipitates out as spherules. This zone facilitates the movement of solutions in and out of the nodule creating progressively larger dissolution voids within the interior of the nodule. Fragments of the pre-existing nodule which are trapped within the forming shell, may develop cortices and become pisoliths.

The cortices of common compound pisoliths are usually well developed, suggesting that common compound pisoliths are more mature than nodular ones. Two packets of cortical layering are recognised around common compound pisoliths while only one very thin cortical layer is observed around nodular compound pisoliths. At one stage in their development, common compound pisoliths may have resembled nodular ones, albeit more smoother and ellipsoidal in shape (stage 1 of Figure 9.15). Further bauxitisation formed the first cortex around them (stage 2). This may have been followed by a kaolinisation/ferruginisation event causing the brecciation of some compound pisoliths and the agglomeration of clayey material (stage 3). The last bauxitisation episode was responsible for the formation of the outer cortex (stage 4).

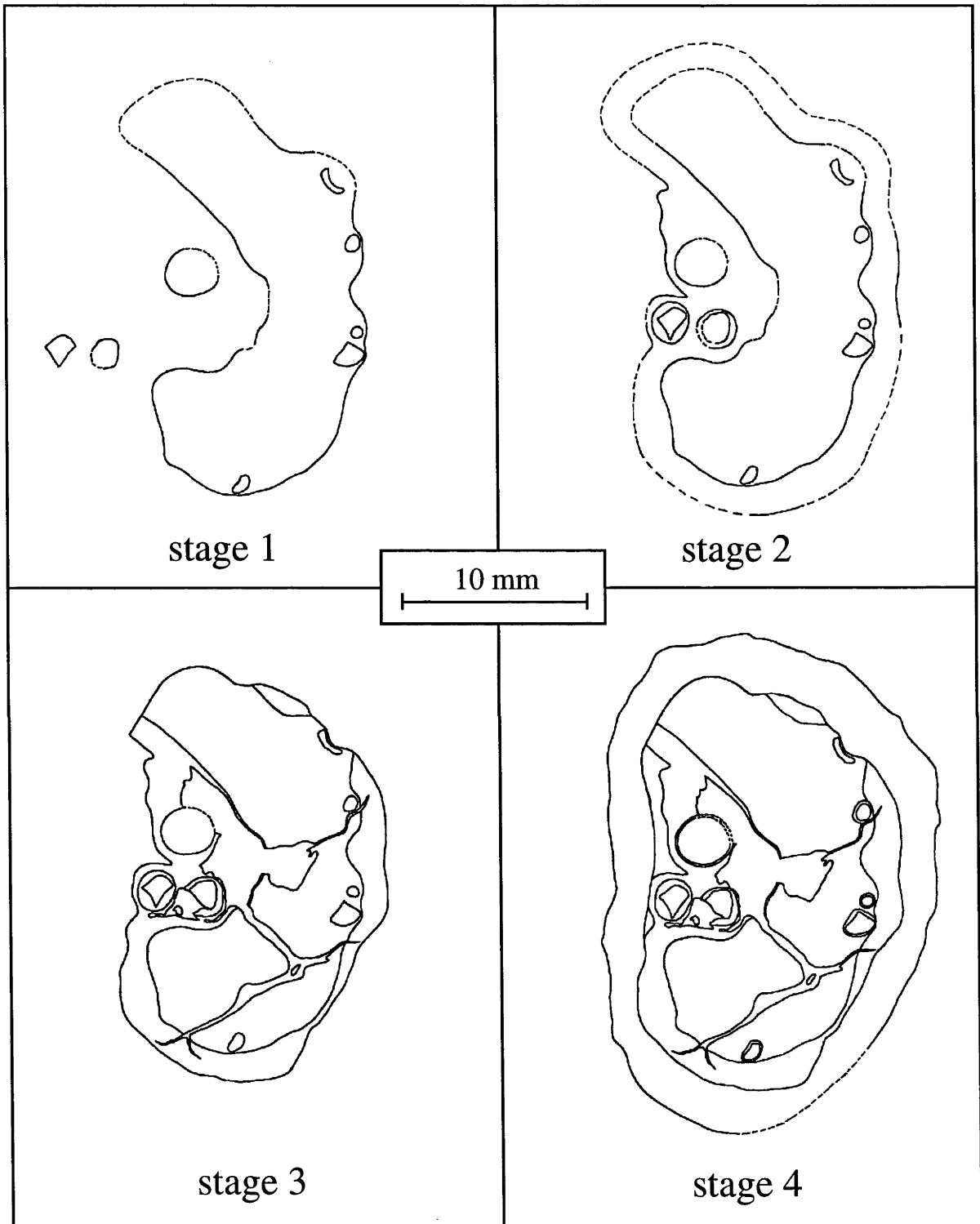


Figure 9.15

Stages in the development of a common compound pisolith from the Longtom mine, Weipa.

A layer of smooth and ellipsoidal ferruginous-kaolinite nodules, exposed at the Weipa end of the Weipa to Andoom railway cutting, grades into a common compound pisolith layer, up dip along the exposure (Figure 9.16). Within this zone, the cortices of common compound pisoliths become progressively thicker and more complex with increasing maturity.

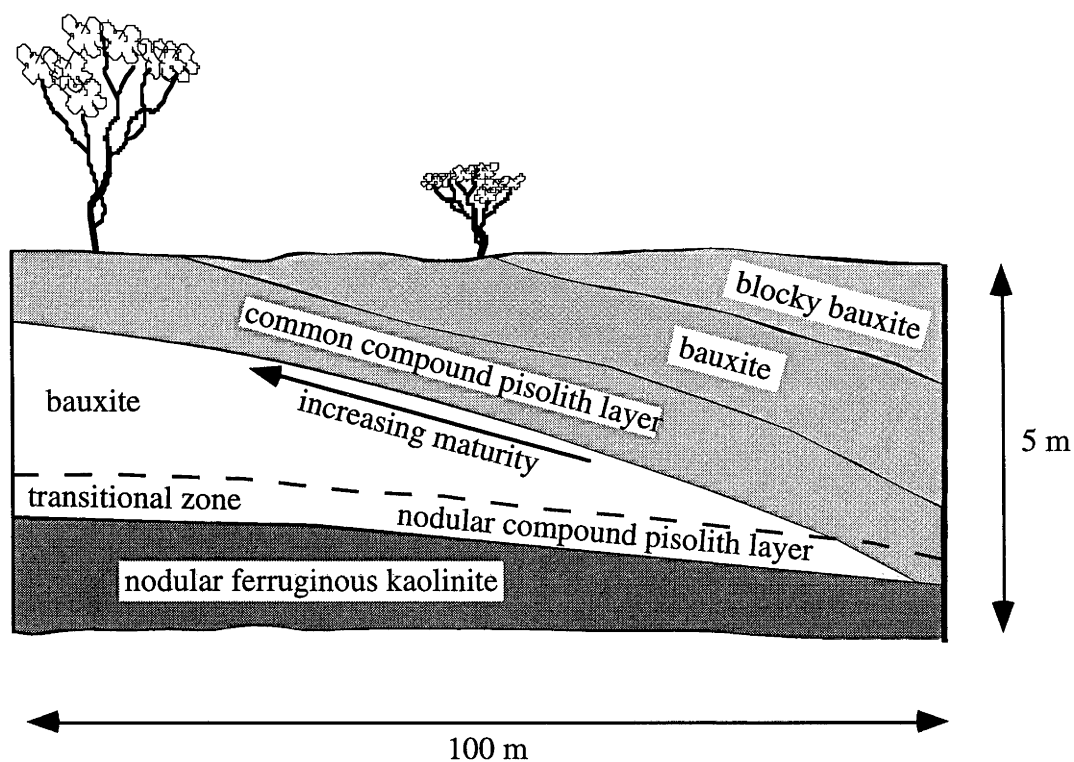


Figure 9.16

Exposure at the Weipa end of the Weipa to Andoom railway cutting.

The changing internal morphology of the nodules and compound pisoliths within this zone, provides clear evidence for the transformation of ferruginous-kaolinite nodules into common compound pisoliths. However, a direct link between common and nodular compound pisoliths cannot be made in most areas because a layer of bauxite which contains very few if any compound pisoliths separates the common and nodular compound pisolith layers. It is probable that a layer of ferruginous-kaolinite nodules once existed at the top of the weathering profile. A change in the climate and/or hydrological conditions may have favoured bauxitisation, resulting in the transformation of the nodules to compound pisoliths while the underlying mottled zone developed into single pisoliths. During the ferruginisation/kaolinisation stage which followed, a layer of ferruginous-kaolinite nodules developed at a deeper level which later became nodular compound pisoliths during a subsequent stage of bauxitisation.

Chapter 10

The evolution of bauxitic pisoliths

10.1 Introduction

The previous chapter brought to light compelling evidence that ferruginous-kaolinite nodules are precursory to the development of common and nodular compound pisoliths. A proportion of single bauxitic pisoliths, particularly those which have quartz-rich cores, may also be derived from the modification of ferruginous-kaolinite nodules. However, the majority of concentrically-banded bauxitic pisoliths and those with vitreous cores evolve in a similar manner to that proposed by Nahon (1991), except that aluminium accumulates during centripetal three-dimensional glaebulisation rather than iron. In the case of vitreous-core pisoliths composed of PDM, their dense cores are produced when there is total epigenetic replacement of kaolinite with tohdite and/or eta-alumina. If pisolith formation relied solely on the bauxitisation of ferruginous-kaolinite nodules, pisolith cores would be dominantly porous and/or quartz-rich.

10.2 The mobilisation and accumulation of iron

The addition of new material to the outside surface of an existing pisolith is termed *agglomeration*. Agglomeration is associated with the epigenetic replacement of kaolinite with hematite, resulting in the formation of ferruginous-kaolinite nodules. Under the same climatic and/or hydrological conditions, the kaolinisation of bauxite may also occur, resulting in the formation of kaolinite and its adhesion together with residual quartz grains onto the outer surface of spherules and older generation pisoliths (Figure 10.1.1). During kaolinisation, bauxitic pisoliths may become brecciated due to expansion (Figure 10.1.2). The existence of quartz-rich zones between 2 sets of cortical layering within bauxitic pisoliths may be explained by the process of agglomeration. In such cases an agglomerative phase occurred between two phases of cortication (i.e. bauxitisation→kaolinisation→bauxitisation).



Figure 10.1.1

Bauxite undergoing kaolinisation in the mottled zone at the "Old Kaolin Pit", Nanagai, East Weipa.

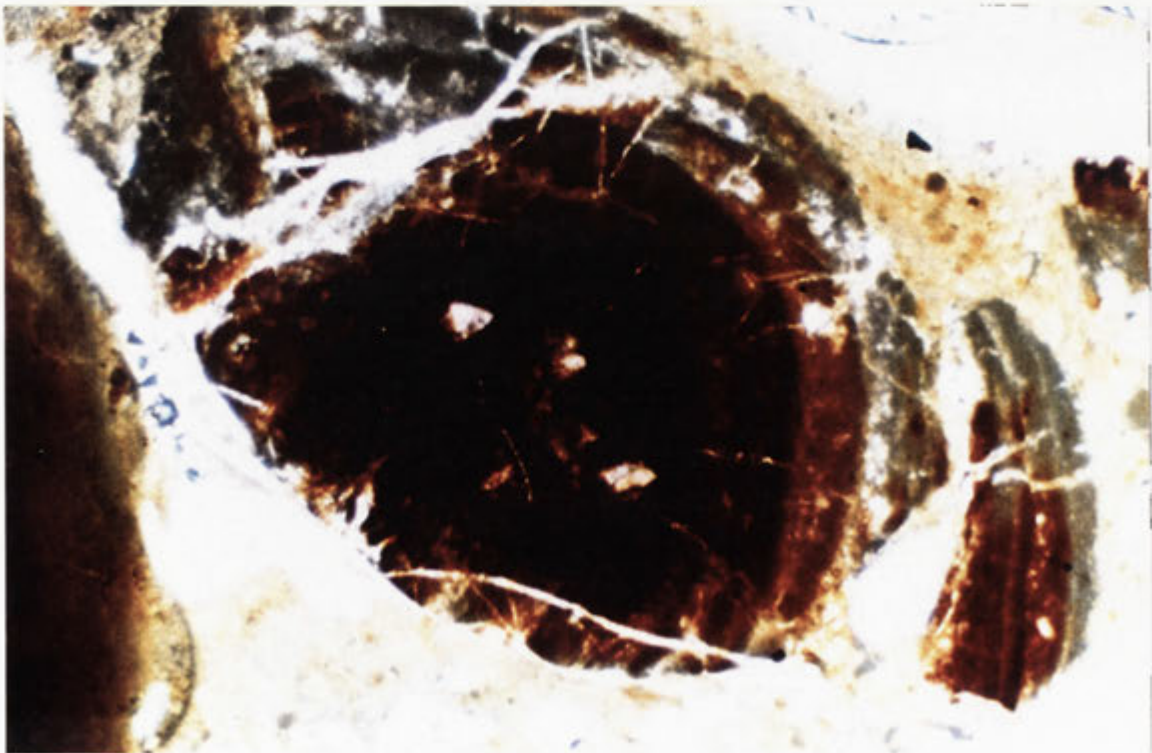
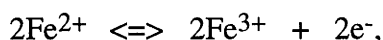


Figure 10.1.2

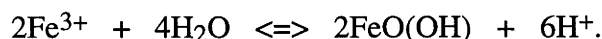
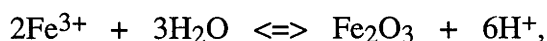
Close-up of one of the bauxitic pisoliths undergoing kaolinisation. Silicification and localised deferruginisation result in the brecciation of bauxitic pisoliths.

Centripetal three-dimensional glaebulization begins when iron becomes mobilised in a reducing environment in the form of Fe^{2+} . Migration of these ions occurs from one site to another due to differences in oxido-reduction potential (Eh), porosity variations and differential drying of the argilloferruginous plasma. According to Bourrie and Pedro (1979), when a weathering profile drains and dries out after a wet period, water is retained in pores of progressively smaller size. It is in these zones of finer porosity, associated with a higher kaolinite concentration, that iron tends to accumulate in the form of aluminous hematite rather than aluminous goethite, due to the lower activity of water. In larger voids, for example those that are produced by the dissolution of quartz grains, the activity of water is much higher, therefore favouring the precipitation of Al-goethite.

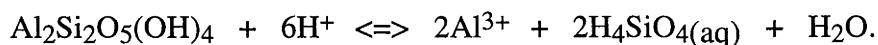
The chemical processes responsible for iron accumulation are the oxidation of the soluble Fe^{2+} cation to Fe^{3+} :



and the subsequent precipitation of hematite or goethite:



During the precipitation of hematite or goethite, kaolinite is dissolved by means of protons liberated during hydrolysis of the Fe^{3+} ion (Nahon 1991). The following equation represents the dissolution of kaolinite:



Within the mottled zone of the weathering profile, iron accumulation and the accompanying dissolution of kaolinite, leads to the development of ferruginous-kaolinite nodules and mottles. In the zones adjacent to iron accumulation percolating water dissolves quartz grains. The remaining kaolinite grains become disaggregated and removed by the percolating water. Tubular macrovoids are produced which may subsequently infill with very fine authigenic kaolinite or kaolinite derived from overlying or upslope layers.

10.3 Nodule to pisolith transformation

When a ferruginous-kaolinite nodule is bauxitised, either η -alumina, tohdite, boehmite or gibbsite will form depending on the water activity (a_w) of the micro-environment. If the kaolinite grains within the nodule are very small, then the intercrystalline voids are correspondingly so. The activity of water within such fine pores may be so low that η -alumina may form. The resultant size of crystals is related to the pore diameter and the space available for crystal growth, therefore η -alumina and tohdite can only exist as very small (≈ 10 nm) crystals within pisoliths. Where pore sizes are a little larger and a slightly higher water activity prevails, boehmite becomes the dominant aluminium-rich mineral. Boulangé (1983) noted that boehmite tended to be more concentrated in the core of pisoliths than in the surrounding plasma. In the largest pores, dissolution voids and in the plasma that surrounds nodules and pisoliths, only gibbsite normally crystallises, as the water activity is usually too high for the more dehydrated phases to form. Under such conditions, well-formed gibbsite crystals up to $10\ \mu\text{m}$ in length can develop.

A morphological continuum exists between compound and quartz-rich pisoliths, suggesting that similar processes were responsible for their evolution (Figure 10.2). It is probable that the size of the parent ferruginous-kaolinite nodule governs the morphology and dimensions of the resulting compound or quartz-rich pisolith: large ferruginous-kaolinite nodules transform into compound pisoliths while small ones evolve into single quartz-rich pisoliths. Alternatively, the cores of quartz-rich pisoliths may be the broken remnants of compound pisoliths.

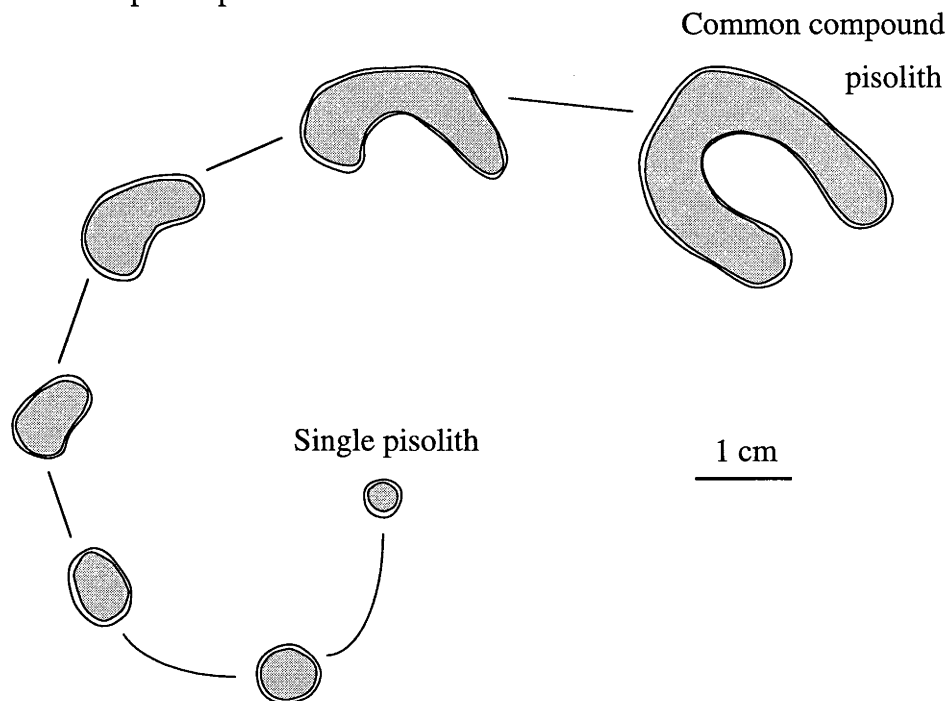


Figure 10.2

Apparent continuum in the morphology of quartz-rich single and compound pisoliths.

10.4 The mobilisation and accumulation of aluminium

Spherulisation is the development of aluminous spherules in a kaolinitic plasma due to the progressive epigenetic replacement of kaolinite with either gibbsite, boehmite, tohdite or eta-alumina.

During the formation of ferruginous-kaolinite nodules, aluminium and silica mobilises and migrates out of the developing mottles and nodules into the surrounding kaolinite-rich tubules. In solution, dissolved aluminium can exist in many different forms. The most important species in the absence of other ligands are Al^{3+} , $\text{Al}(\text{OH})^{2+}$, $\text{Al}(\text{OH})_2^+$, $\text{Al}(\text{OH})_3$ and $\text{Al}(\text{OH})_4^-$ (Figure 10.3).

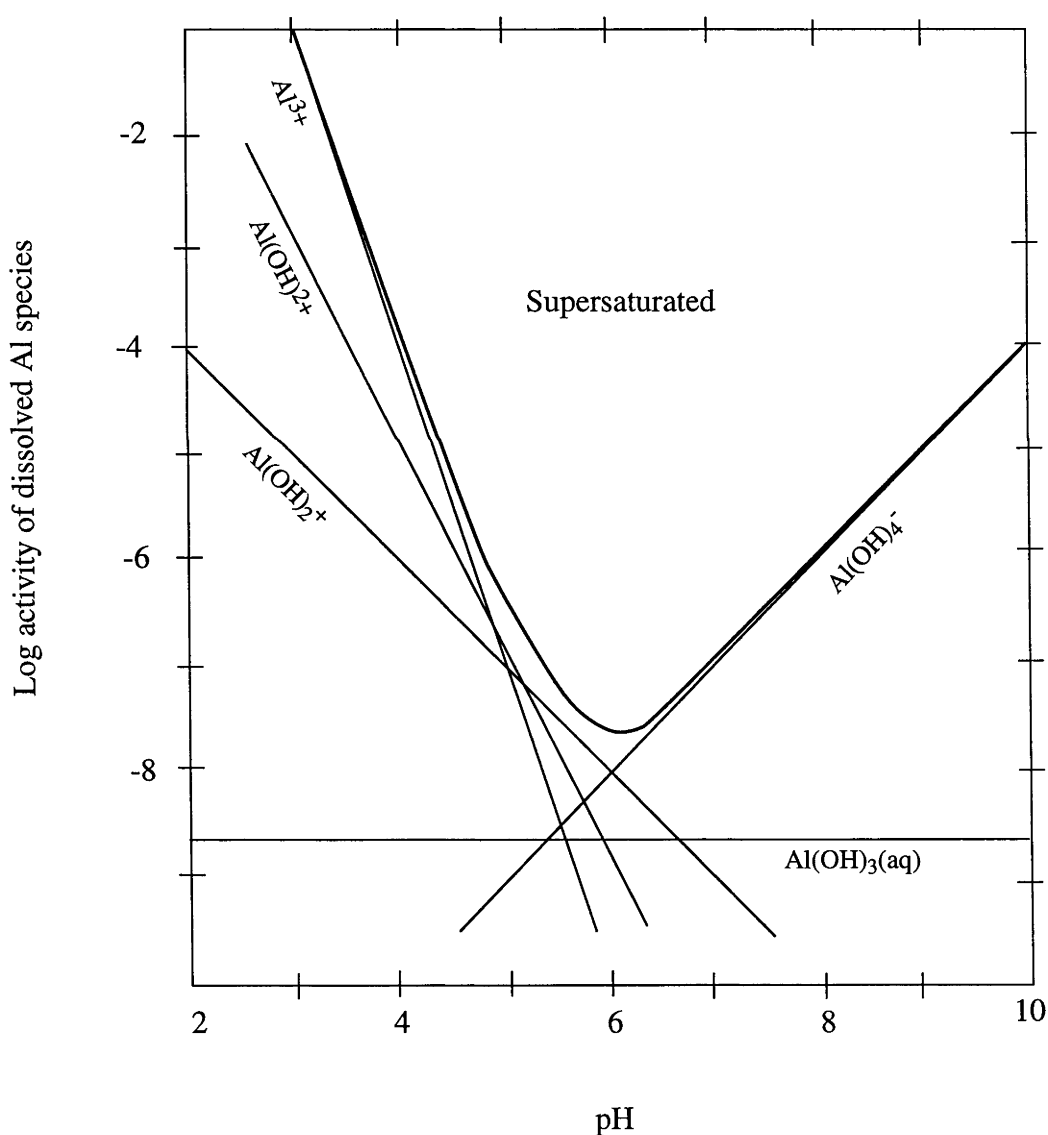
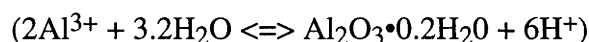
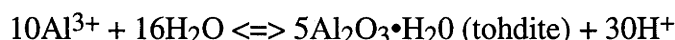
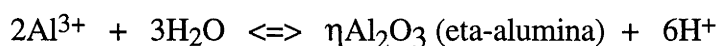


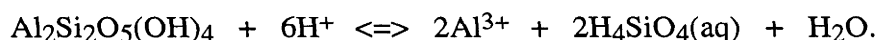
Figure 10.3

Activities of dissolved aluminium species in equilibrium with gibbsite at 25°C. Bold line represents the sum of the individual activities (after Drever, 1988).

At low pH, the Al^{3+} ion is the dominant species in solution (Drever, 1988). Within the kaolinite-rich tubules of the mottled zone, dissolved aluminium and silica may recombine to form authigenic kaolinite. Alternatively, dissolved aluminium may migrate into and epigenetically replace the kaolinitic plasma with PDM or other bauxite minerals while dissolved silica is flushed away in the percolating water.



During the precipitation of gibbsite, boehmite, tohdite or eta-alumina, the dissolution of kaolinite occurs as a result of protons liberated during hydrolysis of the Al^{3+} ion. The following equation represents the dissolution of kaolinite:



As centripetal three-dimensional glaebulization proceeds, kaolinite is progressively replaced, resulting in the formation of aluminous nodules. Different stages in the evolution of pisoliths can be seen in the mine face of the "New Kaolin Pit" at Nanagai (Figure 10.4). Aluminous spherules and pisoliths are found at different stages of development within the kaolinite-rich tubules of the mottled zone. The adjacent ferruginous-kaolinite nodules appear to be in the process of transforming into nodular compound pisoliths. The majority of pisoliths have kaolinitic cortices which suggests that the resilicification of bauxite is the dominant process at present. Bauxitisation of a mottled zone such as this, will result in the development of a pisolitic bauxite horizon containing scattered compound pisoliths (Figures 10.5 and 10.6).



Figure 10.4

The upper part of the mottled zone exposed in the mine face of the "New Kaolin Pit" at Nanagai, East Weipa.

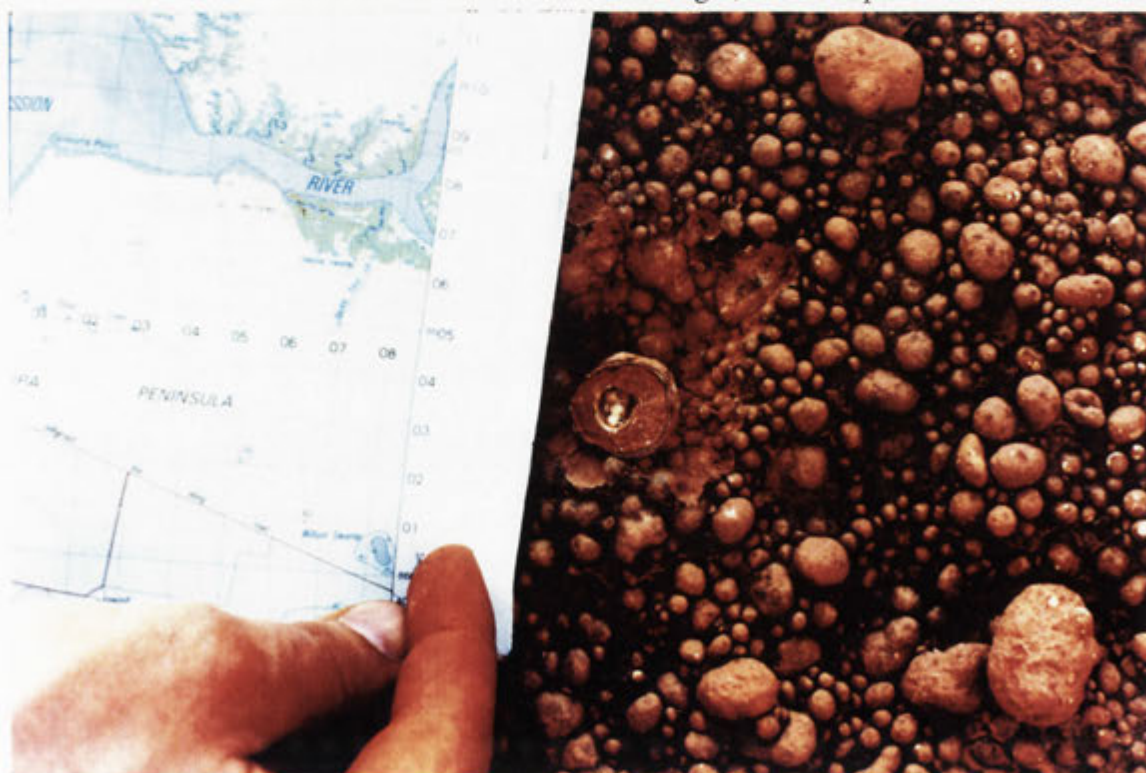


Figure 10.5

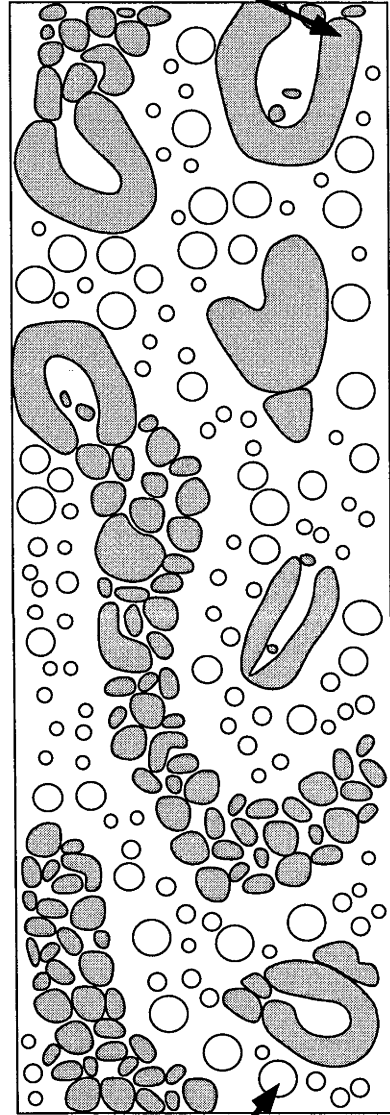
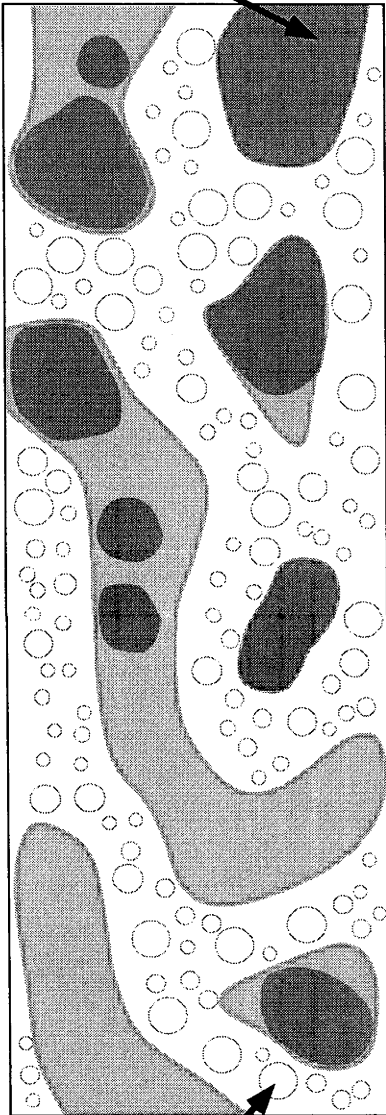
The upper part of the bauxite horizon in the road cutting between the East Weipa mine centre and the Jewfish mine.

Mottled Zone

Bauxite Horizon

ferruginous-kaolinite
nodule

bauxitic compound
pisolith



aluminous spherule

bauxitic pisolith

Bauxitisation



Figure 10.6

Model for the bauxitisation of a mottled horizon. The process leads to the development of a pisolitic bauxite containing scattered compound pisoliths.

10.5 Cortical development

The process of *cortication*, which is intrinsically linked to bauxitisation, leads to the formation of concentrically-banded cortices around spherules and nodules. Chemical reactions which contribute to cortication include hydration, dehydration, silicification, desilicification, ferruginisation and deferruginisation.

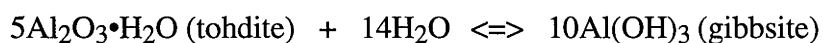
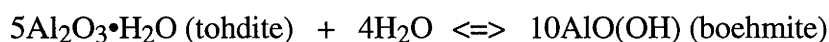
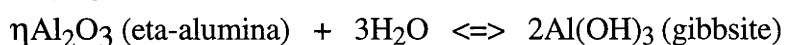
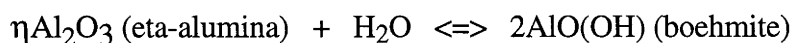
It is widely accepted that accretionary processes are responsible for the formation of calcareous oöliths and pisoliths in a marine environment. Bauxitic pisoliths from Weipa display similar features which give the impression that they too may have formed by the process of accretion. Such pisoliths are composed of angular segments which have their zoning sharply truncated by the surrounding envelope (Figure 10.7). Carozzi (1960) described such structures as having been formed by the successive growth, fracturing and regrowth of material around pisolith fragments.

Alternatively, the same structures may be explained by the progressive inward modification of a pisolith during weathering (Figure 10.8). The first step towards centripetal reorganisation as described by Jones (1965), involves the disruption of the concentric structure in one part of a pisolith. The next step involves the replacement of the disorganised area, by similar material having zoning which is often discordant to the underlying banding.

Jones indicated that both processes exist, and that in most cases it is extremely difficult to interpret which one is responsible for cortical development. However he did conclude, that pisoliths which formed in a lateritic environment, were most probably derived from the progressive centripetal modification of a nodule.

Tardy and Nahon's (1985) theory of pisolith formation is based on the centripetal evolution of pisoliths from pre-existing nodules. For iron-rich pisoliths, the transformation occurs when Al-goethite forms at the expense of earlier formed Al-hematite.

Similarly, the process of progressive rehydration may explain the formation of cortices around bauxitic pisoliths. Here, dehydrated phases such as η -alumina and tohdite become progressively rehydrated resulting in the formation of either a gibbsitic or boehmitic cortex (Figure 10.9).



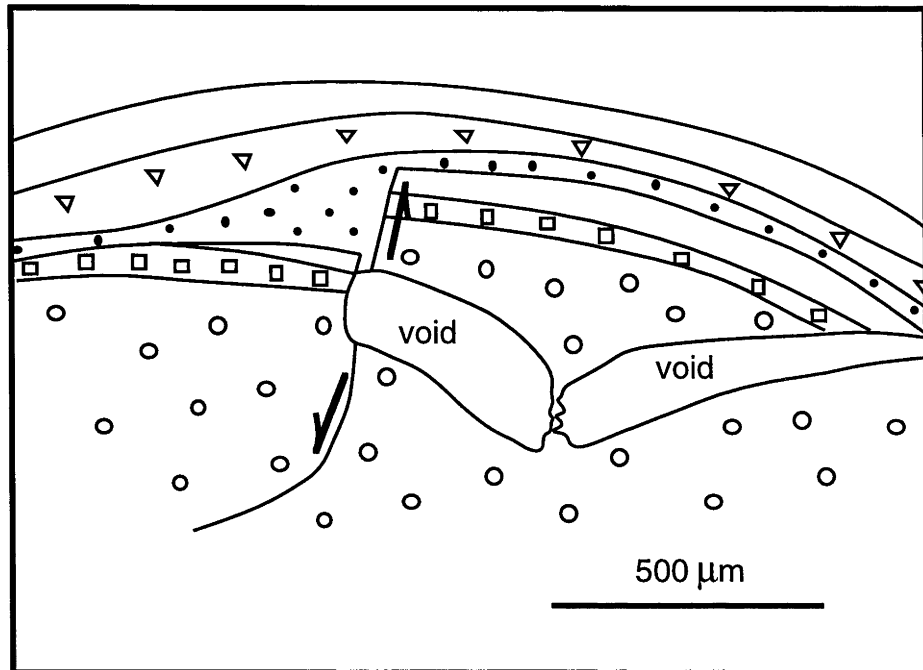


Figure 10.7

Sedimentological evidence indicating the outward growth of bauxitic pisoliths. Micro-faulting of the pisolith was followed by the deposition of material. The fine-scale banding in the outer cortex appears to drape over the fault.

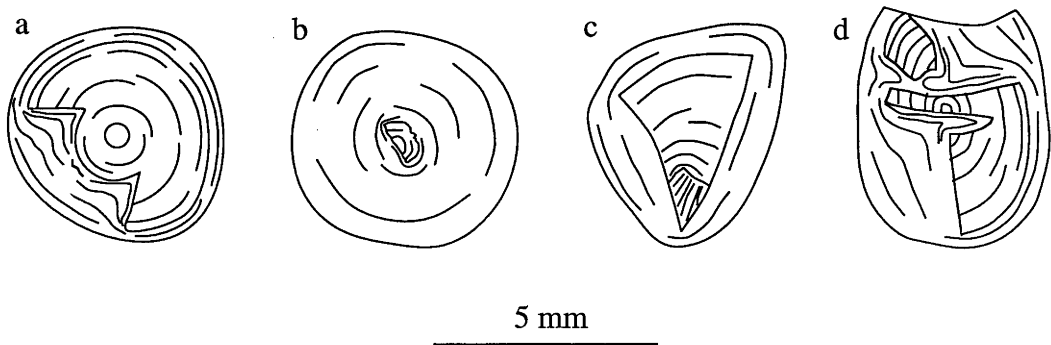


Figure 10.8

Pisoliths displaying centripetal replacement structures from Lokoja and Birnin Kebbi, Nigeria. (a) An early stage in the replacement of a pisolith. (b) An advanced stage in the replacement of a pisolith. (c) Interruption of the replacing process and recommencement on a different part of the pisolith results in complex structures such as this. (d) Replacement originating from cracks in the pisolith. Fragments of the original pisolith now isolated by replacing material can be identified (from Jones, 1965).

The Theory of Pisolith Formation

(modified from Nahon, 1991)

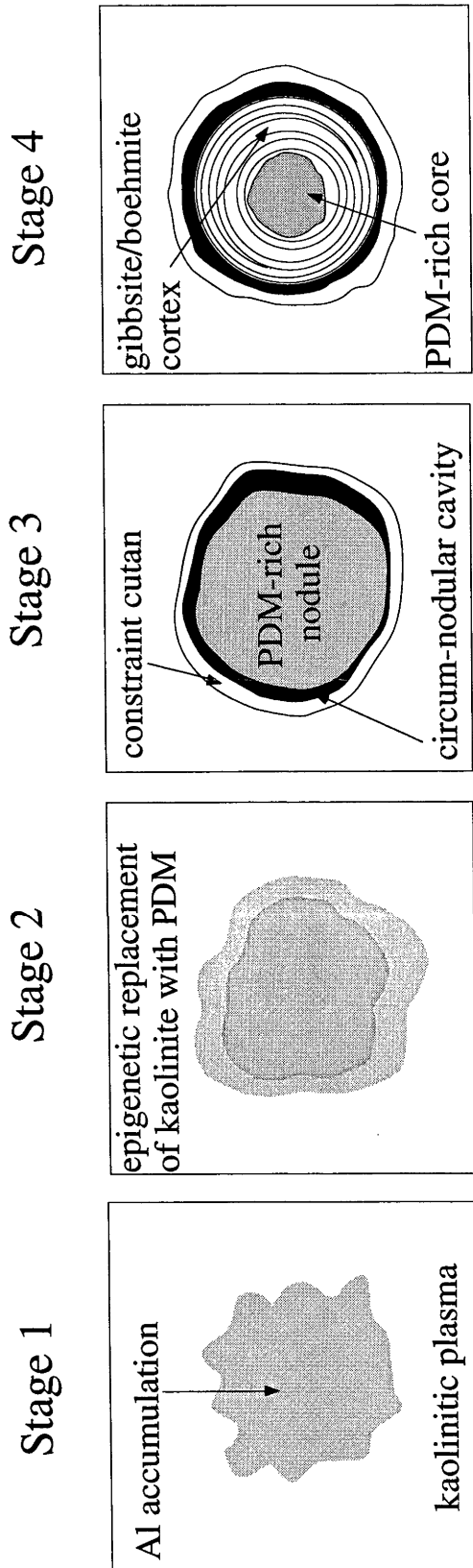


Figure 10.9

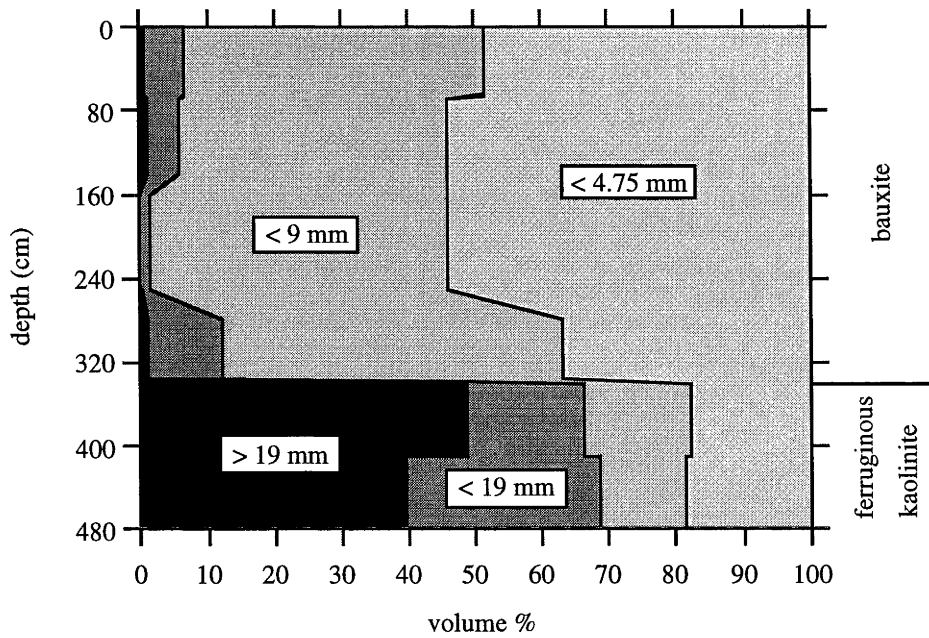
In the process, average crystal sizes tend to become larger. If quartz is present it may become etched, leading to the formation of dissolution voids. These voids provide ideal sites for the growth of well-formed and relatively large gibbsite crystals. Reduction of hematite and mobilisation of iron occurs in the core of the nodule. Diffusion of iron progresses outwardly with subsequent oxidation and precipitation of hematite in the outer cortex. Sometimes iron-rich diffusional bands may become destabilised, by the reduction of hematite and mobilisation of iron out of the pisolith. At any stage during the formation of the cortex, silica-rich ground waters can alter the previously formed gibbsite or boehmite back into kaolinite. The interplay of these processes effectively reorganises the structure and mineralogy of pisoliths. Progressive reorganisations result in the pisoliths becoming increasingly smooth and spherical with strongly banded cortices.

A maximum of three distinct packets of cortical layering are recognised within the pisoliths of Weipa. A relative concentration of quartz often marks the boundary between two packets of cortical layering. When quartz is absent, there is invariably evidence for a hiatus in the form of truncated cortical banding and/or radial cracks. Bauxitic pisoliths from Weipa appear to have undergone a maximum of three separate phases of bauxitisation during their evolution. In the intervening periods, kaolinisation and ferruginisation were the dominant processes, leading to mottle and nodule formation.

10.6 Evolution of the Weipa bauxite deposit

Calculations performed by Loughnan & Bayliss (1961) and Jepsen & Schellmann (1974), indicate that the bauxite deposit at Weipa is early Tertiary in age. Within a time span of 50 million years it is conceivable that the Weipa Peninsular, as with other parts of the world, has undergone periodic changes in climate. Such climatic changes, could have produced the mineralogical and structural complexities seen in bauxitic pisoliths and the profiles they exist in. The realisation that common compound pisoliths form from ferruginous-kaolinite nodules, allows us to interpret the distribution of compound pisoliths within the weathering profile as zones where ferruginous-kaolinite nodules once existed. Analysis of the particle sizes within the weathering profile highlights the distribution of compound pisoliths; i.e. particles > 19 mm (Figure 10.10). The appearance of the weathering profile at specific times in the past can be reconstructed using such information (Figure 10.11). The evolution of the weathering profile determined by this method is directly correlatable with the evolution of compound pisoliths determined independently from thin-section studies. The evolutionary model can be extended to single bauxitic pisoliths with good agreement.

Size distribution in the Weipa-Andoom railway cutting



Size distribution in the Jewfish road cutting

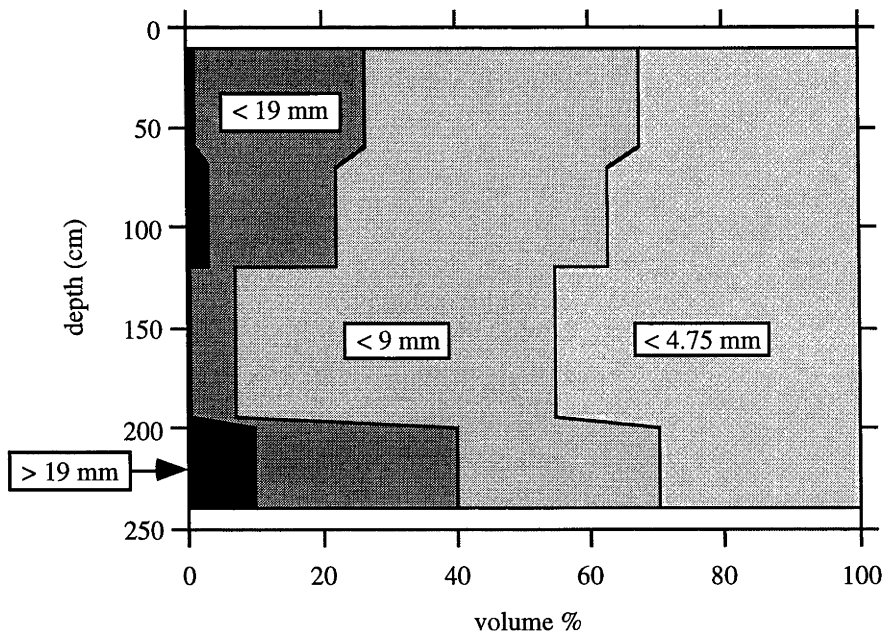


Figure 10.10

Particle size distributions within the bauxite horizon.

Evolution of the Weipa bauxite deposit

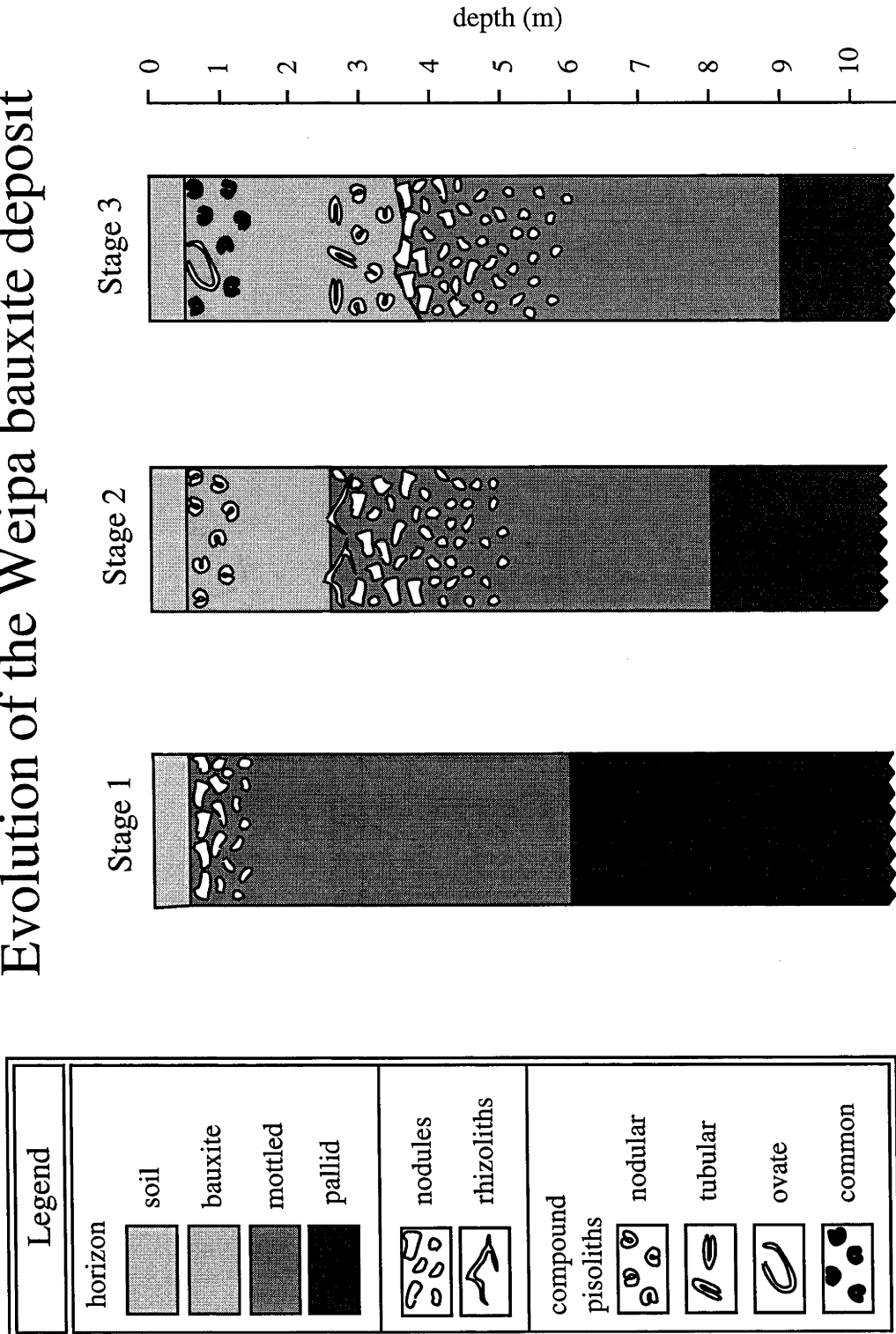


Figure 10.11

Model for the evolution of the Weipa bauxite deposit

10.7 Evolution of the weathering profile

A study by Dammer *et al.* (1994) of weathering-related cryptomelane ((K,Ba)MnO₁₆.xH₂O) from Groote Eylandt, Northern Territory yielded K-Ar ages in 3 groups: 6-20 Ma (Middle to Late Miocene), 30-40 Ma (Oligocene) and 46-54 Ma (Early to Middle Eocene). Dammer *et al.* (1994) interpreted the distribution of ages as evidence for three major periods of intense chemical weathering, corresponding to more humid conditions. Coincidentally, bauxitic pisoliths in the Weipa area contain evidence for up to three separate phases of cortication, attributed to three distinct episodes of bauxitisation. The similar latitudes of the two sites (Groote Eylandt; 14°S and Weipa; 12.5°S) and their close proximity to each other (600 kilometres) allows for a correlation to be made between the relative ages obtained in bauxitic pisoliths with those absolute ages derived from the K-Ar dating of cryptomelane.

Before the first period of bauxitisation, conditions were more favourable for the formation of a mottled zone composed of ferruginous-kaolinite mottles and kaolinite-rich tubules. The profile at this stage may have resembled the "immature" profile developed on the Embley Range, east of Weipa. The ferruginous-kaolinite mottles and nodules within this profile are composed of kaolinite (≈40%), goethite (≈30%), hematite (≈10%) and quartz (≈20%). Based on Dammer *et al.*'s (1994) work, intense chemical weathering, which may be associated with bauxitisation, probably began during the Early Eocene. Leaching of iron and silica from the mottled zone led to the formation of small aluminous spherules. Further bauxitisation formed gibbsitic or boehmitic cortices around these aluminous spherules leading to the evolution of protopisoliths and oöoliths.

By the Middle Eocene, the climate may have become increasingly arid and seasonal, (Dammer *et al.*, 1994) resulting in the cessation of bauxitisation. Kaolinisation of the profile resulted in the brecciation of protopisoliths. The highly fluctuating water table favoured the reinstatement of a mottled zone and a layer of ferruginous-kaolinite nodules near the surface.

The onset of the second bauxitisation episode, possibly during the Oligocene (Dammer *et al.*, 1994), may have resulted in the transformation of large ferruginous-kaolinite nodules into compound pisoliths. Further bauxitisation formed a cortex around compound and single pisoliths. By the end of the second bauxitisation phase, the top part of the profile may have been composed predominantly of bauxite.

The reinstatement of monsoonal conditions, associated with a seasonally fluctuating water table, may have been responsible for the development of a mottled zone beneath the bauxite horizon. A layer of ferruginous-kaolinite nodules and rhizoliths formed at the top of the mottled zone. Partial kaolinisation of the profile resulted in the fragmentation of pisoliths. The development of cracks within pisoliths probably occurred during this time.

The last major period of more intense chemical weathering and associated bauxitisation, possibly spanning the Middle and Late Miocene (Dammer *et al.*, 1994), resulted in the transformation of ferruginous-kaolinite nodules into nodular compound pisoliths. During the same period, rhizoliths transformed into tubular compound pisoliths and the outer cortex formed around single and common compound pisoliths. The bauxite horizon became thicker and more concentrated in alumina.

The present-day monsoonal climate is not conducive to bauxitisation. The conditions are more favourable for the development of ferruginous-kaolinite nodules topping a mottled zone. Kaolinisation of the overlying bauxite is presently occurring, resulting in the formation of kaolinite in the outer cortex of bauxitic pisoliths.

APPENDICES

Appendix 1 Bauxite sample catalogue

Drill Hole	Location (mine coordinates)	Depth Interval (metres)	Sample name
WEIPA			
WB837EH	25000E 9000N	0.62-0.75	W1
		0.75-1.00	W2
		1.00-1.25	W3
		1.25-1.50	W4
		1.50-2.00	W5
		2.00-2.50	W6
		2.50-2.75	W7
		2.75-3.00	W8
		3.00-3.25	W9
		3.25-3.50	W10
WB823EH	19000E 25000N	0.50-0.75	W11
		0.75-1.00	W12
		1.00-1.50	W13
		1.50-2.00	W14
		2.00-2.25	W15
		2.25-2.50	W16
		2.50-2.75	W17
		2.75-3.00	W18
		3.00-3.25	W19
WB791EH	31000E 25000N	0.50-0.75	W20
		0.75-1.00	W21
		1.00-1.25	W22
		1.25-1.50	W23
		1.50-1.75	W24
		1.75-2.25	W25
		2.25-2.75	W26
		2.75-3.00	W27
3.00-3.25	W28		
WB772EH	25000E -5000N	1.00-1.25	W29
		1.25-1.50	W30
		1.50-2.00	W31
		2.00-2.25	W32
		2.25-2.50	W33
		2.50-2.75	W34
		2.75-3.00	W35
		3.00-3.25	W36
		3.25-3.50	W37
3.50-3.75	W38		
WB857EH	3000E 25000N	0.75-1.00	W39
		1.00-1.25	W40
		1.25-1.50	W41
		1.50-2.00	W42
		2.00-2.50	W43
2.50-3.00	W44		

Drill Hole	Location (mine coordinates)	Depth Interval (metres)	Sample name
		3.00-3.25	W45
		3.25-3.50	W46
		3.50-3.75	W47
		3.75-4.00	W48
WB839EH	8960E 1000N	0.00-0.25	W49
		0.25-0.50	W50
		0.50-0.75	W51
		0.75-1.00	W52
		1.00-1.50	W53
		1.50-1.75	W54
		1.75-2.00	W55
		2.00-2.25	W56
		2.25-2.50	W57
		2.50-2.75	W58
WB754EH	37000E 7000N	0.50-0.75	W59
		0.75-1.00	W60
		1.25-1.50	W61
		1.50-2.00	W62
		2.00-2.50	W63
		2.50-2.75	W64
		2.75-3.00	W65
		3.00-3.25	W66
		3.25-3.50	W67
		3.50-3.75	W68
WB781EH	17000E -9000N	0.75-1.00	W69
		1.00-1.50	W70
		1.50-1.75	W71
		1.75-2.25	W72
		2.25-2.75	W73
		2.75-3.25	W74
		3.25-3.50	W75
		3.50-3.75	W76
		3.75-4.00	W77
		4.00-4.25	W78

ANDOOM

TR221AB	-13500E 46750N	0.50-1.00	A1
		1.00-1.50	A2
		1.50-2.00	A3
		2.00-2.50	A4
		2.50-3.00	A5
		3.00-3.50	A6
TR057AB	-33000E 30250N	0.50-1.00	A7
		1.00-1.50	A8
		1.50-2.00	A9
		2.00-2.50	A10
		2.50-3.00	A11
		3.00-3.50	A12
		3.50-4.00	A13
		4.00-4.50	A14
		4.50-5.00	A15

Drill Hole	Location (mine coordinates)	Depth Interval (metres)	Sample name
AB074BF	-5000E 9000N	0.50-0.75	A16
		0.75-1.00	A17
		1.00-1.25	A18
		1.25-1.50	A19
		1.50-1.75	A20
		1.75-2.25	A21
		2.25-2.75	A22
		2.75-3.25	A23
		3.25-3.50	A24
		3.50-3.75	A25
AB003BF	-4000E 36000N	0.50-1.00	A26
		1.00-1.50	A27
		1.50-2.00	A28
		2.00-2.50	A29
		2.50-3.00	A30
AB059BF	6000E 16000N	0.50-1.00	A31
		1.00-1.50	A32
		1.50-2.00	A33
		2.00-2.50	A34
		2.50-3.00	A35
		3.00-3.50	A36
		3.50-4.00	A37
		4.00-4.50	A38
		4.50-5.00	A39
		5.00-5.50	A40
TR067AB	-21500E 38750N	0.00-0.50	A41
		0.50-1.00	A42
		1.00-1.50	A43
		1.50-2.00	A44
		2.00-2.50	A45
		2.50-3.00	A46
		3.00-3.50	A47
		3.50-4.00	A48
		4.00-4.50	A49
		4.50-4.75	A50
AB012BF	-2000E 50000N	0.50-1.00	A51
		1.00-1.50	A52
		1.50-2.00	A53
		2.00-2.50	A54
		2.50-3.00	A55
TR150AB	-20875E 27125N	0.50-1.00	A56
		1.00-1.50	A57
		1.50-2.00	A58
		2.00-2.50	A59
		2.50-3.00	A60
		3.00-3.50	A61
		3.50-4.00	A62
4.00-4.50	A63		

Appendix 2 Bauxite bulk chemistry
(ANALABS, Welshpool, WA)

	Al	P	Ca	Ti	Mn	Fe	Ga	Rb	Sr	Th	U
units	%	ppm	ppm	%	ppm	%	ppm	ppm	ppm	ppm	ppm
LOD	0.02	100	50	0.005	15	0.01	0.5	0.05	2	0.05	0.05
method	ICP-OES	OES	OES	OES	OES	OES	ICP-MS	MS	MS	MS	MS

Weipa

W5	31.3	157	<50	1.67	29	2.87	71.1	0.73	4	31.2	6.18
W14	28.0	186	67	1.58	78	5.87	66.7	1.58	5	41.7	6.53
W23	29.0	124	<50	1.48	42	4.14	66.8	1.72	5	39.4	7.25
W33	23.9	105	98	1.39	78	7.38	74.7	3.08	6	53.5	8.10
W43	27.0	248	54	1.60	30	3.03	84.2	1.41	4	34.6	5.63
W53	28.4	157	<50	1.47	29	3.58	73.6	0.91	4	42.2	6.60
W63	26.7	124	<50	1.46	42	3.48	66.8	1.72	5	40.5	5.65
W73	29.0	352	<50	1.49	51	2.84	92.5	0.92	3	36.1	5.95

Andoom

A3	23.0	408	98	1.35	98	14.3	58.2	1.49	3	16.4	4.23
A10	22.5	559	<50	1.43	52	9.35	68.4	0.61	2	16.0	2.99
A20	26.2	226	<50	1.67	87	8.72	54.5	1.15	3	22.1	4.03
A27	23.7	177	64	1.49	100	7.62	52.3	1.06	3	18.8	5.92
A35	26.4	139	64	1.79	154	7.41	56.2	0.80	6	19.5	3.72
A45	21.6	366	<50	1.33	70	12.4	62.2	0.88	2	16.7	2.75
A52	25.5	181	<50	1.45	116	10.0	62.9	1.20	4	18.2	4.97
A59	29.5	271	<50	1.94	80	6.78	56.9	0.90	4	16.9	5.63

LOD = Limit of detection

Appendix 3 Bauxite bulk chemistry
(Comalco Mineral Products XRF laboratory, Weipa)

	<u>Al₂O₃</u>	<u>SiO₂</u>	<u>Fe₂O₃</u>	<u>TiO₂</u>	<u>LOI</u>	(wt%)
Weipa						
W11	49.93	18.80	9.22	1.91	20.05	
W15	58.93	6.48	6.08	2.15	26.39	
W19	56.71	7.09	5.79	2.46	27.87	
W20	52.26	13.50	13.45	1.97	18.78	
W24	59.43	4.89	5.40	2.42	27.80	
W28	57.82	4.92	6.99	2.13	27.98	
W34	50.08	15.09	10.92	2.43	21.45	
W38	48.84	18.99	9.07	2.57	20.67	
W44	55.71	8.67	4.98	2.39	28.41	
W48	51.84	11.25	8.17	2.13	26.61	
W54	54.96	10.26	4.94	2.39	27.23	
W58	56.06	9.78	5.84	2.34	26.38	
W70	59.07	5.71	7.17	2.42	25.45	
W74	59.58	5.75	4.28	2.48	27.88	
W78A	54.67	7.62	7.50	2.25	28.04	
W78B	46.54	12.77	15.10	1.79	23.72	
Andoom						
A11	51.71	1.37	16.30	2.62	27.64	
A21	52.43	4.81	12.79	2.81	27.09	
A28	55.63	2.55	9.28	3.05	29.61	
A36	51.09	6.92	12.44	2.68	27.67	
A53	48.05	7.38	17.10	2.26	24.36	
A60	55.40	3.68	11.47	2.94	26.43	

Appendix 4 Bulk bauxite chemistry (wt%)
(Geology Department XRF laboratory, ANU)

	W3	W6	W10	W60	W64	W68
SiO ₂	4.89	6.46	7.37	15.09	7.76	11.39
TiO ₂	2.31	2.37	2.12	1.98	2.44	2.34
Al ₂ O ₃	59.25	58.01	54.99	47.92	57.46	53.56
Fe ₂ O ₃	4.58	3.65	6.58	12.28	4.71	6.06
MnO	0.00	0.00	0.00	0.02	0.00	0.00
MgO	0.16	0.15	0.16	0.16	0.16	0.15
CaO	0.00	0.03	0.00	0.01	0.01	0.01
Na ₂ O	0.12	0.05	0.11	0.11	0.10	0.11
K ₂ O	0.01	0.01	0.01	0.02	0.01	0.02
P ₂ O ₅	0.04	0.08	0.05	0.04	0.05	0.06
S	0.05	0.04	0.03	0.02	0.03	0.02
sum	71.41	70.84	71.43	77.65	72.74	73.72
LOI	28.79	29.60	29.23	22.65	27.61	26.62
loss @ 100°C	1.50	2.61	1.58	3.11	1.87	1.95

BIBLIOGRAPHY

- ANAND, R. R. and GILKES, R.J. (1984): Weathering of ilmenite in a lateritic pallid zone: *Clays and Clay Minerals*, v 32, pp 363-374.
- BAKER, G. (1958): Heavy minerals from the Weipa bauxites and associated sands. CSIRO, mineragr. Inv. Rep. 751 (unpubl.).
- BAKER, G.F.U., (1972): Origin of Darling Range bauxites, Western Australia; *Econ. Geol.* 67, 981-982.
- BARDOSSY, Gy. and ALEVA, G.J.J., (1990); Lateritic Bauxites; *Developments in Economic Geology*, 27, Elsevier.
- BARDOSSY, Gy., (1989); Lateritic bauxite deposits: a worldwide survey of observed facts;
- BARDOSSY, Gy., (1963); Die Entwicklung der Bauxitgeologie seit 1950; *Symp. Bauxites, Zagreb*, 1, 31-50.
- BATES, R.L. and JACKSON, J.A. (ed.), (1987); Glossary of Geology (3rd ed.); *American Geological Institute, Alexandria, Virginia.*
- BERNER, R. A., SJOBERG, E. L., VELBEL, M. A. & KROM, M. D. (1980): Dissolution of pyroxenes and amphiboles during weathering: *Science* v 207, 1205 - 1206.
- BERTHIER, P., (1821); Analyse de l'alumine hydratée; *Ann. des Mines*, 6, 531-534.
- BIRD, M.I. and CHIVAS, A.R., (1988); Oxygen isotope dating of the Australian regolith; *Nature*, v 331, no. 6156, pp 513-516.
- BIRD, M.I. and CHIVAS, A.R., (1989); Stable-isotope geochronology of the Australian regolith; *Geochimica et Cosmochimica Acta*, v 53, pp 3239-3256.
- BIRD, M.I., CHIVAS, A.R. and ANDREW, A.S. (1989); A stable-isotope study of lateritic bauxites; *Geochimica et Cosmochimica Acta*, v. 53, pp.1411-1420.
- BOULANGE, B., (1984); Les formations bauxitiques latéritiques de Côte d'Ivoire; *Travaux et documents d'ORSTOM, Paris*, 175, 341 pp.
- BOURKE, D.J., McCONACHIE, B.A., SENAPATI, N. and SLADE, J.C. (1988); A tectonic reconstruction for the basement rocks beneath the Carpentaria Basin; *Synopsis of paper presented at the 9th Australian Geological Convention, Brisbane.*
- BOURRIE, G. & PEDRO, G. (1979): La notion de pF, sa signification physicochimique et ses implications pedogenetiques, signification physicochimique. Relations entre le pF et l'activite de l'eau. *Sci. Sol*, 4, pp.313-322.
- BRAND, U. & VEIZER, J., (1983); Origin of Coated Grains: Trace Element Constraints;
- BRANTLEY, S.L., CRANE, S.R., CRERAR, D.A., HELLMANN, R. and STALLARD, R. (1986); Dissolution at dislocation etch pits in quartz; *Geochimica et Cosmochimica Acta*, v. 50, pp. 2349-2361.

- BREWER, R. (1964): Fabric and Mineral Analysis of Soils: *John Wiley & Sons, Inc.*
- BRIMHALL, G.H. & LEWIS, C.J., (1992); Bauxite and Lateritic Soil Ores; *Encyclopedia of Earth System Science, vol 1.*
- BRYCE, S.M., (1989); Weipa-Andoom Bauxite Pisolith Study; *Comalco technical report, W.T.R. 89/28.*
- BUCHANAN, F., (1807); A journey from Madras through the countries of Mysore, Canara and Malabar; *East India Co., London, 2, 436-461.*
- BUTTY, D.L. & CHAPALLAZ, C.A. (1984); Bauxite Genesis. In: JACOB, L. Jr. (ed.) (1984); Bauxite, Proceedings of the 1984 Bauxite Symposium, Los Angeles, California, February 27-March 1, 1984. *Society of Mining Engineers of American Institute of Mining, Metallurgical and Petroleum Engineers, Inc.*
- CAMPBELL, I.D., (1990) Study of Weipa bauxite pisoliths in thin-section; *Comalco technical report, WTR 90/22.*
- CAROZZI, A. V. (1960); *Microscopic Sedimentary Petrography*; Wiley, New York, 485 p.
- CHESWORTH, W., (1972); The stability of gibbsite and boehmite at the surface of the earth; *Clays and Clay Minerals*, v. 20, 369 - 374.
- CLAYBOURN, M., COLOMBEL, P. & CHALMERS, J. (1991) *Applied Spectroscopy*, v.45, p.280.
- COFFEY, D.D. and HOLLINGSWORTH, P.C. (1971); Shallow aquifer investigation, Weipa, North Queensland; *Comalco Limited, Melbourne.*
- CRUZ, M.D.R. and REAL, L.M. (1991); Practical determination of allophane and synthetic alumina and iron oxide gels by X-ray diffraction; *Clay Minerals*; v.26, pp.377-387.
- DAMMER, D., CHIVAS, A.R. & McDOUGALL, I. (Abstract) (1994); K-Ar dating of weathering-related cryptomelane and alunite from western and northern Australia; Abstracts of the 8th. International Conference on Geochronology, Cosmochronology and Isotope Geology; *U.S. Geological Survey Circular 1107*, p. 74.
- DANGIC, A. (1985): Kaolinisation of bauxite: a study in the Vlasenica bauxite area, Yugoslavia. 1. Alteration of Matrix; *Clays and Clay Minerals*, Vol. 33, No. 6, 517-524.
- DIDIER, P., FRITZ, B., NAHON, D. & TARDY, Y., (1983); Fe³⁺-kaolinites, Al-goethites, Al-hematites in tropical ferricretes. In: Petrology of Weathering and Soils, NAHON, D. & NOACK, Y., eds., *Mem. Sci. Geol., Strasbourg*, 71, pp. 35-44.
- DRENNEN, J.K. & LODDER, R.A. (1993): Pharmaceutical Applications of Near-infrared Spectrometry in PATONAY, G. ed. (1993): *Advances in Near-infrared Measurements*: JAI Press Inc. p. 93-112.

- DREVER, J. I. (1988): The geochemistry of natural waters - 2nd edition: Prentice Hall, Inc.
- DUBROEUCQ, D., GAVAUD, M. and MILLOT, G., (1988); A high bauxitic surface in the Amazone Territory of Venezuela; *Sci. Géol., Bull.*, 41, 1, 99-111.
- EDDINGTON, J.W., (1974); The operation and calibration of the electron microscope; *Philips Technical Library, Monographs in Practical Electron Microscopy in Materials Science*, mon. 1.
- EDWARDS, A.B. (1957): Quartz and heavy minerals in Weipa bauxite. CSIRO, minerag. Inv. Rep. 749 (unpub.).
- EDWARDS, A.B. (1958): Quartz and heavy minerals in bauxite of Weipa N10000/W15000 pit. *Ibid.*, 750 (unpub.).
- EGGLETON, R.A., (1987); Noncrystalline Fe-Si-Al-oxyhydroxides, *Clays and Clay Minerals*, vol. 35, no. 1, 29-37.
- EVANS, H.J., (1965); Bauxite deposits of Weipa. Geology of Australian ore deposits; *8th Comm. Min. Metall. Conf.*, 1, 396-401.
- EVANS, H.J., (1959); The geology and exploration of the Cape York Peninsula bauxite deposits in northern Queensland, *Qld. Govt. Min. J.*, 58, 679-88.
- FITZPATRICK, R.W. and SCHWERTMANN, U. (1982): Al-substituted goethite, an indicator of pedogenic and other weathering environments in South Africa. *Geoderma*, v. 27, p. 335-347.
- FREDERICKS, P.M., TATTERSALL, A. & DONALDSON, R. (1987): Near-Infrared Reflectance Analysis of Iron Ores: *Applied Spectroscopy*, v. 41, p. 1039-1042.
- FRITZ, B. and TARDY, Y., (1973); Étude thermodynamique et simulation du système gibbsite, quartz, kaolinite et gaz carbonique. Application á la genése des podzols et des bauxites; *Sci. Géol. Bull. Strasbourg*, 26, 339-367.
- FROST, R.L., FREDERICKS, P.M., CATTARIN, L., EGGLETON, R.A. & TILLEY, D.B., Abstract (1993); Mineral Mapping by Infra-red Microspectroscopy; *AIPEA 10th International Clay Conference*, July 1993 P-126.
- FULLER, H.W. and HALE, M.E., (1960); Determination of magnetisation distribution in thin films using electron microscopy; *Journal of Applied Physics*, v 31, p 238.
- GARDNER, L. R. (1970): A chemical model for the origin of gibbsite from kaolinite: *The American Mineralogist*, v 55, 1380 - 1389.
- GARRELS, R.M. & CHRIST, C.L. (1965): *Solutions, Minerals and Equilibria*, Harper and Row, New York.
- GOLDSTEIN, J.I. and YAKOWITZ, H., (1975); Practical scanning electron microscopy- Electron and ion microprobe analysis; *Plenum Press*.
- GRUBB, P.L.C. (1970): Mineralogy, geochemistry, and genesis of the bauxite deposit on the Gove and Mitchell Plateaux, Northern Australia: *Mineralium Deposita*, Berlin., 5, 248-272.

- GRUBB, P.L.C. (1971): Genesis of the Weipa bauxite deposits, N.E. Australia: *Mineralium Deposita*, Berlin. 6, 265-274.
- HEMMINGWAY, B.S. (1982): Gibbs free energies of formation for bayerite, nordstrandite, $\text{Al}(\text{OH})_2^+$, aluminium mobility and the formation of bauxites and laterites: *Advances in Physical Geochemistry*, vol. 2, 285-315.
- HEWAT, A. W. (1973): Harwell Report 73 / 239 and Ill. Report 74 / H625.
- HILL, R. J. & HOWARD, C. J. (1986): AAEC Report M112, Lucas Heights Research Laboratories, Menai, N.S.W. Australia.
- HILLEL, D., (1971); Soil and Water; *Academic Press, London*, 288pp.
II. Observations of soil grains: *Amer. J. Sci.* v. 282, 1214 - 1231.
In: PERYT, T.M., (1983) ed. Coated Grains; *Springer-Verlag*.
- INOUE, M., KITAMURA, K., TANINO, H., NAKAYAMA, H. and INUI, T., (1989): Alcohothermal treatments of gibbsite: mechanisms for the formation of boehmite: *Clays and Clay Minerals*, Vol. 37, No. 1, 71-80.
- JACOB, L. Jr. (ed.) (1984): Bauxite, Proceedings of the 1984 Bauxite Symposium, Los Angeles, California, February 27-March 1, 1984. Society of Mining Engineers of American Institute of Mining, Metallurgical and Petroleum Engineers, Inc.
- JEPSEN, K. & SCHELLMANN, W. (1974): Über den Stoffbestand und die Bildungsbedingungen der Bauxitlagerstätte Weipa, Australien: *Geologisches Jahrbuch*, Hannover. d.7, 19-106.
- JONES, H. A. (1965); Ferruginous oolites and pisolites; *Journal of Sedimentary Petrology*, v. 35, pp. 838-845.
- KISS, A.B., KERESZTURY, G. and FARKAS, L. (1980); Raman and i.r. spectra and structure of boehmite ($\gamma\text{-AlOOH}$); *Spectrochimica Acta*; v.36, pp. 653-658.
- KLUG, H. P. & ALEXANDER, L. E. (1974): *X-ray diffraction procedures for polycrystalline and amorphous materials*: Second edition, J. Wiley and Sons, New York.
- KOLESOVA, V.A. and RYSKIN, I.I. (1959); Infrared absorption spectrum of hydrargillite $\text{Al}(\text{OH})_3$; *Optics and Spectroscopy*; v.7, no.2, pp.165-167.
- KRINSLEY, D.H. and DOORNKAMP, J.C. (1973); Atlas of quartz sand surface textures; *Cambridge University Press* ; 91pp.
- LEA, A.M., (1925); Notes on some calcareous insect puparia: Record of the South Australian Museum v.3, pp. 35-36.
- LEEDER, M.R., (1982); Sedimentology, Process and Product; *George Allen & Unwin*.
- LOUGHNAN, F. C. & BAYLISS, P. (1961): The mineralogy of the bauxite deposits near Weipa, Queensland: *Amer. Mineral.* v 46, 209 - 217.

- LOUGHNAN, F.C. & SADLEIR, S.B., (1984); Geology of established bauxite-producing areas in Australia in JACOB, L. Jr. (ed.) (1984): Bauxite, Proceedings of the 1984 Bauxite Symposium, Los Angeles, California, February 27-March 1, 1984. *Society of Mining Engineers of American Institute of Mining, Metallurgical and Petroleum Engineers, Inc.*
- LOVERING, T.S., (1959); Significance of accumulator plants in rock weathering, *Bull. Geol. Soc. Amer.*, 70, 781-800.
- MACGEEHAN, P. (1972): Vertical zonation within the Aurukun bauxite deposit, north Queensland, Australia. 24th. Int. geol. Cong., Canada, 4, 424-434.
- MAIGNIEN, R., (1966); Review of research on laterites; *Unesco* .
- MAWSON, R., (1975); The geology of the Windellama area, New South Wales; *Journal and Proceedings, Royal Society of N.S.W.*, v 108, pp 29-36.
- MCCORMACK, C. (1985); Laterite Pisolites, *A.N.U. Dept. of Geol., unpubl. rept.*
- MCFARLANE, M.J., (1976); Laterite and Landscape; *Academic Press.*
- MCFARLANE, M.J., (1983); Laterites, in GOUDIE, A.S. and PYE, K., eds., Chemical sediments and geomorphology, *Academic Press, London*, 7-58.
- MCMILLAN, P.F. and HOFMEISTER, A.M., (1988); Infrared and Raman Spectroscopy; Reviews in mineralogy, v18, *Spectroscopic methods in mineralogy and geology, Mineralogical Society of America.*
- MELFI, A.J., TRESCASES, J., CARVALHO, A., BARROS DE OLIVEIRA, S.M., RIBEIRO FILHO, E., LAQUINTINE FORMOSO, M.L., (1988); The lateritic ore deposits of Brazil; *Sci. Géol., Bull.*, 41, 1, p 5-36, Strasbourg.
- MESSERSCHMIDT, R.G. & HARTHCOCK, M.A. (1988); Infra-red Microspectroscopy. Theory and Applications, *Marcel Dekker Inc.*, New York.
- MIKHAILOV, B.M., (1964); On the role of vegetation in lateritic weathering in the mountainous areas of the Liberian Shield (in Russian); *Doklady An SSSR, Moscow*, 157, 856-858.
- MÖLLER, K.D. & ROTHSCHILD, W.G. (1971); Far infra-red Spectroscopy; *Wiley-Interscience*; pp 128 - 160.
- MORGAN, M. (1992): The CMP4 method for calculating Bayer mineralogy: Comalco Mineral Products technical report, W.T.R. 92/14.
- MULHOLLAND, C. St. J., (1941); Bauxite Bungonia Windellama, *N.S.W. Dept. Mineral Resources GS 1941/013, unpublished.*
- NAHON, D., CAROZZI, A.V., PARRON, C. (1980); Lateritic weathering as a mechanism for the generation of ferruginous ooids. *Journal of Sedimentary Petrology*, vol. 50, No. 4, pp. 1287-1298.
- NAHON, D., JANOT, C., KARPOFF, A.M., PAQUET, H., & TARDY, Y. (1977): Mineralogy, petrography and structures of iron crusts (ferricretes) developed on sandstones in the western part of Sénégal. *Geoderma*, v. 19, p. 263-277.

- NAHON, D.B. (1976): Cuirasses ferrugineuses et encroûtements calcaires au Sénégal occidental et en Mauritanie. Systèmes évolutifs: géochimie, structures, relais et coexistence: Strasbourg, *Mém. Sci. Géol.*, No.44, 232 p.
- NAHON, D.B. (1991): Introduction to the petrology of soils and chemical weathering. John Wiley & Sons, Inc.
- OWEN, H.B., (1954): Bauxite in Australia; *Aus. Bur. Miner. Res. Geol. Geoph. Bull.* 24, 234 pp.
- PERSONS, B.S., (1970); Laterite: Genesis, Location, Use; *Plenum Press*.
- PERYEA, F.J. and KITTRICK, J.A. (1988): Relative Solubility of Corundum, Gibbsite, Boehmite and Diaspore at Standard State Conditions. *Clays and Clay Minerals*, v. 36, p. 391-396.
- PLUMB, K.A. & GOSTIN, V.A. (1973): Origin of Australian Bauxite Deposits. BMR Geology and Geophysics, record 1973 / 156.
- REIMER, T.O., (1983): Accretionary Lapilli in Volcanic Ash Falls: Physical Factors Governing Their Formation. In: PERYT, T.M., (1983) ed. Coated Grains; *Springer-Verlag*.
- RIETVELD, H. M. (1969): A profile refinement method for nuclear and magnetic structures: *Journal of Applied Crystallography*, v. 2, 65 - 71.
- SAMAMA, J. C. (1986): Ore Fields and Continental Weathering; Evolution of Ore Field Series: *A Hutchinson Ross Publication*: p. 267-297.
- SANGWAL, K. (1986): Etching processes and the investigation of minerals in RODRIGUEZ-CLEMENTE, R and TARDY, Y. ed. (1986); *Geochemistry and Mineral Formation in the Earth Surface; Proceedings of the International Meeting "Geochemistry of the Earth Surface and Processes of Mineral Formation"*; Granada, Spain, pp 715-731.
- SHELLMANN, W., (1983); A new definition of laterite; *Natural Resources and Development, Hannover/Tübingen*, 18, 7-21.
- SCHULZE, D. G. (1984): The influence of aluminum on iron oxides. VIII. Unit-cell dimensions of Al-substituted goethites and estimation of Al from them. *Clays and Clay Minerals*, vol 32, no.1, 36-44.
- SCHWERTMANN, U. (1985): Formation of secondary iron oxides in various environments (Abstract) in DREVER, J. I. (ed.), *The Chemistry of Weathering*, 119-120; D. Reidel Publishing Company.
- SCHWERTMANN, U. (1988): Occurrence and Formation of Iron Oxides in Various Pedoenvironments: in J.W. Stucki *et al.* (eds.), *Iron in Soils and Clay Minerals* : D.Reidel Publishing Company, p. 267 - 308.
- SCHWERTMANN, U. (1988); Some properties of soil and synthetic iron oxides, in STUCKI, J.W. *et al.* (eds.), *Iron in soils and clay minerals*, 203-250; D. Reidel Publishing Company.

- SHPANOV, Y. P., SIDORENKO, G.A. & STOLYAROVA, T.I. (1971): Akdalaite, a new hydrated variety of alumina: *International Geology Review*, v. 13, no. 5, pp. 675-680.
- SINGER, A. & HUANG, P. M. (1990): Effects of humic acid on the crystallisation of aluminium hydroxides: *Clays and Clay Minerals*, v 38, no. 1, 47 - 52.
- SOMM, A.F., (1975); Gove Bauxite Deposits, *N.T.; Econ. Geol. Aust. & Papua N.G., Aust. Inst. Min. & Metall. Mono 5*, vol. 1, pp. 964-968.
- SPECHT, R.L., SALT, R.B. & REYNOLDS, S.T. (1977): Vegetation in the vicinity of Weipa, North Queensland: *Proc. R. Soc. Qd.* vol. 88 pp. 17-38.
- STUMPF, H.C., RUSSELL, A.S., NEWSOME, J.W. and TUCKER, C.M. (1950): Thermal transformations of aluminas and alumina hydrates; *Industrial and Engineering Chemistry*; v.42, pp 1398-1403.
- TARDY, Y. & ROQUIN, C. (1992): Geochemistry and evolution of lateritic landscapes in Martini, I.P. & Chesworth, W. (eds.) *Developments in Earth Surface Processes 2: Weathering, Soils and Paleosols*: Elsevier, pp. 407-443.
- TARDY, Y. (1992): Diversity and terminology of lateritic profiles in Martini, I.P. & Chesworth, W. (eds.); *Developments in Earth Surface Processes 2: Weathering, Soils and Paleosols*: Elsevier, pp. 379-405.
- TARDY, Y. and NAHON, D., (1985); Geochemistry of laterites, stability of Al-goethite, Al-hematite, and Fe³⁺-kaolinite in bauxites and ferricretes: an approach to the mechanism of concretion formation; *Am. J. of Sc.*, v 285, p 865-903.
- TARDY, Y., BARDOSSY, G. & NAHON, D. (1988a): Fluctuations de l'activité de l'eau et successions de minéraux hydratés et déshydratés au sein des profils latéritiques ferrugineux et bauxitiques. *C.R. Acad. Sci., Paris, Ser.II*, 307: 753-759.
- TARDY, Y., BOEGLIN, J., NOVIKOFF, A. & ROQUIN, C. (1993): Petrological and geochemical classification of bauxites and iron-rich laterites: *AIPEA 10th International Clay Conference*.
- TAYLOR, G. and RUXTON, B.P., (1987); A duricrust catena in South-east Australia, *Z. Geomorph. N.F.*, 31, 4, pp 385-410, Berlin, Stuttgart.
- TAYLOR, G., EGGLETON, R. A., HOLZHAUER, C. C., MACONACHIE, L. A., GORDON, M., BROWN, M. C. & MCQUEEN, K. G. (1992): Cool Climate Lateritic and Bauxitic Weathering: *The Journal of Geology*, v. 100, p. 669 -677.
- TAYLOR, J. C. (1991): Computer Programs for Standardless Quantitative Analysis of Minerals Using the Full Powder Diffraction Profile: *Powder Diffraction*, v. 6, no. 1, 2 - 9.
- TETTENHORST, R. & HOFMANN, D. A. (1980): Crystal chemistry of boehmite: *Clays and Clay Minerals*, v. 28, no. 5, 373 -380.
- THOMPSON, R. and OLDFIELD, F., (1986); Environmental magnetism; *Allen & Unwin..*

- TROLAND, F. & TARDY, Y. (1987): The stabilities of gibbsite, boehmite, amorphous goethites and aluminous hematites in bauxites, ferricretes and laterites as a function of water activity, temperature and particle size: *Geochim. Cosmochim. Acta*, v. 51, 945-957.
- VAIL, P.R. and HARDENBOL, J. (1979); Sea-level changes during the Tertiary; *Oceanus* 22; pp.71-79.
- VALETON, I. and MELFI, A.J., (1988); Distribution pattern of bauxites in the Cataguases area (SE-Brazil), in relation to Lower Tertiary palaeogeography and younger tectonics; *Sci. Géol., Bull.*, 41, 1, p 85-98, Strasbourg.
- VALETON, I., (1972); Developments in Soil Science 1, Bauxites; *Elsevier Publishing Company, Amsterdam*.
- VIOLANTE, A. & HUANG, P.M. (1992): Effect of tartaric acid and pH on the nature and physicochemical properties of short-range ordered aluminium precipitation products. *Clays and Clay Minerals*, vol. 40, No.4, 462-469.
- WILES, D. B. & YOUNG, R. A. (1981): *Journal of Applied Crystallography* , v. 14, 149 - 151.
- WILL, HUANG & PARRISH (1983): *Journal of Applied Crystallography* , v. 26, 611 - 622.
- WORMALD, J., (1973); *Diffraction Methods*; *Oxford University Press*.
- YAMAGUCHI, G., YANAGIDA, H. & ONO, S. (1964a): A New Alumina Hydrate, Tohdite ($5\text{Al}_2\text{O}_3 \cdot \text{H}_2\text{O}$): *Chem. Soc. Japan Bull.*, v. 37, no. 5.
- YAMAGUCHI, G., YANAGIDA, H. & ONO, S. (1964b): The Crystal Structure of Tohdite: *Chem. Soc. Japan Bull.*, v. 37, no. 10.